RUTHENIUM NANOCRYSTALS WITH A FACE-CENTERED CUBIC STRUCTURE AND WELL-CONTROLLED FACETS

A Dissertation
Presented to
The Academic Faculty

by

Ming Zhao

In Partial Fulfillment
of the Requirements for the Degree
of Doctor of Philosophy in the
School of Chemistry and Biochemistry

Georgia Institute of Technology
August 2019

RUTHENIUM NANOCRYSTALS WITH A FACE-CENTERED CUBIC STRUCTURE AND WELL-CONTROLLED FACETS

Approved by:

Dr. Younan Xia, Advisor
Department of Biomedical Engineering
Georgia Institute of Technology

Dr. Angus P. Wilkinson
School of Chemistry and Biochemistry
Georgia Institute of Technology

Dr. Ronghu Wu
School of Chemistry and Biochemistry
Georgia Institute of Technology

Dr. Z. John Zhang
School of Chemistry and Biochemistry
Georgia Institute of Technology

Dr. Seung Woo Lee
School of Mechanical Engineering
Georgia Institute of Technology

Date Approved: [April 25, 2019]

Dedicated to my parents, Denglou Zhao and Chuanhong Jiang, and my girlfriend, Shi Shi, for their constant love and support throughout this journey.

ACKNOWLEDGEMENTS

The journey to this final stage of my Ph.D. study could not have been possible without the constant support and help of many people in my life. First and foremost, I would like to express my deepest gratitude to my graduate advisor, Professor Younan Xia, for the tremendous support and guidance. His expertise, enthusiasm, and kindness were critical to my development as a scientist and I have learnt an enormous amount from him. I would also like to extend my thanks to Professors Angus P. Wilkinson, Ronghu Wu, John Zhang, and Seung Woo Lee for serving on my dissertation committee, and for all of their advice and support.

My special thanks go to Professor Dong Qin, for her advice and constant support, not only on research but also on life as well. I would also like to make special thanks to Dr. Xuan Yang and Jessica Shang for helping me to start my research and new life in Atlanta. Additionally, I sincerely appreciate the support from many people at Georgia Tech: Dr. Zach Hood, Dr. Kyle D. Gilroy, Dr. Madeline Vara, Dr. Da Huo, Dr. Jiajia Xue, Dr. Shan Zhou, Dr. Aleksey Ruditskiy, Dr. Legna Figueroa-Cosme, Zhiheng Lyu, Zitao Chen, Zhenming Cao, Ruhui Chen, Minghao Xie, Yifeng Shi, and many other current and former members of the Xia Group. I also want to extend my great thanks to Professor Manos Mavrikakis, Dr. Luke T. Roling, Dr. Ahmed O Elnabawy, Lang Xu for their computational efforts and Dr. Miaofang Chi for the electron microscopy analysis.

My sincerest thanks go to my parents, Denglou Zhao and Chuanhong Jiang, my sister and nephew, Jing Zhao and Zichen Li, and my girlfriend, Shi Shi. It is your love and support that help me move forward and make me positive all the time.

TABLE OF CONTENTS

ACKNOWLEDGEMENTS **iv**

LIST OF TABLES **viii**

LIST OF FIGURES **x**

LIST OF SYMBOLS AND ABBREVIATIONS **xix**

SUMMARY **xxii**

CHAPTER

1. Introduction **1**

1.1 Colloidal Noble-Metal Nanocrystals 1

1.1.1 Facet-Controlled Synthesis 4

1.1.2 Phase-Controlled Synthesis 6

1.2 Ruthenium Nanocrystals: Challenges and Opportunities 8

1.3 Homogeneous *vs.* Heterogeneous Nucleation 10

1.4 Scope of This Work 13

1.5 Notes to Chapter 1 16

1.6 References 17

2. Synthesis and Characterization of Ruthenium Cubic Nanocages with a Face-Centered Cubic Structure by Templating with Palladium Nanocubes **22**

2.1 Introduction 22

2.2 Results and Discussion 24

2.3 Conclusion 45

2.4 Experimental Section 46

2.5 Notes to Chapter 2 52

2.6 References 53

3. Facile Synthesis of Ruthenium-Based Octahedral Nanocages with Ultrathin Walls in a Face-Centered Cubic Structure 59

3.1 Introduction 59

3.2 Results and Discussion 62

3.3 Conclusion 82

3.4 Experimental Section 82

3.5 Notes to Chapter 3 89

3.6 References 90

4. Synthesis of Ruthenium Icosahedral Nanocages with a Face-Centered-Cubic Structure and Evaluation of Their Catalytic Properties 94

4.1 Introduction 94

4.2 Results and Discussion 97

4.3 Conclusion 126

4.4 Experimental Section 127

4.5 Notes to Chapter 4 136

4.6 References 137

5. Ruthenium Octahedral Nanocrystals with a Face-Centered Cubic Structure, {111} Facets, Thermal Stability up to 400 °C and Enhanced Catalytic Activity 142

5.1 Introduction 142

5.2 Results and Discussion 146

5.3 Conclusion 166

5.4 Experimental Section 167

5.5 Notes to Chapter 2 170

5.6 References 171

6. Ruthenium Nanoframes in the Face-Centered Cubic Phase: Facile Synthesis and Their Enhanced Catalytic Performance 176

6.1 Introduction 176

6.2 Results and Discussion 178

6.3 Conclusion 198

6.4 Experimental Section 198

6.5 Notes to Chapter 6 201

6.6 References 202

7. Conclusion and Future Directions 207

7.1 Conclusion 207

7.2 Future Directions 211

7.3 Notes to Chapter 7 213

7.4 References 214

LIST OF TABLES

Table 2.1 Binding energies of 14 atomic and molecular species on all six model surfaces studied. 39

Table 2.2 Preferred binding sites of atomic and molecular species on all model surfaces studied. 41

Table 2.3 Calculated binding energies of N* and N_2*, and activation energy barriers to N_2* dissociation on *hcp* and *fcc* Ru surface models. 42

Table 3.1 Comparison of the elemental compositions for Pd@Ru core–shell octahedra and Ru nanocages prepared using the standard procedure except for the use of different amounts of Ru(III) precursor. 70

Table 3.2 Binding energies of 14 atomic and molecular species on all surfaces studied. 77

Table 3.3 Preferred binding sites of 14 atomic and molecular species on all surfaces studied. 78

Table 3.4 Binding energies calculated for the adsorbed atomic nitrogen and molecular nitrogen, activation energy barriers to the dissociation of N_2* to N*. 80

Table 4.1 Molar ratio between Br^- and Ru before and after washing for three times. 111

Table 4.2 Binding energies and sites of 14 atomic and molecular species on the pure Ru icosahedral (*fcc*) model surface. 118

Table 4.3 Binding energies calculated for the adsorbed atomic nitrogen and molecular nitrogen, activation energy barriers to the dissociation of N_2* to N*. 122

Table 4.4 Convergence of the binding energy of atomic N versus unit cell size for octahedral nanocages. 132

Table 5.1 Comparison of the catalytic performance of the Ru catalysts in the present work with those of the representative Ru/RuO_2 systems reported in the literature toward oxygen evolution reaction. 165

LIST OF FIGURES

Figure 1.1	Examples of different Au suspensions that display various colors.	2
Figure 1.2	Examples of metal nanocrystals with different shapes.	3
Figure 1.3	Pd nanocrystals with various surface structures and their surface structure-dependent catalytic performance.	5
Figure 1.4	Fe-Pt nanoparticles with a face-centered tetragonal structure and their catalytic and magnetic properties.	7
Figure 1.5	Examples of Ru nanocrystals with different shapes.	9
Figure 1.6	Plots showing the comparison of homogeneous and heterogenous nucleation.	12
Figure 2.1	Schematic illustration of the major steps involved in the synthesis of Ru nanocages。	24
Figure 2.2	TEM images of 6-, 10-, and 18-nm Pd nanocubes.	25
Figure 2.3	TEM and EDX mapping images of Pd@Ru core–shell nanocubes.	26
Figure 2.4	TEM images of Pd@Ru nanocrystals prepared using the standard protocol except for the absence of PVP in the precursor solution.	26
Figure 2.5	TEM images of Pd@Ru nanocrystals prepared using the standard protocol except for the use of different injection rates of the precursor solution.	28

Figure 2.6 TEM images of typical Pd@Ru core−shell nanocubes prepared from 10-nm Pd cubes using the standard procedure except at different reaction temperature. 30

Figure 2.7 TEM and EDX mapping images of Ru cubic nanocages. 31

Figure 2.8 TEM images of Pd@Ru core−shell nanocubes and Ru cubic nanocages prepared using 6- and 18-nm Pd cubic seeds. 34

Figure 2.9 XRD patterns of Ru nanocages prepared using the standard protocol except for the use of different amount of Ru(III) precursor. 35

Figure 2.10 TEM images of Pd@Ru nanocrystals prepared using the standard protocol except for the use of different amount of Ru(III) precursor. 36

Figure 2.11 TEM images of hollow Ru nanocrystals prepared using the standard protocol except for the use of different amount of Ru(III) precursor. 37

Figure 2.12 Potential energy surfaces for N_2 dissociation on the surfaces of *fcc* and *hcp* Ru nanocrystals. 44

Figure 3.1 TEM images of Pd octahedra with different edge lengths. 61

Figure 3.2 TEM and EDX mapping images of the Pd@Ru core–shell nanocrystals synthesized from 18-nm Pd octahedral seeds. 62

Figure 3.3 TEM and EDX mapping images of the Ru octahedral nanocrystals synthesized from 18-nm Pd octahedral seeds. 63

Figure 3.4 XRD pattern of the 18-nm Ru octahedral nanocages. 65

Figure 3.5 TEM images of Pd@Ru nanocrystals and hollow Ru nanocrystals prepared using the standard protocol except for the use of different injection rates of Ru(III) precursor. 66

Figure 3.6 TEM images of Pd@Ru nanocrystals and hollow Ru nanocrystals prepared using the standard protocol except for the absence of KBr and the use of different reaction temperature. 68

Figure 3.7 TEM images of Pd@Ru nanocrystals and hollow Ru nanocrystals prepared using the standard protocol except for the use of different amount of Ru(III) precursor. 70

Figure 3.8 TEM images of 12- and 26-nm Pd@Ru core–shell octahedra and Ru octahedral nanocages. 72

Figure 3.9 The *in-situ* XRD patterns of the *fcc* Ru nanocages. 73

Figure 3.10 Comparison of the catalytic activities towards the reduction of 4-nitrophenol for Ru cubic and octahedral nanocages. 74

Figure 3.11 Potential energy surfaces for N_2 dissociation on the surface of *hcp* Ru nanoparticles and *fcc* Ru octahedral nanocages. 76

Figure 3.12 All four Ru nanocage models with Pd impurities and the associated six surfaces studied. 87

Figure 4.1 Schematic illustrating the major steps involved in the formation of Pd@Ru core−shell icosahedra and Ru icosahedral nanocages. 97

Figure 4.2 TEM and EDX mapping images of Pd@Ru core–shell icosahedra. 98

Figure 4.3 TEM images of Ru icosahedral nanocages. 99

Figure 4.4 XRD pattern of Ru icosahedral nanocages. 100

Figure 4.5 TEM images of Pd@Ru nanocrystals prepared using the standard protocol except for the absence of KBr and use of different amounts of Ru(III) precursor. 101

Figure 4.6 Quantitative analysis of the conversion of Ru(III) ions to Ru(0) atoms during the synthesis of Pd@Ru core−shell icosahedra under different conditions. 102

Figure 4.7 TEM images of Pd@Ru nanocrystals and their corresponding nanocages prepared from 12 nm Pd icosahedra using the standard procedure except using different injection rates. 105

Figure 4.8 TEM images of Pd@Ru nanocrystals and their corresponding nanocages prepared from 12 nm Pd icosahedra using the standard procedure except introducing different amounts of $RuCl_3$. 106

Figure 4.9 TEM images of the Pd@Ru nanocrystals prepared from 12-nm Pd icosahedra using the standard procedure except at different reaction temperatures. 107

Figure 4.10 TEM images of the products prepared using different etching conditions. 108

Figure 4.11 *In situ* XRD patterns of *fcc* Ru icosahedral nanocages. 110

Figure 4.12 TEM images of Ru icosahedral nanocages heated to different temperatures 110

Figure 4.13 Absorption spectra of the reaction solutions for the reduction of 4-nitrophenol at different times points in the presence of Pd@Ru core−shell nanocrystals and Ru nanocages with cubic, octahedral, and icosahedral shapes. 112

Figure 4.14 Comparison of the catalytic activities of Pd@Ru core−shell cubes, octahedra, and icosahedra toward the reduction of 4-nitrophenol by $NaBH_4$ and the decomposition of hydrazine. 114

Figure 4.15 Comparison of the catalytic activities of Ru cubic, octahedral and icosahedral nanocages toward the reduction of 4-nitrophenol by $NaBH_4$ and the decomposition of hydrazine. 116

Figure 4.16 Top and side views of the pure *fcc*-Ru icosahedral nanocage model. 119

Figure 4.17 Potential energy surfaces for N_2 dissociation on the surfaces of *hcp*-Ru nanoparticles and *fcc*-Ru nanocages. 123

Figure 4.18 All *fcc*-Ru icosahedral nanocage models with Pd impurities studied. 133

Figure 4.19 All *fcc*-Ru octahedral nanocage models with Pd impurities studied. 135

Figure 5.1 TEM image of the Rh cubic seeds for the standard synthesis. 145

Figure 5.2 TEM and EDX mapping images of *fcc*-Ru octahedra. 145

Figure 5.3 XPS spectra of Rh cubic seeds and *fcc*-Ru octahedra. 147

Figure 5.4 TEM images of the Ru nanocrystals collected at different stages of a standard synthesis. 148

Figure 5.5 TEM images of the Ru nanocrystals prepared using the standard protocol except for the use of different amounts of Rh cubic seeds. 149

Figure 5.6 TEM images of the Ru nanocrystals prepared using the standard protocol except for the use of different amounts of precursor. 150

Figure 5.7 TEM image of the Ru nanocrystals prepared using the standard protocol except for the use of different volumes of HCHO. 151

Figure 5.8 TEM images of the Ru nanocrystals prepared using the standard protocol except for the use of different reaction temperatures. 152

Figure 5.9 *In situ* HRTEM images recorded from the same Ru octahedron heated at various temperatures. 154

Figure 5.10 EDX mapping analysis of the Ru octahedra annealed at 400 °C. 155

Figure 5.11 XPS analysis of the Ru octahedra annealed at 400 °C. 156

Figure 5.12 *In situ* XRD patterns of *fcc* Ru octahedral nanocrystals heated to temperatures. 157

Figure 5.13 TEM images of the Ru nanocrystals prepared from 6- and 10-nm Pd nanocubes. 158

Figure 5.14 TEM images of *hcp* and *fcc* Ru nanoparticles. 159

Figure 1.15 CV curves of different Ru catalysts. 160

Figure 5.16 Comparison of the catalytic properties of different Ru catalysts toward oxygen evolution. 161

Figure 5.17 Mass activity of different Ru catalysts toward oxygen evolution. 162

Figure 5.18 XPS spectrum of the Ru octahedra after electrochemical test. 163

Figure 5.19 STEM images of the Ru octahedra after electrochemical test. 164

Figure 6.1 TEM image of the Pd cubic seeds for the synthesis of Ru cuboctahedral nanoframes. 179

Figure 6.2 TEM and EDX mapping images of Pd@Ru core–frame cuboctahedra. 180

Figure 6.3 TEM images of the intermediate products obtained at different stages of a standard synthesis. 181

Figure 6.4 TEM and EDX mapping images of Ru cuboctahedral nanoframes. 182

Figure 6.5 XRD patterns of Ru cuboctahedral nanoframes. 183

Figure 6.6 TEM images of the solid products obtained using the standard protocol except for the absence of Ru(III) precursor and Pd cubes. 184

Figure 6.7 TEM images of the Ru cuboctahedral nanoframes prepared using truncated Pd nanocubes as seeds. 185

Figure 6.8 TEM images of the Pd–Ru nanocrystals prepared using the standard protocol except for the involvement of different amounts of KBr and Ru(III) precursor. 186

Figure 6.9 TEM images of Pd–Ru nanocrystals and the corresponding Ru nanoframes prepared using the standard protocol except for the use of different amounts of precursor. 187

Figure 6.10 TEM images of the Pd–Ru nanocrystals prepared using the standard protocol except for the use of different temperatures. 190

Figure 6.11 TEM images of the hollow Ru nanocrystals prepared from 6- and 18-nm Pd nanocubes. 190

Figure 6.12 Schematic illustration of major steps involved in the formation of Ru cuboctahedral nanoframes. 192

Figure 6.13 TEM images of the Ru cuboctahedral nanoframes upon heating for 1 h at various temperatures. 194

Figure 6.14 XRD patterns recorded *in situ* from the Ru cuboctahedral nanoframes after heating to different temperatures. 194

Figure 6.15 TEM images of XRD patterns of *hcp* and *fcc* Ru nanoparticles. 196

Figure 6.16 Comparison of the activities of various catalysts based upon *hcp*-Ru nanoparticles, *fcc*-Ru nanoparticles, and *fcc*-Ru cuboctahedral nanoframes towards hydrazine decomposition. 197

LIST OF SYMBOLS AND ABBREVIATIONS

AA	ascorbic acid
bcc	body-centered cubic
BE	binding energy
$C_6H_5NO_3$	4-nitrophenol
C_{dl}	double layer capacitance
CI-NEB	climbing image nudged elastic band
CV	cyclic voltammetry
D	diffusion coefficient
D_0	diffusion pre-exponential factor
DFT	density functional theory
DI	deionized
E_a	activation energy
ECSA	electrochemical surface area
E_{diff}	potential energy barrier to diffusion
EDX	energy-dispersive X-ray spectroscopy
EG	ethylene glycol
FAO	formic acid oxidation
fcc	face-centered cubic
fct	face-centered tetragonal
$FeCl_3$	iron(III) chloride
GGA	generalized gradient approximation

H_2SO_4	sulfuric acid
HAABF	high-angle annular bright-field
HAADF	high-angle annular dark-field
HCHO	formaldehyde
HCl	hydrochloric acid
hcp	hexagonal close-packed
HRTEM	high-resolution transmission electron microscopy
ICP-MS	inductively-coupled plasma mass spectrometry
IEN	Institute for Electronics and Nanotechnology
k	rate constant
KBr	potassium bromide
KCl	potassium chloride
LSPR	localized surface plasmon resonance
LSV	linear sweep voltammogram
MTP	multi-twinned particle
$N_2H_4{\cdot}H_2O$	hydrazine monohydrate
Na_2PdCl_4	sodium tetrachloropalladate(II)
Na_3RhCl_6	sodium hexachlororhodate(III)
$NaBH_4$	sodium borohydride
N-N TS	transition state of N_2 dissociation
ORNL	Oak Ridge National Laboratory
ORR	oxygen reduction reaction
PAW	projector augmented wave

PES	potential energy surface
PGM	platinum-group metal
ppb	part per billion
PTFE	polytetrafluoroethylene
PVP	poly(vinyl pyrrolidone)
R	ideal gas constant
RHE	reversible hydrogen electrode
$Ru(acac)_3$	2,4-pentaedionate
$RuCl_3 \cdot xH_2O$	ruthenium(III) chloride hydrate
SHE	standard hydrogen electrode
STEM	scanning transmission electron microscopy
T	absolute temperature
TEG	triethylene glycol
TEM	transmission electron microscopy
UV-vis	ultraviolet–visible
VASP	Vienna *ab initio* Simulation Package
XRD	X-ray diffraction

SUMMARY

Ruthenium (Ru) is an intriguing catalytic material for a variety of reactions. However, its extremely low abundance in the earth crust and ever-increasing price have created a barrier to the large-scale use of this metal. One solution to this issue is to engineer the shape or surface structure, as well as the crystal phase of Ru nanocrystals, in an attempt to optimize their catalytic properties. This dissertation is focused on the development of synthetic strategies for the facile synthesis of Ru nanocrystals with a face-centered cubic (*fcc*) phase and well-defined surface structures. Based on the integration of seed-mediated growth and wet chemical etching, I was were able to fabricate Ru nanocages with a cubic, octahedral, or icosahedral shape. The as-synthesized nanocages were characterized by ultrathin and porous walls (< 1.2 nm) as well as well-controlled surface structures. Most interestingly, the Ru nanocages adopted an *fcc* phase rather than the conventional hexagonal close-packed (*hcp*) structure typical of bulk Ru. Both the *fcc* phase and surface structures of the nanocages could be well preserved up to 300 °C. The facet-dependent properties of the *fcc*-Ru nanocages were evaluated toward the reduction of 4-nitrophenol and hydrazine decomposition. Density functional theory calculations suggested the enhanced catalytic performance of the *fcc*-Ru nanocages toward N_2 dissociation for ammonia synthesis relative to *hcp*-Ru nanoparticles. I also developed a hydrothermal approach to the synthesis of *fcc*-Ru octahedra with enhanced thermal stability using Rh nanocubes as the seeds. In particular, the *fcc*-Ru octahedra could retain both the crystal phase and the octahedral shape up to 400 °C. When benchmarked against the *hcp*-Ru nanoparticles, the octahedral nanocrystals exhibited enhancement in terms of specific

activity toward oxygen evolution. In the last project, I developed a facile method for the synthesis of *fcc*-Ru cuboctahedral nanoframes *via* the galvanic replacement between Pd seeds and a Ru(III) precursor. The nanoframes could largely retain the *fcc* phase and frame structure up to 350 °C. When used as catalysts for hydrazine decomposition, both the activity and selectivity of the *fcc*-Ru nanoframes were substantially improved relative to *hcp*-Ru nanoparticles.

CHAPTER 1

INTRODUCTION

1.1 Colloidal Noble-Metal Nanocrystals

Noble metals play an indispensable role in a variety of applications including catalysis, photonics, electronics, energy, and biomedicine, among others [1–8]. A majority of these applications require the use of noble metals in the form of nanocrystals with at least one dimension in the range of 1–100 nm. Simply by decreasing the size to nanometer scale, noble metals exhibit many fascinating properties that can not be achieved by their bulk counterparts [9–11]. One impressive example can be found in the substantially increased surface-to-volume ratio of nanomaterials for catalysis. For a certain amount of catalytic materials, when the size shrinks from 10 μm to 10 nm, their surface area will be increased by 1000 times. Since the surface atoms are those that directly serve as the active sites for catalytic reactions, this method could theoretically reduce the loading of catalytic materials by 1000 times and thus facilitate the sustainable use of noble metals in various applications.

Another compelling example is gold (Au), whose bulk state shines a bright metallic yellow and is considered as the least reactive metal. When processed as nanomaterials, Au displays a range of surprising properties different from its bulk form. The most striking features are the various colors displayed by the suspensions of Au nanoparticles with different sizes or shapes, as shown in Figure 1.1 [12]. The unique optical properties of Au nanomaterials, known as localized surface plasmon resonance (LSPR), have enabled many applications in chemistry and medicine, including sensing, drug delivery, image contrast enhancement, and cancer theranostics [12–17]. Additionally, Au nanoparticles with

diameters less than 10 nm was found to show remarkable catalytic activity toward many reactions such as CO oxidation and propylene epoxidation, opening new opportunities for this metal.

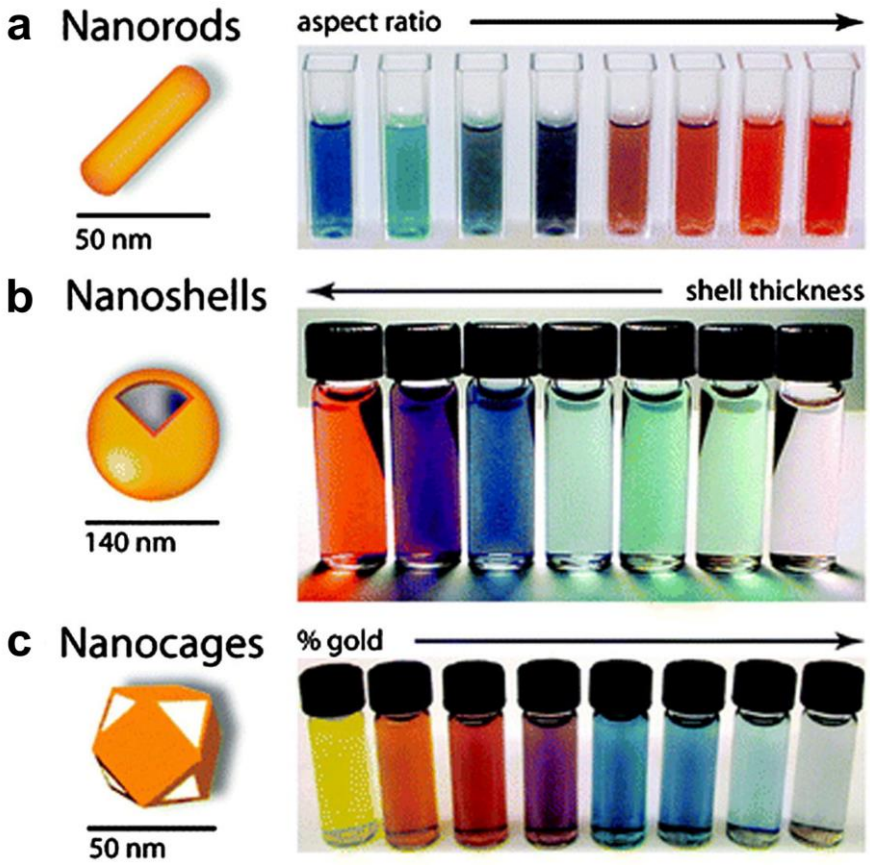

Figure 1.1. Gold nanoparticles commonly applied to biomedical applications. (a) Gold nanorods, (b) silica@gold core–shell nanoparticles, and (c) gold nanocages. The different colors of these suspensions arise from the collective excitation of their conduction electrons, or localized surface plasmon resonance modes. The photon absorption varies with (a) aspect ratio, (b) shell thickness, and/or (c) galvanic displacement by gold. (Reprinted with permission from [13]. Copyright 2012 The Royal Society of Chemistry.)

Despite the intriguing properties of noble-metal nanocrystals, several obstacles still need to overcome in order to apply them to the large-scale use. The major issue lies in their

extremely low abundance in the earth crust (typically parts per billion or ppb level) and ever-increasing prices [18]. To this end, one has to decrease the loading of noble metals by improving their performance, especially for catalytic applications. However, one can not rely on continuously decreasing the size of nanomaterials because the catalytic performance would be ultimately compromised by the presence of increased portion of less desired corner and edge atoms (*e.g.*, Pt nanoparticles for oxygen reduction) [18–21]. Additionally, when the particle size is reduced, the sintering of nanoparticles during long-term operation became another issue. Therefore, there is an urgent need to explore new strategies for the design of noble-metal nanocrystals with enhanced properties.

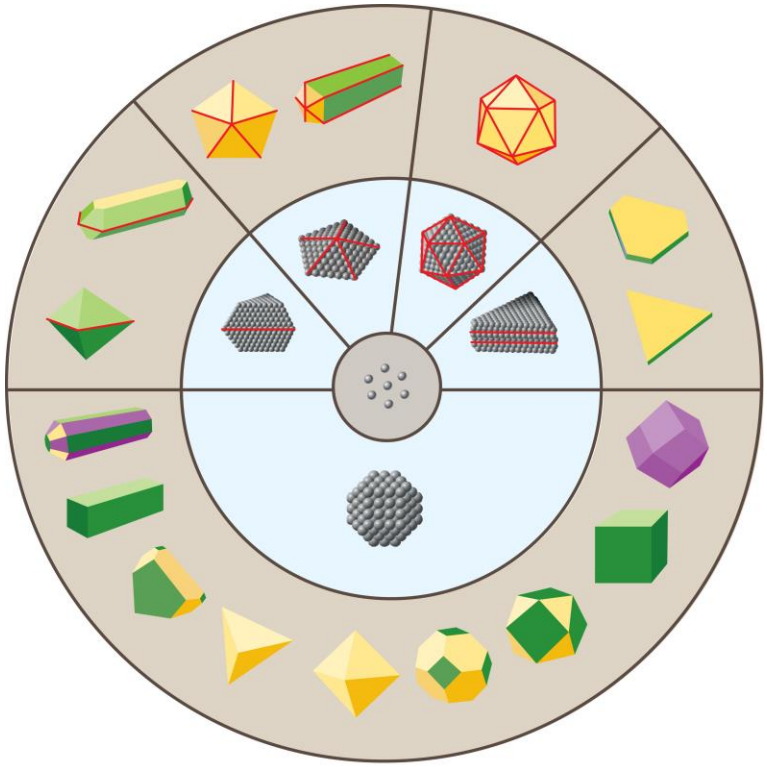

Figure 1.2. Examples of metal nanocrystals with different shapes, including those with single-crystal, single- and multiply-twinned, and nanocrystals with staking fault-lined structures. (Reprinted with permission from [22]. Copyright 2016 Annual Reviews.)

1.1.1 Facet-Controlled Synthesis

One powerful method for enhancing the properties of noble-metal nanocrystals is to engineer their facets and thus surface structures given the fact that the surface atoms essentially define the active sites and energetics of a catalytic reaction [22]. The last decade has witnessed the great accomplishment in controlling the synthesis of noble-metal nanocrystals with diverse internal structures and shapes. Typical examples include single-crystal and twinned nanocrystals, as well as those with planer defects or stacking faults. The representative shapes contain sphere, cube, cuboctahedron, octahedron, decahedron, icosahedron, right bipyramid, plate, rod, and wires (Figure 1.2) [22]. Significantly, the properties of noble-metal nanocrystals show strong dependence on their internal and/or surface structure. Our group have synthesized Pd nanocubes, bipyramids, octahedra, tetrahedra, decahedra, and icosahedra (Figure 1.3a–f) to comprehensively investigate the correlation between the surface structure and catalytic performance [23]. When used as catalysts for formic acid oxidation (FAO), all the Pd nanocrystals with well-defined shapes exhibited enhanced specific activity relative to the commercial Pd black catalyst. In particular, the Pd{100} facets were found to be catalytically more active than Pd{111} facets in catalyzing the oxidation of formic acid molecules while the twin defects showed superior performance than both the {100} and {111} facets (Figure 1.3g). In addition to the catalytic activity, the surface structure also has a significant impact on the selectivity of noble-metal catalysts toward various reactions. When Pt nanocrystals were employed as catalysts for benzene hydrogenation, only cyclohexane was produced on the {100}-enclosed Pt nanocubes while both cyclohexane and cyclohexene were formed on Pt cuboctahedral nanocrystals, which were enclosed by a mix of {100} and {111} facets [24].

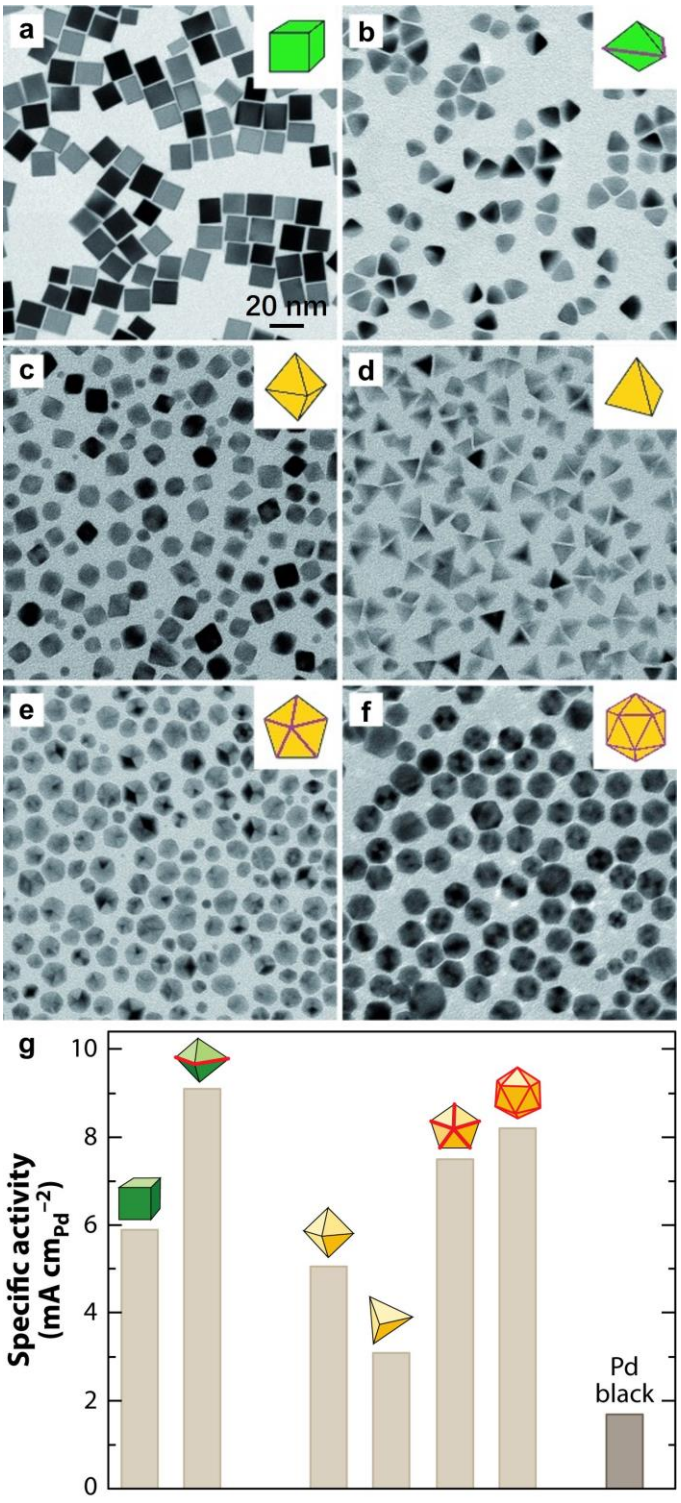

Figure 1.3. TEM images and corresponding models of the Pd nanocrystals tested for formic acid oxidation (FAO): (a) cubes; (b) right bipyramids; (c) octahedra; (d) tetrahedra; (e) decahedra; and (f) icosahedra. The scale bar in panel (a) applies to all panels in (a–e). (g) Comparison of the activity toward FAO between various Pd nanocrystals and against commercial Pd black. (Reprinted with permission from [23]. Copyright 2017 Wiley-VCH.)

1.1.2 Phase-Controlled Synthesis

In addition to diverse surface structures, it was recently found that noble-metal nanocrystals could also take on a crystal phase distinct from that in bulk [25–27]. This phenomenon can be rationalized by the fact that when the size of noble metals shrinks to the nanometer scale, the surface energy would be dominant in the total energy [27]. As a consequence, the noble-metal atoms may exhibit a different packing preference under certain conditions such as pressure, temperature, and the presence of template. Xia and co-workers found that the crystal phase of Pd nanocrystals would transit from face-centered cubic (*fcc*) to face-centered tetragonal (*fct*) after subjecting to a pressure of 24.8 GPa [28]. Zhang and co-workers reported the facile synthesis of Au square sheets by templating with graphene oxide sheets, in which the Au nanosheets crystallized in a hexagonal close-packed (*hcp*) phase rather than the *fcc* structure typical of bulk Au [29]. Since the arrangement of atoms is strongly correlated with the physiochemical properties of those metals, these demonstrations open the door to another avenue for enhancing the optimization of the properties of noble-metal nanocrystals.

One representative example can be found in the Fe-Pt bimetallic system, which adopts body-centered cubic (*bcc*) and *fcc* structures in bulk, respectively. Sun and co-workers reported the facile synthesis of *fcc* Fe-Pt alloy nanoparticles, which then served as a precursor to the formation of fully ordered *fct* Fe-Pt alloy nanoparticles upon annealing (Figure 1.4, a and b) [30]. The ordering of the *fct* Fe-Pt nanoparticles could be readily tuned by varying the annealing time. When used as catalysts toward oxygen reduction reaction (ORR), the fully ordered *fct* Fe-Pt nanoparticles exhibited 3.3- and 3.7-fold, and 11.3- and 5.3-fold enhancements in terms of specific and mass activities relative to the *fcc* Fe-Pt

nanoparticles and the commercial Pt/C, respectively (Figure 1.4, c and d). Even after 20,000 cycles of accelerated durability test, no obvious loss of the performance was observed for the *fct* Fe-Pt nanoparticles (Figure 1.4e), demonstrating the outstanding durability. Moreover, the Fe-Pt nanoparticles with different crystal structures also displayed distinctive magnetic properties. In contrast to the *fcc* Fe-Pt nanoparticles that are superparamagnetic, the *fct* Fe-Pt nanoparticles are strongly ferromagnetic (Figure 1.4f).

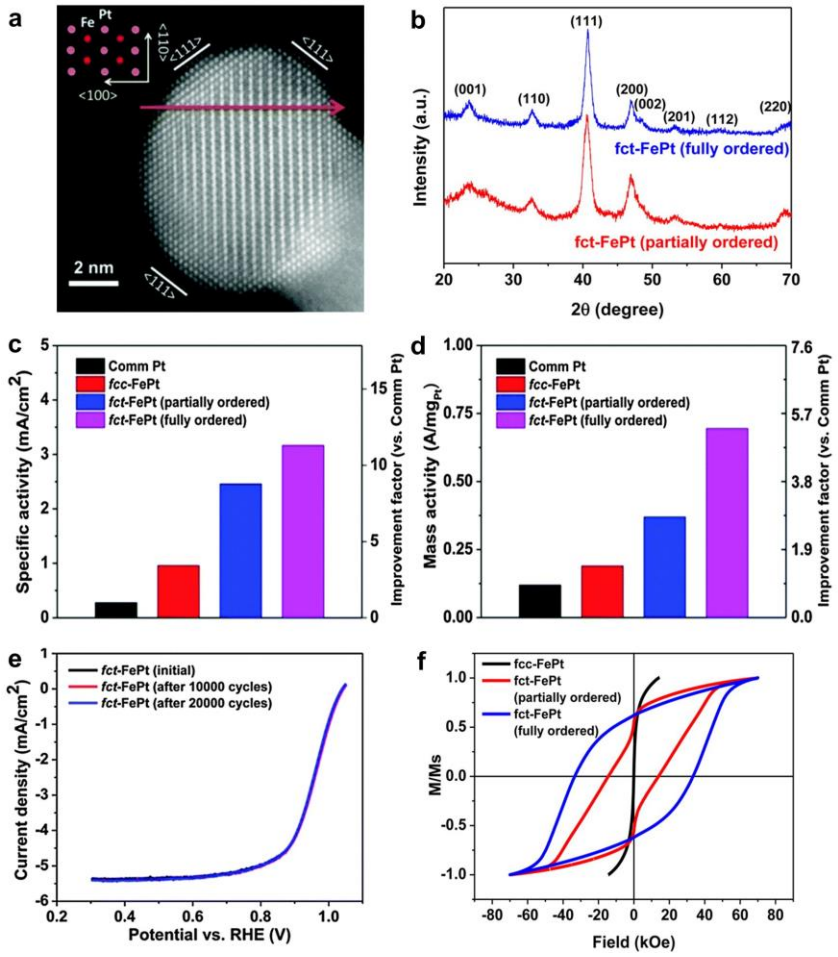

Figure 1.4. (a) HAADF-STEM image of a representative fully ordered *fct* Fe-Pt nanoparticles. (b) XRD patterns of the fully and partially ordered *fct* Fe-Pt nanoparticles. (c) Specific activities of different catalysts at 0.9 V. (d) Mass activities of different catalysts at 0.9 V. (e) ORR polarization curves of the fully ordered *fct* Fe-Pt nanoparticles before and after potential scans between 0.6 and 1.0 V. (Reprinted with permission from [30]. Copyright 2015 American Chemical Society.)

Thus far, phase-controlled synthesis has been accomplished for many noble metals, including Au, Ag, Ru, Rh, and Pd [25–27]. Unfortunately, only limited crystal phases (*fcc* or *hcp*) were achieved for each metal and a majority of the reported nanocrystals showed poorly defined shapes. As such, the shape or facet-dependent properties of the noble metals with a novel crystal phase remain ambiguous. How to engineer both the crystal phase and surface structure of noble-metal nanocrystals is an interesting research subject that deserves more studies.

1.2 Ruthenium Nanocrystals: Challenges and Opportunities

Ruthenium (Ru) nanocrystals have received tremendous interest recently owing to their compelling catalytic properties toward a variety of applications such as ammonia synthesis, CO oxidation, Fischer-Tropsch synthesis, batteries, and supercapacitors [28–35]. Although shape-controlled synthesis has been accomplished for many noble metals including Pd, Pt, Ag, Au, and Rh [36–40], it is still a grand challenge to engineer the shape or surface structure of Ru nanocrystals. There are several reasons responsible for the dilemma. First, distinct from the aforementioned metals (*i.e.*, Pd, Pt, Ag, Au, and Rh) that have an *fcc* structure, Ru crystallizes in an *hcp* lattice. As such, the anisotropy in the *c*-axis of the intrinsic arrangement of Ru atoms (lattice constant: a =2.71 Å and c = 4.28 Å) would lead to different growth paces along the *a*- and *c*-direction, and thereby the preferential formation of nanoplates and nanowires. Additionally, the cohesive and surface energies of Ru are much greater than those of Pd, Pt, Ag, Au, and Rh [41, 42]. As a result, the Ru atoms are required to overcome a high energy barrier in order to form nanocrystals with diverse surface structures. Another challenge lies in the low reduction potential of Ru(III)

ions (0.39 *versus* the standard hydrogen electrode or SHE for Ru^{3+}/Ru) [43], making it difficult to generate Ru atoms through chemical reduction of Ru(III) ions. Consequently, it has been a challenging task to manipulate the growth kinetics of Ru atoms as a means to engineer the shape of Ru nanocrystals.

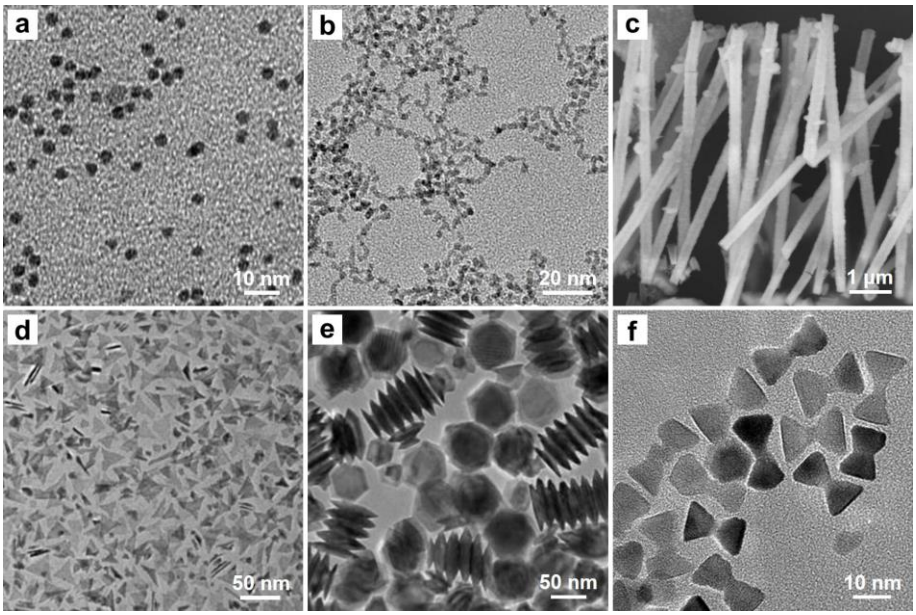

Figure 1.5. TEM images of Ru nanocrystals with various shapes: (a) nanoparticles, (b) nanochains, (c) nanowires, (d) nanoplates, (e) capped columns, and (f) hourglass. (Figure 1.4a was adapted from [44]. Copyright 2010 American Chemical Society. Figure 1.4b was adapted from [45]. Copyright 2016 American Chemical Society. Figure 1.4c was adapted from [46]. Copyright 2013 American Chemical Society. Figure 1.4, d and e, was adapted from [47]. Copyright 2012 American Chemical Society. Figure 1.4f was adapted from [48]. Copyright 2013 American Chemical Society.)

Given these challenges, the synthesis of Ru nanocrystals typically involves harsh reaction conditions. For the synthesis of Ru nanoparticles and nanowires (Figure 1.5, a and b) [44, 45], a strong reductant ascorbic acid (AA) was used for the reduction of Ru(III) ions to Ru atoms in an ethylene glycol (EG) solution while the reaction temperature was set to

200 °C, nearly the boiling point of EG. To facilitate the reduction of Ru(III) ions, Wong and co-workers employed H_2 as the reductant, which was generated from the decomposition of sodium borohydride ($NaBH_4$), for the synthesis of Ru nanowires (Figure 1.5c) [46]. Another strategy is based on the solvothermal method, in which the solvent is brought to temperatures above its boiling point in conjunction with the increased autogenous pressure, thereby greatly increasing the reactivity of reactants. Figure 1.5d–f shows the nanoplates, capped columns, and hourglass synthesized using the hydrothermal method [47, 48]. Despite the accomplishments, the nanocrystals reported in literature typically featured an *hcp* structure and poorly defined facets.

Recently, Kitagawa and co-workers discovered that Ru nanoparticles with a novel *fcc* structure could be obtained by employing an appropriate pair of the Ru precursor and solvent [49], which provides a new strategy for the optimization of catalytic properties of Ru nanocrystals. However, similar to the reported *hcp*-Ru nanocrystals, the as-synthesized *fcc*-Ru nanoparticles were also characterized by poorly defined shapes, creating a barrier to further improvement of their catalytic performance. Taken together, there is a pressing need to develop facile synthetic protocols for the production of Ru nanocrystals with both well-defined crystal phases and surface structures, and thereby veiling their phase- and facet-dependent catalytic properties.

1.3 Homogeneous *versus* Heterogeneous Nucleation

For the Ru nanocrystals shown in Figure 1.5, they were all synthesized using the one-pot approach, which involves homogeneous nucleation and is expected to follow the LaMer model (Figure 1.6a) [50]. Typically, metal precursors are reduced to generate zerovalent

metal atoms first and the concentration of the atoms will increase steadily as the reaction proceeds. Upon reaching the minimum concentration of supersaturation, the metal atoms will start to aggregate to form nuclei. The nucleation process will continue until the concentration of metal atoms drops below the concentration of supersaturation. Afterwards, the as-formed nuclei will undergo growth and form nanocrystals with increasing sizes. Although the one-pot approach has shown its versatility in the synthesis of nanocrystals, it has several drawbacks. Since homogeneous nucleation is extremely sensitive to experimental conditions, one has to keep a tight control over the reaction parameters in order to obtain desirable products with high quality and reproducibility. Another drawback lies in the difficulty to separate the nucleation and growth processes in the one-pot synthesis, which is essential to the manipulation of growth kinetics of the generated metal atoms and thus the formation of kinetically controlled products.

To address this issue, one can introduce pre-formed seeds into the synthesis (the so-called seed-mediated growth). The presence of seeds allows one to focus on the growth step while the seeds provide the primary sites for the newly formed metal atoms to nucleate, which is referred to as heterogeneous nucleation (Figure 1.6b) [51, 52]. In particular, when the seeds and deposited atoms share similar chemical identities, the deposited atoms could replicate the atomic arrangement of the underlying seeds. As such, one can readily tune both the crystal phase and surface structures of the second metal of interest simply by using seeds with desirable merits. It is worth noting that the energy threshold for heterogeneous nucleation is lower than that for homogeneous nucleation (Figure 1.6c), and the correlation can be expressed as following:

$$\Delta G^{*}_{hetero} = \left(\frac{2 - 3\cos\theta + \cos^{3}\theta}{4}\right)\Delta G^{*}_{homo}$$

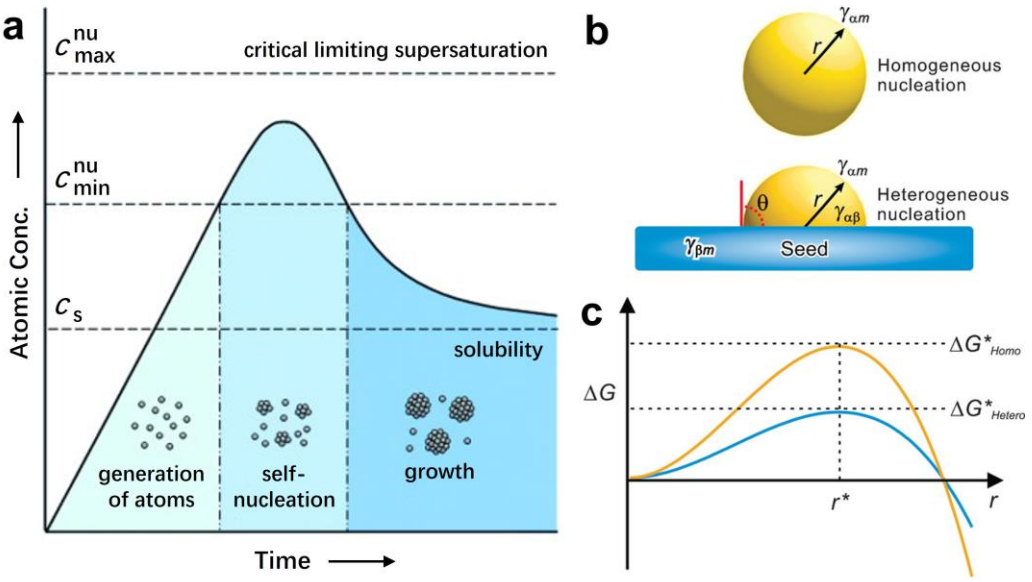

Figure 1.6. (a) Plot of the concentration of atoms as a function of reaction time, illustrating the processes of atom generation, self-nucleation, and growth. (b) Illustration of two different nucleation modes: (top) homogeneous nucleation in the reaction solution and (bottom) heterogeneous nucleation on the surface of a seed. (c) Plot showing the change in Gibbs free energy as a function of particle size for homogeneous (yellow line) and heterogeneous nucleation (blue line). (Figure 1.6a was modified with permission from [50]. Copyright 1950 American Chemical Society. Figure 1.6, b and c, was reprinted with permission from [51]. Copyright 2017 Wiley-VCH.)

where ΔG^*_{homo} and ΔG^*_{hetero} stand for the energy barriers to homogeneous and heterogeneous nucleation, respectively, while θ is the contact angle of a nucleus on the seed, defined by the Yong equation. Especially, when θ is a right angle, the energy barrier to heterogeneous nucleation is only half of that to homogeneous nucleation. Given these advantages, seed-mediated growth has been widely leveraged for the synthesis of colloidal nanocrystals and a variety of nanostructures has been fabricated such as core–shell and core–frame structures, as well as those formed through asymmetric growth [51, 52]. One typical example can be found in the fabrication of Pt-based nanocages [53–58]. By conformally depositing a few layers of Pt atoms on Pd nanocubes, octahedra, decahedra,

or icosahedra, our group reported the facile synthesis of Pd@Pt core–shell nanocrystals with a cubic, octahedral, decahedral, or icosahedral shape [53–56]. After subjecting the core–shell nanocrystals to wet chemical etching for the selective removal of the Pd cores, we obtained Pt-based nanocages enclosed by well-defined {100} and {111} facets as well as different densities of twin boundaries [56–58]. Additionally, Zhang and co-workers demonstrated the synthesis of Au@Rh core–sheath nanoribbon by templating with the 4H/*fcc*-structured Au nanoribbon (the 4H/*fcc* denotes the crystal phase that has mixed packing periods of ABCB (4H) and ABC (*fcc*)). Interestingly, the Rh atoms in the sheath were also crystallized in the 4H/*fcc* phase rather than the conventional *fcc* lattice typical of bulk Rh [59].

1.4 Scope of This Work

The aim of this dissertation is to explore new synthetic protocols based on seed-mediated growth for the facile synthesis of Ru nanocrystals with controllable crystal phases and surface structures, in an attempt to achieve properties that are superior to those associated with the conventional *hcp* phase. The dissertation mainly focuses on three categories of *fcc*-Ru nanocrystals: *i*) nanocages that are characterized by hollow interiors, ultrathin (< 1.2 nm) and porous walls, as well as well-controlled surface structures; *ii*) solid octahedral nanocrystals with well-defined {111} facets; and *iii*) nanoframes that are composed of only corners and edges. All these *fcc*-Ru nanocrystals were subjected to thermal stress for the evaluation of thermal stability in terms of both the crystal phase and surface structures, and examined as catalysts for the study of crystal phase- and surface structure-dependent catalytic properties.

In Chapter 2, I demonstrate a polyol method for the facile synthesis of Pd@Ru core–shell nanocubes by templating with Pd cubic seeds, followed by the fabrication of Ru cubic nanocages *via* wet chemical etching. The key to the success of this synthesis is to ensure layer-by-layer deposition of Ru atoms on the surface of Pd cubic seeds by controlling the reaction temperature and the injection rate of a Ru(III) precursor. Most importantly, the Ru nanocages adopt an *fcc* crystal structure rather than the *hcp* structure observed in bulk Ru. By tuning the growth mode of Ru atoms from layer-by-layer to island growth, I found that the atomic packing of Ru shells was switched from *fcc* to *hcp* phase. Density functional theory (DFT) calculations were also conducted by collaborators to evaluate the catalytic performance of the Ru cubic nanocages toward N_2 dissociation for ammonia synthesis.

In Chapter 3, I demonstrate a facile approach to the synthesis of Ru octahedral nanocages by integrating seed-mediated growth with wet chemical etching. The as-synthesized Ru octahedral nanocages are characterized by well-defined {111} facets, five atomic layers in thickness, and tunable size in the range of 12–28 nm. The Ru atoms are also crystallized in an *fcc* phase and the *fcc* phase in the octahedral nanocages could be well preserved up to 300 °C. The Ru cubic and octahedral nanocages were used as catalysts for studying the facet-dependent catalytic properties toward the reduction of 4-nitrophenol. DFT calculations were conducted by collaborators to disclose the role of Pd impurities left behind in the nanocages during etching in enhancing the catalytic performance toward N_2 dissociation.

In Chapter 4, I report a strategy for the facile synthesis of Ru icosahedral nanocages that feature well-defined {111} facets and twin boundaries, as well as an *fcc* phase. A quantitative study was performed to investigate the role of Br^- ions in ensuring the layer-

by-layer growth of Ru atoms on the Pd icosahedral seeds. The thermal stability of the icosahedral shape and *fcc* phase was also assessed, and both were found to be well retained up to 300 °C. The evaluation of catalytic properties for the Ru nanocages with a cubic, octahedral, and icosahedral shapes demonstrate the enhanced activity and durability stemming from the twin structure relative to the {100} and {111} facets. DFT calculations conducted by collaborators also suggest the superior performance of *fcc*-Ru icosahedral nanocages relative to *hcp*-Ru nanoparticles toward N_2 dissociation.

In Chapter 5, I describe a facile route to the synthesis of Ru octahedral nanocrystals with an *fcc* structure and an edge length of 9 nm. The success of this synthesis relies on the use of Rh seeds because they can resist oxidative etching under the harsh condition for Ru overgrowth; they can be readily prepared as nanocubes with edge lengths below 5 nm; and their atoms have a size close to that of Ru atoms. Both the octahedral shape and the *fcc* crystal structure could be well preserved up to 400 °C, which is more than 100 °C higher than what was reported for Ru octahedral nanocages. When utilized as catalysts, the Ru octahedral nanocrystals exhibited enhanced specific activity toward oxygen evolution relative to *hcp*-Ru nanoparticles. It was also demonstrated that Ru{111} facets were more active than Ru{100} facets in catalyzing the oxygen evolution reaction.

In Chapter 6, I demonstrate a facile route to the synthesis of Ru cuboctahedral nanoframes crystallized in an *fcc* phase. The synthesis was built around Pd nanocubes, which quickly evolved into a truncated cubic shape upon mixing with a Ru(III) precursor owing to the involvement of oxidative etching. Afterwards, the galvanic replacement reaction between the Pd seeds and Ru(III) precursor kicked in, resulting in the formation of Pd@Ru core–frame cuboctahedra due to the selective deposition of Ru atoms on the

corners and edges. Both the frame structure and crystal phase of the *fcc*-Ru cuboctahedral nanoframes could be preserved up to 350 °C. When benchmarked against *hcp*-Ru nanoparticles, the *fcc*-Ru nanoframes exhibited substantial enhancements in terms of activity and H_2 selectivity toward hydrazine decomposition.

1.5 Notes to Chapter 1

Part of this chapter is adapted from the review article "Toward Affordable and Sustainable Use of Precious Metals in Catalysis and Nanomedicine" co-authored by me and published in *MRS Bulletin* [18], and "Hollow Metal Nanocrystals with Ultrathin, Porous Walls and Well-Controlled Surface Structures" published in *Advanced Materials* [19].

1.6 References

[1] Somorjai, G. A. *Chem. Rev.* **1996**, *96*, 1223–1236.

[2] Ertl, G. *Handbook of Heterogeneous Catalysis*, Wiley-VCH, Weinheim, **2008**.

[3] Talapin, D. V.; Lee, J.-S.; Kovalenko, M. V.; Shevchenko, E. V. *Chem. Rev.* **2010**, *110*, 389–458.

[4] Maier, S. A.; Brongersma, M. L.; Kik, P. G.; Meltzer, S.; Requicha, A. A. G.; Atwater, H. A. *Adv. Mater.* **2001**, *13*, 1501–1505.

[5] Gupta, M. C.; Ballato, J. *The Handbook of Photonics*, CRC Press, Taylor & Francis Group, Boca Raton, **2006**.

[6] Murray, C. B.; Sun, S.; Doyle, H.; Betley, T. *MRS Bull.* **2001**, *26*, 985–991.

[7] Jain, P. K.; El-Sayed, I. H.; El-Sayed, M. A. *Nano Today* **2007**, *2*, 18–29.

[8] Burda, C.; Chen, X.; Narayanan, R.; El-Sayed, M. A. *Chem. Rev.* **2005**, *105*, 1025–1102.

[9] Zhang, L.; Webster, T. J. *Nano Today* **2009**, *4*, 66–80.

[10] Zhang, Q.; Uchaker, E.; Candelaria, S. L.; Cao, G. *Chem. Soc. Rev.* **2013**, *42*, 3127–3171.

[11] Roduner, E. *Chem. Soc. Rev.* **2006**, *35*, 583–592.

[12] Spicer, C. D.; Jumeaux, C.; Gupta, B.; Stevens, M. M. *Chem. Soc. Rev.* **2018**, *47*, 3574–3620.

[13] Dreaden, E. C.; Alkilany, A. M.; Huang, X.; Murphy, C. J.; El-Sayed, M. A. *Chem. Soc. Rev.* **2012**, *41*, 2740–2779.

[14] Yang, X.; Yang, M.; Pang, B.; Madeline, V.; Xia, Y. *Chem. Rev.* **2015**, *115*, 10410–10488

[15]Grzelczak, M.; Perez-Juste, J.; Mulvaney, P.; Liz-Marzan, L. M. *Chem. Soc. Rev.* **2008**, *37*, 1783–1791.

[16] Daniel, M.-C.; Astruc, D. *Chem. Rev.* **2004**, *104*, 293–346.

[17] Skrabalak, S. E.; Chen, J.; Sun, Y.; Lu, X.; Au, L.; Cobley, C. M.; Xia, Y. *Acc. Chem. Res.* **2008**, *41*, 1587–1595.

[18] Xia, Y.; Zhao, M.; Wang, X.; Huo, D. *MRS Bull.* **2018**, *43*, 860–869.

[19] Zhao, M.; Wang, X.; Yang, X.; Gilroy, K. D.; Qin, D.; Xia, Y. *Adv. Mater.* **2018**, *30*, 1801956.

[20] Nessekberger, M.; Ashton, S.; Meier, J. C.; Katsounaros, I.; Mayrhofer, K. J. J.; Arenz, M. *J. Am. Chem. Soc.* **2011**, *133*, 17428–17433.

[21] Shao, M.; Peles, A.; Shoemaker, K. *Nano Lett.* **2011**, *11*, 3714–3719.

[22] Ruditskiy, A.; Peng, H.-C.; Xia, Y. *Annu. Rev. Chem. Biomol. Eng.* **2016**, *7*, 327–348.

[23] Choi, S.-II; Herron, J. A.; Scaranto, J.; Huang, H.; Wang, Y.; Xia, X.; Lv, T.; Park, J.; Peng, H.-C.; Mavrikakis, M.; Xia, Y. *ChemCatChem* **2015**, *7*, 2077–2084.

[24] Bartlie, K. M.; Lee, H.; Komvopoulos, K.; Yang, P.; Somorjai, G. A. *Nano Lett.* **2007**, *7*, 3097–3101.

[25] Fan, Z.; Zhang, H. *Acc. Chem. Res.* **2016**, *49*, 2841−2850.

[26] Cheng, H.; Yang, N.; Lu, Q.; Zhang, Z.; Zhang, H. *Adv. Mater.* **2018**, *30*, 1707189.

[27] Fan, Z.; Zhang, H. *Chem. Soc. Rev.* **2016**, *45*, 63−82.

[28] Guo, Q.; Zhao, Y.; Mao, W. L.; Wang, Z.; Xiong, Y.; Xia, Y. *Nano Lett.* **2008**, *8*, 972–975.

[29] Huang, X.; Li, S.; Huang, Y.; Wu, S.; Zhou, X.; Li, S.; Gan, C. L.; Boey, F.; Mirkin, C. A.; Zhang, H. *Nat. Commun.* **2011**, *2*, 292.

[30] Li, Q.; Wu, L.; Wu, G.; Su, D.; Lv, H.; Zhang, S.; Zhu, W.; Casimir, A.; Zhu, H.; Mendoza-Garcia, A.; Sun, S. *Nano Lett.* **2015**, *15*, 2468–2473.

[31] Kitano, M.; Kanbara, S.; Inoue, Y.; Kuganathan, N.; Sushko, P. V.; Yokoyama, T.; Hara, M.; Hosono, H. *Nat. Commun.* **2015**, *6*, 6731.

[32] Li, W.; Liu, J.; Gu, J.; Zhou, W.; Yao, S.; Si, R.; Guo, Y.; Su, H.; Yan, C.; Li, W.; Zhang, Y.; Ma, D. *J. Am. Chem. Soc.* **2017**, *139*, 2267–2276.

[33] Kong, X.; Xu, K.; Zhang, C.; Dai, J.; Oliaee, S. N.; Li, L.; Zeng, X.; Wu, C.; Peng, Z. *ACS Catal.* **2016**, *6*, 1487–1492.

[34] Wang, J.; Wei, Z.; Mao, S.; Li, H.; Wang, Y. *Energy Environ. Sci.* **2018**, *11*, 800–806.

[35] Yang, S.; Qiao, Y.; He, P.; Liu, Y.; Cheng, Z.; Zhu, J.; Zhou, H. *Energy Environ. Sci.* **2017**, *10*, 972–978.

[36] Wiley, B.; Sun, Y.; Xia, Y. *Acc. Chem. Res.* **2007**, *40*, 1067–1076.

[37] Grzelczak, M.; Perez-Juste, J.; Mulvaney, P.; Liz-Marzan, L. M. *Chem. Soc. Rev.* **2008**, *37*, 1783–1791.

[38] Zhang, H.; Jin, M.; Xiong, Y.; Lim, B.; Xia, Y. *Acc. Chem. Res.* **2013**, *46*, 1783–1794.

[39] Chen, J.; Lim, B.; Lee, E. P.; Xia, Y. *Nano Today* **2009**, *4*, 81–95.

[40] Xie, S.; Liu, X.; Xia, Y. *Nano Res.* **2015**, *8*, 82–96.

[41] Vitos, L.; Ruban, A. V.; Skriver, H. L.; Kollár, J. *Surf. Sci.* **1998**, *411*, 186–202.

[42] Turchanin, M.; Agraval, P. G. *Powder Metall. Met. Ceram.* **2008**, *47*, 26–39.

[43] Lide, D.; Haynes, W. *CRC Handbook of Chemistry and Physics*, 90th ed.; CRC Press; Boca Raton, FL, **2009**.

[44] Joo, S. H.; Park, J. Y.; Renzas, J. R.; Butcher, D. R.; Huang, W.; Somorjai, G. A. *Nano Lett.* **2010**, *10*, 2709–2713.

[45] Ye, H.; Wang, Q.; Catalano, M.; Lu, N.; Vermeylen, J.; Kim, M. J.; Liu, Y.; Sun, Y.; Xia, X. *Nano Lett.* **2016**, *16*, 2812–2817.

[46] Koenigsmann, C.; Semple, D. B.; Sutter, E.; Tobierre, S. E.; Wong, S. S. *ACS Appl. Mater. Interfaces* **2013**, *5*, 5518–5530.

[47] Yin, A.; Liu, W.; Ke, J.; Zhu, W.; Gu, J.; Zhang, Y.; Yan, C. *J. Am. Chem. Soc.* **2012**, *134*, 20479–20489.

[48] Watt, J.; Yu, C.; Chang, S. L. Y.; Cheong, S.; Tilley, R. D. *J. Am. Chem. Soc.* **2013**, *135*, 606–609.

[49] Kusada, K.; Kobayashi, H.; Yamamoto, T.; Matsumura, S.; Sumi, N.; Sato, K.; Nagaoka, K.; Kubota, Y.; Kitagawa, H. *J. Am. Chem. Soc.* **2013**, *135*, 5493–5496.

[50] Lamer, V. K.; Dinegar, R. H. *J. Am. Chem. Soc.* **1950**, *72*, 4847−4854.

[51] Xia, Y.; Gilroy, K. D.; Peng, H.-C.; Xia, X. *Angew. Chem. Int. Ed.* **2017**, *56*, 60–95.

[52] Gilroy, K. D.; Ruditskiy, A.; Peng, H.-C.; Qin, D.; Xia, Y. *Chem. Rev.* **2016**, *116*, 10414–10472.

[53] Xie, S.; Choi, S.-II, Lu, N.; Roling, L. T.; Herron, J. A.; Zhang, L.; Park, J.; Wang, J.; Kim, M. J.; Xie, Z.; Mavrikakis, M.; Xia, Y. *Nano Lett.* **2014**, *14*, 3570–3576.

[54] Park, J.; Zhang, L.; Choi, S.-II; Roling, L. T.; Lu, N.; Herron, J. A.; Xie, S.; Wang, J.; Kim, M. J.; Mavrikakis, M.; Xia, Y. *ACS Nano* **2015**, *9*, 2635–2647.

[55] Wang, X.; Choi, S.-II; Roling, L. T.; Luo, M.; Ma, C.; Zhang, L.; Chi, M.; Liu, J.; Xie, Z.; Herron, J. A.; Mavrikakis, M.; Xia, Y. *Nat. Commun.* **2015**, *6*, 7594.

[56] Wang, X.; Vara, M.; Luo, M.; Huang, H.; Ruditskiy, A.; Park, J.; Bao, S.; Liu, J.; Howe, J.; Chi, M.; Xie, Z.; Xia, Y. *J. Am. Chem. Soc.* **2015**, *137*, 15036−15042.

[57] Zhang, L.; Roling, L. T.; Wang, X.; Vara, M.; Chi, M.; Liu, J.; Choi, S.-II; Park, J.; Herron, J. A.; Xie, Z.; Mavrikakis, M.; Xia, Y. *Science* **2015**, *349*, 412−416.

[58] Wang, X.; Figueroa-Cosme, L.; Yang, X.; Luo, M.; Liu, J.; Xie, Z.; Xia, Y. *Nano Lett.* **2016**, *16*, 1467−1471.

[59] Fan, Z.; Chen, Y.; Zhu, Y.; Wang, J.; Li, B.; Zong, Y.; Han, Y.; Zhang, H. *Chem. Sci.* **2017**, *8*, 795−799.

CHAPTER 2

SYNTHESIS AND CHARACTERIZATION OF RUTHENIUM CUBIC NANOCAGES WITH A FACE-CENTERED CUBIC STRUCTURE BY TEMPLATING WITH PALLADIUM NANOCUBES

2.1 Introduction

Noble-metal nanocrystals with well-controlled shapes have received great interest owing to their shape-dependent properties in the context of catalysis [1, 2], electronics[3], and plasmonics [4, 5], among others. Many efforts have been devoted to their syntheses over the past two decades [6−8]. In particular, seed-mediated growth has emerged as the most powerful and versatile approach in terms of experimental controls over composition, size, shape, and structure [9, 10]. Compared to conventional methods based on homogeneous nucleation, seed-mediated growth allows one to fully separate growth from nucleation and thus concentrate on the growth step, making it much easier to manipulate and control the resultant nanocrystals. Thus far, seed-mediated growth has successfully produced many different types of nanocrystals, including those with mono-, bi-, and multi-metallic compositions [11−24]. When more than one metal is involved, seed-mediated growth can be used to conveniently produce nanocrystals with core−shell and core−frame structures, as well as concave facets [19−25]. Afterwards, chemical etching may be applied to selectively remove the cores, leaving behind novel nanocrystals, such as nanocages and nanoframes, with a highly open structure. Among them, nanocages are particularly attractive as a new class of materials for catalysis because of their high utilization efficiency

of atoms and their ability to maintain well-defined facets or surface structures [26−28]. Nanocages have been fabricated from a number of noble metals crystals in a face-centered cubic (*fcc*) structure, including Pd, Pt, and Au, and further applied to electrocatalytic applications [13, 14, 16].

Ruthenium and Ru-based nanocrystals have proven to be of great importance in catalysis for their widespread use in an array of reactions, including aromatic hydrogenation [29, 30], CO oxidation [31−33], ammonia synthesis [34−36], and CO_2 methanation [37, 38], among others. The activity and selectivity of a Ru-based catalyst strongly depend on the surface structure and thus the nanocrystal shape. Recently, Ru nanoplates [39], nanowires [40, 41], hourglasses [42], nanoframes [43], and several other types of nanostructures [44−46] have been reported. However, to the best of our knowledge, the synthesis of Ru nanocages has not been demonstrated. Herein, I report a versatile approach to the synthesis of Ru cubic nanocages based on seed-mediated growth and selective chemical etching. The Ru nanocages could be made with a wall thickness as thin as 1.1 nm or about six atomic layers. Most importantly, the Ru atoms in the nanocages can be crystallized in an *fcc* structure rather than the hexagonal close-packed (*hcp*) structure of bulk Ru [47, 48]. The transition from an *hcp* to an *fcc* crystal structure can be attributed to the templating effect of the Pd nanocubes serving as seeds for the epitaxial deposition of Ru. This strategy has been successfully applied to the synthesis of Ru cubic nanocages with edge lengths controlled at 6, 10, and 18 nm, respectively. As the edge length is increased, it becomes necessary to either reduce the deposition rate or accelerate the surface diffusion rate due to the longer distance for the Ru adatoms to diffuse in order to generate a conformal, uniform shell.

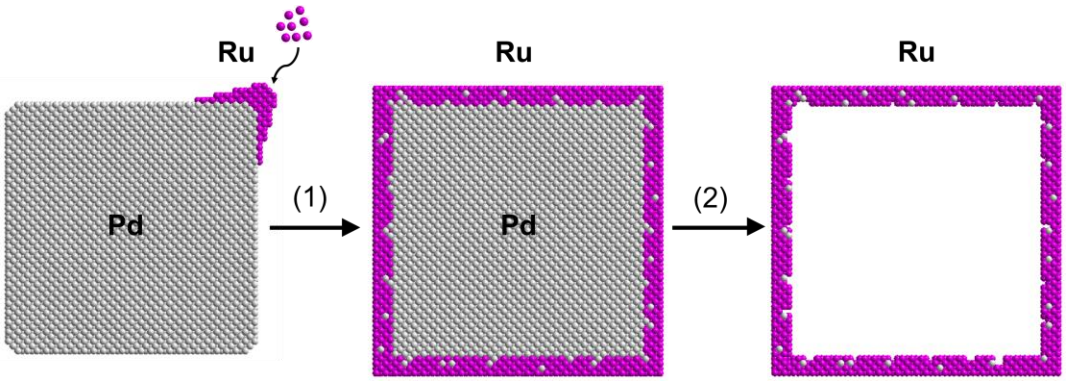

Figure 2.1. Schematic illustration of the major two steps involved in the synthesis of Ru nanocages: (1) selective deposition of Ru atoms at the corner sites of a Pd nanocube, followed by diffusion to the edges and side faces, to generate a Pd@Ru core−shell nanocube and (2) formation of a Ru cubic nanocage by selectively etching away the Pd core.

2.2 Results and Discussion

As illustrated in Figure 2.1, the synthesis of Ru cubic nanocages involves two major steps. In the first step, Ru atoms are deposited onto the corners of a Pd cubic seed due to the higher strain and/or lower coordination number at these sites, as well as the Br^- ions chemisorbed on the side faces [49]. The Ru adatoms then diffuse to the edges and side faces, resulting in the formation of a Pd@Ru core−shell nanocube. In the second step, the Pd core is selectively etched away to generate a cubic Ru nanocage. I evaluated Pd nanocubes with three different sizes (Figure 2.2, 6, 10, and 18 nm in edge length) to understand how this parameter affects the surface diffusion process. All samples of Pd nanocubes showed slight truncation at the corners and edges. As our group has demonstrated before, it is critical to manipulate the atom deposition rate relative to the surface diffusion rate in order to control the growth mode and thus the shape or morphology of the resultant nanocrystals [50]. For the present system, I found that a relatively high

temperature of 200 °C and a relatively slow injection rate of 1 mL h^{-1} were required to ensure the formation of a core−shell structure.

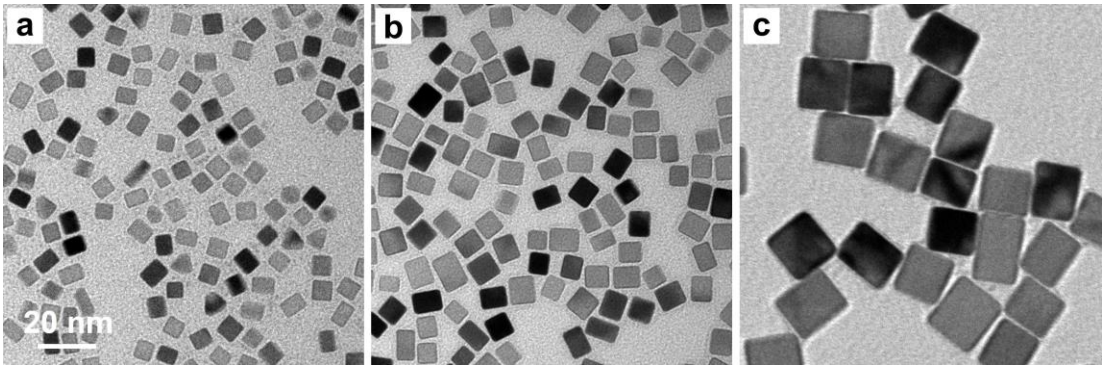

Figure 2.2. TEM images of Pd seeds with different edge lengths. (a) 6 nm, (b) 10 nm, and (c) 18 nm. The scale bar in panel a applies to all panels in (a–c).

Figure 2.3 shows electron microscopy images and energy dispersive X-ray (EDX) mapping of Pd@Ru core−shell nanocubes derived from the 10-nm Pd cubic seeds. The transmission electron microscopy (TEM) image in Figure 2.3a indicates that the cubic shape of the original Pd seeds was largely retained during Ru deposition while the average edge length was increased to approximately 12 nm. The scanning transmission electron microscopy (STEM) images (Figure 2.3, b and c) taken from an individual core−shell nanocube clearly show that a Ru shell was conformally deposited around each Pd nanocube. The side faces were flat and smooth, implying that the diffusion of Ru adatoms was adequately fast relative to the atom deposition. The lattice fringe spacing of 1.9 Å for

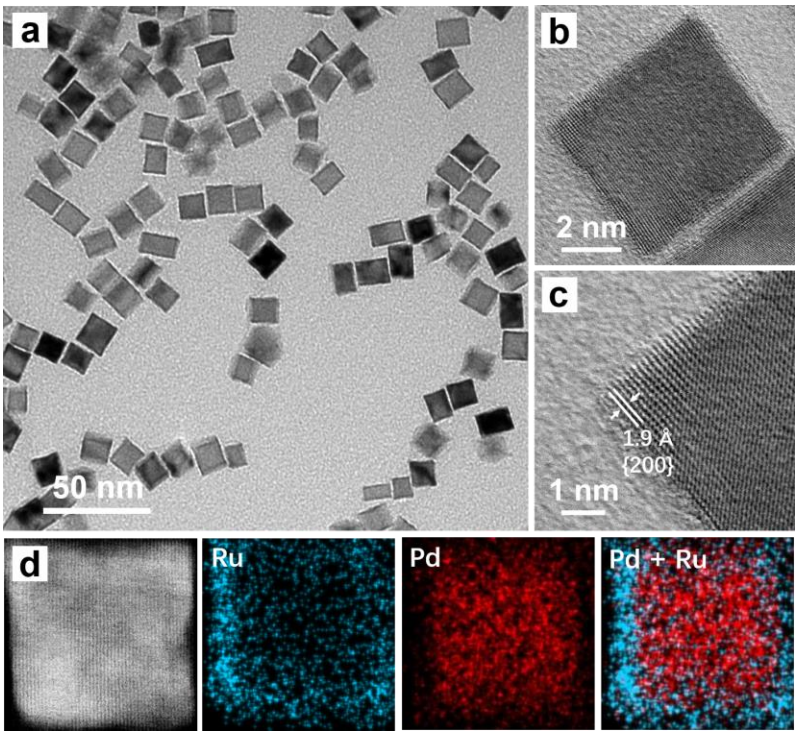

Figure 2.3. (a) TEM image of the Pd@Ru core−shell nanocubes synthesized from 10-nm Pd nanocubes. (b) HRTEM image of an individual core−shell nanocube. (c) Atomic-resolution image taken from the corner region of the core−shell nanocube in (b). (d) HAADF-STEM image and EDX mapping (blue = Ru, red = Pd) of an individual core−shell nanocube.

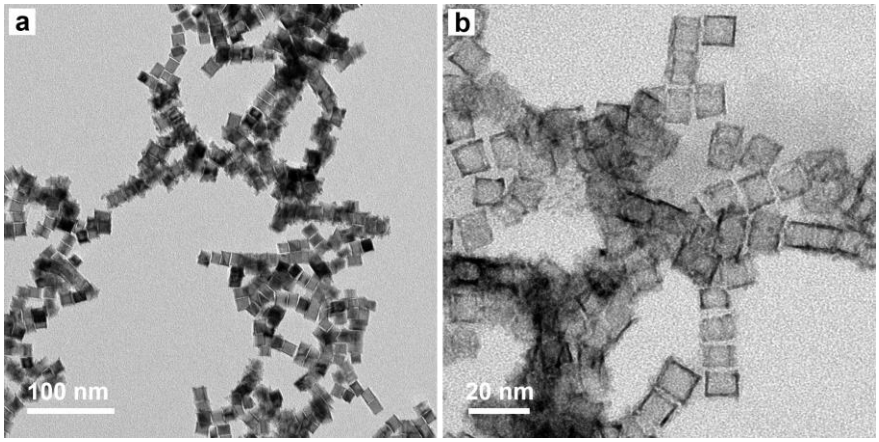

Figure 2.4. TEM images of (a) typical Pd@Ru nanocrystals prepared from 10-nm Pd cubes using the standard procedure without adding PVP into the Ru precursor solution, (b) Ru nanocages produced after chemical etching of (a).

the deposited Ru overlayers could be indexed to the {200} planes of *fcc* Ru. It is well-known for bulk Ru to adopt an *hcp* structure. However, since the Pd and Ru have very similar radii and the lattice mismatch between Pd and *fcc* Ru is only 1.8% (3.89 Å *vs.* 3.82 Å) [51], it is possible for Ru adatoms to follow the crystal packing of the underlying Pd atoms due to the epitaxial deposition. This core−shell structure was further confirmed through EDX mapping (Figure 2.3d). The Pd core and Ru shell can be easily differentiated and spatially resolved. The Ru adatoms were distributed not only at the corners and edges, but also on the side faces of the Pd nanocubes, demonstrating a core−shell structure.

To achieve a better understanding of the formation of Pd@Ru core−shell nanocubes, I also conducted a set of control experiments. I first investigated the role played by poly(vinylpyrrolidone) (PVP) in the synthesis, which has been widely used in the chemical synthesis of colloidal nanocrystals [52−54], and is generally considered as a colloidal stabilizer. Although the terminal hydroxyl group in PVP does have mild reducing power [55], this function can be largely neglected in the current synthesis owing to the comparatively strong reducing power of L-ascorbic acid (AA) and ethylene glycol (EG). Figure 2.4a shows a typical TEM image of the nanocrystals obtained using the standard procedure without the introduction of any PVP. In contrast to the well-defined core−shell nanocrystals shown in Figure 2.3a, I observed significant agglomeration in the product. There was also a large number of small nanoparticles attached to the surface of the larger nanocrystals, validating the critical importance of PVP in the synthesis of colloidal nanocrystals. When the Ru(III) precursor was introduced into the reaction solution, it was quickly reduced by AA to generate Ru(0) atoms. The presence of PVP could protect these

Ru(0) atoms from agglomeration and thus inhibit homogeneous nucleation [56, 57].Taken together, it is necessary to introduce an adequate amount of PVP into the synthesis.

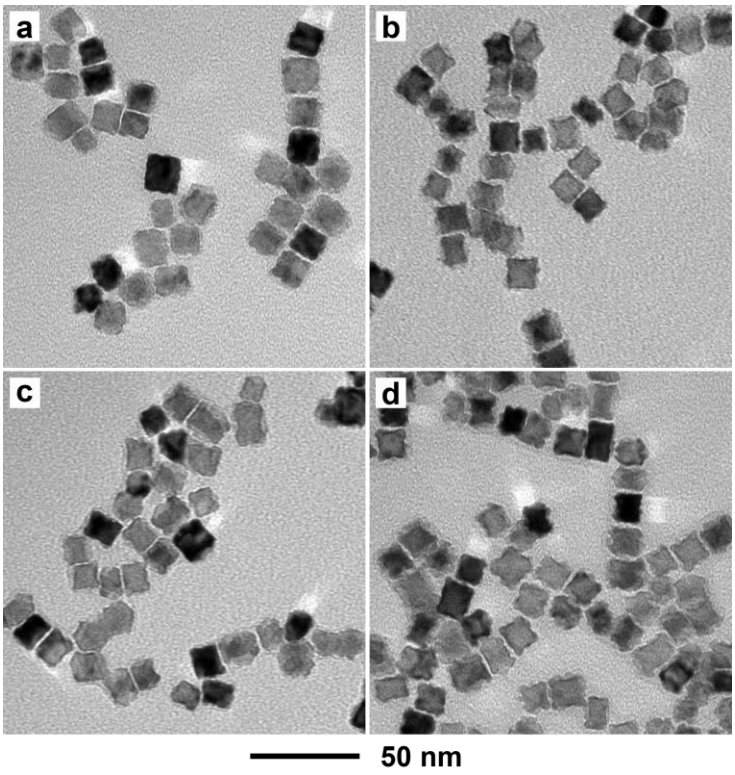

Figure 2.5. TEM images of typical Pd@Ru nanocubes prepared from 10-nm Pd cubes using the standard procedure except with different injection rates. (a) 2 mL h^{-1}, (b) 5 mL h^{-1}, (c) 10 mL h^{-1}, and (d) 20 mL h^{-1}.

I then investigated the role of the Ru deposition rate relative to the surface diffusion rate in controlling the final shape or morphology. These two parameters can be conveniently tuned by varying the injection rate and reaction temperature, respectively. Figure 2.5 shows typical TEM images of nanocrystals prepared using the standard procedure except varying the injection rates for the precursor solution. When the injection

rate was increased from 1 to 2, 5, 10, and 20 mL h^{-1}, the morphology of the resultant nanocrystals changed significantly. The Ru layers deposited on the side faces showed a rough surface due to the formation of small islands. Additionally, more Ru atoms accumulated at the corner sites, indicating inadequate surface diffusion of the adatoms. When the injection rate was increased, the increased deposition rate led to an island growth mode. I could reduce the deposition rate of Ru(0) adatoms by instead slowing down the injection rate of Ru(III) precursor and thus achieve the deposition of ultrathin, conformal Ru shells on the Pd cubic seeds.

Another critical parameter that impacts the formation of Pd@Ru core–shell nanocubes is the reaction temperature. Because surface diffusion is a thermally activated process, it can be enhanced or suppressed by increasing or decreasing the reaction temperature, respectively [58]. The diffusion coefficient (*D*), which measures the rate of diffusion of an adatom across a surface, can be expressed through the following [50]:

$$D = D_0 exp(-E_{diff}/RT)$$

where D_0 is the diffusion pre-exponential factor, E_{diff} is the potential energy barrier to diffusion, *R* is the ideal gas constant, and *T* is the absolute temperature (in kelvin). In general, temperature affects not only the surface diffusion rate but also the reduction rate of the synthesis procedure, which will, in turn, influence the deposition rate. Considering the strong reducing power of AA and EG, as well as the relatively long period of time allocated to the synthesis, I can focus on the effect of temperature on surface diffusion. To confirm this assumption, I used ICP-MS to analyze the elemental composition of samples

prepared at various temperatures. When the temperature was reduced from 200 to 175, 150, 120, and 100 °C, the mass percentage of Ru in the Pd@Ru nanocrystals only dropped from 31.4 to 29.1, 27.8, 26.7, and 26.0%, respectively. This range is narrow enough to justify our argument that the effect of temperature on reduction rate can be neglected.

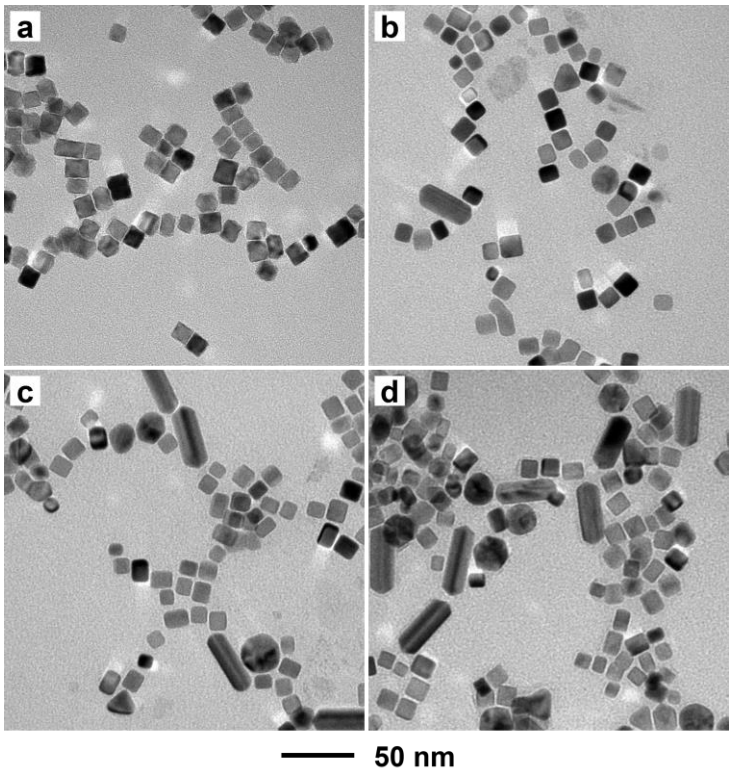

Figure 2.6. TEM images of typical Pd@Ru core−shell nanocubes prepared from 10-nm Pd cubes using the standard procedure except at different reaction temperature. (a) 175 °C, (b) 150 °C, (c) 125 °C, and (d) 100 °C.

Figure 2.6 shows TEM images of nanocrystals prepared using the standard procedure except for the variation in reaction temperature. When the temperature was reduced from 200 to 175 °C (Figure 2.6a), the resultant nanocrystals were still largely cubic, but the corners and edges became noticeably rounded while the side faces became corrugated. If

the reaction temperature was further reduced to 150 °C, some nanorods and irregular nanocrystals appeared (Figure 2.6b). This result can be attributed to asymmetric growth induced by the slow kinetics associated with both reduction and surface diffusion [59]. In particular, when the temperature was reduced to 150 °C, the surface diffusion of Ru adatoms was greatly suppressed while the deposition rate was kept at a relatively stable level, leading to asymmetric growth. When the reaction temperature was further reduced to 125 °C and 100 °C, respectively, the proportions of nanorods and irregular nanocrystals were increased (Figure 2.6, c and d).

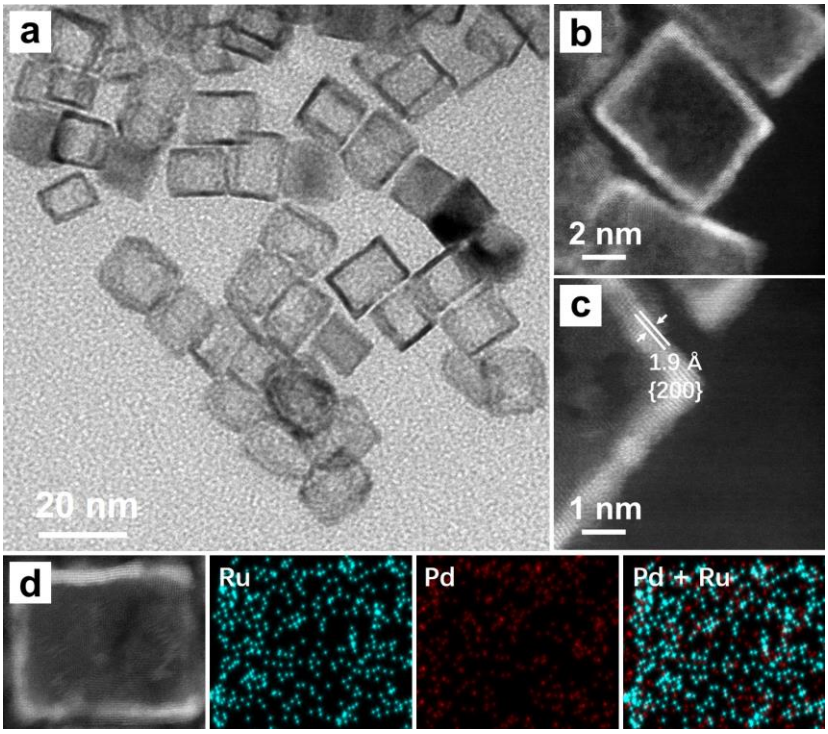

Figure 2.7. (a) TEM image of a typical sample of Ru cubic nanocages prepared from 10-nm Pd cubes. (b) HAADF-STEM image of an individual Ru nanocage. (c) Atomic-resolution HAADF-STEM image taken from the corner region of the Ru nanocage in (b). (d) HAADF-STEM image and EDX mapping (blue = Ru, red = Pd) of an individual Ru nanocage.

The chemical stabilities of Pd and Ru are quite different [60]. Specifically, Pd is more vulnerable to oxidation and etching than Ru. With the use of an appropriate chemical etchant, I was able to obtain Ru nanocages by selectively etching away the Pd cores in the core−shell nanocubes. I conducted the chemical etching in an aqueous solution at 100 °C using an etchant based on the Fe^{3+}/Fe^{2+} pair in the presence of Br^{-} [22]. The Pd cores can be etched away based on the following reaction:

$$Pd + 2Fe^{3+} + 4Br^{-} \rightarrow PdBr_4^{2-} + 2Fe^{2+}$$

Figure 2.7, a and b, show two typical TEM images of the as-obtained Ru nanocages. The HAADF-STEM image in Figure 2.7c shows a lattice spacing of 1.9 Å, which can be assigned to the {200} planes of *fcc* Ru, in agreement with what is shown in Figure 2.3c. This result indicates that the crystal structure of the Ru shells was well preserved during the etching process. The average wall thickness of the Ru nanocages was approximately 1.1 nm, corresponding to about six atomic layers. To examine the elemental composition, EDX mapping was conducted (Figure 2.7d). Compared to what is shown in Figure 2.3d, the Pd content in the core was substantially reduced after etching. This data verifies that the major composition of the nanocages is Ru. I also conducted ICP-MS to quantitatively analyze the elemental composition before and after the etching process. The elemental compositions for the core−shell nanocubes and nanocages were analyzed by ICP-MS, from which the weight percentages of Pd and Ru in the Pd@Ru nanocubes were 68.6% and 31.4%, respectively. After etching, the weight percentage of Pd dropped to 8.8% while the

percentage of Ru increased to 91.2%, indicating a highly efficient Pd etching process. These data confirm that the nanocages were essentially made of Ru.

My collaborators performed first principles, self-consistent density functional theory (DFT [61, 62], GGA-PW91 [63], see experimental section for details) studies to gain additional insights into the mechanisms by which these nanocages form. They first evaluated the activation energy barriers for "hopping" diffusion of Ru adatoms across the Pd(100) surface as would occur during the core−shell synthesis, finding that this diffusion is a highly activated process (1.11 eV) as suggested by the high temperatures required for the formation of a uniform Ru shell over the cubic Pd substrate. They also evaluated the energetics of Ru adatom substitution into the Pd(100) surface, motivated by our previous study of Pt-based nanocage synthesis that showed Pt−Pd intermixing during the growth process is essential for etching and subsequent nanocage formation [28]. At low Ru coverage (1/9 monolayer), they found that Ru substitution into the Pd(100) surface has a barrier of 0.57 eV and is exothermic ($\Delta E = -0.66$ eV), suggesting that Ru substitution should be much more active than Ru hopping (by 5 orders of magnitude at 200 °C). The barrier of Ru substitution into Pd(100) increases to 0.84 eV at higher Ru coverage (1/4 monolayer), while the Ru hopping barrier on Pd(100) remains invariable; substitution will eventually become too difficult to occur as the deposited Ru layers become more fully populated, and hopping will become the dominant mechanism. As a result, and according to the mechanism proposed in our previous work, this substitutional diffusion of Ru will lead to the formation of mixed Pd−Ru overlayers during the core−shell formation process as substitution processes continually mix the top layer of Pd with Ru atoms as they are deposited. The relatively small amount of Pd that is randomly dispersed into the overlayers

can form channels through the shell, enabling the subsequent etching of the Pd core to yield hollow nanocages. The residual Pd (~8.8% from ICP-MS) in the final nanocages represents the Pd that was dispersed in the shell during the growth process but could not be etched away, presumably because it was not part of a contiguous Pd channel to the surface.

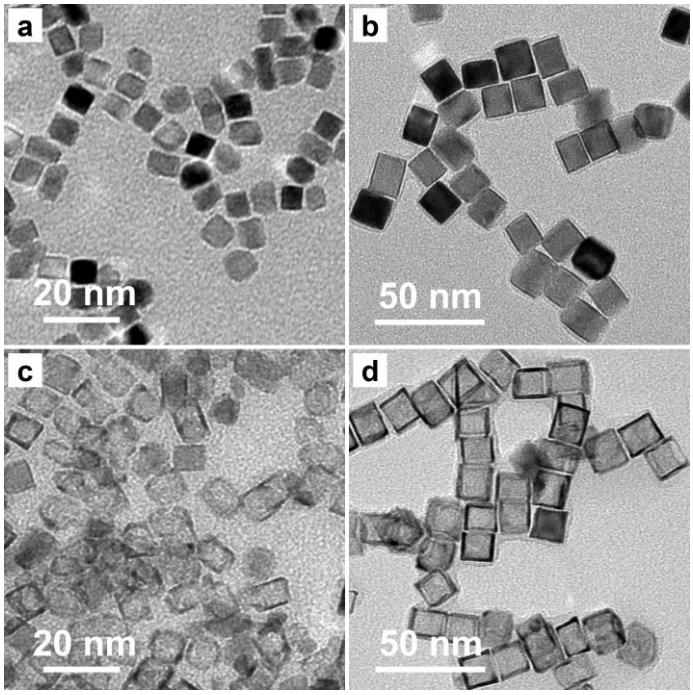

Figure 2.8. TEM images of (a, b) Pd@Ru core−shell nanocubes prepared by templating with (a) 6-nm and (b) and 18-nm cubes, and (c, d) the resultant Ru nanocages obtained after selectively etching away the Pd cores.

I have also extended our synthesis to Pd cubic seeds with two other edge lengths at 6 nm and 18 nm, respectively. In general, smaller Pd seeds are better suited for Ru adatoms to cover the entire surface by diffusion while larger ones would impose a longer distance for the Ru adatoms to diffuse [64]. Figure 2.8, a and b, show the resultant Pd@Ru nanocubes prepared using the Pd seeds of varying lengths, which are uniform in size and

shape. After chemical etching, I also obtained Ru nanocages for both samples (Figure 2.8, c and d). However, compared to the 6-nm Ru nanocages, I observed that more Ru accumulated on the corners and edges for the 18-nm Ru nanocages, implying less effective diffusion of Ru adatoms on the larger Pd seeds. As such, Pd seeds with a smaller size are better-suited for the synthesis of Ru nanocages with flat side faces, while larger seeds can lead to the formation of concave side faces.

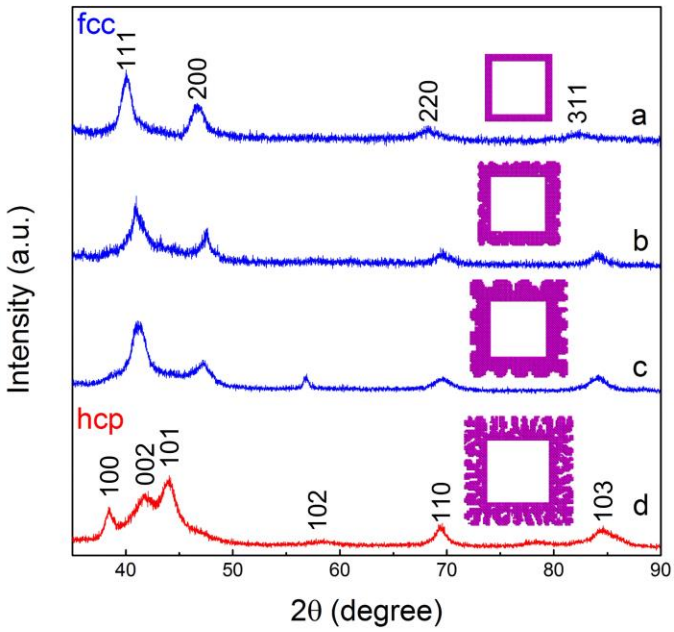

Figure 2.9. XRD patterns of Ru nanocages prepared using the standard procedure. The overall reaction volume was kept at 20 mL, while different amounts of Ru precursor were used: (a) 2 mg, (b) 4 mg, (c) 10 mg, and (d) 20 mg.

Bulk Ru crystallizes in an *hcp* structure. Although *fcc* Ru has been reported for nanoparticles of 2−5.5 nm in diameter [47], the underlying mechanism is still elusive. In our work, seed-mediated deposition seems to be an effective approach to the formation of Ru nanostructures with an *fcc* structure. As shown by the lattice spacing in Figure 2.3c, the

Ru atoms in the shell are packed in an *fcc* structure, which is ideally retained when the Pd cores are etched away. I confirmed this hypothesis by analyzing the Ru nanocages with XRD. Figure 2.9a shows the XRD pattern of the Ru nanocages prepared using the standard procedure. The (111), (200), (220), and (311) diffraction peaks are characteristic of an *fcc* lattice formed as a result of the epitaxial overgrowth of Ru on *fcc* Pd seeds. Since the lattice mismatch between Pd and *fcc* Ru is only 1.8%, the packing of Ru adatoms is dictated by the underlying Pd atoms, forming an *fcc* structure for the first few Ru overlayers. Our results clearly demonstrate that the *fcc* structure could be well retained for Ru shells to at least six atomic layers in thickness.

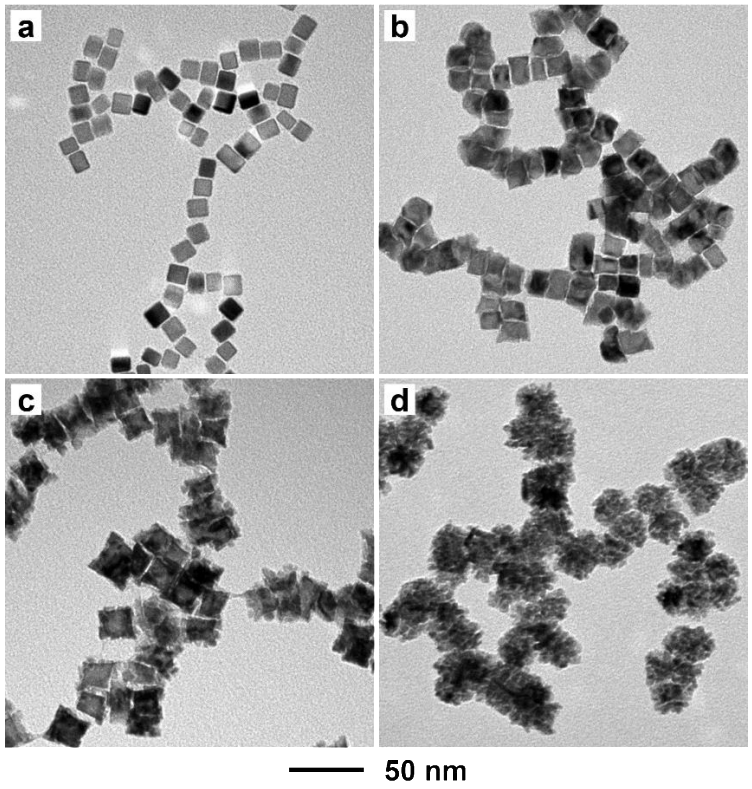

Figure 2.10. TEM images of typical Pd@Ru nanocrystals prepared from 10-nm Pd cubes using the standard procedure except with different amount of Ru precursor while keeping the overall volume 20 mL. (a) 1 mg, (b) 4 mg, (c) 10 mg, and (d) 20 mg.

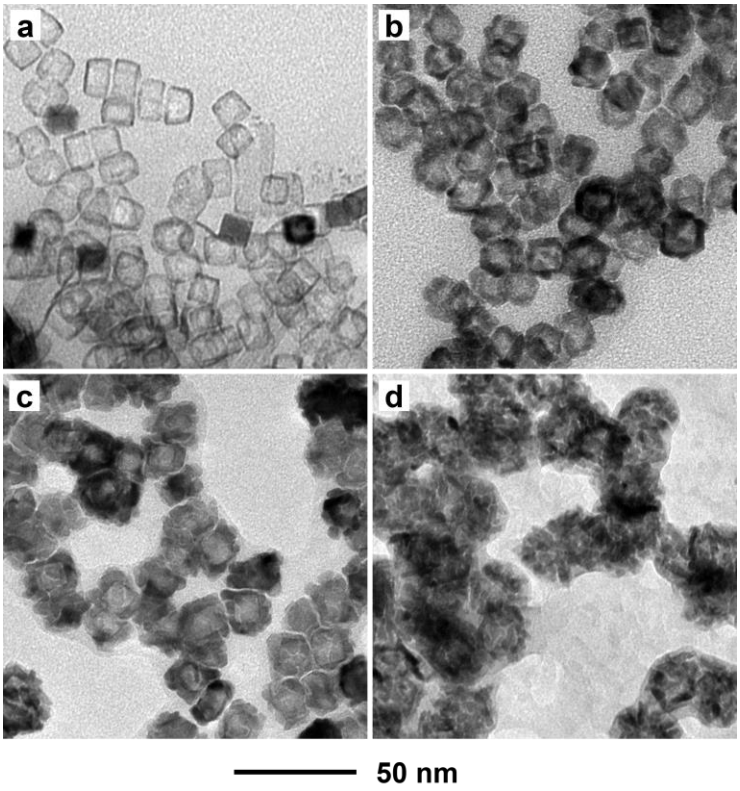

Figure 2.11. Typical TEM images of Pd@Ru nanocages prepared from 10-nm Pd cubes using the standard procedure except employing different amounts of Ru precursor while keeping the overall volume 20 mL. (a) 1 mg, (b) 4 mg, (c) 10 mg, and (d) 20 mg.

I also varied the amount of Ru(III) precursor while keeping the amount of Pd cubic seeds and the total volume of solution fixed to see if I can tune the wall thickness of the Ru nanocages. When the amount of Ru(III) precursor was reduced from 2 mg to 1 mg, the resultant core−shell nanocrystals maintained a cubic shape, with sharp corners and smooth surfaces (Figure 2.10a). However, as the amount of Ru(III) precursor was increased to 4 mg and 10 mg, the surface of the as-obtained nanocrystals became increasingly corrugated, indicating the involvement of a layer-plus-island growth mode. When the amount of Ru(III) precursor was further increased to 20 mg, the surface of each Pd seed was covered by a high density of branched arms, indicating the dominance of island growth (Figure 2.10d).

After selective removal of the Pd cores by etching, I obtained Ru nanocages with a more or less cubic shape, with the Ru walls becoming thinner or thicker relative to the standard synthesis depending on the amount of Ru precursor added (Figure 2.11, a−c). When the amount of Ru(III) precursor was too large, the Ru nanocages were covered by an extremely corrugated surface and presented an irregular shape (Figure 2.11d).

I also conducted XRD to analyze the crystal structure of the Ru nanocages (Figure 2.9, b−d). When the amount of Ru precursor was increased from 2 to 4 and 10 mg, the Ru nanocages still showed an *fcc* structure. Compared to Figure 2.9a, there was a slight shift for the peaks in Figure 2.9, b and c. In particular, for the sample in Figure 2.9c, a weak peak was observed around 58°, which can be assigned to the (102) diffraction of *hcp* Ru. This result implies the co-existence of some Ru nanoparticles with an *hcp* structure, which is consistent with the nanocrystals shown in Figure 2.10c. Interestingly, when the amount of Ru precursor was further increased to 20 mg, the crystal structure of Ru completely changed to *hcp*. Taken together, it can be concluded that the crystal structure of Ru changed from *fcc* to *hcp* as the injected amount of Ru(III) precursor was increased. The transition of Ru crystal structure over the amount of precursor can be attributed to the change of growth mode. When the amount of Ru precursor was low, the deposition rate of Ru atoms was comparable to the diffusion rate and thus Ru adatoms followed the layer-by-layer growth mode. For the first few layers of Ru adatoms, due to the similar properties of Pd and Ru as well as the interaction between them, the arrangement of Ru adatoms followed that of Pd atoms, leading to an *fcc* structure. When the amount of Ru precursor was increased, the growth of Ru adatoms was gradually dominated by deposition rate, which followed the layer-plus-island mode and further island growth mode. In particular, if

deposition rate was too high, self-nucleation of Ru could occur. The subsequently reduced Ru atoms grew on the nuclei and formed Ru nanoparticles. These nanoparticles should adopt *hcp* structure [47]. Then, the driving force of minimizing the total surface energy resulted in the agglomeration of these nanoparticles or adherence to the small Ru islands on the Pd surfaces. Therefore, the crystal structure of Ru was dominated by *hcp* Ru nanoparticles, showing an overall *hcp* structure. By varying the amount of Ru precursor added through seed-mediated growth, I can achieve Ru nanocages with both *fcc* and *hcp* structures.

Table 2.1. Binding energies (in eV) of 14 atomic and molecular species on all six model surfaces studied. Calculated values on surfaces to which each species binds most strongly are shown in bold. Reference energy is adsorbate in the gas phase, at infinite separation from the model surface.

Species	*hcp*-(0001)	*fcc*-(111)	*fcc*-(100)	*cage*-(100)	*cage*-$(100)_{Pd2}$	*cage*-$(100)_{Pd3}$
C	−7.55	−7.76	−8.42	−8.44	**−8.55**	−8.34
N	−6.00	−6.31	−6.25	−6.30	**−6.44**	−6.27
O	−6.00	**−6.25**	−6.00	−6.06	−6.15	−6.07
H	−2.91	−2.92	−2.88	−2.87	**−2.94**	−2.89
CH	−6.85	−7.17	−7.37	−7.35	**−7.73**	−7.33
CH_2	−4.47	−4.64	−4.66	−4.65	**−5.07**	−4.82
CH_3	−2.16	−2.22	−2.25	−2.28	−2.25	**−2.35**
NH	−5.14	−5.40	−5.47	−5.46	**−5.74**	−5.48
NH_2	−3.04	−3.13	−3.49	−3.50	−3.50	**−3.55**
NH_3	−0.75	−0.76	**−0.93**	−0.85	−0.86	−0.90
OH	−3.34	−3.41	−3.76	−3.80	−3.78	**−3.84**
CO	−1.89	−2.01	−2.07	−1.99	**−2.20**	−2.05
NO	−2.67	−2.91	−2.85	−2.82	**−2.96**	−2.89
N_2	−0.61	−0.70	−0.94	−0.94	**−1.34**	−0.96

To predict the catalytic properties of the as-synthesized nanocages, my collaborators performed DFT calculations (see details in the experimental section) to study the adsorption of 14 industrially-relevant atomic and molecular species on six model surfaces. These surfaces were selected to identify fundamental reasons for variations in catalytic descriptors (*i.e.*, binding energies and activation energies) resulting from incrementally transforming the most stable close-packed facet of *hcp* Ru to models representing the as-synthesized *fcc* Ru nanocages (these models are described in detail below and in the experimental section). The binding energies and preferred adsorption sites are provided in Table 2.1 and Table 2.2, respectively. They observed that the binding energy of atomic nitrogen, BE(N), on surfaces representative of the synthesized *fcc* nanocages is substantially stronger than that on the (0001) facet of *hcp* Ru, suggesting that *fcc* Ru structures would be particularly interesting candidates in the context of ammonia synthesis. They therefore chose to investigate N_2 dissociation on relevant model surfaces in detail, since this particular elementary step is widely recognized as the rate-determining step for NH_3 synthesis on Ru catalysts [65−68];the energetics of this elementary step on all surfaces studied are provided in Table 2.3. They caution that the choice of these surfaces, as discussed below, does not describe the actual physical transitions during synthesis as described above, but rather isolates the several factors (including crystal structure, surface morphology, and the ultrathin cage structure) that contribute to the predicted catalytic NH_3 synthesis activities of the as-synthesized Ru nanocages relative to typical *hcp* Ru catalysts.

They first calculate BE(N), BE(N_2), and activation energy of N_2 dissociation (E_a) on Ru(0001) (denoted *hcp*-(0001)), which they consider as a reference model for comparison with *fcc* model surfaces. Importantly, the N_2 dissociation transition state on *hcp*-(0001)

Table 2.2. Preferred binding sites of atomic and molecular species on all model surfaces studied. The site b-h-b denotes a N_2 molecule adsorbed to the surface with both its nitrogen atoms (bridge sites connected *via* a hollow site).

Species	*hcp*-(0001)	*fcc*-(111)	*fcc*-(100)	*cage*-(100)	*cage*-(100)$_{Pd2}$	*cage*-(100)$_{Pd3}$
C	Hcp	Hcp	Hollow	Hollow	Hollow over Ru	Hollow
N	Hcp	Hcp	Hollow	Hollow	Hollow over Ru	Hollow
O	Hcp	Hcp	Hollow	Hollow	Hollow over Ru	Hollow
H	Fcc	Fcc	Bridge	Bridge	Hollow over Pd	Bridge
CH	Hcp	Hcp	Hollow	Hollow	Hollow over Ru	Hollow
CH_2	Hcp	Hcp	Hollow	Hollow	Hollow over Ru	Hollow
CH_3	Fcc	Fcc	Bridge	Bridge	Bridge over Ru	Bridge
NH	Hcp	Hcp	Hollow	Hollow	Hollow over Ru	Hollow
NH_2	Bridge	Bridge	Bridge	Bridge	Bridge over Ru	Bridge
NH_3	Top	Top	Top	Top	Top	Top
OH	Fcc	Fcc	Hollow	Hollow	Hollow over Pd	Hollow
CO	Top	Hcp	Bridge	Bridge	Hollow over Ru	Top
NO	Hcp	Hcp	Bridge	Bridge	Hollow over Ru	Bridge
N_2	Top	Top	b-h-b	b-h-b	b-h-b over Ru	b-h-b

is more than 1 eV higher in energy than the gas-phase N_2, rendering N_2 dissociation non-competitive with N_2 desorption. They then calculated these same energetics on a model for the Ru(111) surface with *fcc* packing (denoted *fcc*-(111)), to determine the effect of changing from *hcp* to *fcc* crystal structure while maintaining a similar hexagonally-arranged surface structure. As shown in Table 2.3, they observe that *fcc*-(111) binds atomic N stronger than *hcp*-(0001) by 0.3 eV, and that E_a is reduced by 0.24 eV. BE(N_2) is also stronger by 0.09 eV, which further lowers the transition state energy for N_2 dissociation relative to N_2 desorption. A potential energy surface (PES) comparing the relative energies

of adsorbed states on these model surfaces is shown in Figure 2.12. Volcano plots for ammonia synthesis have predicted that ideal catalysts would bind atomic nitrogen approximately 0.2−0.5 eV stronger than *hcp* Ru (subject to reaction operating conditions) [67−70]. They thus superimpose on the PES a region showing optimal binding of atomic nitrogen (final state). Figure 2.12 shows that the *hcp* to *fcc* transition moves the energy of adsorbed N* into the optimal region of binding, which together with the reduced E_a and the more efficient competition of dissociation against N_2 desorption on the *fcc*-(111), predicts higher activity for *fcc*-(111) compared to *hcp*-(0001).

Table 2.3. Calculated binding energies of N* and N_2*, and activation energy barriers for N_2* dissociation on hcp and fcc Ru surface models. The difference between the N_2* transition state energy for dissociation and the N_2 gas-phase energy is provided in the last column, as a measure of competition between N_2* desorption (undesired) and dissociation. All values are in eV.

Model	**BE(N*)**	**BE(N_2*)**	**E_a (N_2* → 2N*)**	**$E_{TS} - E_{N2,gas}$**
hcp-(0001)	−6.00	−0.61	1.68	1.07
fcc-(111)	−6.31	−0.70	1.44	0.75
fcc-(100)	−6.25	−0.94	1.36	0.42
cage-(100)	−6.30	−0.94	1.28	0.34
cage-$(100)_{Pd2}$	−6.44	−1.34	1.29	−0.05
cage-$(100)_{Pd3}$	−6.27	−0.96	1.36	0.40

The as-synthesized catalysts preferentially expose (100) facets, however. They therefore compare *fcc*-(111) to the analogous *fcc*-(100) slab model. Although the binding energy of N* is slightly weakened (undesirably) by 0.06 eV, the activation energy barrier

is further reduced on *fcc*-(100) by 0.08 eV. Additionally, N_2* is stabilized by 0.24 eV, so the resulting dissociation process becomes even more competitive with desorption than in the *fcc*-(111) model. This suggests that the change in surface morphology from the *fcc*-(111) surface to the undercoordinated *fcc*-(100) surface will provide an additional enhancement in activity (Figure 12).

Since the as-synthesized catalysts are hollow, in contrast to traditional non-hollow nanoparticles, they also considered the reaction energetics on *cage*-(100) models representing hollow structures (see experimental section for details on model construction). The transition from *fcc*-(100) to *cage*-(100) lowers E_a by an additional 0.08 eV, despite having rather marginal effects on binding energies of N* and N_2*. N_2 dissociation is therefore even more competitive with desorption than in any of the three slab-based models, suggesting that *cage*-(100) should have superior activity to all of them for N_2 dissociation and NH_3 synthesis (Figure 2.12).

They finally consider the role of Pd impurities (8.8%, from ICP-MS) in the nanocage structure, investigating the effect of Pd atoms in the second and third surface layers on adsorption and N_2 dissociation kinetics (see experimental section for details on model formulation). When Pd is in the third surface layer (*cage*-$(100)_{Pd3}$), N* is further destabilized by 0.03 eV, N_2* is stabilized by 0.02 eV, and E_a is increased by 0.08 eV relative to *cage*-(100). Consequently, the transition state is pushed 0.06 eV higher in energy relative to *cage*-(100), and they predict that *cage*-$(100)_{Pd3}$ will have somewhat inferior activity to the *cage*-(100) model without Pd (although still superior to any of the three slab-based models representing non-hollow catalysts). In contrast, when Pd is in the second layer (*cage*-$(100)_{Pd2}$), N* is stabilized by 0.14 eV, N_2* is stabilized by 0.40 eV, and the

activation energy is only higher by a negligible 0.01 eV (all relative to *cage*-(100)). Due to the stabilization of N_2*, the dissociation transition state for *cage*-$(100)_{Pd2}$ is actually lower in energy than the gas-phase level of N_2 (Figure 2.12), so N_2 dissociation is actually preferable to N_2 desorption (in contrast to the other surfaces), which suggests that *fcc*(100) Ru nanocages with some Pd atoms in the layer right below the Ru surface may be a very promising NH_3 synthesis catalyst.

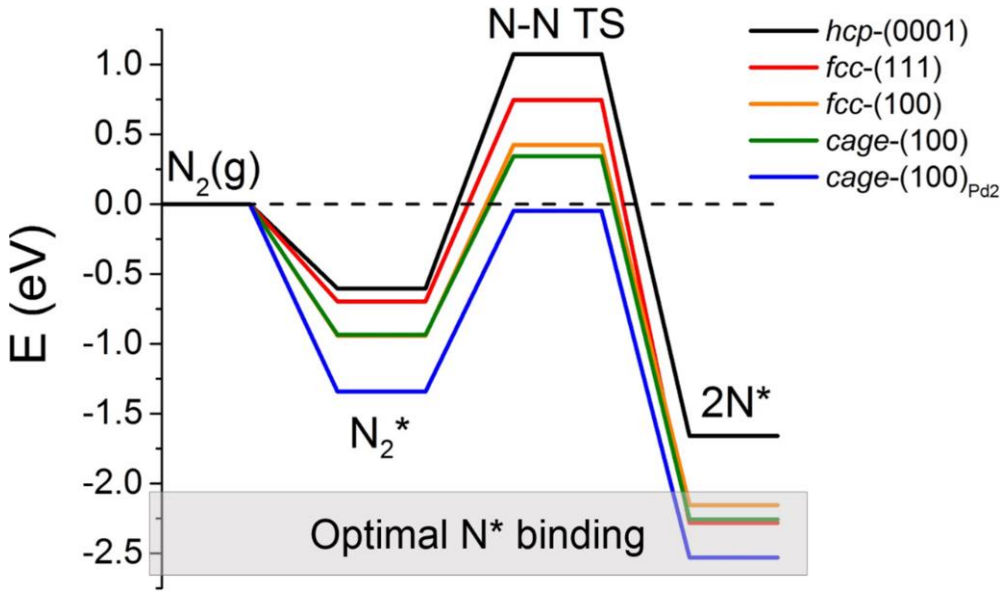

Figure 2.12. Potential energy surfaces for N_2 dissociation on five model surfaces. *hcp*-(0001) represents the *hcp* Ru(0001) slab model, *fcc*-(111) represents the *fcc* Ru(111) slab model, *fcc*-(100) represents the *fcc* Ru(100) slab model, *cage*-(100) is a model representative of the ultrathin, hollow cage structure, and *cage*-$(100)_{Pd2}$ is a cage model with Pd impurity in the second atomic layer of the cage. For clarity, *cage*-$(100)_{Pd3}$ is not shown, although its energetics are provided in Table 2.3 for comparison. All states are referenced to gas-phase N_2, denoted as N_2(g). "*" represents adsorbed states (with 2N* the energy of two adsorbed N* atoms at infinite separation), and "N-N TS" represents the transition state energy of the N-N bond breaking event. The grey region represents the optimal range of N* binding determined from previously published volcano relationships [36, 67, 70], drawn between 0.2 eV and 0.5 eV stronger binding of N* relative to that on *hcp*-(0001).

Regardless of the exact location of the subsurface Pd atoms, these cage models with Pd, which are most representative of the as-synthesized catalysts, should exhibit substantially improved activity for ammonia synthesis relative to *hcp*-(0001). Depending on the specific Pd position, surface sites bind atomic nitrogen between 0.3 and 0.4 eV more strongly than the *hcp*-(0001) model, binding N* in the previously-calculated optimal range. Further, the transition state energy for N_2 dissociation, which on *hcp*-(0001) was more than 1 eV above the gas-phase energy for N_2, is reduced to 0.4 eV above or even slightly below the gas-phase energy (depending on the particular exposed site considering Pd impurities), making N_2 dissociation considerably more competitive with its desorption than on *hcp*-(0001). These catalysts therefore exhibit great promise for ammonia synthesis. I also note that Kitigawa *et al.* have found *fcc* Ru nanoparticles to be stable up to 450 °C, a temperature typical of the Haber-Bosch process [47]. While the stability of these nanocages at high temperatures and reaction conditions has not been investigated, the fact that they are likely more active towards N−N bond-breaking than Ru nanoparticles indicates their potential to be not only active towards ammonia synthesis, but also stable if lower temperatures can be utilized to take advantage of the reduced activation energy barriers. In turn, lower pressures could also be utilized since N_2 is greatly stabilized on these surfaces, thus potentially making the energy-intensive Haber-Bosch process more competitive economically and environmentally.

2.3 Conclusion

In summary, I have demonstrated the seed-mediated synthesis of Ru nanocages with an *fcc* structure. For the polyol-based system, adding enough PVP, slow injection rate, high

reaction temperature, and a proper amount of precursor all played a certain role in enabling the layer-by-layer overgrowth. Epitaxial growth on Pd nanocubes by manipulating the deposition rate and surface diffusion leads to the formation of Pd@Ru core−shell nanocubes with well-controlled shape. Ru nanocages can subsequently be easily achieved through chemical etching. Most significantly, the resultant Ru nanocages show an *fcc* structure, which can be switched to the *hcp* structure by varying the amount of Ru precursor. Our synthesis can be also extended to Pd seeds with different sizes. This work reported here not only represents an effective approach to synthesize Ru nanocages, but also achieves Ru nanocages with an *fcc* structure, which our DFT calculations show will bind atomic N more strongly than *hcp* Ru(0001), leading to reduced activation energies for N_2 dissociation and potentially improved catalytic activities for ammonia synthesis. I believe the strategy in our work can provide insight into tuning the shapes, structures, and ultimately the catalytic activities of noble metals with different crystal structures.

2.4 Experimental Section

Chemicals and Materials. Ethylene glycol (EG, 99%) was obtained from J. T. Baker. Sodium tetrachloropalladate(II) (Na_2PdCl_4, 99.99%), ruthenium(III) chloride hydrate ($RuCl_3 \cdot xH_2O$, 99.99%), poly(vinylpyrrolidone) (PVP, MW $\approx$ 55000), L-ascorbic acid (AA, 99%), potassium bromide (KBr, 99%), potassium chloride (KCl, 99%), hydrochloric acid (HCl, 37%), and iron(III) chloride ($FeCl_3$, 97%) were all obtained from Sigma-Aldrich and used as received. All aqueous solutions were prepared using deionized (DI) water with a resistivity of 18.2 MΩ cm.

Synthesis of 6-nm, 10-nm, and 18-nm Pd Nanocubes. Pd nanocubes (6, 10, and 18 nm in edge length) were synthesized using protocols reported by our group [71]. For the synthesis of 10-nm Pd cubes, PVP (105 mg), AA (60 mg), and KBr (300 mg) were dissolved in DI water (8.0 mL), and then placed in a vial and pre-heated at 80 °C in an oil bath under magnetic stirring for 10 min. Subsequently, 3 mL of aqueous Na_2PdCl_4 solution (19 mg mL^{-1}) was injected into the preheated solution in one shot. The reaction solution was maintained at 80 °C under magnetic stirring for 3 h. The product was collected by centrifugations, washed three times with DI water to remove excess PVP and inorganic ions, and then re-dispersed in 6 mL EG. For the syntheses of 6 nm and 18 nm nanocubes, the procedure was kept the same except that KBr (300 mg) was replaced by KBr (5 mg) and KCl (185 mg), and KBr (600 mg), respectively.

Synthesis of Pd@Ru Core−shell Nanocubes. In a standard synthesis of Pd@Ru core−shell nanocrystals, 50 mg AA and 100 mg PVP were dissolved in 8 mL EG. The resulting solution was preheated at 200 °C under magnetic stirring for 10 min in a three-necked flask. Then, 1 mL of a suspension of 10-nm Pd cubes (2 mg mL^{-1}) was added into the flask and kept at 200 °C under magnetic stirring for 1 hour. Subsequently, 2 mg $RuCl_3 \cdot xH_2O$ and 250 mg PVP were dissolved in 20 mL EG and injected to the flask at a rate of 1 mL h^{-1} using a syringe pump. The reaction was allowed to continue for an additional 10 min to complete. The resultant product was collected by centrifugation, washed once with acetone and twice with water, and then re-dispersed in 8 mL DI water. The procedure for the syntheses of 6 and 18 nm Pd@Ru nanocubes was similar to that of 10 nm Pd@Ru nanocubes. 2 mg of 6-nm and 18-nm Pd nanocubes were used as seeds respectively and 3.64 mg and 1.04 mg $RuCl_3 \cdot xH_2O$ was injected accordingly. The number

of grown Ru layers was the same for these three kinds of Pd seeds. All other synthetic procedures were kept the same as for the 10-nm Pd@Ru cube synthesis.

Formation of Ru Nanocages. Chemical etching was conducted in an acidic aqueous solution to generate Ru nanocages. Typically, KBr (300 mg), PVP (50 mg), $FeCl_3$ (50 mg), HCl (0.3 mL, 37%), DI water (5.7 mL), and 1 mL as-prepared Pd@Ru core−shell nanocrystals were mixed together in an 18-mL vial. The mixture was transferred into an oil bath heated at 100 °C under magnetic stirring for 3 h. After that, the product was collected by centrifugation, washed three times with ethanol, and then re-dispersed in DI water for further characterization.

Morphological, Structural, and Elemental Analysis. Transmission electron microscopy (TEM) was conducted with an HT7700 microscope operated at 120 kV. High-resolution transmission electron microscopy (HRTEM) images were acquired on a Cs-corrected FEI Titan 80/300 kV TEM/STEM microscope at Oak Ridge National Laboratory (ORNL). All high-angle annular dark field scanning transmission electron microscopy (HAADF-STEM) images and energy-dispersive X-ray spectroscopy (EDX) data were acquired using an aberration-corrected Hitachi HD-2700 200 kV STEM equipped with a Brüker Quantax 400/S – STEM EDX detector at Georgia Institute of Technology. Inductively coupled plasma mass spectrometry (ICP-MS, NexION 300Q, PerkinElmer) was used for a quantitative analysis of metal content in the samples. X-ray diffraction (XRD) patterns were obtained with a PANalytical X'Pert PRO Alpha-1 diffractometer using 1.8 kW Ceramic Copper tube source.

DFT Calculations. Periodic, self-consistent density functional theory (DFT) calculations were performed using the Vienna *ab initio* Simulation Package (VASP) code

[72, 73]. Projector augmented wave (PAW) potentials were used to describe electron-ion interactions, and the generalized gradient approximation (GGA-PW91) was used to define the exchange-correlation functional [61–63]. Our calculations expand the wave function in a basis set of plane waves, truncated at a kinetic energy cutoff of 400 eV. All calculations were performed for adsorption on a single side of a metal slab, periodically repeated in a 2×2 unit cell, corresponding to 1/4 monolayer (ML) coverage (except for studies of Ru surface diffusion and substitution, where both 2×2 and 3×3 unit cells were used as explained below). At least 13 Å of vacuum were used to separate periodic images in the *z*-direction, to avoid interactions between images. The first Brillouin zone was sampled using a (6×6×1) Monkhorst-Pack *k*-point mesh [74]. Geometric optimization was performed until the Hellmann-Feynman forces on all atoms converged to less than 0.01 eV/Å. We calculated the binding energies (BE) of surface adsorbates according to:

$$BE = E_{total} - E_{slab} - E_{gas\text{-}phase\ adsorbate}$$

where E_{total} is the total energy of the metal slab with the adsorbate, E_{slab} is the total energy of the slab excluding the adsorbate, and $E_{gas\text{-}phase\ adsorbate}$ is the energy of the adsorbate in the gas phase at infinite separation from the slab. Activation energy barriers for bond dissociation steps and diffusion/substitution events were calculated using the climbing image nudged elastic band (CI-NEB) method [75], in which initial and final states were connected with seven interpolated images that were each converged to forces less than 0.1 eV/Å. Vibrational frequency calculations were performed to confirm a single imaginary vibrational mode for the calculated transition states. The vibrational frequencies of translational, vibrational, and rotational modes assumed a quantum harmonic oscillator,

and were estimated by second-order numerical differentiation of forces, using a step size of 0.015 Å.

Surface diffusion and substitution calculations were performed for Ru adatoms on a four-layer Pd(100) slab model, with the top two layers relaxed and the bottom two fixed at their bulk positions. The optimized lattice constant of Pd was calculated to be 3.958 Å, in good agreement with the experimental value of 3.89 Å [51]. In addition to performing calculations in a 2×2 unit cell, my collaborators also performed these diffusion and substitution calculations in a 3×3 unit cell, corresponding to 1/9 ML coverage, to gauge the effect of surface coverage on the calculated energetics. All parameters for the 3×3 unit cell were kept the same as for the 2×2 unit cell (including 6×6×1 *k*-point mesh).

They performed calculations on six model surfaces to evaluate variations in catalytic activity resulting from the substantial structural differences between the close-packed *hcp*-(0001) Ru structure and the as-synthesized *fcc*-(100) Ru nanocages. They calculated the lattice parameters of bulk *hcp* Ru to be a=2.729 Å and c/a=1.577, in close agreement with the experimental values of a=2.706 Å and c/a=1.582 [51]. These parameters were used to construct the *hcp*-(0001) slab model, which is used as a reference state for traditional *hcp* Ru catalysts. They also calculated the lattice constant of Ru in the bulk *fcc* crystal structure to be 3.821 Å, from which they constructed two slab models to gauge the effect of changing the structure of *hcp*-(0001) Ru to close-packed *fcc*-(111) and undercoordinated *fcc*-(100) surfaces. All three of these slab models utilized four-layer slabs with the bottom two layers fixed at their bulk positions, while the top two layers (and adsorbates) were allowed to fully relax.

Since the as-synthesized Ru catalysts are hollow, free-standing structures, they constructed additional models in a similar fashion to that they used recently for modeling Pt-Pd nanocages [28]. In particular, they modeled the as-synthesized six-layer nanocages as a six-layer membrane with a (100)-like surface arrangement of atoms and all atoms relaxed. The interatomic distance within layers was optimized; for the model consisting of pure Ru (*i.e.*, the *fcc*-(100)-cage), the interatomic distance within each layer was 2.685 Å. They note that these optimized interatomic distances were slightly constricted relative to the *fcc*-(100) slab, which possesses an interatomic distance of 2.702 Å. Finally, in order to model the synthesized structures most accurately, they exchanged two Ru atoms in the cage model with Pd atoms, yielding a mass ratio of 8.7% Pd, consistent with the 8.8% Pd in the nanocages characterized by ICP-MS. The optimized interatomic distance for this structure is 2.690 Å. As in our previous work [28], they assumed that all Pd in contact with the etching agent should be removed during the etching process, so they therefore included no Pd in the exposed top or bottom layers of the membrane. They instead chose to disperse the two Pd atoms in the slab, placing one in the second membrane layer from the top (denoted *cage*-$(100)_{Pd2}$) and one in the fourth membrane layer from the top (i.e. third layer from the bottom, denoted *cage*-$(100)_{Pd3}$). They note that this arrangement of Pd atoms in the membrane structure yields two different surface profiles in our membrane model (one with Pd in the second layer from the surface, and the other with Pd in the third layer from the surface). To elucidate the effect of Pd position within the slab, they therefore performed calculations on both exposed surfaces (one at a time) of the membrane. They expect that the Pd is dispersed somewhat randomly in the interior of the true nanocage structures due to the intermixing of Pd and Ru during the synthesis of the core−shell particles. They

therefore do not attempt to determine the minimum energy position of Pd, but rather investigate this effect of placing Pd in different positions relative to the surface to elucidate the effect of different types of adsorption sites (and the resulting differences in energetics) in the true catalyst.

As a final note, they observe that although 4d transition metals – to which Ru belongs – do not show magnetism in their natural bulk crystal structures, changes to those crystal structures could impart ferromagnetism [76]. In fact, different phases of Ru have been studied computationally for the sole purpose of investigating their magnetic properties [77]. They have performed test spin-polarized calculations with and without adsorbates on all model systems described above, and calculated negligible magnetic moments and negligible differences in total energies when compared to corresponding spin-restricted calculations (consistent with the previous computational work for *fcc* Ru) [77]. As such, all results presented in this work were calculated without spin-polarization.

2.5 Notes to Chapter 2

Part of this chapter is adapted from the paper "Synthesis and Characterization of Ru Cubic Nanocages with a Face-Centered Cubic Structure by Templating with Pd Nanocubes" published in *Nano Letters* [78].

2.6 References

[1] Corma, A.; Concepcion, P.; Boronat, M.; Sabater, M. J.; Navas, J.; Yacaman, M. J.; Larios, E.; Posadas, A.; Lopez-Quintela, M. A.; Buceta, D.; Mendoza, E.; Guilera, G.; Mayoral, A. *Nat. Chem.* **2013**, 5, 775−781.

[2] Xie, J.; Zhang, Q.; Gu, L.; Xu, S.; Wang, P.; Liu, J.; Ding, Y.; Yao, Y.; Nan, C.; Zhao, M.; You, Y.; Zou, Z. *Nano Energy*, **2016**, 21, 247−257.

[3] Smith, P. A.; Nordquist, C. D.; Jackson, T. N.; Mayer, T. S.; Martin, B. R.; Mbindyo, J.; Mallouk, T. E. *Appl. Phys. Lett.* **2000**, 77, 1399−1341.

[4] Mulvihill, M. J.; Ling, X. Y.; Henzie, J.; Yang, P. *J. Am. Chem. Soc.* **2010**, 132, 268−274.

[5] Mahmoud, A. M.; El-Sayed, A. M. *J. Am. Chem. Soc.* **2010**, 132, 12704−12710.

[6] Vinod, C. P.; Kulkarni, G. U.; Rao, C. N. R. *Chem. Phys. Lett.* **1998**, 289, 329−333.

[7] Sreedhala, S.; Sudheeshkumar, V.; Vinod, C. P. *Nanoscale* **2014**, 6, 7496−7502.

[8] Tian, N.; Zhou, Z.; Yu, N.; Wang, L.; Sun, S. *J. Am. Chem. Soc*. **2010**, 132, 7580−7581.

[9] Nikoobakht, B.; El-Sayed, A. M. *Chem. Mater*. **2003**, 15, 1957−1962.

[10] Xia, X.; Zeng, J.; Oetjen, K. L.; Li, Q.; Xia, Y.; *J. Am. Chem. Soc*. **2012**, 134, 1793−1801.

[11] Jana, N. R.; Gearheart, L.; Murphy, C. J. *Chem. Commun*. **2001**, 7, 617−618.

[12] Zeng, J.; Zheng, Y.; Rycenga, M.; Tao, J.; Li, Z. Y.; Zhang, Q.; Zhu, Y.; Xia, Y. *J. Am. Chem. Soc*. **2010**, 132, 8552−8553.

[13] Fan, F.-R.; Liu, D.; Wu, Y.; Duan, S.; Xie, Z; Jiang, Z; Tian, Z. *J. Am. Chem. Soc*. **2008**, 130, 6949−6951.

[14] Habas, S. E.; Lee, H.; Radmilovic, V.; Somorjai, G. A.; Yang, P. *Nat. Mater*. **2007**, 6, 692−297.

[15] Kobayashi, H.; Lim, B.; Wang, J.; Camargo H.C. P.; Yu, T.; Kim, J. M.; Xia, Y. *Chem. Phys. Lett*. **2010**, 494, 249−254.

[16] Xue, C.; Millstone, J. E.; Li, S.; Mirkin, C. A. *Angew. Chem. Int. Ed*. **2007**, 46, 8436−8439.

[17] Jin, M.; Zhang, H.; Xie, Z.; Xia, Y. *Energy Environ. Sci*. **2012**, 5, 6352−6357.

[18] Wang, Y.; Wan, D.; Xie, S.; Xia, X.; Huang, C.; Xia, Y. *ACS Nano* **2013**, 7, 4586−4594.

[19] Park, J.; Zhang, L.; Choi, S.; Roling T. L.; Lu, N.; Herron, A. J.; Xie, S.; Wang, J.; Kim, J. M.; Mavrikakis, M.; Xia, Y. *ACS Nano* **2015**, 9, 2635−2647.

[20] Wang, X.; Vara, M.; Luo, M.; Huang, H.; Ruditskiy, A.; Park, J.; Bao, S.; Liu, J.; Howe, J., Chi, M.; Xie, Z.; Xia, Y. *J. Am. Chem. Soc.* **2015**, 137, 15036−15042.

[21] Wang, X.; Choi, S.; Roling, T. L.; Luo, M.; Ma. C.; Zhang, L.; Chi, M.; Liu, J.; Xie, Z.; Herron, A. J.; Mavrikakis, M.; Xia, Y. *Nat. Commun.* **2015**, 6, 7594−7601.

[22] Xie, S.; Lu, N.; Xie, Z.; Wang, J.; Kim, J. M.; Xia, Y. *Angew. Chem. Int. Ed*. **2012**, 51, 10266−10270.

[23] Wang, C.; Vliet, D.; More, K. L.; Zaluzec, N. J.; Peng, S.; Sun, S.; Daimon, H.; Wang, G.; Greeley, J.; Pearson, J.; Paulikas, A. P.; Karapetrov, G.; Strmcnik, D.; Maekovic, N. M.; Stamenkovic, V. R. *Nano Lett.* **2011**, 11, 919−926.

[24] Mazumder, V.; Chi, M.; More, K. L.; Sun, S. *J. Am. Chem. Soc.* **2010**, 132, 7848−7849.

[25] Zhang, H.; Jin, M.; Wang, J.; Li, W.; Camargo, C. H. P.; Kim, J. M.; Yang, D.; Xie, Z.; Xia, Y. *J. Am. Chem. Soc*. **2011**, 133, 6078−6089.

[26] Skrabalak, S. E.; Au, L.; Li, X. D.; Xia, Y. *Nat. Protoc*. **2007**, 2, 2182−2190.

[27] Zeng, J.; Zhang, Q.; Chen, J.; Xia, Y. *Nano Lett*. **2010**, 10, 30−35.

[28] Zhang, L.; Roling, L. T.; Wang, X.; Vara, M.; Chi, M.; Liu, J.; Choi, S.-I.; Park, K.; Herron, J. A.; Xie, Z.; Mavrikakis, M.; Xia, Y. *Science* **2015**, 349, 412−416.

[29] Nakatsuka, H.; Yamamura, T.; Shuto, Y.; Tanaka, S.; Yoshimura, M.; Kitamura, M. *J. Am. Chem. Soc*. **2015**, 137, 8138−8149.

[30] Westerhaus, A. F.; Wendt, B.; Dumrath, A.; Wienhofer, G.; Junge, K.; Beller, M. *ChemSusChem* **2013**, 6, 1001−1005.

[31] Liu, K.; Wang, A.; Zhang, T. *ACS Catal*. **2012**, 2, 1165−1178.

[32] Su, F.; Lv, L.; Lee, F.; Liu, T.; Copper, A. I.; Zhao, X. *J. Am. Chem. Soc*. **2007**, 129, 14213−14223.

[33] Joo, S. H.; Park, J. Y.; Renzas, J. R.; Butcher, D. R.; Huang, W.; Somorjai, G. A. *Nano Lett*. **2010**, 10, 2709−2713.

[34] Honkala, K.; Hellman, A.; Remediakis, I. N.; Logadottir, A.; Carlsson, A.; Dahl, S.; Christensen, C. H.; Norskov, J. K. *Science* **2005**, 307, 555−558.

[35] Aika, K.; Hori, H.; Ozaki, A. *J. Catal.* **1972**, 27, 424−431.

[36] Jacobsen, C.; Dahl, S.; Hansen, P. L.; Tornqvist, E.; Jensen, L.; Topsoe, H.; Prip, D. V.; Moenshaug, P. B.; Chorkendorff, L. *J. Mol. Catal. A Chem.* **2000**, 163, 19−26.

[37] Kim, H. Y.; Lee, H. M.; Park, J. N. *J. Phys. Chem. C* **2010**, 114, 7128−7131.

[38] Sharma, S.; Hu, Z.; Zhang, P.; Mcfarland, E. W. *J. Catal*. **2009**, 266, 92−97.

[39] Yin, A.; Liu, W.; Ke, J.; Zhu, W.; Gu, J.; Zhang, Y.; Yan, C. *J. Am. Chem. Soc.* **2012**, 134, 20479−20489.

[40] Koenigsmann, C.; Semple, D.; Sutter, E.; Tobierre, S.; Wong, S. *ACS Appl. Mater. Interfaces* **2013**, 5, 5518−5530.

[41] Ghosh, S.; Ghosh, M, Rao, C. *J. Cluster Sci.* **2007**, 18, 97−111.

[42] Watt, J.; Yu, C.; Chang, S.; Cheong, S.; Tilley, R. *J. Am. Chem. Soc.* **2013**, 135, 606−609.

[43] Ye, H.; Wang, Q.; Catalano, M.; Lu, N.; Vermeylen, J.; Kim, J. M.; Liu, Y.; Sun, Y.; Xia, X. *Nano Lett*. **2016**, 2812−2817.

[44] Ge, J.; He, D.; Bai, L.; You, R.; Lu, H.; Lin, Y.; Tan, C.; Kang, Y.; Xiao, B.; Wu, Y.; Deng, Z.; Huang, W.; Zhang, H.; Hong, X.; Li, Y. *J. Am. Chem. Soc*. **2015**, 137, 14566−14569.

[45] Koenigsmann, C.; Wong, S. S. *Energy Environ. Sci.* **2011**, 4, 1161−1176.

[46] Zhou, X.; Gan, Y.; Du, J.; Tian, D.; Zhang, R.; Yang, C.; Dai, Z. *J. Power Sources*, **2013**, 232, 310−322.

[47] Kusada, K.; Kobayashi, H.; Yamamoto, T.; Matsumura, S.; Sumi, N.; Sato, K.; Nagaoka, K.; Kubota, Y.; Kitagawa, H. *J. Am. Chem. Soc*. **2013**, 135, 5493−5496.

[48] Brink, V. M.; Peck, A. M.; More, L. K.; Hoefelmeyer, D. J. *J. Phys. Chem. C* **2008**, 112, 12122−12126.

[49] Zhang, H.; Jin, M.; Xiong, Y.; Lim, B.; Xia, Y. *Acc. Chem. Res*. **2013**, 46, 1783−1794.

[50] Xia, X.; Xie, S.; Liu, M.; Peng, H.; Lu, N.; Wang, J.; Kim, M. J.; Xia, Y. *Proc. Natl. Acad. Sci. U.S.A.* **2013**, 110, 6669−6673.

[51] Lide, D. R, *CRC Handbook of Chemistry and Physics*, CRC Press, 96th edn, **2015**.

[52] Xiong, Y.; McLellan, J. M.; Chen, J.; Wiley, B.; Xia, Y. *J. Am. Chem. Soc.* **2005**, 127, 17118−17127.

[53] Sun, S.; Murray, C. B.; Weller, D.; Folks, L.; Moser, A. *Science* **2000**, 287, 1989−1992.

[54] Chen, J.; Herricks, T.; Xia, Y. *Angew. Chem. Int. Ed.* **2005**, 117, 2645−2648.

[55] Yin, Y.; Alivisatos, A. P. *Nature* **2005**, 437, 664−670.

[56] Wiley, B.; Herricks, T.; Sun, Y.; Xia, Y. *Nano Lett.* **2004**, 4, 1733−1739.

[57] Pastoriza-Santos, I.; Liz-Marzan, L. M. *Nano Lett.* **2002**, 2, 903−905.

[58] Xia, Y.; Xia, X.; Peng, H. *J. Am. Chem. Soc*. **2015**, 137, 7947−7966.

[59] Peng, H.; Park, J.; Zhang, L.; Xia, Y. *J. Am. Chem. Soc*. **2015**, 137, 6643−6652.

[60] Romanenko, A. V.; Tyschishin, E. A.; Moroz, E. M.; Likholobov, V. A.; Zaikovskii, V. I.; Jhung, S. H.; Park, Y. S. *Appl. Catal. A* **2002**, 227, 117−123.

[61] Blochl, P. E. *Phys. Rev. B* **1994**, 50, 17953−17979.

[62] Kresse, G.; Joubert, D. *Phys. Rev. B* **1999**, 59, 1758−1775.

[63] Perdew, J. P.; Wang, Y. *Phys. Rev. B* **1992**, 45, 13244−13249.

[64] Xia, X.; Figueroa-Cosme, L.; Tao, J.; Peng, H.; Niu, G.; Zhu, Y.; Xia, Y. *J. Am. Chem. Soc*. **2014**, 136, 10878−10881.

[65] Rod, T. H.; Logadottir, A.; Norskov, J. K. *J. Chem. Phys.* **2000**, 112, 5343−5347

[66] Vojvodic, A.; Medford, A. J.; Studt, F.; Abild-Pedersen, F.; Khan, T. S.; Bligaard, T.; Norskov, J. K. *Chem. Phys. Lett.* **2014**, 598, 108−112.

[67] Logadottir, A.; Rod, T. H.; Norskov, J. K.; Hammer, B.; Dahl, S.; Jacobesen, C. J. H. *J. Catal.* **2001**, 197, 229−231.

[68] Dahl, S.; Sehested, J.; Jacobsen, C. J. H.; Tornqvist, E.; Chorkendroff, I. *J. Catal.* **2000**, 192, 391−399.

[69] Jacobsen, C. J. H.; Dahl, S.; Boisen, A.; Clausen, B. S.; Topsoe, H.; Logadottir, A.; Norskov, J. K. *J. Catal.* **2002**, 205, 382−387.

[70] Dahl, S.; Logadottir, A.; Jacobsen, C. J. H.; Norskov, J. K. *Appl Catal. A* **2001**, 222, 19−29.

[71] Jin, M.; Liu, H.; Zhang, H.; Xie, Z.; Liu, J.; Xia, Y. *Nano Res.* **2011**, 4, 83−91.

[72] Kresse, G.; Furthmuller, J. *Phys. Rev. B* **1996**, 54, 11169−11186.

[73] Kresse, G. Furthmuller, J. *Comput. Mater. Sci.* **1996**, 6, 15−50.

[74] Monkhorst, H. J.; Pack, J. P. *Phys. Rev. B* **1976**, 13, 5188−5192.

[75] Henkelman, G.; Uberuaga, B. P.; Jonsson, H. *J. Chem. Phys.* **2000**, 113, 9901−9904.

[76] Watanable, S.; Komine, T.; Kai, T.; Shiiki, K. *J. Magn. Magn. Mater.* **2000**, 220, 277−284.

[77] Kobayashi, M.; Kai, T.; Takano, N.; Shiiki, K. *J. Phys.: Condens. Matter* **1995**, 7, 1835−1842.

[78] Zhao, M.; Figueroa-Cosme, L.; Elnabawy, A. O.; Vara, M.; Yang, X.; Roling, L. T.; Chi, M.; Mavrikakis, M.; Xia, Y. *Nano Lett.* **2016**, 16, 5310−5317.

CHAPTER 3

FACILE SYNTHESIS OF RUTHENIUM-BASED OCTAHEDRAL NANOCAGES WITH ULTRATHIN WALLS IN A FACE-CENTERED CUBIC STRUCTURE

3.1 Introduction

Shape-controlled synthesis of noble-metal nanocrystals has received great interest in recent years due to the remarkable performance of these nanocrystals in various applications related to catalysis [1–4], photonics [5,6], electronics [7], and medicine [8–10]. Many different methods have been developed for generating noble-metal nanocrystals with diversified shapes and thereby different types of facets on the surface, in addition to diverse structures (*e.g.*, core-frame *vs.* core-shell or solid *vs.* hollow) [11–14]. Among these methods, seed-mediated growth has emerged as probably the most versatile and powerful approach in terms of experimental control over the shape and structure, as well as the particle size [15–17]. To this end, nanocrystals of various compositions have been successfully prepared with core-frame and core-shell structures [18–21]. Significantly, one can selectively remove the cores through wet etching, generating highly open structures such as nanoframes and nanocages [21–25]. For nanocages, in particular, they are of great interest to catalysis owing to their high utilization efficiency of atoms and the well-defined, controllable facets or surface structures. In a set of recent studies, our group have synthesized Pt-based nanocages with cubic, octahedral, decahedral, and icosahedral shapes and demonstrated their enhanced performance toward the oxygen reduction reaction [23–25]. Remarkably, when a second metal with a different crystal structure is involved, seed-

mediated growth also offers a simple and straightforward method for the preparation of core-shell nanocrystals with an unusual atomic packing for the shell [26–28]. Even after removal of the seed in the core, both the surface and crystal structures in the shell can still be retained.

Ruthenium (Ru) and Ru-based nanocrystals have been widely used in an array of catalytic applications such as hydrogenation reactions [29], ammonia synthesis [30, 31], and CO oxidation [32]. Recently, several groups have reported the syntheses of Ru nanocrystals with various shapes and different crystal structures, and further explored the facet- or structure-dependent catalytic properties [33–35]. Since the discovery of face-centered cubic (*fcc*) Ru [35], chemical synthesis of Ru nanocrystals with this unique crystal structure has become a subject of active research, in an attempt to create properties and applications that are not supported by the conventional hexagonal close-packed (*hcp*) Ru. To this end, I have demonstrated the successful synthesis of *fcc*-structured Ru cubic nanocages by templating with Pd nanocubes [36]. Based upon density functional theory (DFT) calculations, the *fcc*-structured Ru cubic nanocages were found to possess promising catalytic properties toward ammonia synthesis. Meanwhile, another group has also synthesized Ru nanoframes in the *fcc* structure, together with higher catalytic activities toward the reduction of *p*-nitrophenol by sodium borohydride and the dehydrogenation of ammonia borane [37]. Lee and co-workers have reported the one-pot synthesis of hollow Cu-doped Ru octahedral nanocages via an *in-situ* generated metastable Cu nanoparticle template [38]. However, the as-synthesized Ru octahedral nanocages took an *hcp* structure with bumpy surfaces where the facets were not well defined. To our knowledge, there is no report on the synthesis of Ru octahedral nanocages with an *fcc* structure enclosed by

smooth {111} facets. When combined with the Ru cubic nanocages reported in our prior work, the octahedral nanocages would allow for a systematic investigation of their catalytic properties as a function of the facet type or surface structure.

Here I report the successful synthesis of Pd@Ru octahedral nanocrystals based on seed-mediated growth and their transformation into Ru-based octahedral nanocages through wet chemical etching. The nanocages were enclosed by well-defined {111} facets, together with an ultrathin wall thickness of about five atomic layers. Interestingly, the Ru nanocages adopted an *fcc* structure rather than the conventional *hcp* structure of bulk Ru. Such octahedral nanocages with edge lengths of 12, 18, and 26 nm could all be synthesized using the same protocol, except for the use of Pd octahedral templates with different sizes. The thermal stability and shape-dependent properties toward the reduction of 4-nitrophenol were investigated, together with the first-principles, self-consistent DFT calculations to extensively evaluate the catalytic activity of the octahedral nanocages toward ammonia synthesis.

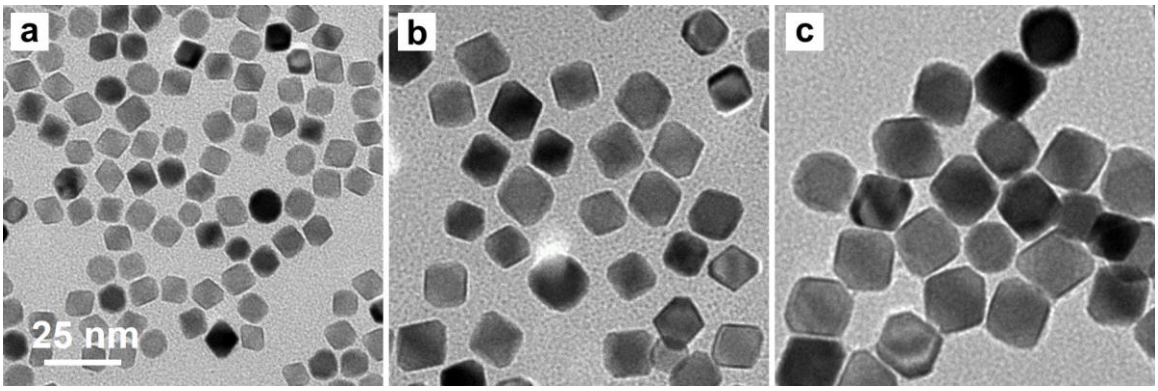

Figure 3.1. TEM images of Pd octahedra with different edge lengths: (a) 12 nm, (e) 18 nm, and (f) 26 nm. The scale bar in panel a applies to all panels in (a–c).

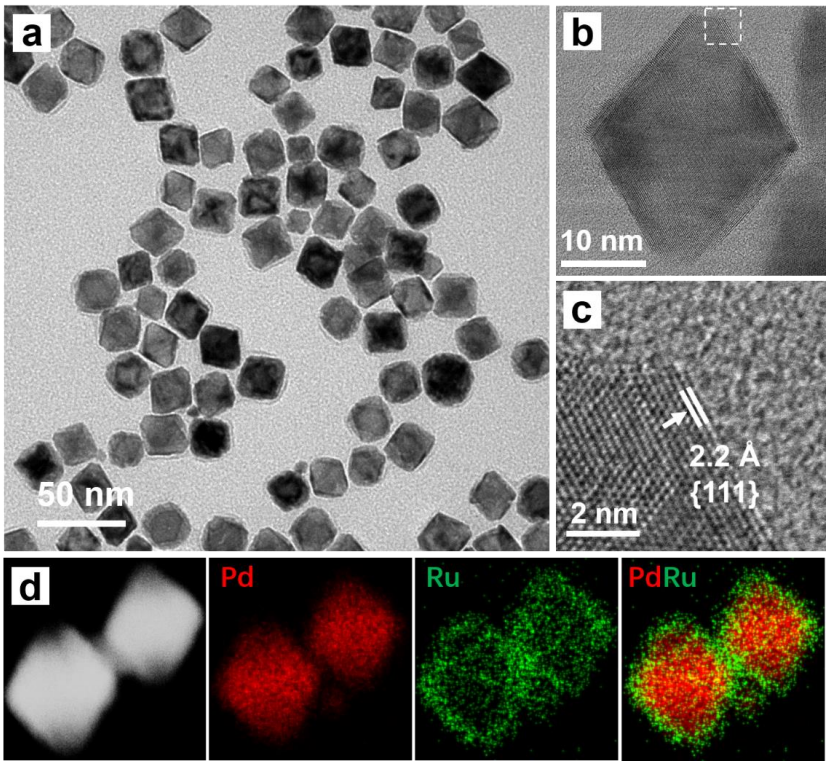

Figure 3.2. (a) Typical TEM image of the Pd@Ru core-shell nanocrystals synthesized from 18-nm Pd octahedral seeds. (b) HRTEM image of a single core-shell octahedron. (c) Atomic-resolution image taken from the region marked by a box in Panel (b). (d) HAADF-STEM image and EDX mapping (red = Pd, green = Ru) of two core-shell octahedra.

3.2 Results and Discussion

Characterization of Pd@Ru Core-shell Octahedra and Ru Octahedral Nanocages. I evaluated Pd octahedra with three different edge lengths (Figure 3.1, 12, 18, and 26 nm) and all of them showed slight truncation at the corners. Figure 3.2a shows a typical TEM image of the products derived from the 18-nm Pd octahedra. The nanocrystals took a well-defined octahedral shape with an average edge length of about 20 nm, indicating the deposition of Ru shells. Figure 3.2b shows HAADF-STEM image taken from an individual particle. The relatively smooth side faces suggest adequate surface diffusion for the Ru adatoms. The lattice fringe spacing of the Ru overlayers was 2.2 Å

(Figure 3.2c), which correlates well with the {111} planes of *fcc* Ru. Although bulk Ru adopts an hcp structure, the small lattice mismatch between *fcc* Pd and *fcc* Ru (3.89 Å vs. 3.82 Å, 1.8% mismatch) [37], as well as their similar atomic radii, make it possible for the Ru adatoms to follow the packing of the underlying Pd atoms through epitaxial growth. Figure 3.2d shows the EDX mapping of two particles, further confirming the formation of a Pd@Ru core-shell structure. The Ru adatoms were uniformly distributed on the side faces and vertices of the Pd octahedral seeds, generating conformal shells.

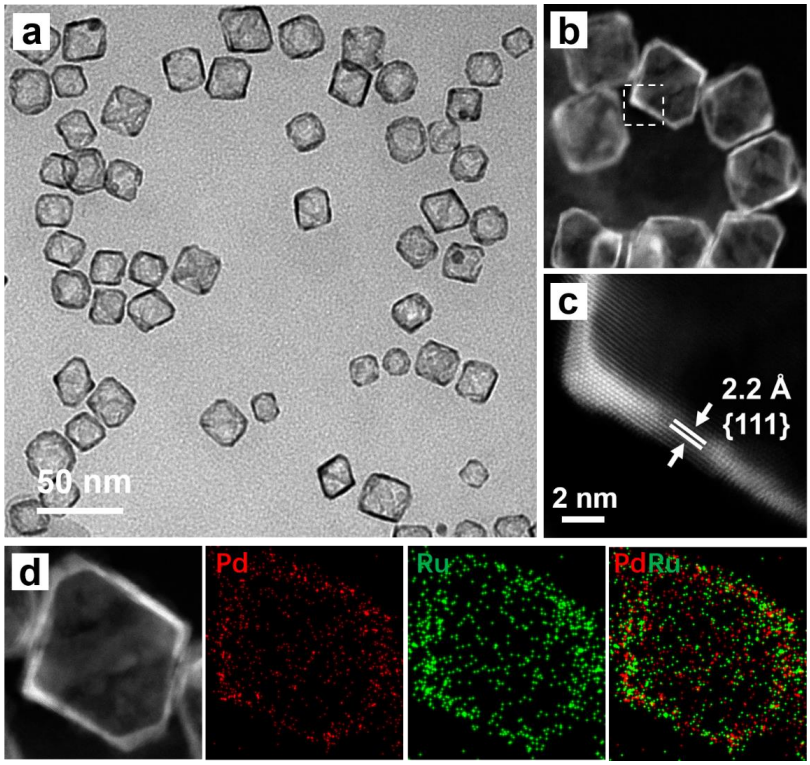

Figure 3.3. (a) Typical TEM image of the Ru octahedral nanocages derived from the core-shell nanocrystals shown in Figure 3.2. (b) HAADF-STEM image of the Ru octahedral nanocages. (c) Atomic-resolution HAADF-STEM image taken from the region marked by a box in Panel (b). (d) HAADF-STEM image and EDX mapping (red = Pd, green = Ru) of an individual Ru nanocage.

In order to obtain Ru octahedral nanocages, wet chemical etching was used to selectively remove the Pd cores. The success of such an etching process relies on the favorable difference in chemical stability between Ru and Pd, and their relative vulnerability toward the oxidative etching process. By exposing the structures to the Fe^{3+}/Br^{-} pair, the Ru will remain unreacted while the Pd cores can be etched away through the following reaction [20]:

$$Pd + 2Fe^{3+} + 4\ Br^{-} \rightarrow PdBr_4^{2-} + 2Fe^{2+}$$

Figure 3.3, a and b, shows typical TEM and HAADF-STEM images of the as-obtained Ru nanocages, clearly demonstrating that the Pd cores were effectively removed during chemical etching. The octahedral shape was well retained in the Ru nanocages. Based on the HAADF-STEM image shown in Figure 3.3c, the lattice spacing of the Ru shell was 2.2 Å, which can be assigned to the {111} planes of *fcc* Ru, in agreement with what is shown in Figure 3.2c. The *fcc* structure of the Ru octahedral nanocages was further confirmed by XRD analysis, as illustrated in Figure 3.4. The (111), (200), (220), and (311) diffraction peaks can all be assigned to the *fcc* Ru, in agreement with the data shown in Figure 3.2c and Figure 3.3c. EDX mapping was used to examine the elemental composition of the Ru nanocage. Figure 3.3d shows that the Pd core was selectively removed while the Ru shell was well-preserved. Different from what is shown in Figure 3.2d, Ru became the dominant element in the products after chemical etching. ICP-MS measurement was conducted to quantitatively analyze the elemental compositions before and after Pd etching. After etching, the weight percentage of Pd dropped from 73.5% in the core-shell octahedra to

9.9% in the nanocages, while the weight percentage of Ru increased from 26.5% to 90.1%, indicating a highly efficient etching process for Pd. The calculated thickness of Ru nanocages was approximately 4.5 atomic layers in terms of pure Ru and 5.0 atomic layers when including both Pd and Ru. The ICP-MS data is consistent with what is shown in Figure 3.3d, confirming that the resultant nanocages was dominated by Ru. Taken together, these results clearly establish that seed-mediated growth is a powerful method for generating nanocrystals with unusual crystal structures.

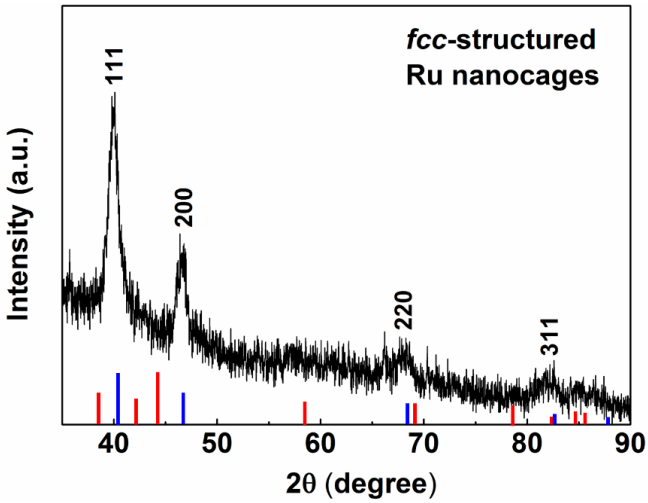

Figure 3.4. XRD pattern of the Ru nanocages derived from the 18-nm Pd octahedra, indicating the formation of an *fcc* crystal structure. Blue bars: JCPDS no. 88-2333 (*fcc* Ru). Red bars: JCPDS no. 06-0663 (*hcp* Ru).

Investigation into the Mechanisms Involved in the Synthesis. To investigate the mechanism involved in the formation of Pd@Ru_{nL} core-shell octahedra, I conducted a set of control experiments. Since the Ru shells could be well-preserved during wet chemical etching, the nanocrystals before and after wet chemical etching were compared to

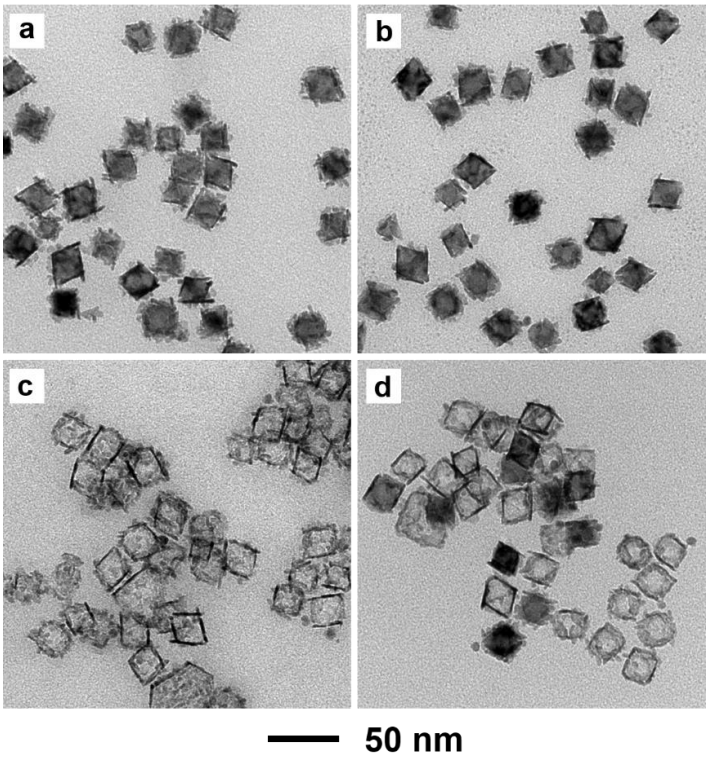

Figure 3.5. TEM images of (a, b) the core-shell nanocrystals and (c, d) their corresponding nanocages prepared from 18-nm Pd octahedra using the standard procedure, except for the use of different injection rates for the Ru(III) precursor: (a, c) 5 mL h^{-1} and (b, d) 20 mL h^{-1}, respectively.

quantitatively elucidate the mechanism involved in the synthesis. I first examined the impact of the injection rate of the Ru(III) precursor, which had a direct correlation with the deposition rate of the Ru atoms. When the injection rate was increased from 1 to 5 mL h^{-1}, the surfaces of the as-obtained products were covered by plenty of small particles (Figure 3.5a). Along with the increased injection rate, the deposition rate of Ru atoms was also increased accordingly and even became greater than the surface diffusion rate. As a result, the growth mode of Ru atoms on the Pd octahedral seeds was switched from layer-by-layer to layer-plus-island, leading to the formation of a rough surface. When I further increased the injection rate to 20 mL h^{-1}, self-nucleation also appeared (Figure .35b). After selectively

etching away the Pd cores, I could clearly resolve the distribution of Ru atoms in the parent core-shell nanocrystals, as shown in Figure 3.5, c and d. The surfaces of the resultant Ru nanocages were also covered by abundant small particles, consistent with those shown in Figure 3.5, a and b. Other than these small particles attached to the side faces, there were more Ru atoms deposited on the edges than on the side faces, implying that the Ru atoms preferred to nucleate from the edges because of their higher reactivity [15]. As shown in Figure 3.5d, the Pd cores could not be completely removed from some of the core-shell nanocrystals, which could be attributed to the larger proportion of Ru in the core-shell nanocrystals. Compared to the Pd@Ru_{nL} nanocrystals obtained using the standard synthesis, the weight percentage of Ru in the nanocrystals prepared with an injection rate of 20 mL h^{-1} was higher (31.5% *vs.* 26.5%). The thicker Ru shells made it harder to remove some of the Pd cores completely [24].

The introduction of KBr and the use of a proper reaction temperature were both critical factors contributing to the successful synthesis of Pd@Ru core-shell octahedra. Previously, our group has demonstrated the successful synthesis of Ru cubic nanocages [36]. Different from the reaction conditions used in that work, I added KBr into the growth solution before injecting the Ru(III) precursor. As an effective additive in the syntheses of Pt nanocages with different shapes [23–25], KBr can slow down the reduction rate of Pt(II) precursor and promote the formation of conformal Pt shells. Here, I also conducted a control experiment to investigate the role of KBr in the synthesis. Figure 3.6, a and b, shows the as-obtained Pd@Ru nanocrystals and Ru nanocages prepared using the standard procedure, except for the absence of KBr. The resultant Pd@Ru nanocrystals all possessed rough surfaces (Figure 3.6a), demonstrating an island growth mode for the Ru adatoms. After

removing the Pd cores, the Ru nanocages still exhibited a rough surface (Figure 3.6b), which was consistent with the original core-shell nanocrystals (Figure 3.6a). This observation indicates inadequate surface diffusion for the Ru adatoms during the deposition process. Since the reaction temperature was kept the same at 200 ^{o}C, the surface diffusion rate should be essentially the same as in the standard protocol. Adding KBr could reduce the deposition rate for the Ru atoms through ligand exchange. By adding enough KBr into the reaction solution, I could achieve a favorable surface diffusion kinetics over atom deposition, enabling a layer-by-layer growth mode for the Ru atoms.

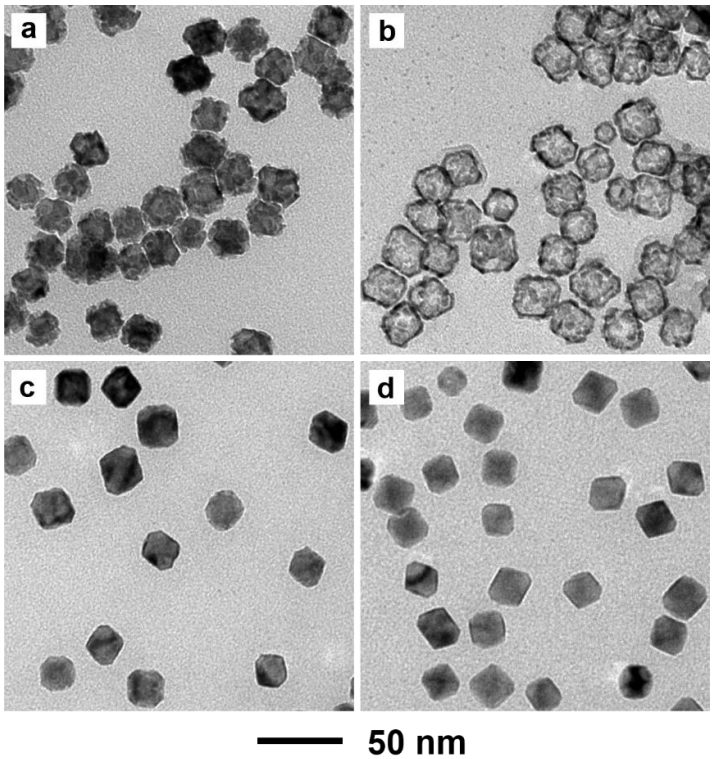

Figure 3.6. TEM images of (a, b) the core-shell nanocrystals and the corresponding Ru nanocages prepared from 18-nm Pd octahedra using the standard procedure (at 200 ^{o}C) except for the absence of KBr in the reaction solution, and (c, d) the core-shell nanocrystals obtained using the standard protocol but at other temperatures: (c) 175, and (d) 150 ^{o}C, respectively.

Since surface diffusion is a thermally activated process, it can be accelerated or deaccelerated by varying the reaction temperature. To this end, I also varied the reaction temperature to investigate its impact on the synthesis. Figure 3.6, c and d, shows TEM images of the core-shell nanocrystals prepared using the standard procedure except for the use of different reaction temperatures. In both cases, even though the temperature was reduced from 200 to 175 ^{o}C and further to 150 ^{o}C, the resultant Pd@Ru nanocrystals still possessed a smooth surface. The decrease in reaction temperature not only decelerated the surface diffusion, but also weakened the reducing power of the reducing agent. Based on the ICP-MS data, the weight percentages of Ru contained in the core-shell nanocrystals dropped from 26.5% to 16.2% and 5.6%, respectively, when the reaction temperature was reduced from 200 to 175 and 150 ^{o}C. Accordingly, the thickness of Ru shells decreased along with the compromise in reduction power. Despite the suppression in surface diffusion, the decrease in deposition rate arising from the weakened reducing power could still maintain a favorable surface diffusion kinetics over atom deposition.

I also varied the amount of the injected Ru(III) precursor while keeping all other conditions unchanged to see if I can tune the wall thickness of the Ru nanocages. As shown in Figure 3.7, a and b, when the injected amount of Ru(III) precursor was increased to 0.8 mg, the as-obtained Pd@Ru_{nL} nanocrystals still maintained a good octahedral shape while their surfaces became slightly rough. As the injected amount of Ru(III) precursor was further increased to 1.2 mg, the surfaces of the resultant nanocrystals became much rougher. According to the ICP-MS data in Table 3.1, the weight percentages of Ru in the aforementioned core-shell nanocrystals were 30.8% and 34.3%, corresponding to approximately 4.9 and 5.7 atomic layers, respectively. Chemical etching was then applied

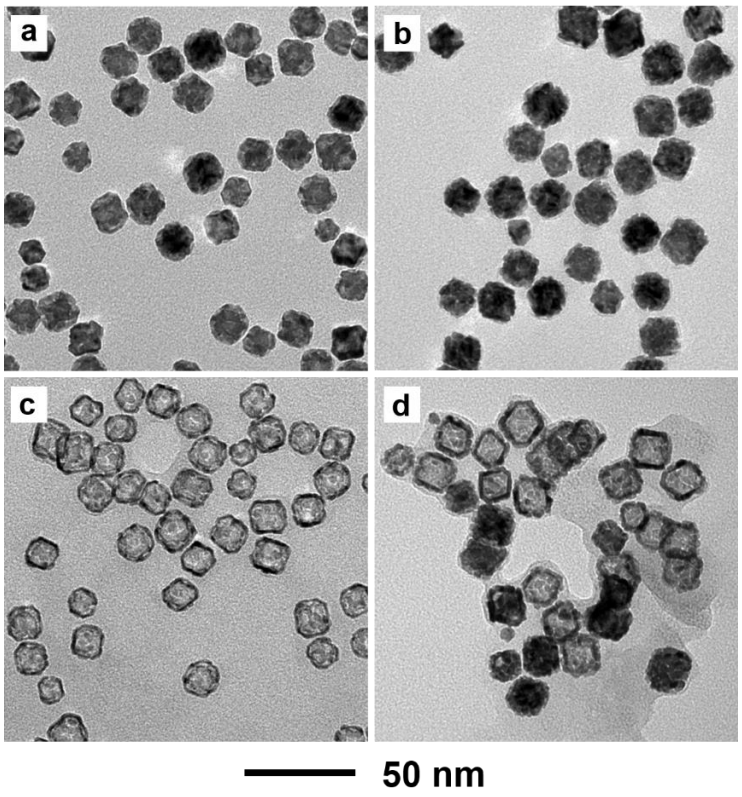

Figure 3.7. TEM images of (a, b) the core-shell nanocrystals and (c, d) their corresponding Ru nanocages prepared from 18-nm Pd octahedra using the standard procedure except for the addition of different amounts of Ru(III) precursor into 20 mL of EG: (a, c) 0.8 mg and (b, d) 1.2 mg, respectively.

Table 3.1. Comparison of the elemental compositions for Pd@Ru core-shell octahedra and Ru nanocages prepared using the standard procedure except for the use of different amounts of Ru(III) precursor.

	$RuCl_3 \cdot xH_2O$ (mg)	Percentage of Pd (wt.%)	Percentage of Ru (wt.%)
Before etching	0.8	69.2	30.8
	1.2	65.7	34.3
After etching	0.8	9.2	90.8
	1.2	44.6	55.4

to these samples to selectively remove the Pd cores. As shown in Figure 3.7c, the Pd cores could be completely etched away to obtain Ru octahedral nanocages when the Ru shells were 4.9 atomic layers. The surfaces of the Ru nanocages were not as smooth as the sample obtained using the standard procedure due to the increase in atom deposition rate caused by the increase in Ru(III) concentration.

For the sample with 5.7 atomic layers of Ru in the shell (Figure 3.7d), about 40% of the Pd cores could not be removed. According to our previous work [24], the wet etching is initiated by the oxidation of the Pd atoms in the outmost layer of the Ru shell to generate vacancies, followed by diffusion of Pd atoms from the underlying layers to generate more vacancies. If the Ru shells are too thick, it will be difficult for the Pd atoms to diffuse to the outmost layer to generate the initial vacancies. As a result, the etching process would be suppressed. Since the Ru shells on the nanocrystals shown in Figure 3.7d were approximately 5.7 atomic layers, they were too thick for the Pd atoms to diffuse through, leaving behind the Pd cores untacked. A composition of the aforementioned two types of Ru nanocages was given in Table 3.1. For the sample with 4.9 atomic layers of Ru, the weight percentage of Pd decreased from 69.2% to 9.2% after etching, indicating that the Pd cores were removed effectively. For the sample with 5.7 atomic layers of Ru, the weight percentage of Pd remained at 44.6% after etching, in agreement with the nanocrystals shown in Figure 3.7d.

I have also extended the synthesis to Pd octahedral seeds with two other edge lengths of 12 and 26 nm. Generally, smaller Pd octahedral seeds are better suited for Ru adatoms to diffuse across the entire surface because of the shorter distance to cover. Figure 3.8, a and b, shows the resultant Pd@Ru_{nL} octahedra using 12- and 26-nm Pd octahedral seeds,

respectively, both of which exhibited good uniformity in terms of size and shape. After wet etching, I also obtained Ru nanocages from both samples (Figure 3.8, c and d). Both of the nanocages maintained a well-defined octahedral shape, together with a smooth surface, verifying the sufficient surface diffusion of Ru adatoms in both cases. In short, the synthetic protocol can be applied to fabricate Ru octahedral nanocages with different sizes.

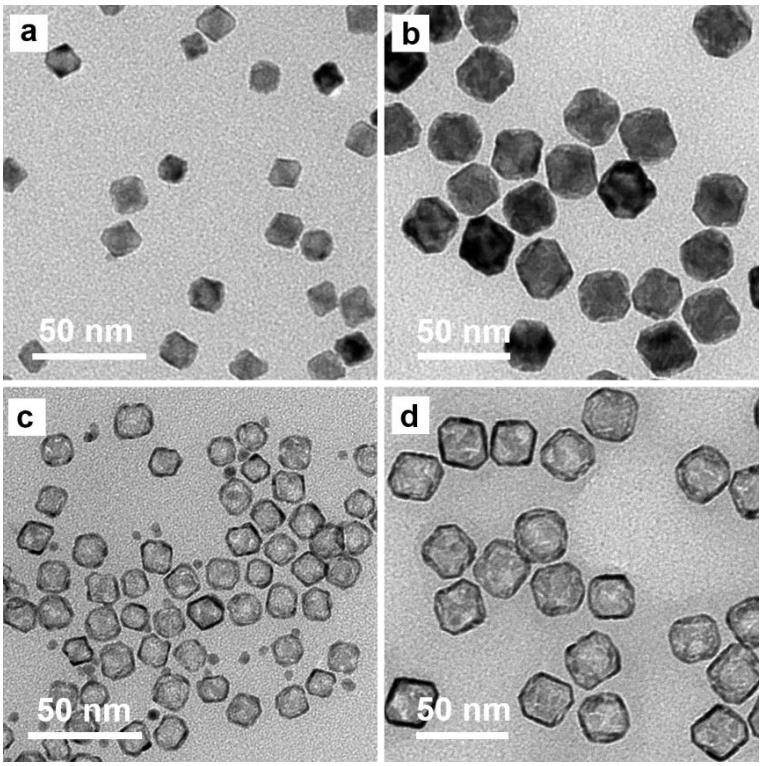

Figure 3.8. TEM images of (a, b) the core-shell nanocrystals and (c, d) their corresponding nanocages prepared using the standard procedure except for the use of Pd octahedra with two other edge lengths: (a, c) 12 nm and (b, d) 26 nm, respectively.

Thermal Stability Evaluation. The thermal stability of Ru octahedral nanocages was investigated using *in-situ* XRD. Figure 3.9 shows the spectra collected at different temperatures ranging from 200 to 450 ^{o}C. The *fcc* structure of Ru octahedral nanocages

was stable at 300 °C, demonstrated by the distinctive peaks of *fcc* structure. When the heating temperature was increased to 350 °C, in addition to *fcc*-(111) peak, the appearance of *hcp*-(101) peak was also observed, indicating the initiation of crystal structure transformation from *fcc* to *hcp*. As the temperature was further increased to 400 and 450 °C, the characteristic peaks of *fcc* structure disappeared and the intensity of characteristic peaks of *hcp* structure kept increasing drastically, verifying the complete crystals structure transformation from *fcc* to *hcp*.

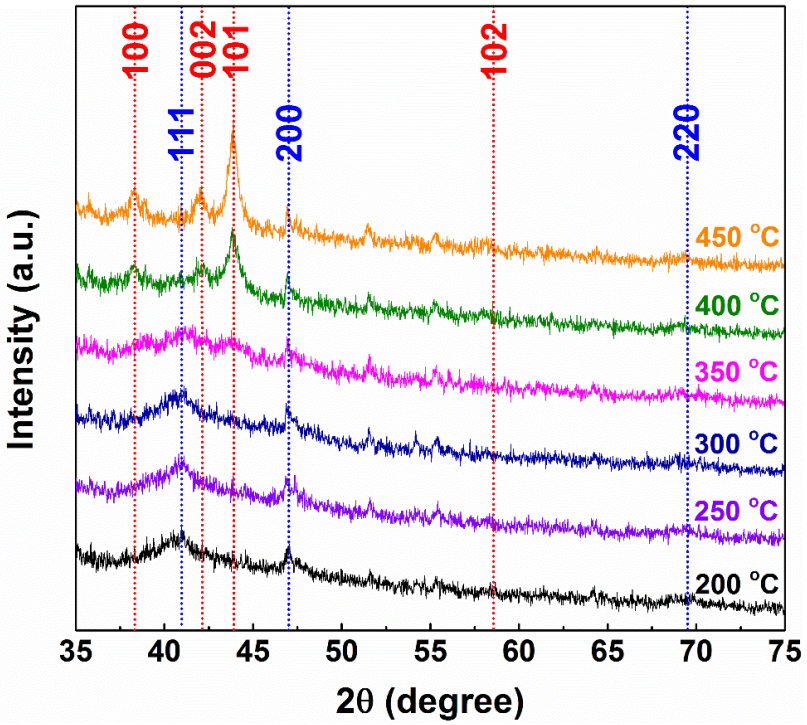

Figure 3.9. The *in-situ* XRD patterns of the *fcc* Ru nanocages measured under Ar atmosphere in the temperature range between 200 and 450 °C, showing the transformation of crystal structure from *fcc* to *hcp*. The characteristic peaks of *fcc* and *hcp* Ru are labelled using blue and red colors, respectively.

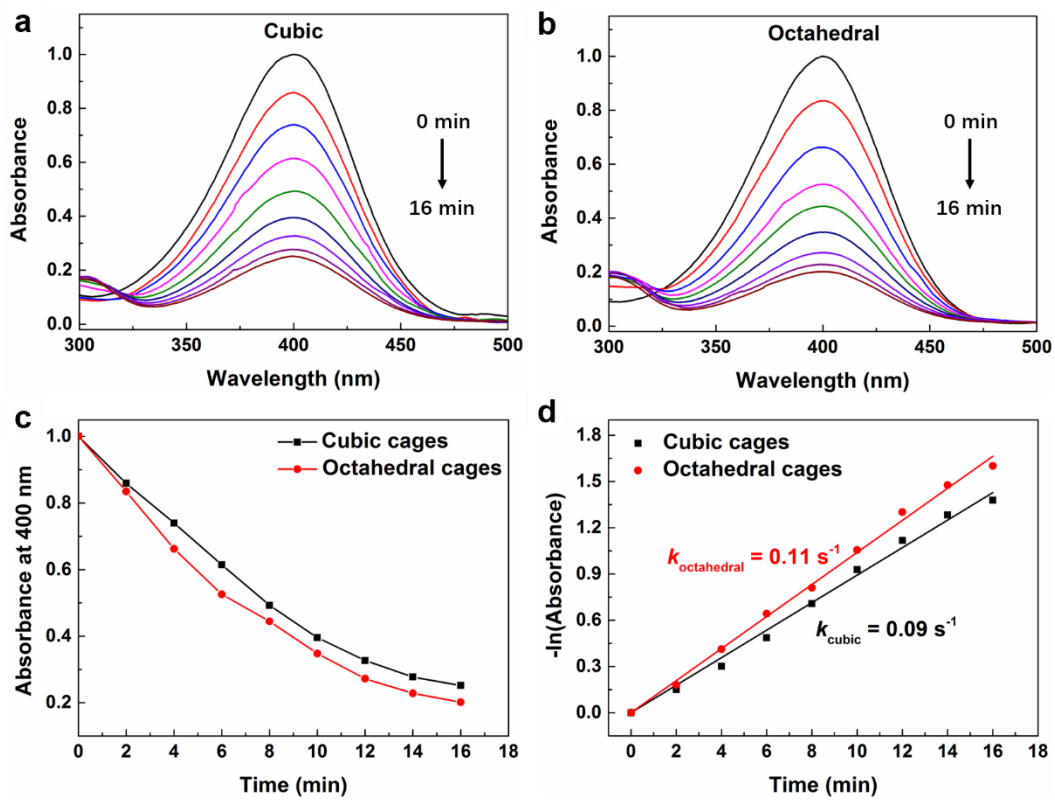

Figure 3.10. Comparison of the catalytic activities towards the reduction of 4-nitrophenol for Ru cubic and octahedral nanocages. The absorbance spectra of reaction solutions at different times using (a) cubic and (b) octahedral nanocages. (c) Normalized absorbance at 400 nm peak for 4-nitrophenol as a function of time for both cubic and octahedral cages. (d) Line plot comparing the -ln(Absorbance) versus reaction time generated from the data in (c), where the rate constant can be determined taking the slope of the lines.

Evaluation of Catalytic Properties toward the Reduction of 4-Nitrophenol. The reduction of 4-nitrophenol was used as model reaction to evaluate the facet-dependent properties of Ru nanocages. Ru cubic nanocages with an average size of 10 nm were prepared as previously reported and their performance was compared with that of 12-nm Ru octahedral nanocages [36]. For the reduction of 4-nitrophenol, the kinetics can be conveniently monitored by measuring the absorption of 4-nitrophenolate anions which has a distinctive peak located at 400 nm. Figure 3.10, a and b, shows the UV-vis absorption

spectra in the presence of Ru cubic and octahedral nanocages as the catalysts, respectively. The peaks show a gradual decay throughout the catalytic process. The normalized absorbance at 400 nm is plotted as a function of reaction time (Figure 3.10c), indicating faster decay in absorbance when the octahedral nanocages were used as the catalyst. As the reduction of 4-nitrophenol follows pseudo-first-order kinetics [37, 39], the plot of -ln(absorbance) vs. reaction time is linear. Figure 3.10d shows the rate constants derived from these linear relationships. The rate constant of the octahedral nanocages was measured to be 0.11 s^{-1}, 1.22 times higher than that of cubic nanocages (0.09 s^{-1}), confirming the superior performance of {111} facets toward the reduction of 4-nitrophenol.

Understanding N_2 Dissociation using DFT Calculations. To evaluate the performance of the *fcc* Ru octahedral nanocages toward heterogeneously catalyzed reactions, my collaborators performed a self-consistent DFT (GGA-PW91)[40] study of the atomic and molecular adsorption of 14 distinct reaction intermediates relevant to a wide range of industrial applications (see Table 3.2 and Table 3.3). They performed these calculations on a number of *fcc* Ru(111) cage models with selected amounts of Pd impurities as observed in experiments. To isolate the effect of Pd impurity, they compare the results on these surfaces to those on a pure Ru nanocage. Additionally, they compare the results on all these surfaces to those on an *hcp* Ru(0001) slab model, which represents the typical Ru nanoparticles with the conventional *hcp* structure. Given that Ru has been extensively investigated for ammonia synthesis, they choose here to elaborate on N_2 dissociation, the rate-determining step of ammonia synthesis, to atomic nitrogen on each of our models, along the same lines of our previous work on Ru cubic nanocages [36]. The dissociation of adsorbed molecular nitrogen (N_2*) to atomic nitrogen (N*) has been

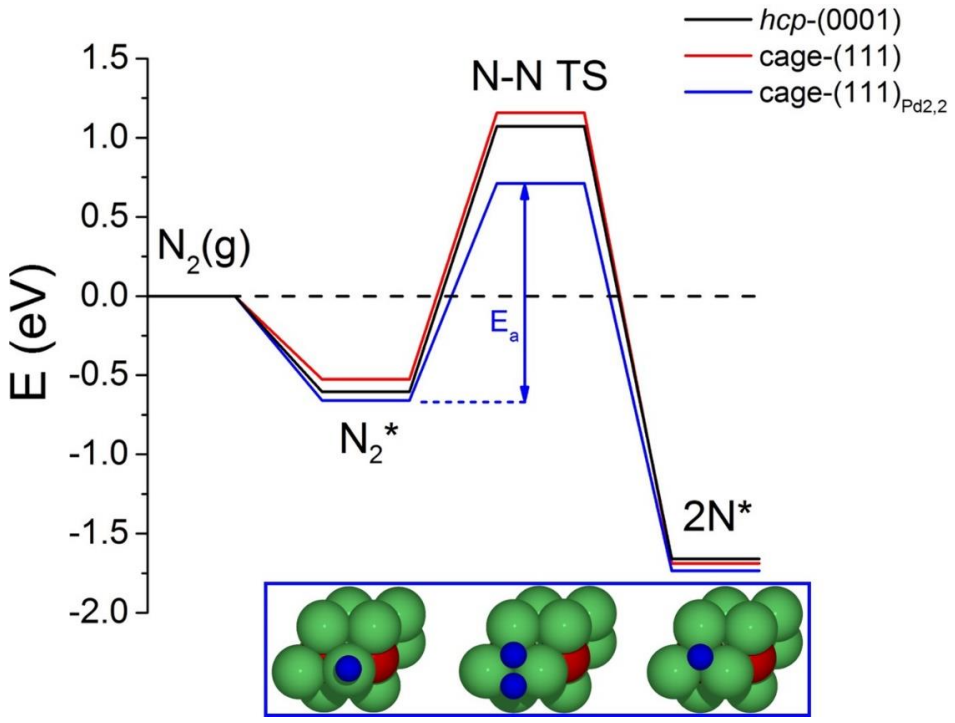

Figure 3.11. Potential energy surfaces for N_2 dissociation on three model surfaces. *hcp*-(0001) represents an *hcp* pure Ru(0001) slab as a model for conventional Ru nanoparticles; cage-(111) is a cage model of pure Ru exposing the close-packed facet in an *fcc* stacking; and cage-(111)$Pd_{2,2}$ represents a cage model exposing the {111} facet with two Ru atoms in the immediate subsurface layer exchanged with two Pd atoms. "*" represents an adsorbed state, 2N* is the energy of two N* adatoms adsorbed at infinite separation, and "N-N TS" refers to the transition state of the N_2* bond-breaking event. The energies of all the states are referenced to that of the gas-phase nitrogen, denoted as N_2(g). The activation energy barrier (E_a, values on all surfaces are tabulated in Table 3.4) is the difference between the transition state energy and the energy of N_2*, as depicted by the blue double-arrowed line. The model cage-(111)$Pd_{2,2}$ – among all other surfaces – offers the strongest stabilization of N-N TS, which is depicted in the middle graphic of the inset, in between the left graphic that depicts an initial state of N_2* adsorbed vertically atop a Ru atom and the right graphic that depicts an N* at infinite separation from the second N* adsorbed on an *hcp* site. In the inset, N is represented by blue spheres, Pd is represented by red spheres, and Ru is represented by green spheres.

described as the rate-determining step for ammonia synthesis on Ru-based catalysts [40–43], and hence studying this step could allow us to predict the suitability of the Ru nanocages in catalyzing this industrially important reaction. They specifically aim to gauge

the promise of our model surfaces to catalyze ammonia synthesis based on the stabilization of the transition state of N_2 dissociation (N-N TS). Table 3.4 lists this metric along with other quantities, and Figure 3.11 depicts a potential energy surface for the dissociation process on: the pure *hcp* Ru(0001) slab model, the pure *fcc* Ru(111) cage model, and the *fcc* Ru(111) cage model with Pd impurities that stabilize N-N TS the most.

Table 3.2. Binding energies (in eV) of 14 atomic and molecular species on all surfaces studied. The adsorbate/surface combinations with the strongest binding energies are shown in bold. The reference energy is chosen for adsorbate in the gas phase, at infinite separation from the model surface.

Species	*hcp*-(0001)	cage-(111)	cage-$(111)_{Pd3,3}$	cage-$(111)_{Pd2,3}$	cage-$(111)_{Pd3,4}$	cage-$(111)_{Pd2,4}$	cage-$(111)_{Pd2,2}$	cage-$(111)_{Pd4,4}$
C	-7.55	-7.47	-7.65	**-7.73**	-7.72	-7.58	-7.58	-7.42
N	-6.00	-6.02	-6.21	-6.21	**-6.29**	-6.08	-6.04	-6.04
O	-6.00	-6.01	-6.22	-6.23	**-6.28**	-6.10	-6.02	-6.05
H	-2.91	-2.86	-2.84	-2.86	-2.89	-2.90	**-2.93**	-2.90
CH	-6.85	-6.91	-6.78	**-7.14**	-7.12	-7.05	-7.08	-6.95
CH_2	-4.47	-4.38	-4.52	**-4.57**	-4.56	-4.47	-4.51	-4.39
CH_3	-2.16	-2.08	-2.11	-2.17	-2.16	**-2.18**	-1.99	-2.10
NH	-5.14	-5.17	-5.36	**-5.42**	-5.39	-5.30	-5.28	-5.20
NH_2	-3.04	-2.94	-2.98	-3.08	-3.03	-3.07	**-3.19**	-2.95
NH_3	**-0.75**	-0.59	-0.64	-0.66	-0.63	-0.64	-0.66	-0.61
OH	-3.34	-3.28	**-3.37**	-3.35	-3.36	-3.31	-3.35	-3.24
CO	-1.89	-1.82	-1.93	-1.92	-1.81	-1.88	**-2.04**	-1.86
NO	-2.67	-2.69	-2.78	**-2.89**	-2.86	-2.79	-2.84	-2.73
N_2	-0.61	-0.53	-0.65	-0.56	-0.59	-0.52	**-0.66**	-0.52

Table 3.3. Preferred binding sites of 14 atomic and molecular species on all surfaces studied. In the context of close-packed facets, the symbol "t" refers to top site, "b" refers to bridge site, "h" refers to *hcp* site, and "f" refers to *fcc* site. On surfaces where Pd is present, a symbol could be suffixed with "/Pd" or "/Ru" to denote which site is involved. For example, "f/Pd" means that the preferred binding takes place on the Pd *fcc* site rather than the Ru *fcc* site.

Species	*hcp*-(0001)	cage-(111)	cage-$(111)_{Pd3,3}$	cage-$(111)_{Pd2,3}$	cage-$(111)_{Pd3,4}$	cage-$(111)_{Pd2,4}$	cage-$(111)_{Pd2,2}$	cage-$(111)_{Pd4,4}$
C	h	h	h$^{!}$	h/Pd	h$^{@}$	h/Pd	h/Pd	h
N	h	h	h$^{!}$	h/Pd	h$^{@}$	h/Pd	h/Pd	h
O	h	h	h$^{!}$	h/Pd	h$^{@}$	h/Pd	h/Pd	h
H	h	f	f/Pd	h/Pd	f/Pd	f**	f**	f
CH	h	h	h$^{!}$	h/Pd	h$^{@}$	h/Pd	h/Pd	h
CH_2	h	h	h$^{!}$	h/Pd	h$^{@}$	h/Pd	h/Ru	h
CH_3	f	f	f/Pd	f/Pd	f/Pd	f$^{\%}$	h/Pd	f
NH	h	h	h$^{!}$	h/Pd	h$^{@}$	h/Pd	h/Pd	h
NH_2	b	b	b/Ru	b$^{!}$	b$^{!}$	b$^{\%}$	b$^{\%}$	b
NH_3	t	t	t$^{!}$	t$^{\#}$	t$^{@}$	t$^{\#}$	t**	t
OH	f	f	f/Ru	h/Pd	h$^{@}$	f$^{\%}$	b$^{\%}$	f
CO	t	h	t$^{!!}$	h/Pd	b$^{!}$	h/Pd	f**	h
NO	h	h	h$^{!}$	h/Pd	h$^{@}$	h/Pd	h/Pd	h
N_2	t	t	t$^{!!}$	t*	t$^{!}$	t**	t***	t

! one adjacent *fcc* site is occupied by Pd.
!! two adjacent *fcc* sites are occupied by Pd.
none of the adjacent *fcc* or *hcp* sites are occupied by Pd.
* one adjacent *hcp* site and an adjacent *fcc* site are occupied by Pd.
** one adjacent *hcp* site is occupied by Pd.
*** two adjacent *hcp* sites are occupied by Pd.
@ the adjacent *fcc* site(s) are (is) not occupied by Pd.
% the adjacent *hcp* site(s) are (is) not occupied by Pd.

They first present our results on *hcp*-(0001) which is represented by an *hcp* pure Ru slab model. The transition state energy is 1.07 eV higher than N_2(g), making N_2* desorption far easier than its dissociation on that model surface. Switching to the cage-(111) model, which represents an octahedral nanocage of *fcc* pure Ru, does not make N_2* dissociation easier. With respect to *hcp*-(0001), the *fcc* cage-(111) destabilizes N_2* by 0.08 eV, and N-N TS by 0.09 eV, while marginally stabilizing N* by a mere 0.01 eV.

They then turn our attention to the Ru-cage models with Pd impurities, which are more representative of experimental reality. Table 3.4 shows the positive impact of Pd impurities on N_2* dissociation. With the exception of cage-$(111)_{Pd4,4}$, all surfaces stabilize the N-N TS relative to pure *hcp* Ru(0001). Specifically, cage-$(111)_{Pd2,2}$ reduces the E_a for N_2* dissociation by 0.31 eV with respect to *hcp* Ru-(0001). These results for *hcp*-Ru(0001), *fcc*-Ru cage-(111), and cage-$(111)_{Pd2,2}$ are plotted in Figure 3.11. It is interesting that the best-performing surface (cage-$(111)_{Pd2,2}$) has both Pd atoms in the immediate subsurface, and that the transition state occurs in the immediate vicinity of these Pd atoms. While it might be improbable for a high concentration of contiguous-Pd sites to exist after etching (Pd is rather randomly distributed within the Ru nanocage, as shown in Figure 3.3d), the improvement offered by cage-$(111)_{Pd2,2}$ represents an upper bound on the expected activity of the octahedral nanocages. As an important take away from these DFT calculations, if they can control the doping position and concentration of Pd atoms in the sub-surface of the Ru nanocages, they will create an avenue by which the catalytic properties of the Ru nanocages can be systematically improved. However, at this time, they are unable to utilize our synthesis method to control these critical aspects, but they strongly believe that it will be a meaningful topic worthy of exploring in the near future.

Table 3.4. Calculated binding energies for the adsorbed atomic nitrogen (BE(N*)) and molecular nitrogen (BE(N_2*)), activation energy barriers for the dissociation of N_2* to N* (E_a (N_2*→2 N*), see Figure 3.11 for definition), and the difference between transition state energies of N_2* dissociation and gas-phase nitrogen ($E_{TS} - E_{N2,gas}$), as a measure of competition between the desired dissociation and the undesired desorption of N_2*. All values are in eV. Binding Energies (BE) are referred to the respective gas phase species.

Model	BE(N*)	BE(N_2*)	E_a (N_2*→2 N*)	$E_{TS}^{\|} - E_{N2,gas}$
***hcp*-(0001)**	-6.00	-0.61	1.68	1.07
cage-(111)	-6.02	-0.53	1.68	1.16
cage-(111)$_{Pd3,3}$	-6.21	-0.65	1.66	1.02
cage-(111)$_{Pd2,3}$	-6.21	-0.56	1.51	0.95
cage-(111)$_{Pd3,4}$	-6.29	-0.59	1.62	1.04
cage-(111)$_{Pd2,4}$	-6.08	-0.52	1.47	0.96
cage-(111)$_{Pd2,2}$	-6.04	-0.66	1.37	0.71
cage-(111)$_{Pd4,4}$	-6.04	-0.52	1.66	1.14

$E_{TS}^{|}$ is the energy of the transition state. The last column offers insight into the competition between N_2* desorption (undesired) and its dissociation to 2N*. The lower this difference is, the more competitive the dissociation becomes.

To summarize, our modeling results indicate that cage-(111) models with Pd impurities, which most faithfully represent the as-synthesized Ru octahedral nanocages, should generally improve catalysis for ammonia synthesis as compared to the conventional *hcp* Ru nanoparticles. The reduced E_a for N_2 dissociation on the nanocages would provide more efficient competition against molecular desorption of N_2, translating into decreased

reactor pressures, and would allow for milder temperatures of the Haber-Bosch process. Since ammonia synthesis is an exothermic process, milder temperatures (allowed by lower activation energy barriers) would also lead to more favorable reaction equilibrium during the synthesis, thus further reducing the high pressures typical of the Haber-Bosch process. These constitute potentially major improvements and energy savings for the energy-intensive Haber-Bosch process. They also note that past literature reports have found that *fcc* Ru nanoparticles can retain their *fcc* structure up to temperatures as high as 300 °C, which makes these nanocages potentially-stable catalysts for ammonia synthesis, especially given that they preferentially expose the stable, close-packed {111} facet. Finally, they note that our previous study of cage-(100) surfaces [36], representing cubic nanocages, predicted more improved performance than *hcp*-(0001) toward ammonia synthesis relative to the current study of octahedral nanocages. Specifically, on the best-performing cubic nanocage – with Pd impurities in the immediate subsurface layer – the transition state energy of N_2* dissociation is 0.05 eV lower than the energy of N_2(g), which indicates that N_2* dissociation is favorable over desorption [36]. This superiority of cubic nanocages is an expected result, and can generally be attributed to electronic factors such as the enhanced binding (of N_2) and lower activation energy barriers for bond-breaking events on the more open and less coordinated {100} facets. Additionally, a geometric factor exists in the way N_2* adsorbs on either surface. While N_2* adsorbs di-σ to the {100} facets of the cubic nanocages in a bridge-hollow-bridge configuration [36], it prefers to adsorb vertically on a top site on the {111} facets of octahedral nanocages. Therefore, on the {111} facets, the N_2* needs to tilt first to a horizontal position before the N-N bond breaking event takes place. This tilting process has been found to be endothermic by 0.53–0.75 eV

across our surfaces, a significant energy cost which could only be increased by additional kinetic barriers for the tilting process.

3.3 Conclusion

I have demonstrated the synthesis of Ru octahedral nanocages with an *fcc* structure through seed-mediated growth and selective etching. These Ru octahedral nanocages were uniform in size and shape, with a wall thickness approaching five atomic layers. Based on a systematic study, the use of KBr, a slow injection rate, and an elevated reaction temperature were all critical to the successful synthesis to ensure the deposition of smooth, uniform, and conformal Ru shells. This approach was successfully applied to Pd seeds with different edge lengths ranging from 12 nm to 26 nm. *In-situ* XRD analysis indicates that the *fcc* structure of Ru nanocages can be stable at 300 ^{o}C. For the evaluation of catalytic activity, {111} facets exhibited enhanced performance than {100} facets toward the reduction of 4-nitrophenol. I and my collaborators also assessed the promise of these *fcc*-structured nanocages toward ammonia synthesis using DFT calculations, and derived the activation energy barriers to N_2 dissociation, as well as the stabilization of molecular and atomic nitrogen. Our calculations show that the Pd impurities in the nanocages generally play a synergistic role in stabilizing and activating nitrogen, thus allowing the octahedral nanocages to potentially be more promising than the conventional *hcp* Ru catalysts. In whole, this work provides an effective strategy towards the synthesis of active and atom-efficient hollow nanocages with precise facet structures and sizes.

3.4 Experimental Section

Chemicals. Sodium tetrachloropalladate(II) (Na_2PdCl_4, 99.99%), potassium bromide (KBr, 99%), poly(vinylpyrrolidone) (PVP, MW≈55000), formaldehyde (HCHO, 36.5–38%), L-ascorbic acid (AA, 99%), ruthenium(III) chloride hydrate ($RuCl_3 \cdot xH_2O$, 99.99%), potassium chloride (KCl, 99%), hydrochloric acid (HCl, 37%), sodium borohydride ($NaBH_4$, 99%), 4-nitrophenol ($C_6H_5NO_3$, 99%), and iron(III) chloride ($FeCl_3$, 97%) were all obtained from Sigma-Aldrich and used as received. Ethylene glycol (EG, 99%) was ordered from J. T. Baker. All aqueous solutions were prepared using deionized (DI) water with a resistivity of 18.2 MΩ cm at room temperature.

Synthesis of 6-, 10-, and 14-nm Pd Cubes. For the synthesis of 10-nm Pd cubes [44], 105 mg of PVP, 60 mg of AA, and 300 mg of KBr were dissolved in 8.0 mL of water, and then placed in a vial and heated at 80 °C in an oil bath under magnetic stirring for 10 min. Subsequently, 3 mL of aqueous Na_2PdCl_4 (19 mg mL^{-1}) was injected into the preheated solution in one shot. The reaction solution was maintained at 80 °C under magnetic stirring. After 3 h, the product was collected by centrifugation, washed three times with water to remove excess PVP and ionic species, and then re-dispersed in water for further use. The concentration and quality of Pd cubes in the suspension were determined using a combination of inductively-coupled plasma mass spectrometry (ICP-MS) and electron microscopy analysis, respectively. For the syntheses of 6- and 14-nm Pd cubes, the procedure was essentially the same except that KBr (300 mg) was replaced by a mixture of KBr (5 mg) and KCl (185 mg), and KBr (500 mg), respectively.

Synthesis of 12-, 18- and 26-nm Pd Octahedra. In a typical synthesis [45], 8 mL of an aqueous mixture containing 315 mg of PVP, 50 μL of HCHO, and 2.73 mg of Pd cubic seeds (6-nm cubes for 12-nm octahedra, 10-nm cubes for 18-nm octahedra, or 14-nm cubes

for 26-nm octahedra) was placed in an oil bath and heated to 60 ^{o}C for 10 min under magnetic stirring. Then, 3 mL of an aqueous solution containing 175 mg Na_2PdCl_4 was injected into the reaction solution in one shot. After 3 h, the product was collected by centrifugation, washed twice with water, and then re-dispersed in EG for further use. The concentration and quality of Pd octahedral seeds were determined using a combination of ICP-MS and electron microscopy, respectively.

Synthesis of Pd@Ru Core-Shell Octahedra. In the standard synthesis of 18-nm core-shell octahedra, AA (50 mg), KBr (20 mg), PVP (100 mg), and Pd octahedral seeds (0.62 mg) were mixed in EG, and the total volume of the final solution was adjusted to 9 mL by adding EG. The mixture was placed in an oil bath and heated at 200 ^{o}C under magnetic stirring. Subsequently, 0.6 mg of $RuCl_3 \cdot xH_2O$ was dissolved in 20 mL of EG and injected into the growth solution at a rate of 1 mL h^{-1} using a syringe pump. The reaction was allowed to continue for an additional 2 h to complete. The final product was collected by centrifugation, washed once with acetone and twice with water, and then re-dispersed in water for further use. The procedure for the syntheses of 12- and 26-nm core-shell octahedra was similar except that the amounts of $RuCl_3 \cdot xH_2O$ introduced were adjusted to 1.35 and 0.29 mg, respectively, to ensure that the thicknesses of the Ru shells were more or less the same for all three samples.

Fabrication of Ru Octahedral Nanocages. In a typical process [36], 300 mg of KBr, 30 mg of $FeCl_3$, 0.18 mL of HCl, 50 mg of PVP, and 4.82 mL water were mixed in a 20-mL glass vial. The mixture was placed in an oil bath held at 90 ^{o}C under magnetic stirring. Afterwards, an aqueous suspension of the as-synthesized core-shell octahedra (~0.1 mg)

was introduced. After etching for 1.5 h, the product was collected by centrifugation, followed by washing with water three times.

Instrumentation. Transmission electron microscopy (TEM) imaging was conducted with a Hitachi 7700 microscope operated at 120 kV. All high-resolution transmission electron microscopy (HRTEM), high-angle annular dark field scanning transmission electron microscopy (HAADF-STEM) images and energy-dispersive X-ray spectroscopy (EDX) data were acquired using an aberration-corrected Hitachi HD2700 microscope operated at 200 kV. ICP-MS (NexION 300Q, PerkinElmer) was used to quantitatively analyze the metal content in a sample. X-ray diffraction (XRD) patterns were obtained with a PANalytical X'Pert PRO diffractometer with a Cu Kα X-ray source. UV-vis absorption spectra were recorded using a Perkin-Elmer Lambda 750 UV-vis-NIR spectrometer.

***In-situ* XRD measurements.** The thermal stability of *fcc* Ru octahedral nanocages was investigated by *in-situ* XRD. High temperature XRD patterns were collected with an Anton Paar XRK hot stage over the range 200 °C ≤ T ≤ 450 °C between 2θ = 30° and 90°, and the patterns were analyzed with HighScore Plus, a software package provided by PANalytical. An ethanol solution containing Ru octahedral nanocages was dispersed onto a square silicon wafer before high temperature XRD measurements. To avoid sample oxidation, a stream of ultra-high purity Argon was passed through the hot stage. Each pattern was collected for an hour to obtain sufficient signals every 50 ^{o}C, with a heating rate of 5 ^{o}C/min.

Reduction of 4-nitrophenol by $NaBH_4$. The reaction was conducted with an aqueous suspension at room temperature. In a typical experiment, an aqueous suspension of Ru nanocages was first diluted to 0.1 mM in terms of Ru element based on the ICP-MS data.

Afterwards, 1 mL of aqueous $NaBH_4$ (20 mM) was mixed with 1 mL of 4-nitrophenol (0.2 mM) in water, and the colorless solution turned yellow immediately. Then, 0.5 mL of the aqueous suspension of Ru nanocages was quickly added into the aforementioned solution. The reaction kinetics was monitored using a UV-vis spectrometer, which recorded the absorption peaks of the reactant and product in the cuvette over time.

DFT Calculations. The Vienna *ab initio* Simulation Package (VASP) code was used to perform periodic, self-consistent DFT calculations [46, 47]. The exchange-correlation functional was described by the generalized gradient approximation (GGA-PW91) [48], and the electron-ion interactions were described using the projector augmented wave potentials (PAW) [49, 50]. The wave function was expanded in a basis set of plane waves, truncated at 400 eV kinetic energy cutoff. All calculations were performed on (2×2) unit cells, corresponding to 1/4 ML coverage of adsorbates, with (6×6×1) Monkhorst-Pack *k*-point mesh sampling of the first Brillouin zone [51]. Adsorption was allowed on a single surface of a slab at a time, with energies corrected for dipole moments. Hellmann-Feynman forces on all atoms were made to converge to 0.01 eV/Å during geometric optimization. Calculations were tested for spin-polarization, and total energies were found to be negligibly affected, in accordance with the computational literature on *fcc* Ru [52]. As such, all results presented here are spin-restricted. My collaborators define the binding energy (BE) of an adsorbate as:

$$BE = E_{adsorbate} - E_{surface} - E_{adsorbate,gas}$$

where $E_{adsorbate}$ is the total energy of the species adsorbed on the surface model, $E_{surface}$ is the energy of the clean surface, and $E_{adsorbate,gas}$ is the energy of the adsorbate in the gas phase at infinite separation from the surface.

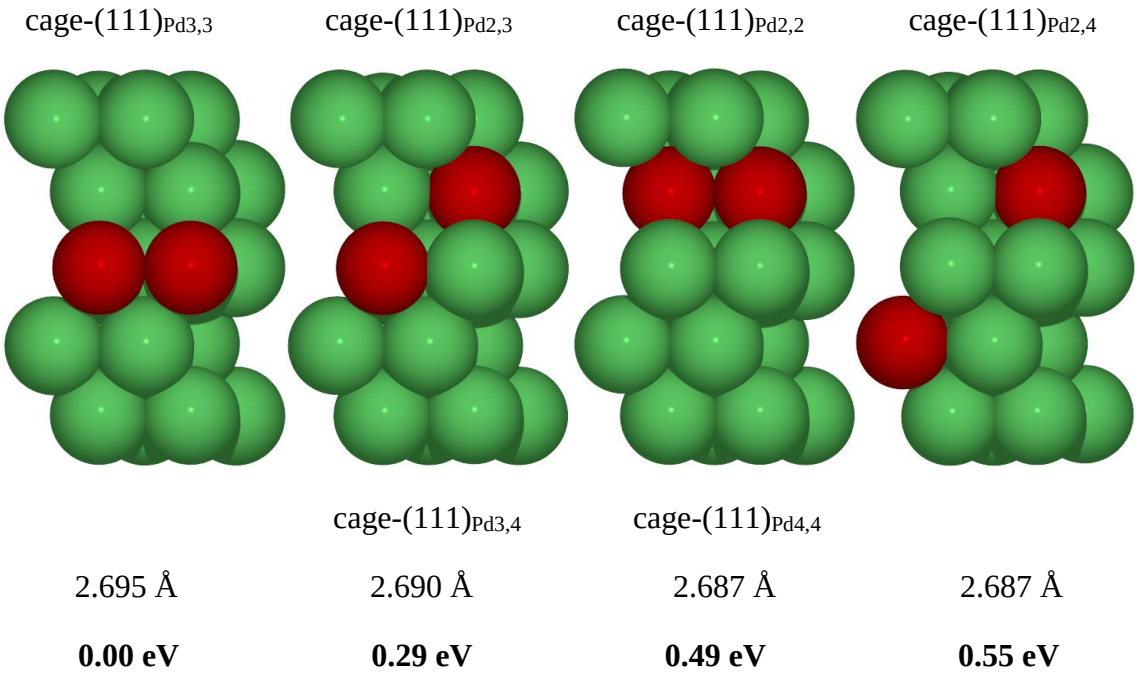

Figure 3.12. All four Ru nanocage models with Pd impurities and the associated six surfaces studied. The optimized interatomic distances within metal layers are listed beneath each model, in Å. The bold values beneath each image are energies relative to the most stable structure (leftmost), in eV. Cage-$(111)_{Pd3,3}$ represents a surface with two Pd atoms in the third layer, cage-$(111)_{Pd2,3}$ represents a surface with a Pd atom in the second layer and a Pd atom in the third layer, cage-$(111)_{Pd3,4}$ represents a surface with a Pd atom in the third layer and a Pd atom in the fourth layer, cage-$(111)_{Pd2,2}$ represents a surface with two Pd atoms in the second layer, cage-$(111)_{Pd4,4}$ represents a surface with two Pd atoms in the fourth layer, and cage-$(111)_{Pd2,4}$ represents a surface with a Pd atom in the second layer and a Pd atom in the fourth layer. The Ru and Pd atoms are represented by green and red spheres, respectively.

Put this way, the BE is an energy gain (or loss) incurred as the adsorbate approaches the surface, and as such, more negative binding energies indicate stronger adsorption. The climbing image nudged elastic band (CI-NEB) was used to calculate activation energy barriers for N_2 dissociation [53]. The method interpolates the initial and final states with seven intermediate images, and forces on each image were converged to less than 0.1 eV/Å. The transition state was verified with a single imaginary vibrational mode. The vibrational

frequency calculations of translational, rotational, and vibrational modes were estimated using second-order numerical differentiation of forces using a 0.015 Å step size, within the framework of a harmonic oscillator.

The lattice parameters of bulk *hcp* Ru were calculated as a=2.729 Å and c/a=1.577, which agree well with experimental data (a=2.706 Å and c/a=1.582) [54]. These parameters were used to construct the *hcp*-(0001) slab models with four metal layers each; the bottom two layers were fixed at their bulk positions while all other atoms – including the adsorbates – were allowed to fully relax. The hollow, free-standing Ru nanocages were modeled with five layers of Ru atoms exposing the (111) facet, and possessing an *fcc*-like structure. The optimization of the interatomic distances within a metal layer was done with all atoms of the system allowed to fully relax. Using this method, the optimized interatomic distance within a layer for a five-layered pure Ru nanocage (cage-(111)) was calculated as 2.687 Å.

To model the Pd impurities in the as-synthesized Ru nanocages, they replaced two Ru atoms in the nanocage with Pd atoms, so as to yield a 10.5 wt.% Pd concentration, which was close to the 9.9 wt.% of Pd obtained by ICP-MS. Importantly, no Pd atoms were allowed in the exterior layers (topmost and bottommost), with the assumption that the etching agent would only fail to extract Pd atoms from the interior of the nanocage, along the lines of our previous work [24, 36]. They developed four models, each representing a different configuration of the Pd impurities within the Ru nanocage. These models cover all possible combinations of Pd atoms in the subsurface layers. Figure 3.12 depicts all the models investigated, showing that our models span a wide stability range of 0.55 eV. These models reveal that Pd atoms prefer to segregate together as far from the surface as possible,

absent any adsorbates. Given the lack of evidence of any specific structure of Pd impurities in the Ru nanocage, likely because the etching process would leave the Pd impurities in random positions, they decided to study all the surfaces provided by our models. Specifically, they performed calculations on surfaces with: both Pd atoms in the third layer (cage-$(111)_{Pd3,3}$), a Pd atom in the second layer and a Pd atom in the third layer (cage-$(111)_{Pd2,3}$), a Pd atom in the third layer and a Pd atom in the fourth layer (cage-$(111)_{Pd3,4}$), a Pd atom in the second layer and a Pd atom in the fourth layer (cage-$(111)_{Pd2,4}$), both Pd atoms in the second layer (cage-$(111)_{Pd2,2}$), and both Pd atoms in the fourth layer (cage-$(111)_{Pd4,4}$). The surfaces on which adsorption was studied are labeled for each model in Figure 3.12. The figure also lists the optimized interatomic distance for each model, estimated in a similar manner to the pure Ru nanocage as discussed above. For all models (slab and nanocage), a minimum of 13 Å of vacuum was used to separate vertical images to avoid unphysical interactions along the z-direction.

3.5 Notes to Chapter 3

Part of this chapter is adapted from the paper "Facile Synthesis of Ru-Based Octahedral Nanocages with Ultrathin Walls in a Face-Centered Cubic Structure" published in *Chemistry of Materials* [55].

3.6 References

[1] Porter, N. S.; Wu, H.; Quan, Z.; Fang, J. *Acc. Chem. Res.* **2013**, *46*, 1867–1877.

[2] Peng, Z.; Yang, H. *Nano Today* **2009**, *4*, 143–164.

[3] Zhou, K.; Li, Y. *Angew. Chem. Int. Ed.* **2012**, *51*, 602–613.

[4] Ruditskiy, A.; Peng, H. C.; Xia, Y. *Annu. Rev. Chem. Biomol. Eng.* **2016**, *7*, 327–348.

[5] Camden, J. P.; Dieringer, J. A.; Zhao, J.; Van Duyne, R. P. *Acc. Chem. Res.* **2008**, *41*, 1653–1661.

[6] Rycenga, M.; Cobley, C. M.; Zeng, J.; Li, W.; Moran, C. H.; Zhang, Q.; Qin, D.; Xia, Y. *Chem. Rev.* **2011**, *111*, 3669–3721.

[7] Talapin, D. V.; Lee, J. S.; Kovalenko, M. V.; Shevchenko, E. V. *Chem. Rev.* **2010**, *110*, 389–458.

[8] Jain, P. K.; Huang, X.; El-Sayed, I. H.; El-Sayed, M. A. *Acc. Chem. Res.* **2008**, *41*, 1578–1586.

[9] Dreaden, E. C.; Alkilany, A. M.; Huang, X.; Murphy, C. J.; El-Sayed, M. A. *Chem. Soc. Rev.* **2012**, *41*, 2740–2779.

[10] Yang, X.; Yang, M.; Pang, B.; Vara, M.; Xia, Y. *Chem. Rev.* **2015**, *115*, 10410–10488.

[11] Xia, Y.; Xiong, Y.; Lim, B.; Skrabalak, S. E. *Angew. Chem. Int. Ed.* **2009**, *48*, 60–103.

[12] Tao, A. R.; Habas, S.; Yang, P. *Small* **2008**, *4*, 310–325.

[13] Murphy, C. J.; Sau, T. K.; Gole, A. M.; Orendorff, C. J.; Gao, J.; Gou, L.; Hunyadi, S. E.; Li, T. *J. Phy. Chem. B* **2005**, *109*, 13857–13870.

[14] Liz-Marzan, L. M. *Langmuir* **2006**, *22*, 32–41.

[15] Xia, Y.; Gilroy, K. D.; Peng, H. C.; Xia, X. *Angew. Chem. Int. Ed.* **2016**, *55*, 2–38.

[16] Chen, Y.; Hung, H.; Huang, M. H. *J. Am. Chem. Soc.* **2009**, *131*, 9114–9121.

[17] DeSantis, C. J.; Sue, A. C.; Bower, M. M.; Skrabalak, S. E. *ACS Nano* **2012**, *6*, 2617–2628.

[18] Habas, S. E.; Lee, H.; Radmilovic, V.; Somorjai, G. A.; Yang, P. *Nat. Mater.* **2007**, *6*, 692–697.

[19] Xie, J.; Zhang, Q.; Gu, L.; Xu, S.; Wang, P.; Liu, J.; Ding, Y.; Yao, Y.; Nan, C.; Zhao, M.; You, Y.; Zou, Z. *Nano Energy* **2016**, *21*, 247–257.

[20] Xie, S.; Lu, N.; Xie, Z.; Wang, J.; Kim, M. J.; Xia, Y. *Angew. Chem. Int. Ed.* **2012**, *51*, 10266–10270.

[21] Bian, T.; Zhang, H.; Jiang, Y.; Jin, C.; Wu, J.; Yang, H.; Yang, D. *Nano Lett.* **2015**, *15*, 7808–7815.

[22] He, D.; He, D.; Wang, J.; Lin, Y.; Yin, P.; Hong, X.; Wu, Y.; Li, Y. *J. Am. Chem. Soc.* **2016**, *138*, 1494–1497.

[23] Wang, X.; Figueroa-Cosme, L.; Yang, X.; Luo, M.; Liu, J.; Xie, Z.; Xia, Y. *Nano Lett.* **2016**, *16*, 1467–1471.

[24] Zhang, L.; Roling, L. T.; Wang, X.; Vara, M.; Chi, M.; Liu, J.; Choi, S.; Park, J.; Herron, J. A.; Xie, Z.; Mavrikakis, M.; Xia, Y. *Science* **2015**, *349*, 412–416.

[25] Wang, X.; Vara, M.; Luo, M.; Huang, H.; Ruditskiy, A.; Park, J.; Bao, S.; Liu, J.; Howe, J.; Chi, M.; Xie, Z.; Xia, Y. *J. Am. Chem. Soc.* **2015**, *137*, 15036–15042.

[26] Fan, Z.; Zhang, H. *Acc. Chem. Res.* **2016**, *49*, 2841–2850.

[27] Gu, J.; Guo, Y.; Jiang, Y.; Zhu, W.; Xu, Y.; Zhao, Z.; Liu, J.; Li, W.; Jin, C.; Yan, C.; Zhang, Y. *J. Phys. Chem. C* **2015**, *119*, 17697–17706.

[28] Fan, X.; Huang, X.; Han, Y.; Bosman, M.; Wang, Q.; Zhu, Y.; Liu, Q.; Li, B.; Zeng, Z.; Wu, J.; Shi, W.; Li, S.; Gan, C. L.; Zhang, H. *Nat. Commun.* **2015**, *6*, 6571–6579.

[29] Zhao, T.; Luo, Y.; Yang, Y.; Song, Q. *J. Hazard. Mater.* **2017**, *332*, 124–131.

[30] Honkala, K.; Hellman, A.; Remediakis, I. N.; Logadottir, A.; Carlsson, A.; Dahl, S.; Christensen, C. H.; Nørskov, J. K. *Science* **2005**, *307*, 555–558.

[31] Kitano, M.; Kanbara, S.; Inoue, Y.; Kuganathan, N.; Sushko, P. V.; Yokoyama, T.; Hara, M.; Hosono, H. *Nat. Commun.* **2015**, *6*, 6731–6739.

[32] Joo, S. H.; Park, J. Y.; Renzas, J. R.; Butcher, D. R.; Huang, W.; Somorjai, G. A. *Nano Lett*. **2010**, *10*, 2709–2713.

[33] Yin, A.; Liu, W.; Ke, J.; Zhu, W.; Gu, J.; Zhang, Y.; Yan, C. *J. Am. Chem. Soc.* **2012**, *134*, 20479–20489.

[34] Watt, J.; Yu, C.; Chang, S.; Cheong, S.; Tilley, R. D. *J. Am. Chem. Soc.* **2013**, *135*, 606–609.

[35] Kusada, K.; Kobayashi, H.; Yamamoto, T.; Matsumura, S.; Sumi, N.; Sato, K.; Nagaoka, K. Kubota, Y.; Kitagawa, H. *J. Am. Chem. Soc.* **2013**, *135*, 5493–5496.

[36] Zhao, M.; Figueroa-Cosme, L.; Elnabawy, A. O.; Vara, M.; Yang, X.; Roling, L. T.; Chi, M.; Mavrikakis, M.; Xia, Y. *Nano Lett.* **2016**, *16*, 5310–5317.

[37] Ye, H.; Wang, Q.; Catalano, M.; Lu, N.; Vermeylen, J.; Kim, J. M.; Liu, Y.; Sun, Y.; Xia, X. *Nano Lett*. **2016**, *16*, 2812–2817.

[38] Yoon, D.; Park, S.; Park, J.; Kim, J.; Baik, H.; Yang, H.; Lee, K. *Nanoscale* **2014**, *6*, 12397–12402.

[39] Zhang, Z.; Liu, Y.; Chen, B.; Gong, Y.; Gu, L.; Fan, Z.; Yang, N.; Lai, Z.; Chen, Y.; Wang, J.; Huang, Y.; Sindoro, M.; Niu, W.; Li, B.; Zong, Y.; Yang, Y.; Huang, X.; Huo, F.; Huang, W.; Zhang, H. *Adv. Mater.* **2016**, *28*, 10282−10286.

[40] Rod, T. H.; Logadottir, A.; Nørskov, J. K. *J. Chem. Phys.* **2000**, *112*, 5343–5347.

[41] Vojvodic, A.; Medford, A. J.; Studt, F.; Pedersen, F. A.; Khan, T. S.; Bligaard, T.; Nørskov, J. K. *Chem. Phys. Lett.* **2014**, *598*, 108–112.

[42] Logadottir, A.; Rod, T. H.; Nørskov, J. K.; Hammer, B.; Dahl, S.; Jacobsen, C. J. H. *J. Catal.* **2001**, *197*, 229–231.

[43] Dahl, S.; Sehested, J.; Jacobsen, C. J. H.; Tornqvist, E.; Chorkendroff, I. *J. Catal.* **2000**, *192*, 391−399.

[44] Jin, M.; Liu, H.; Zhang, H.; Xie, Z.; Liu, J.; Xia, Y. *Nano Res.* **2011**, *4*, 83−91.

[45] Jin, M.; Zhang, H.; Xie, Z.; Xia, Y. *Energy Environ. Sci.* **2012**, *5*, 6352–6357.

[46] Kresse, G.; Furthmüller, J. *Phys. Rev. B* **1996**, *54*, 11169–11186.

[47] Kresse, G. Furthmuller, J. *Comput. Mater. Sci.* **1996**, *6*, 15−50.

[48] Perdew, J. P.; Wang, Y. *Phys. Rev. B* **1992**, *45*, 13244–13249.

[49] Blöchl, P. E. *Phys. Rev. B*, **1994**, 50, 17953–17979.

[50] Kresse, G.; Joubert, D. *Phys. Rev. B* **1999**, *59*, 1758–1775.

[51] Monkhorst, H. J.; Pack, J. P. *Phys. Rev. B* **1976**, *13*, 5188−5192.

[52] Kobayashi, M.; Kai, T.; Takano, N.; Shiiki, K. *J. Phys.: Condens. Matter* **1995**, *7*, 1835−1842.

[53] Henkelman, G.; Uberuaga, B. P.; Jonsson, H. *J. Chem. Phys.* **2000**, *113*, 9901−9904.

[54] Lide, D. R, *CRC Handbook of Chemistry and Physics*, CRC Press, 96th ed., **2015**.

[55] Zhao, M.; Elnabawy, A. O.; Vara, M.; Xu, L.; Hood, Z. D.; Yang, X.; Gilroy, K. D.; Figueroa-Cosme, L.; Chi, M.; Mavrikakis, M.; Xia, Y. *Chem. Mater.* **2017**, *29*, 9227−9237.

CHAPTER 4

SYNTHESIS OF RUTHENIUM ICOSAHEDRAL NANOCAGES WITH A FACE-CENTERED-CUBIC STRUCTURE AND EVALUATION OF THEIR CATALYTIC PROPERTIES

4.1 Introduction

Noble-metal nanocrystals have found widespread use in an array of applications ranging from catalysis to photonics, sensing, imaging, and medicine [1-6]. In recent years, many efforts have been devoted to controlling the shapes of noble-metal nanocrystals because of the correlations between the properties and shapes and thus surface structures, with typical examples including cubes, cuboctahedra, octahedra, tetrahedra, bipyramids, decahedra, icosahedra, and plates [7-11]. Among them, nanocrystals with one or more twin defects, often referred to as multi-twinned particles (MTPs), have received considerable interest because the associated strains can give rise to augmented properties. For icosahedral nanocrystals, they are comprised of 20 single-crystal, apex and facet-sharing tetrahedral subunits interconnected through 30 twin defects to give a shape enclosed by 20 triangular {111} facets. Due to the presence of a large number of twin defects, vertices, and edges, as well as the inhomogeneous distribution of strains, icosahedral nanocrystals are anticipated to display unique properties for various applications [12-15]. Besides, icosahedral nanocrystals can serve as seeds to realize the epitaxial growth of a second metal and thereby the formation of core−shell nanocrystals with a uniform thickness and a smooth surface [16]. Subsequently, icosahedral nanocages of the second metal can be obtained through selective removal of the cores, with both the shape and twin structure

being well preserved. Different from its solid counterpart, a nanocage is characterized by a hollow interior, ultrathin (< 2 nm) walls, and a porous structure, which could substantially improve the utilization efficiency of metal atoms. In addition, the relatively larger dimension of nanocages allows one to engineer the surface structure to optimize their catalytic activities, while it is extremely challenging for small solid nanoparticles. To this end, our group recently reported the facile synthesis of Pd@Pt core−shell icosahedra and then Pt-based icosahedral nanocages of about six atomic layers in wall thickness, together with a surface enclosed by both {111} facets and twin boundaries [17]. Compared with the commercial Pt/C, the Pt-based icosahedral nanocages exhibited a 6.7-fold and 10-fold enhancements in mass and specific activities, respectively, toward the oxygen reduction reaction (ORR).

As a member of the platinum-group metals (PGMs), Ru has a hexagonal close-packed (*hcp*) structure distinct from the face-centered cubic (*fcc*) structure of other PGMs, including Pd, Pt, Rh, and Ir. In recent years, Ru and Ru-based nanocrystals have received great interest because of their great performance in various applications such as ammonia synthesis [18, 19], Fischer-Tropsch synthesis [20], and CO oxidation [21], among others. In addition to the reports on Ru nanocrystals with the conventional *hcp* structure [22, 23], synthesis of Ru nanocrystals with an *fcc* structure has recently emerged as an active subject of research [24]. To this end, Kitagawa and co-workers reported the synthesis of *fcc*-Ru nanoparticles with tunable sizes by optimizing the combination of solvent and metal precursor [25]. However, they were unable to obtain *fcc*-Ru nanocrystals with well-controlled shapes and surface structures. Xia and co-workers combined seed-mediated growth with wet chemical etching for the facile synthesis of Ru octahedral nanoframes in

an *fcc* structure. When benchmarked against *hcp*-Ru nanowires, the nanoframes displayed greatly enhanced performance toward both the reduction of 4-nitrophenol and the dehydrogenation of ammonia borane [26]. Additionally, our groups have demonstrated the syntheses of *fcc*-structured Ru cubic and octahedral nanocages with tunable sizes by templating with Pd nanoscale cubes and octahedra, respectively. According to the results from density functional theory (DFT) calculations, the Ru nanocages are promising catalysts toward ammonia synthesis [27, 28].

Herein, I report a facile synthesis of Ru icosahedral nanocages covered by {111} facets and twin boundaries, together with an average wall thickness of five atomic layers. Notably, Ru atoms in the icosahedral nanocages were crystallized in an *fcc* structure differing from the conventional *hcp* structure found in bulk Ru. Based on *in situ* XRD, the *fcc* structure could be retained up to a temperature as high as 300 ^{o}C. In addition, the icosahedral shape of the Ru nanocages could be largely preserved at a temperature up to 300 ^{o}C. I further evaluated the shape-dependent catalytic activities of Pd@Ru core−shell nanocrystals and the *fcc*-Ru nanocages using two model reactions based on the reduction of 4-nitrophenol and decomposition of hydrazine. Our results indicated that Ru nanocages displayed superior activities than their parental Pd@Ru core−shell nanocrystals toward both the reduction of 4-nitrophenol and decomposition of hydrazine. Furthermore, the Ru icosahedral nanocages exhibited greatly enhanced performance than their cubic and octahedral counterparts due to the presence of twin boundaries on the surface. As an estimate of their potential toward ammonia synthesis, I and my collaborators also performed periodic DFT calculations to evaluate the capability of the Ru icosahedral nanocages to dissociate molecular nitrogen and found that *fcc*-structured Ru icosahedral

nanocages with Pd impurities in the subsurface are more promising than the conventional *hcp*-Ru nanoparticles in catalyzing ammonia synthesis.

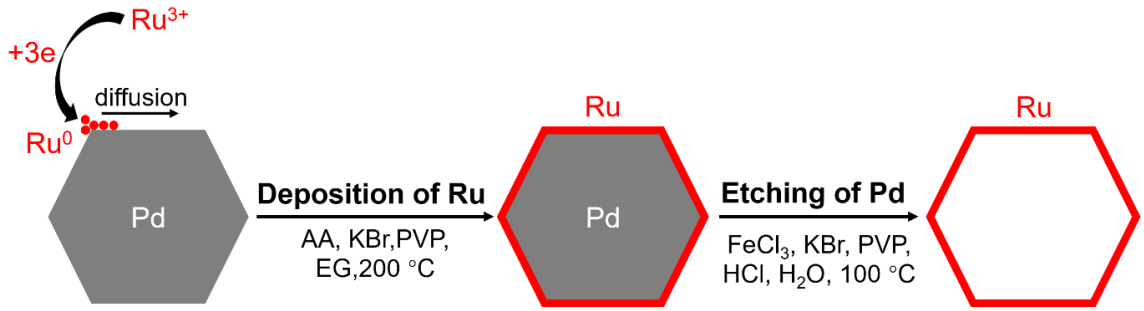

Figure 4.1. Schematic illustrating the two main steps, together with the reaction conditions, involved in the formation of Pd@Ru core–shell icosahedra and Ru icosahedral nanocages: *i*) the deposition of Ru atoms on Pd icosahedral seeds in a layer-by-layer growth mode and *ii*) the selective removal of Pd cores through wet chemical etching.

4.2 Results and Discussion

Characterization of Pd@Ru Core–Shell Icosahedra and Ru Icosahedral Nanocages. As illustrated in Figure 4.1, the fabrication of Ru icosahedral nanocages involves two major steps: the deposition of Ru atoms on Pd icosahedral seeds in a layer-by-layer growth mode and the selective removal of Pd cores through wet chemical etching. The synthesis started with the preparation of Pd icosahedra (Figure 4.2a), which served as seeds for the conformal deposition of Ru shells. Based on the histogram of size distribution shown in Figure 4.2b, the Pd icosahedra had an average size of 12 ± 3nm. After AA, PVP and KBr had been dissolved in EG and then mixed with a suspension of the as-synthesized Pd icosahedral seeds, the mixture was heated to 200 °C in an oil bath under magnetic stirring. Subsequently, an EG solution of $RuCl_3 \cdot xH_2O$ was titrated into the reaction mixture at a rate of 1 $mL \cdot h^{-1}$. After completion of titration, the reaction was continued for another

two hours. Figure 4.2c shows the TEM image of a typical sample of the Pd@Ru core–shell icosahedra, which took a well-defined icosahedral shape and a uniform size. As evident from the HAADF-STEM image shown in the inset, the icosahedral shape and twin structure can be well recognized. To confirm the core–shell structure, I conducted EDX mapping to differentiate the distribution of Pd and Ru in the nanocrystals, as illustrated in Figure 4.2d. Based on the clear contrast between the Pd cores and Ru shells, the Ru adatoms were well distributed on the outer layers of Pd cores, demonstrating a core–shell structure.

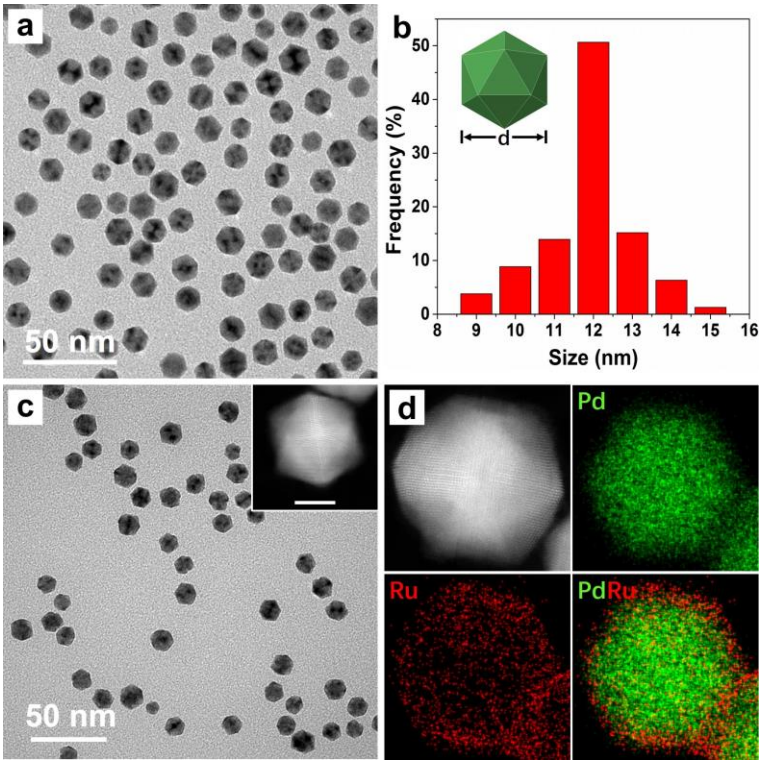

Figure 4.2. (a) TEM image of the Pd icosahedral seeds. (b) Size distribution of the Pd icosahedral seeds. The inset shows the definition of size. (c) TEM image of the Pd@Ru core–shell icosahedra synthesized from 12-nm Pd icosahedra. The inset shows the STEM image of an individual Pd@Ru core–shell icosahedron (scale bar: 5 nm). (d) STEM images and EDX mapping (green = Pd, red = Ru) of an individual core–shell icosahedron.

To obtain Ru icosahedral nanocages, the Pd cores were selectively removed through chemical etching. During the etching process, $FeCl_3$ and KBr worked together as an etchant while HCl was added to prevent the hydrolysis of both Fe^{3+} and Fe^{2+} ions [29]. The chemical reaction involved in the etching process can be summarized as:

$$Pd + 2Fe^{3+} + 4Br^{-} \rightarrow PdBr_4^{2-} + 2Fe^{2+}$$

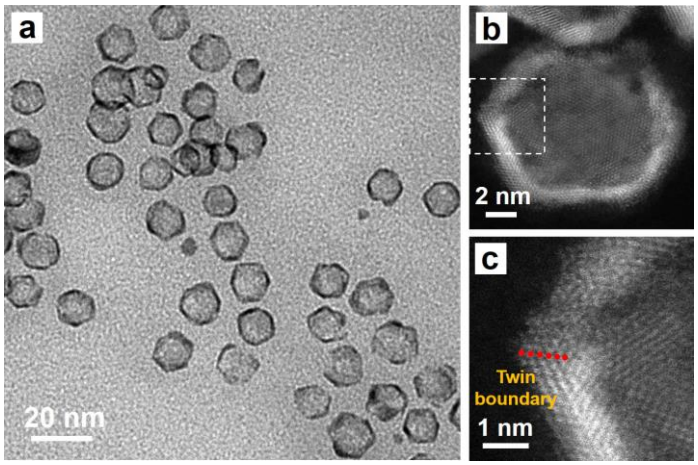

Figure 4.3. (a) TEM image of the Ru icosahedral nanocages synthesized from 12-nm Pd icosahedra. (b) HAADF-STEM image of an individual Ru icosahedral nanocage and (c) atomic-resolution image taken from the edge marked by a box in panel (b), revealing the twin boundary.

Figure 4.3a shows TEM image of the Ru icosahedral nanocages after chemical etching, where the Pd cores were effectively etched away while the icosahedral shape of the Ru shells was well preserved. Based on the HAADF-STEM images shown in Figures 4.3b and c, the twin boundary in the Ru icosahedral nanocage can be well resolved. The average thickness of the Ru shells was approximately 1.1 nm, corresponding to five atomic layers.

ICP-MS measurement was conducted to quantitatively analyze the elemental compositions of the Pd@Ru core−shell icosahedra and Ru icosahedral nanocages. After etching, the weight percentage of Pd dropped from 75.0 wt.% in the core−shell icosahedra to 12.5 wt.% in the nanocages, demonstrating the sufficient removal of Pd cores through wet chemical etching. Meanwhile, the weight percentage of Ru increased from 25.0 wt.% in the core−shell icosahedra to 87.5 wt.% in the nanocages, indicating the dominance of Ru in the icosahedral nanocages.

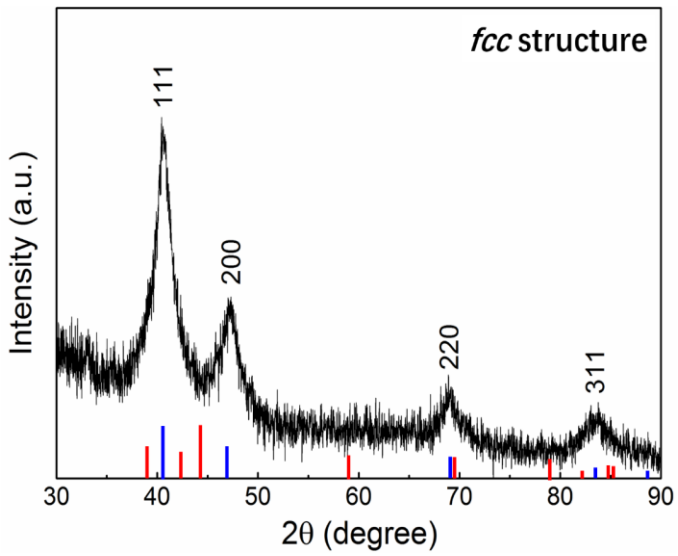

Figure 4.4. XRD pattern of Ru icosahedral nanocages synthesized from 12 nm Pd icosahedra, demonstrating their *fcc* structure. Blue bars: JCPDS no. 88-2333 (*fcc* Ru). Red bars: JCPDS no. 06-0663 (*hcp* Ru).

Seed-mediated growth has been reported as a straightforward and versatile method for generating noble-metal nanocrystals with unusual crystal structures [24].Recently, by templating with Pd cubes and octahedra, Ru cubic and octahedral nanocages with an *fcc* structure have been successfully prepared [27, 28]. Here, I also conducted XRD analysis

to determine the crystal structure of the Ru icosahedral nanocages. Figure 4.4 shows an XRD pattern of the Ru nanocages prepared from 12-nm Pd icosahedra. The characteristic peaks of *fcc*-structured Ru, including (111), (200), (220) and (311), could all be resolved. Due to the small lattice mismatch between Pd and *fcc* Ru (~1.8%), the surface atoms of Pd icosahedral seeds would force the deposited Ru adatoms to faithfully replicate the surface atomic structure of the Pd seeds through epitaxial growth. Taken together, the Ru adatoms in the shells would crystallize in an *fcc* structure, where both the {111} facets and twin structure could be well preserved.

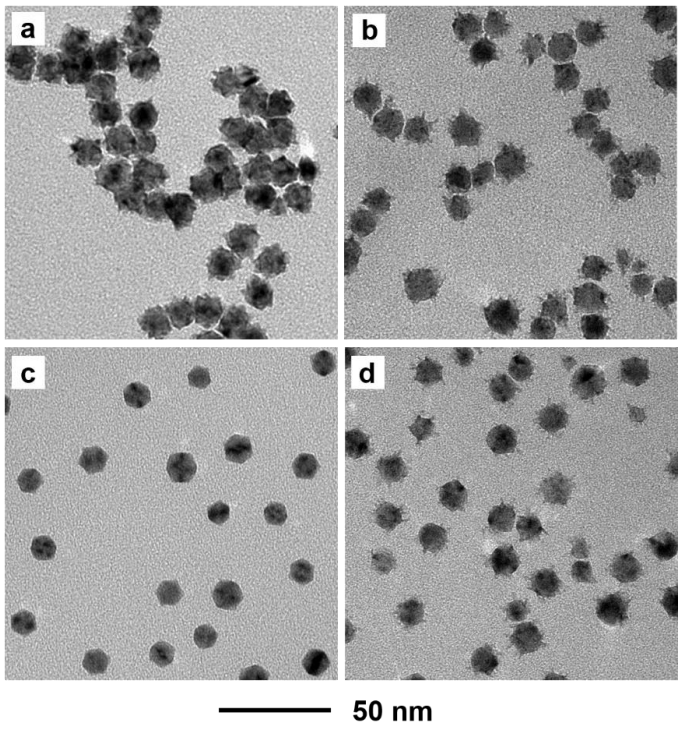

Figure 4.5. TEM images of typical Pd@Ru nanocrystals prepared from 12 nm Pd icosahedra using the standard procedure except (a) in the absence of KBr; and (b) decreasing the amount of $RuCl_3$ to 0.48 mg; (c) collecting the product after 5 h injection; (d) in the absence of KBr, decreasing the amount of $RuCl_3$ to 0.48 mg, and collecting the product after 5 h injection.

Investigation of the Deposition Mechanism. The essence of forming Pd@Ru core−shell icosahedra is to ensure a layer-by-layer deposition for the Ru adatoms, which can be realized by controlling the rate of atom deposition relative to surface diffusion [30]. In order to achieve preferential surface diffusion over atom deposition, I introduced KBr into the growth solution, which has been proven to be an effective additive in achieving conformal coating of Pt on Pd seeds. Its role is to retard the reduction rate of the Pt precursor, in other words, to decrease the deposition rate of Pt adatoms and promote the formation of conformal coating [17]. Figure 4.5a shows the resultant Pd@Ru nanocrystals prepared in the absence of KBr. The nanocrystals exhibited rough surfaces, characteristic of an island growth mode. To elucidate the deposition mechanism of Ru atoms on Pd cores, I investigated the reduction kinetics by measuring the instantaneous concentrations of unreacted Ru(III) ions in the reaction solution at different time points (Figure 4.6a).

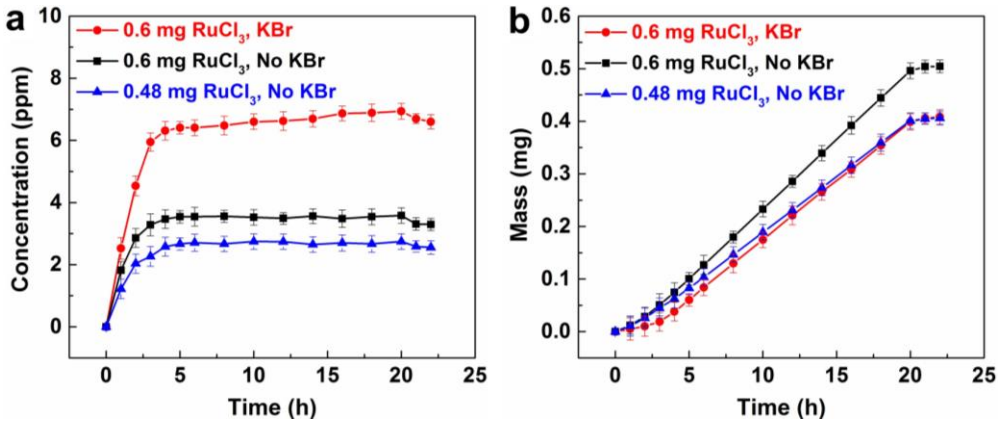

Figure 4.6. Quantitative analysis of the conversion of Ru(III) ions to Ru(0) atoms during the synthesis of Pd@Ru core−shell icosahedra under different conditions. (a) The instantaneous concentration of unreacted $RuCl_3$ in the reaction solution. (b) The accumulated mass of Ru(0) atoms throughout a synthesis, as derived from the data shown in (a). The Ru(III) precursor was injected in the first 20 h and the reaction was then continued for another 2 h to completion.

According to our prior work related to the kinetic analysis of seed-mediated growth [31], when Ru(III) precursor was introduced by dropwise addition, the Ru(III) ions should be gradually accumulated in the growth solution as the number of drops is increased in the initial stage. Afterwards, the concentration of Ru(III) ions will reach a steady state and only fluctuate in a narrow range defined by n_{up} and n_{low}, corresponding to the upper and lower limits, respectively, for the number of precursor ions normalized to the number of seeds. Specifically, during the steady state, the number of Ru(III) ions will promptly increase from n_{low} to n_{up} upon introducing a new drop of Ru(III) precursor, and then exponentially decay from n_{up} to n_{low} until the addition of the next drop [31]. For both samples synthesized with (denoted standard synthesis) and without KBr, the concentrations of Ru(III) precursor in the reaction solution increased dramatically during the first 5 h and then became relatively stable in the following 15 h, in agreement with our previously reported model [31]. After all the precursor solution had been injected, the concentration of the Ru(III) precursor dropped a little and then became relatively stable. In the case of no KBr, the final concentration of Ru(III) precursor was lower than that of the standard synthesis, indicating a higher conversion of Ru(III) ions to Ru(0) atoms (31.5 wt.% Ru in the as-obtained Pd–Ru nanocrystals). Figure 4.6b shows the accumulated masses of Ru(0) atoms during the syntheses under different reaction conditions, also confirming the higher conversion of Ru(III) ions to Ru(0) atoms in the absence of KBr.

In order to probe the role of KBr in determining the growth modes of Ru adatoms under the same Ru(III) conversion conditions, I reduced the amount of Ru(III) precursor to 0.48 mg while keeping all other reaction conditions the same as the standard procedure. The product is denoted by sample/0.48, and a TEM image is shown in Figure 4.5b. The

weight percentage of Ru in sample/0.48 was 24.8 wt.%, similar to that of the standard sample (25.0 wt.%). With regard to the reduction kinetics of sample/0.48, the measured instantaneous concentration of unreacted Ru(III) precursor took the same trend as the standard synthesis, but the value was lower due to the decrease in concentration for the Ru(III) precursor (Figure 4.6a). Although the weight percentages of Ru in the final products were almost the same for sample/0.48 and the standard sample, their accumulated masses of Ru(0) atoms were different throughout the synthesis, as illustrated in Figure 4.6b. Especially, for sample/0.48, the accumulated mass of Ru(0) atoms was much higher than that of the standard sample in the first 5 h and then gradually became closer in the following hours. Figures 4.5c and d show TEM images of the standard sample and sample/0.48, respectively, collected after the Ru(III) precursor had been injected for 5 h. Notably, the nanocrystals in the standard sample possessed a well-defined icosahedral shape with a smooth surface, while those in sample/0.48 took a rough surface due to the presence of plenty branches. This result confirms that the Ru adatoms in the standard synthesis and the sample/0.48 followed different growth modes in the initial stage: layer-by-layer and island, respectively. Taken together, the introduction of KBr was critical in enabling a layer-by-layer growth pattern for the Ru adatoms throughout the synthesis, leading to the formation of conformal Ru shells.

I also investigated the roles of injection rate, the amount of Ru(III) precursor, and reaction temperature; all of which could affect the atom deposition and/or surface diffusion. I first studied the effect of injection rate, which is directly related to the atom deposition rate, on the formation of Pd@Ru core−shell icosahedra, as shown in Figure 4.7. When the injection rate of Ru(III) precursor was increased to 5 $mL \cdot h^{-1}$ and further to 20 $mL \cdot h^{-1}$, the

surfaces of the as-obtained Pd@Ru nanocrystals became rough and were covered by plenty of branch-like particles (Figures 4.7a and b, respectively). After selective removal of the Pd cores, the resultant Ru nanocages showed rough surfaces, indicating insufficient surface diffusion (Figures 4.7c and d, respectively), in agreement with their initial Pd@Ru nanocrystals. As the injection rate was increased, the resultant Ru nanocages were covered by more small particles and cracks on the surface, and more Ru adatoms were confined to the corners and edges. It is because, during the epitaxial growth, Ru(0) atoms preferred to be deposited on the low-coordination atoms first, in our case, atoms on the vertices and edges [32]. If the deposition rate was greater than the surface diffusion rate, more Ru atoms would aggregate at the vertices and edges, generating non-uniform shells.

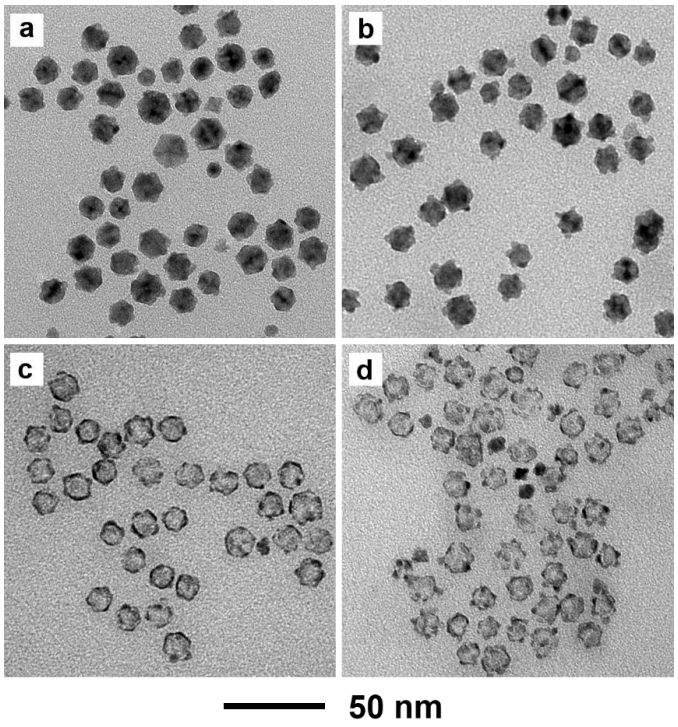

Figure 4.7. TEM images of typical Pd@Ru nanocrystals and their corresponding nanocages prepared from 12 nm Pd icosahedra using the standard procedure except using different injection rates. (a, c) 5 mL h^{-1}, (b, d) 20 mL h^{-1}.

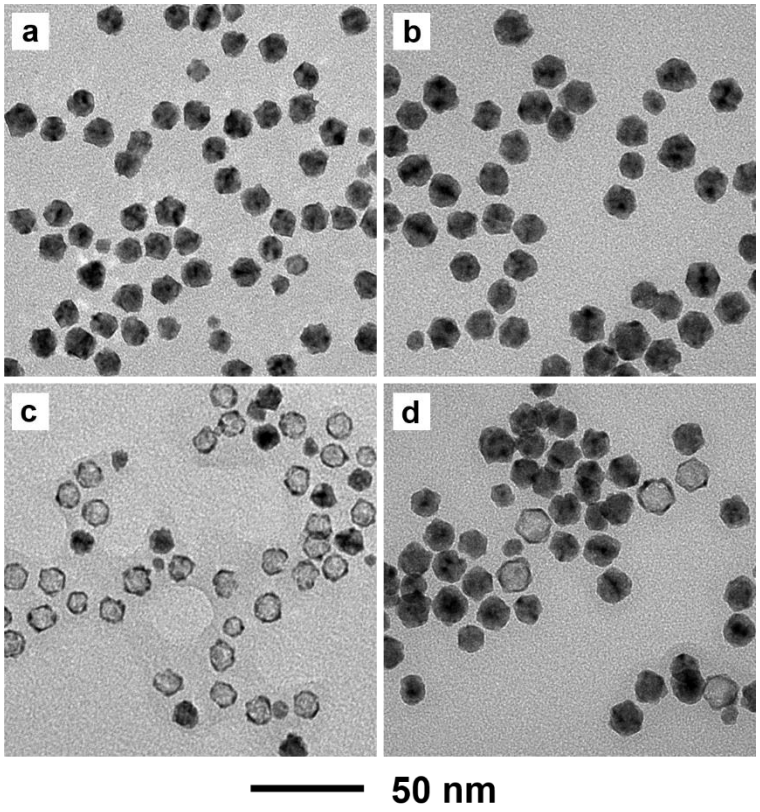

Figure 4.8. TEM images of typical Pd@Ru nanocrystals and their corresponding nanocages prepared from 12 nm Pd icosahedra using the standard procedure except introducing different amounts of $RuCl_3$ while keeping the overall volume of injected solution at 20 mL. (a, c) 0.8 mg, (b, d) 1.2 mg.

I also varied the amount of Ru(III) precursor while keeping the total volume unchanged to see whether I can tune the thickness of the Ru shells. Figures 4.8a and b show TEM images of typical Pd@Ru nanocrystals prepared using the standard procedure except increasing the amount of Ru(III) precursor to 0.8 and 1.2 mg, respectively. The sizes of resultant Pd@Ru nanocrystals grew to approximately 14.5 (Figure 4.8a) and 15.5 nm (Figure 4.8b), respectively. However, the surfaces of these nanocrystals became relatively rough. Based on the elemental compositions determined using ICP-MS, the calculated thicknesses of the Ru shells were approximately 6.2 and 7.8 atomic layers for the

nanocrystals (denoted by $Pd@Ru_{6.2L}$ and $Pd@Ru_{7.8L}$) obtained with the introduction of 0.8 and 1.2 mg of Ru(III) precursor, respectively. For $Pd@Ru_{6.2L}$, 85% of them could be converted into Ru nanocages (Figure 4.8c) through wet chemical etching, while only a small portion (~15%) of the $Pd@Ru_{7.8L}$ nanocrystals could be transformed into Ru nanocages (Figure 4.8d). This result can be attributed to the increase in thickness of the Ru shells. When the Ru shells became too thick, they could block the Pd atoms in the cores from diffusing to the surface during the etching process [33].

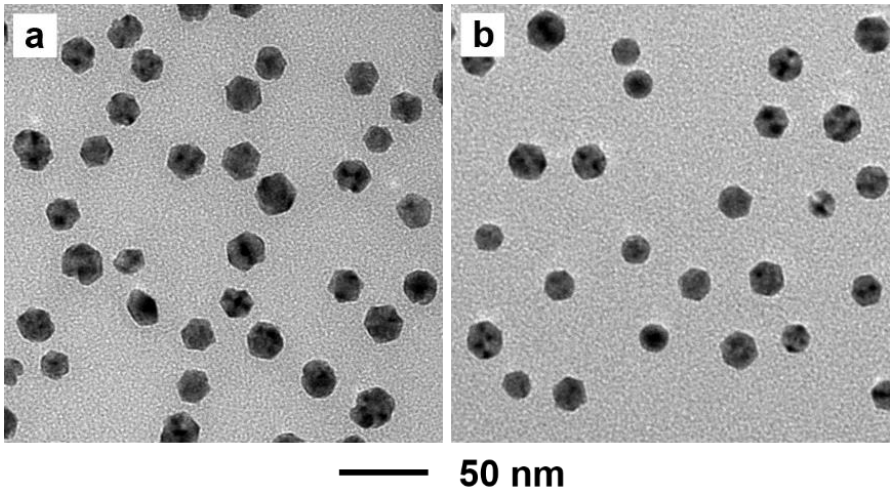

Figure 4.9. TEM images of typical Pd@Ru nanocrystals prepared from 12 nm Pd icosahedra using the standard procedure except at different reaction temperatures. (a) 175 °C and (b) 150 °C.

Reaction temperature was another important parameter in determining the formation of Pd@Ru core−shell icosahedra. On the one hand, since the surface diffusion of adatoms is a thermally activated process, I are able to promote or suppress it accordingly by manipulating reaction temperature. On the other hand, reaction temperature was also found

to significantly affect the atom deposition rate during our synthesis [27, 28]. When the reaction temperature was decreased to 175 °C and further to 150 °C, the resultant Pd@Ru icosahedra still possessed smooth surfaces and sharp edges (Figures 4.9a and b, respectively). However, according to the ICP-MS results, the weight percentages of Ru in the nanocrystals prepared at 175 °C and 150 °C were 16.2 wt.% and 5.6 wt.%, corresponding to 2.6 and 0.8 atomic layers, respectively. Although surface diffusion was suppressed with the decrease in reaction temperature, the atom deposition rate was retarded simultaneously. Therefore, I could still achieve preferential surface diffusion over atom deposition at a lower temperature, but with compromise in thickness for the Ru shells.

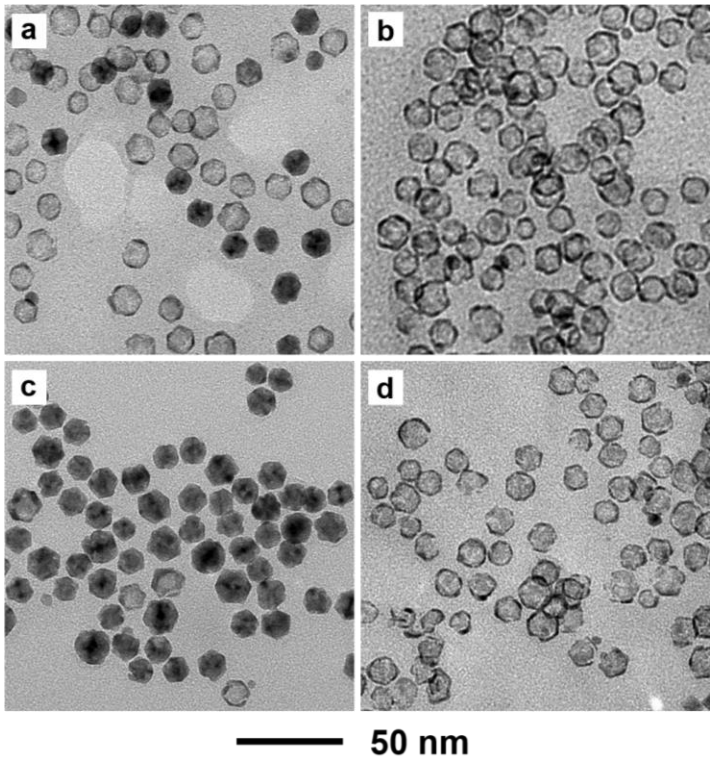

Figure 4.10. TEM images of products prepared using the standard etching protocol except etching for (a) 60 min and (b) 180 min, and the use of (c) 5 mg $FeCl_3$ and 30 μL HCl; and (d) 90 mg $FeCl_3$ and 540 μL HCl.

After obtaining Pd@Ru core−shell icosahedra using the standard procedure (denoted by Pd@$Ru_{4.5L}$), I conducted chemical etching to selectively remove the Pd cores for the formation of Ru nanocages with a well-retained icosahedral shape and good dispersity. Here, I examined the samples obtained at different stages of etching to optimize the etching process. When the Pd@$Ru_{4.5L}$ icosahedra were etched for 60 min using the standard etching protocol, 70% of them could be converted to nanocages (Figure 4.10a). If the etching time was extended to 180 min, all the Pd cores could be etched away; however, the resultant Ru nanocages started to aggregate (Figure 4.10b). In addition, the amount of etchant was also critical to the formation of Ru nanocages. When I proportionally decreased the amounts of HCl and $FeCl_3$ to 30 μL and 5 mg, respectively, only a fraction of the Pd@$Ru_{4.5L}$ core−shell icosahedra was transformed into Ru nanocages. In contrast, if the amounts of HCl and $FeCl_3$ were proportionally increased to 540 μL and 90 mg, respectively, Ru nanocages were obtained in high purity. Thus, by controlling the etching time and using an adequate amount of the etchant, I can achieve Ru icosahedral nanocages with good dispersity and high quality.

Evaluation of Thermal Stability. The thermal stability of both the *fcc* structure and the icosahedral shape of the Ru icosahedral nanocages was investigated. Figure 4.11 shows the *in situ* XRD patterns collected every 50 °C in the temperature range of 100−500 °C. When the nanocages were heated to temperatures ranging from 100 to 300 °C, the *fcc* structure was well preserved, as demonstrated by the characteristic peaks (dashed blue lines). However, when I further elevated the temperature to 350 °C, the *hcp*-(101) peak started to appear, implying the initiation of structural transition from *fcc* to *hcp*. When the heating temperature reached 400 °C, the characteristic peaks of *hcp* structure, including

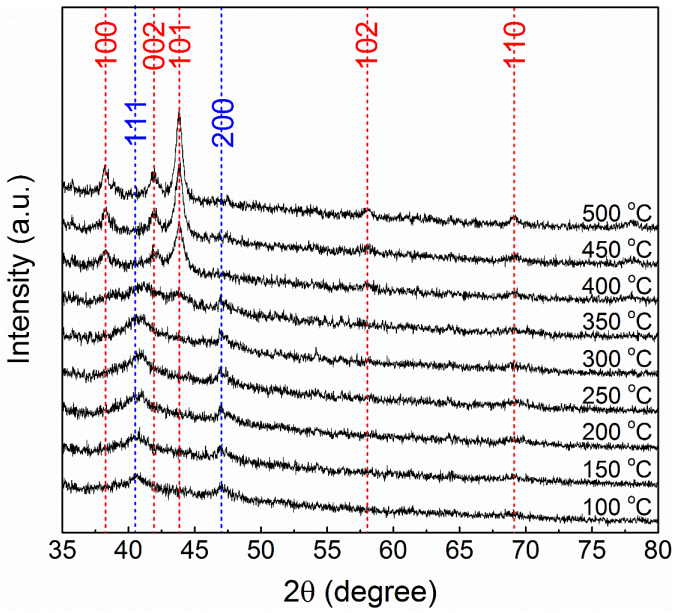

Figure 4.11. *In situ* XRD patterns of the *fcc* Ru icosahedral nanocages measured under Ar atmosphere in the temperature range between 100 and 500 °C, indicating that the *fcc* structure could be retained up to 300 °C. The characteristic peaks of *fcc* and *hcp* are shown by blue and red dashed lines, respectively.

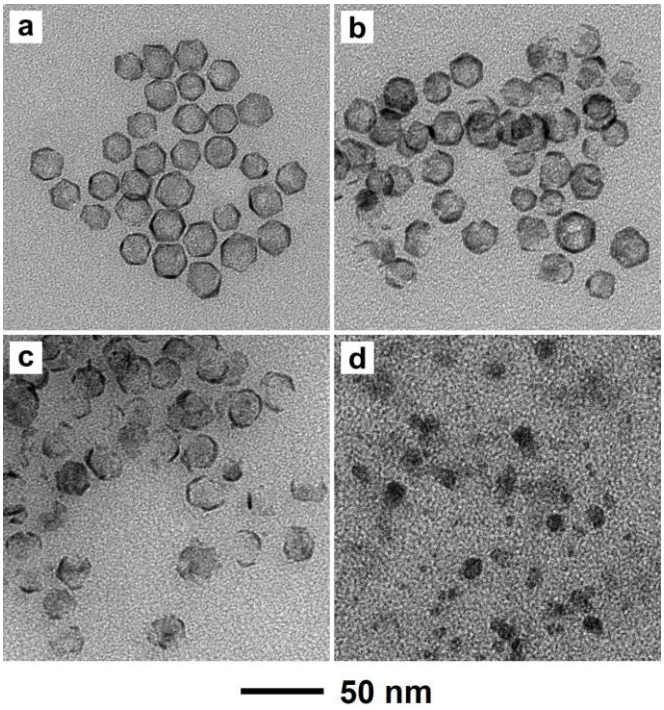

Figure 4.12. TEM images of Ru icosahedral nanocages heated to different temperatures for 1 h. (a) 250 °C, (b) 300 °C, (c) 350 °C and (a) 400 °C, suggesting that the icosahedral shape could be largely preserved up to 300 °C.

(100), (002), (101), (102) and (110), became dominant and their intensities kept increasing as the heating temperature was elevated to 500 °C, suggesting that the crystal structure of the Ru icosahedral nanocages had been completely transformed from *fcc* to *hcp*.

Figure 4.12 shows TEM images of the Ru icosahedral nanocages after heating to different temperatures. When the nanocages were heated at 250 °C for 1 h, their icosahedral shape could be essentially preserved (Figure 4.12a). As the temperature was elevated to 300 °C, a majority of the nanocages could retain the icosahedral shape while a small portion of them were fragmented, generating cracks on the surface (Figure 4.12b). When the temperature reached 350 °C, most of the icosahedral nanocages were broken into small fragments and the icosahedral shape was largely lost (Figure 4.12c). If I further heated the sample to 400 °C, all the nanocages evolved into small particles (Figure 4.12d). Taken together, both the *fcc* structure and the icosahedral shape of the Ru icosahedral nanocages could be retained up to 300 °C. As the temperature was elevated to 350 °C and higher, the *fcc* structure would be transformed into *hcp* structure, and at the same time, the icosahedral shape would be lost.

Table 4.1. Molar ratio between Br^- and Ru before and after washing for three times.

	Br^- / $Ru_{core-shell}$ (mol/mol)	Br^- / $Ru_{nanocages}$ (mol/mol)
Before washing	84.57 : 1	2547.84 : 1
1st washing	0.03 : 1	0.41 : 1
2nd washing	0.00 : 1	0.00 : 1
3rd washing	0.00 : 1	0.00 : 1

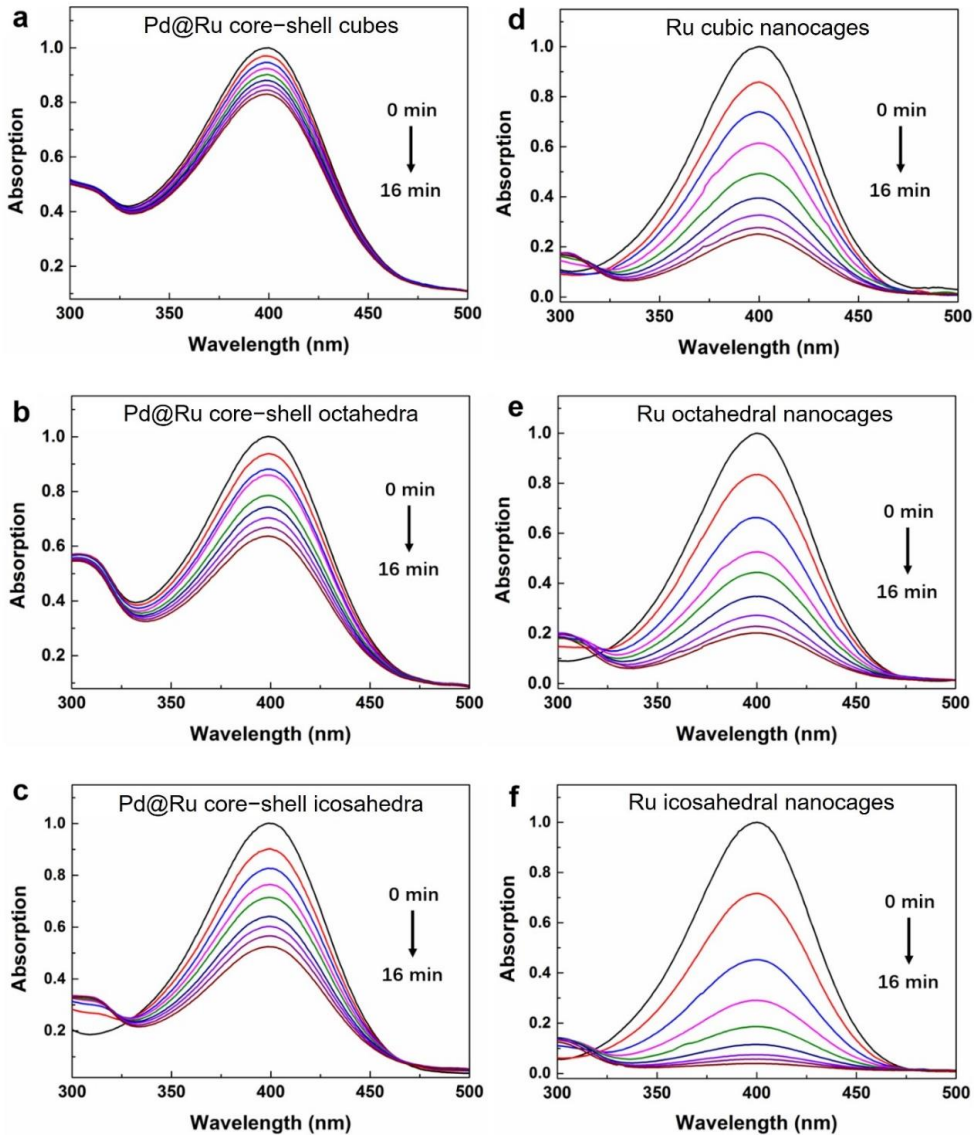

Figure 4.13. Absorption spectra of the reaction solutions for the reduction of 4-nitrophenol at different times points in the presence of Pd@Ru core−shell nanocrystals and Ru nanocages with a (a, d) cubic, (b, e) octahedral and (c, f) icosahedral shape, respectively.

Evaluation of the Catalytic Activities toward the Reduction of 4-Nitrophenol and Decomposition of Hydrazine. Since I used a relatively large amount of Br^- into the reaction system, I conducted ICP-MS analysis to determine whether I could effectively remove the Br^- by washing the samples with water for three times. As shown in Table 4.1,

there existed a large amount of Br^- in the reaction system before the washing process. However, after washing twice with water, the amount of Br^- dropped dramatically to a level unable to be detected by ICP-MS (sensitivity: parts per billion or ppb), demonstrating the sufficient removal of Br^- by washing with water. To evaluate the shape- and structure-dependent catalytic activities of the Pd@Ru core−shell nanocrystals and Ru nanocages, both the reduction of 4-nitrophenol and decomposition of hydrazine were selected as model reactions. The reduction of 4-nitrophenol has been shown to be surface- or structure-sensitive to Ru nanocrystals [24, 26, 34–36]. For comparison, I also prepared Pd@Ru core−shell nanocrystals and Ru nanocages with cubic and octahedral shapes, as well as a similar size, according to our prior reports, in which the Ru atoms were also crystallized in an *fcc* structure [27, 28].

I first evaluated the catalytic activities of the Pd@Ru core−shell cubes, octahedra, and icosahedra. Figure 4.13a–c shows the recorded UV-vis spectra, which could be used to monitor the reaction kinetics by measuring the decreasing absorbance of 4-nitrophenolate anions at 400 nm. The absorbance at 400 nm was then normalized and plotted as a function of reaction time, as illustrated in Figure 4.14a, showing a 17%, 26% and 48% decay for the Pd@Ru core−shell cubes, octahedra, and icosahedra, respectively, within a period of 16 min. Since $NaBH_4$ was in excess during the reaction, the reduction of 4-nitrophenol could be treated as a pseudo-first-order reaction [37], in which -ln(absorbance) showed a liner dependence on reaction time, as confirmed in Figure 4.14b. Based on the linear relationship, the mass-normalized rate constants of the Pd@Ru core−shell cubes, octahedra, and icosahedra were determined as 3.29, 5.71 and 8.32 s^{-1} mg^{-1}, respectively. Clearly, the {111}-enclosed Pd@Ru octahedra exhibited enhanced

performance than their cubic counterpart enclosed with {100} facets, demonstrating that the {111} surface was more catalytically active than the {100} surface. The Pd@Ru icosahedra, combined with {111} facets and twin defects, displayed the greatest activity among all the three types of catalysts, verifying the role of twin defects in further enhancing the catalytic performance.

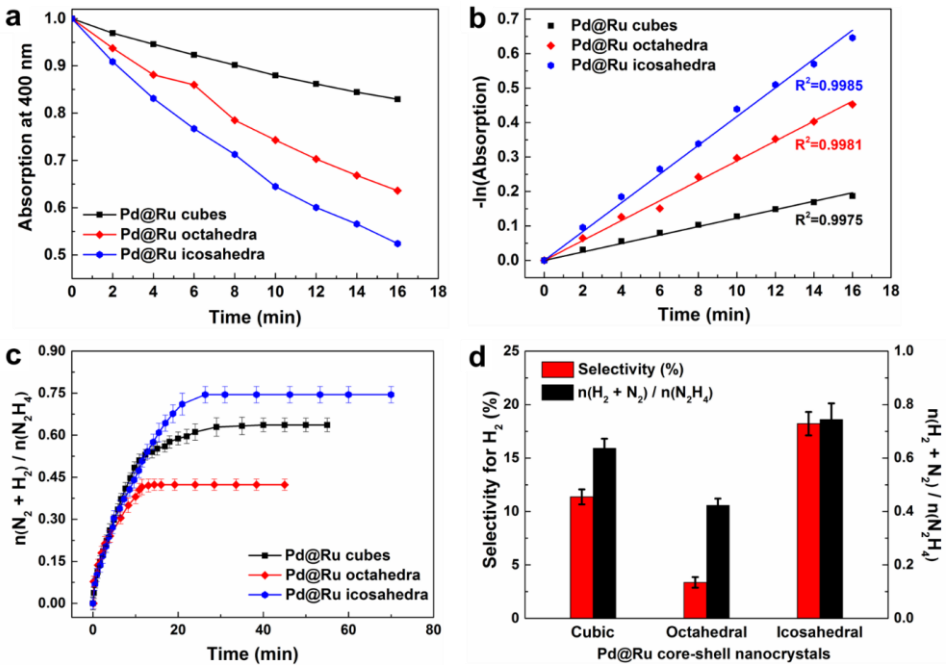

Figure 4.14. Comparison of the catalytic activities of Pd@Ru core–shell cubes, octahedra, and icosahedra toward the reduction of 4-nitrophenol by $NaBH_4$ and the decomposition of hydrazine. (a) Normalized absorbance at 400 nm for 4-nitrophenol as a function of time. (b) Plots of -ln(absorbance) versus reaction time generated from (a). (c) Time course plots for the decomposition of hydrazine in aqueous solutions in the presence of different Pd@Ru core–shell nanocrystals as catalysts. (d) Selectivity for hydrogen generation from the decomposition of hydrazine catalyzed over different Pd@Ru core–shell nanocrystals.

In addition to Pd@Ru core–shell nanocrystals, I also evaluated the catalytic activities of Ru cubic, octahedral and icosahedral nanocages toward the reduction of 4-nitrophenol.

As illustrated in Figure 4.13d–f, the recorded UV-vis spectra dropped gradually throughout the catalytic process. Figure 4.15a shows the normalized absorbance at 400 nm plotted as a function of reaction time, in which the peak intensity at 400 nm decayed by 74.82%, 79.81% and 96.04% for the Ru cubic, octahedral and icosahedral nanocages, respectively, within a period of 16 min. The icosahedral nanocages, due to a combination of twin boundaries and {111} facets, displayed the greatest activity relative to the cubic and octahedral nanocages, which were enclosed by {100} and {111} facets, respectively. Based on the linear relationship between -ln(absorbance) versus reaction time (Figure 4.15b), the calculated mass-normalized rate constants (*k*) of Ru cubic, octahedral and icosahedral nanocages were 17.62, 20.64, and 41.21 s^{-1} mg^{-1}, respectively, indicating a more than 4-times enhancement in mass activity than their parental core−shell nanocrystals. The enhancement in activity was attributed to the nanocage structure characterized by a hollow interior, ultrathin walls, and porous structure, where both the interior and exterior surfaces could be involved in catalyzing the reaction. Specifically, the rate constant of icosahedral nanocages was 2.34 and 2.00 times greater than those of cubic and octahedral nanocages, respectively, confirming the outstanding catalytic properties of Ru icosahedral nanocages with twin boundaries. The enhanced performance of the icosahedral nanocages than their cubic and octahedral counterparts can be attributed to the strain derived from the high density of twin defects, which has been demonstrated to improve the catalytic activities pronouncedly [38, 39].

In addition, Ru is also known for its great performance toward the decomposition of hydrazine at room temperature [40]. Here, the successful synthesis of Pd@Ru core−shell nanocrystals and Ru nanocages with cubic, octahedral and icosahedral shapes allowed us

to evaluate the facet- or structure-dependent properties of various Ru nanocages toward hydrazine decomposition. Figure 4.14c shows the plots for the decomposition of hydrazine as a function of reaction time in aqueous solutions containing the Pd@Ru core−shell nanocrystals. The $n(N_2+H_2)/nN_2H_4$ ratios were 0.64, 0.42 and 0.74 for the Pd@Ru core−shell cubes, octahedra, and icosahedra, in which the icosahedral nanocrystals showed a 1.2- and 1.8-times enhancement in activity than their cubic and octahedral counterparts, respectively.

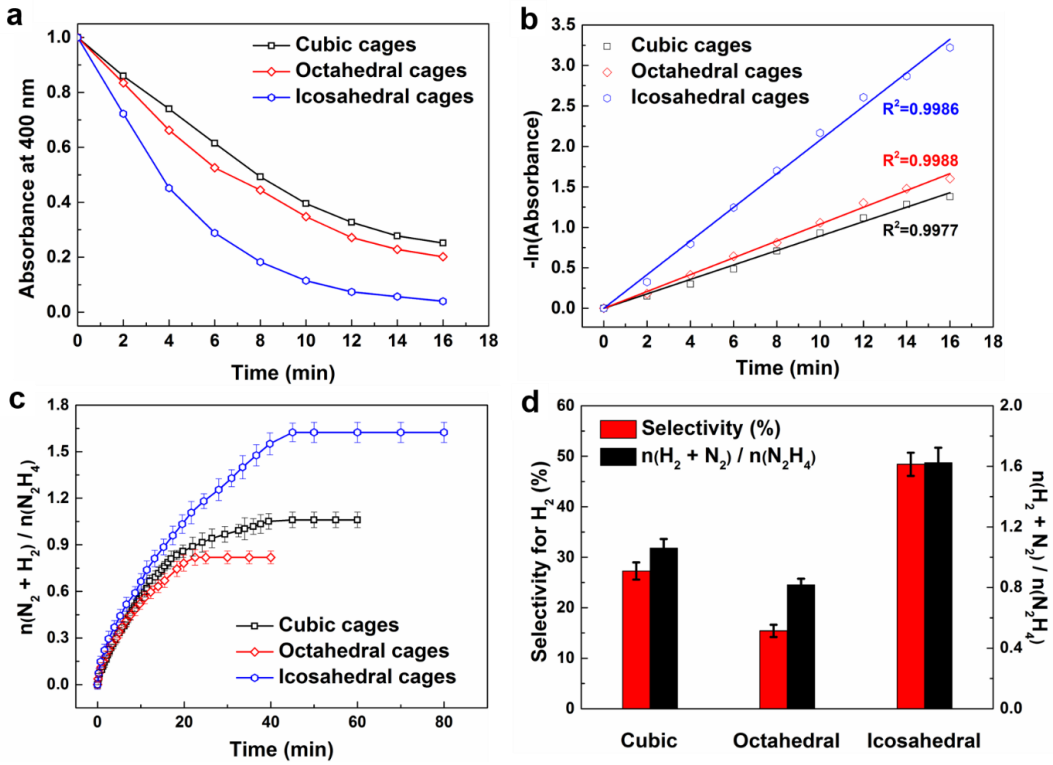

Figure 4.15. Comparison of the catalytic activities of Ru cubic, octahedral and icosahedral nanocages toward the reduction of 4-nitrophenol by $NaBH_4$ and the decomposition of hydrazine. (a) Normalized absorbance at 400 nm for 4-nitrophenol as a function of time. (b) Plots of -ln(absorbance) versus reaction time generated from (a). (c) Time course plots for the decomposition of hydrazine in aqueous solutions in the presence of different Ru nanocages as catalysts. (d) Selectivity for hydrogen generation from the decomposition of hydrazine catalyzed over different Ru nanocages.

The selectivity of different types of nanocrystals toward H_2 generation was calculated and summarized in Figure 4.14d. Although the {100}-enclosed cubic nanocrystals were more catalytically active than the {111}-enclosed octahedral nanocrystals, the Pd@Ru core−shell icosahedra with twin boundaries on the surface exhibited the greatest H_2 selectivity than their cubic and octahedral counterparts (Figure 4.14d), indicating that the catalytic activities of {100}, {111} facets, and twin defects should increase in the order: {111} < {100} < twin defects. Besides, the Ru cubic, octahedral, and icosahedral nanocages were also used as catalysts toward the decomposition of hydrazine, as summarized in Figure 4.15c. The $n(N_2+H_2)/nN_2H_4$ ratios were determined as 1.06, 0.82 and 1.62 for the cubic, octahedral and icosahedral nanocages, respectively. Compared to their parental core−shell nanocrystals, the $n(N_2+H_2)/nN_2H_4$ ratios of nanocages showed a more than 1.7-times enhancement in activity, verifying the role of hollow structure in enhancing the catalytic performance of Ru nanocrystals toward the decomposition of hydrazine. Specifically, the $n(N_2+H_2)/nN_2H_4$ ratio of icosahedral nanocages was 1.53 and 1.98 times greater than those of cubic and octahedral nanocages, respectively, which can be attributed to the large density of twin boundary regions present in the icosahedral nanocages. Figure 4.15d compares the H_2 selectivity of Ru cubic, octahedral and icosahedral nanocages. The selectivity toward H_2 generation was 27.27%, 15.42% and 48.41% for the cubic, octahedral and icosahedral nanocages, respectively. The icosahedral nanocages showed the greatest H_2 selectivity, which was 1.78 and 3.14 times greater than those of cubic and octahedral nanocages, respectively. Taken together, nanocages with hollow interiors, ultrathin walls and porous structure are more promising catalysts than their parental core−shell nanocrystals. When compared with {100} and {111} facets, the

presence of twin defects on icosahedral nanocages substantially enhance the activity and H_2 selectivity of Ru nanocages toward the decomposition of hydrazine.

Table 4.2. Binding energies and sites of 14 atomic and molecular species on the pure Ru icosahedral (*fcc*) model surface. The position of each binding site is illustrated in Figure 4.16.

Species	BE (eV)	Site	Species	BE (eV)	Site
C	-7.58	h4	OH	-3.92	b1
H	-2.90	b1	NH	-5.28	h4
O	-6.11	h4	NH_2	-3.69	b1
N	-6.23	h4	NH_3	-1.00	t1
N_2	-0.90	t1	CH	-7.03	h4
CO	-2.12	t1	CH_2	-4.55	b1
NO	-2.96	t1	CH_3	-2.49	b1

Evaluation of Properties toward N_2 Dissociation using DFT Calculations. In order to further assess the catalytic properties of the *fcc*-Ru icosahedral nanocages, my collaborators performed periodic DFT (GGA-PW91) calculations over a Ru slab model which explicitly accounts for the twin boundary regions of the icosahedra. They explored the adsorption properties of the surface of an icosahedral nanocage by computing the binding structures and energies of 14 atomic and molecular adsorbates commonly involved in ammonia synthesis and other industrial processes. The results are summarized in Table 4.2. Although step edge atoms have lower coordination numbers and generally considered more reactive than terrace atoms, interestingly, not all the adsorbates prefer to bind to the step edge (right on top of the twin boundary) of the model surface. They suggest two

reasons for this: *i*) several species always prefer to bind on hollow sites, whereas only bridge and top sites are present right on top of the step edge; and *ii*) there are uneven local strain fields on the surface (see Figure 4.16), and the three-fold hollow site (h1 site) immediately adjacent to the step edge experiences compressive strain, which likely reduces its binding strength. The five adsorbates that prefer to bind to the {111} terrace all bind the strongest to the h4 sites, where the largest local lattice expansion (1.6%) is observed.

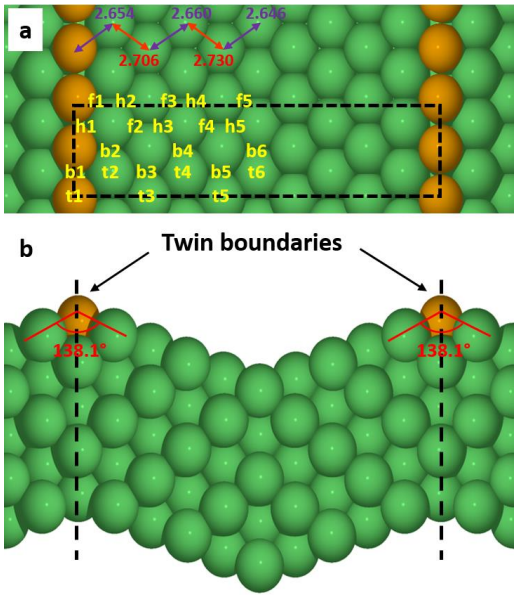

Figure 4.16. (a) Top and (b) side views of the pure Ru icosahedral (*fcc*) nanocage model. Orange spheres represent the surface Ru atoms at the top of the step edge; the other Ru atoms are represented by green spheres. The black dash lines indicate the unit cell boundaries. The yellow labels indicate all the high-symmetry sites evaluated for the adsorption studies. The arrows and numbers (in Å) indicate the neighboring distances of the surface atoms after relaxation. Red denotes local expansive strain; purple denotes local compressive strain. The calculated value for the distance between adjacent surface atoms in an unstrained *fcc* Ru nanocage is 2.687 Å.

They then used DFT calculations to predict the catalytic performance of the Ru icosahedral nanocages towards ammonia synthesis. Due to the enormous industrial impact

of the ammonia synthesis process, as well as the wide research interest in using Ru for this chemistry, they consider ammonia synthesis as a potential application for our Ru nanocage catalysts. Developing the energetics of the entire reaction network is beyond the scope of this work. To efficiently assess the reactivity of various surface models, here they adopted an approach similar to that of our previous studies of Ru cubic and octahedral nanocages [27, 28], by focusing only on the dissociation of N_2 to atomic nitrogen, since the N_2 dissociation step is considered as the rate-determining step for ammonia synthesis on Ru catalysts [41–44]. Specifically, they used the energy difference between the transition state of N_2* dissociation and the gas-phase nitrogen ($E_{TS} - E_{N2,gas}$) to assess the competition between the dissociation reaction and the (undesired) desorption of N_2*. A smaller value of $E_{TS} - E_{N2,gas}$ would indicate a better ammonia synthesis catalyst. The reaction energetics for N_2 dissociation on all the surface models investigated is summarized in Table 4.3, and the potential energy surfaces of best-performing model surfaces are shown in Figure 4.17.

They first present the results on the pure Ru icosahedral nanocage models. Here they explored various N_2 dissociation paths across the model surface, including on both the step edge (twin boundary region, $cage_{ico}$-edge) and the {111} terrace ($cage_{ico}$-(111)). The energetics of the lowest-barrier pathways for both cases is listed in Table 4.3. Although N_2 binds more strongly to the step edge (BE(N_2*) = -0.90 eV) than to the terrace (BE(N_2*) = -0.56 eV), the dissociation of N_2* (E_a (N_2* → 2N*)) over the step edge is hindered by a large activation barrier of 1.97 eV, which is 0.40 eV greater than that on the terrace. They attribute the difference in activation barrier to the strain effect as discussed above. At the step edge, the dissociation occurs over a locally compressed region while on the terrace, the lowest-barrier pathway occurs over a locally expanded region. Overall, the values of

$E_{TS} - E_{N2,gas}$ are 1.01 eV and 1.07 eV on the {111} terrace and the step edge of the pure Ru icosahedral nanocage model, respectively. Therefore, they conclude that N_2 dissociation would prefer to occur on the {111} terrace of pure Ru icosahedral nanocages rather than its step edge. Neither of the pure Ru icosahedral models shows better performance over the pure Ru octahedral nanocage model (denoted by $cage_{oct}$-(111) in Table 4.3), on which the value of $E_{TS} - E_{N2,gas}$ is 0.88 eV; that is, 0.13 eV and 0.19 eV lower than those for the $cage_{ico}$-(111) and $cage_{ico}$-edge, respectively.

Introducing subsurface Pd impurities to the slab models changes the reaction energetics significantly. Similar to our previous studies of the cubic and octahedral nanocages [27, 28], they observed notable stabilization of the N_2 dissociation transition state on the Ru icosahedral nanocage model when the Pd impurities are placed close to the surface layer, as summarized in Table 4.3. The strongest stabilization effects occur when the Pd atoms are in the immediate subsurface layer right underneath the reaction site ($cage_{ico}$-$edge_{Pd2,2\text{-}line}$ and $cage_{ico}$-$(111)_{Pd2,2\text{-}line}$ for step edge and terrace, respectively). Interestingly, this stabilization is much more pronounced at the step edge than on the terrace. On $cage_{ico}$-$edge_{Pd2,2\text{-}line}$, the N_2 dissociation transition state is stabilized by 0.48 eV compared to that on the step edge of the pure Ru icosahedral nanocage; on $cage_{ico}$-$(111)_{Pd2,2\text{-}line}$, the stabilization of the transition state relative to that on the {111} terrace of the pure Ru icosahedral nanocage is only 0.23 eV. As a result, when the subsurface Pd impurities are present underneath the twin boundary, the N_2 dissociation prefers to occur over the step edge with an $E_{TS} - E_{N2,gas}$ value of 0.59 eV; that is, 0.19 eV lower than the corresponding value (0.78 eV, as shown in Table 4.3 for $cage_{ico}$-$(111)_{Pd2,2\text{-}line}$) for the reaction path on the terrace.

Table 4.3. Calculated binding energies for the adsorbed: atomic nitrogen (BE(N*)) and molecular nitrogen (BE(N_2*)), calculated activation energy barriers for the dissociation of N_2* to N* (Ea (N_2* → 2N*), see Figure 4.17 for definition), and the calculated energy difference between transition state for N_2* dissociation and gas-phase nitrogen (E_{TS} – $E_{N2,gas}$). The smaller that quantity (E_{TS} – $E_{N2,gas}$) is, the more competitive the ammonia synthesis reaction is. The surface with the lowest E_{TS} – $E_{N2,gas}$ value for each set of nanocage models is shown boldfaced.

Model	BE(N*)[a]	BE(N_2*)[a]	Ea (N_2*→ 2N*)	E_{TS}[b] – $E_{N2,gas}$
Nanoparticle (*hcp*) models				
hcp-(0001)	-6.20	-0.64	1.52	0.88
Icosahedral nanocage (*fcc*) models (step edge)				
$cage_{ico}$-edge	-5.96	-0.90	1.97	1.07
$cage_{ico}$-$edge_{Pd2,2\text{-}line}$	**-6.24**	**-1.06**	**1.65**	**0.59**
$cage_{ico}$-$edge_{Pd2,2}$	-6.09	-1.00	1.83	0.83
$cage_{ico}$-$edge_{Pd2,3}$	-6.16	-1.01	1.87	0.86
$cage_{ico}$-$edge_{Pd2,4}$	-6.17	-1.00	1.78	0.78
$cage_{ico}$-$edge_{Pd3,3}$	-5.94	-0.92	2.04	1.12
$cage_{ico}$-$edge_{Pd3,4}$	-5.94	-0.93	2.05	1.12
Icosahedral nanocage (*fcc*) models ((111) terrace)				
$cage_{ico}$-(111)	-6.23	-0.56	1.57	1.01
$cage_{ico}$-$(111)_{Pd2,2\text{-}line}$	**-6.17**	**-0.70**	**1.48**	**0.78**
$cage_{ico}$-$(111)_{Pd2,2}$	-6.20	-0.61	1.60	1.00
$cage_{ico}$-$(111)_{Pd2,3}$	-6.27	-0.61	1.55	0.94
$cage_{ico}$-$(111)_{Pd2,4}$	-6.28	-0.62	1.50	0.88
$cage_{ico}$-$(111)_{Pd3,3}$	-6.03	-0.55	1.77	1.23
$cage_{ico}$-$(111)_{Pd3,4}$	-6.06	-0.59	1.79	1.20
Octahedral nanocage (*fcc*) models				
$cage_{oct}$-(111)	-6.27	-0.67	1.54	0.87
$cage_{oct}$-$(111)_{Pd2,2\text{-}line}$	-6.18	-0.67	1.35	0.68
$cage_{oct}$-$(111)_{Pd2.2}$	**-6.19**	**-0.74**	**1.30**	**0.56**
$cage_{oct}$-$(111)_{Pd2,3\text{-}far\_fcc}$	-6.40	-0.74	1.42	0.68
$cage_{oct}$-$(111)_{Pd2,3}$	-6.29	-0.63	1.42	0.79
$cage_{oct}$-$(111)_{Pd2,4}$	-6.25	-0.66	1.47	0.81
$cage_{oct}$-$(111)_{Pd3,3\text{-}line}$	-6.28	-0.63	1.60	0.97

[a] All values are in eV. Binding energies (BE) are referenced to the respective gas-phase species. [b] E_{TS} is the energy of the transition state.

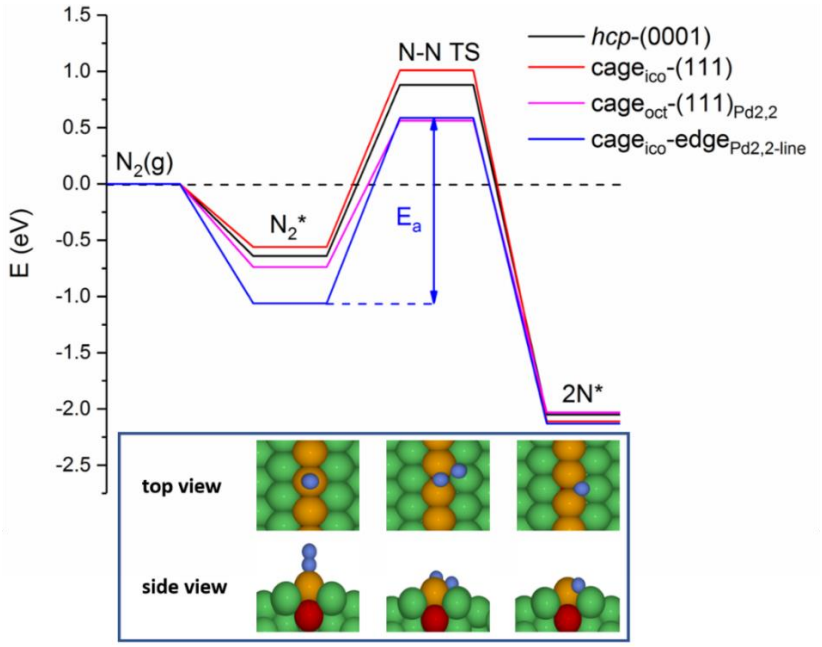

Figure 4.17. Potential energy surfaces for N_2 dissociation on four model surfaces. *hcp*-(0001) represents an *hcp* pure Ru(0001) slab as a model for conventional *hcp* Ru nanoparticles; cage$_{ico}$-(111) represents the pure *fcc*-Ru icosahedral nanocage model, where the reaction occurs on the {111} terrace; cage$_{oct}$-(111)$_{Pd2,2}$ is the best-performing *fcc*-Ru octahedral nanocage model exposing the {111} facet with two Ru atoms in the immediate subsurface layer exchanged with two Pd atoms; and cage$_{ico}$-edgePd$_{2,2\text{-line}}$ represents the best-performing *fcc*-Ru icosahedral nanocage model with two Ru atoms in the immediate subsurface layer beneath the step edge exchanged with two Pd atoms. "*" represents an adsorbed state, "2N*" reflects the energy of two N* adatoms adsorbed on the respective model at infinite separation from each other, and "N-N TS" refers to the transition state of the N_2* dissociation event. The energies of all states are referenced to that of the gas-phase nitrogen (N_2(g)). The activation energy barrier (E_a) is the difference between the transition state energy and the energy of N_2*, as depicted by the blue double-headed arrow. The graphics in the inset depict (from left to right) the initial state of N_2* adsorbed vertically atop a Ru atom, the N-N TS, and the final state with an N* at infinite separation from the second N* adsorbed on an *hcp* site on the cage$_{ico}$-(111)Pd$_{2,2\text{-line}}$ surface. In the inset, N atoms are represented by blue spheres, Pd atoms are represented by red spheres (see side views in inset), Ru atoms on the step edge are represented by orange spheres, and the other Ru atoms are represented by green spheres.

They then turn our attention to the Ru octahedral nanocage models with subsurface Pd impurities, on which the reaction energetics are also listed in Table 4.3 for comparison. Among those, the best-performing model also has both of the Pd atoms in the immediate

subsurface layer ($cage_{oct}$-$(111)_{Pd2,2}$). On $cage_{oct}$-$(111)_{Pd2,2}$, the $E_{TS} - E_{N2,gas}$ value is 0.56 eV, merely 0.03 eV lower than that on $cage_{ico}$-$edge_{Pd2,2\text{-}line}$. A comparison among the best-performing icosahedral and octahedral nanocage models ($cage_{ico}$-$edge_{Pd2,2\text{-}line}$ and $cage_{oct}$-$(111)_{Pd2,2}$, respectively), the best-performing pure Ru icosahedral model ($cage_{ico}$-(111)), and the model surfaces for conventional *hcp*-Ru nanoparticles (*hcp*-(0001)) is illustrated by the potential energy surfaces shown in Figure 4.17. The stability of the N_2 dissociation transition state is similar on the two nanocage surfaces with Pd impurities, suggesting comparable catalytic performance towards ammonia synthesis. Both types of nanocages, octahedral and icosahedral, with Pd impurities, should be more catalytically active than the conventional *hcp*-Ru nanoparticles due to the notably lower $E_{TS} - E_{N2,gas}$ values.

Overall, our DFT calculations suggest a significant role of Pd impurities in improving the catalytic activity of Ru icosahedral nanocages toward ammonia synthesis. When Pd atoms are present in the immediate subsurface layer, the twin boundary regions of Ru icosahedra can be active for N_2 dissociation due to the much stabilized transition state, which, in turn, leads to a more favorable competition with the desorption process of N_2*. They predict that the Ru icosahedral nanocage catalyst would be superior over conventional *hcp*-Ru nanoparticles for ammonia synthesis. However, in our study of *fcc*-Ru cubic nanocages using cage-(100) as the model surface, they predicted an even higher ammonia synthesis activity because of a much lower calculated $E_{TS} - E_{N2,gas}$ value of -0.05 eV [27]. As they have discussed in our previous work [28], the superiority of cubic nanocages can be attributed to the more open nature of the {100} facet, as well as a different N_2* adsorption geometry. N_2* is adsorbed on the {100} facet of the cubic nanocage with the molecule parallel to the surface through a di-σ configuration; whereas on the {111}

facet of the icosahedral/octahedral nanocages, N_2* is adsorbed vertical to the surface, and an endothermic tilting process (0.53-0.76 eV) is required before the bond-breaking event can take place, which, in turn, significantly increases the overall activation barrier.

One thing needed to be pointed out is that the Haber-Bosch process on Fe-based catalysts operates at high temperatures in excess of 400 °C [42]. However, the higher activity of *fcc* Ru icosahedral nanocages toward activating molecular nitrogen could potentially reduce the energy costs associated with the Haber-Bosch process by lowering the high temperature, and in turn, pressure, needed in the industrial process for current catalysts. Additionally, both the *fcc* structure and icosahedral shape of our Ru nanocages have been demonstrated to be stable up to 300 °C, making the Ru nanocages feasible to work as catalysts in Haber-Bosch process. To further precisely assess this potential, *in situ* characterization of our icosahedral nanocages under Haber-Bosch conditions will be needed to confirm the stability of the *fcc* Ru nanocages under temperatures and pressures necessary for ammonia synthesis. In addition to the Haber-Bosch process, the electrochemical method has recently emerged as an alternative for ammonia synthesis, which is conducted at room temperature and under ambient pressure. As a good candidate for the catalyst, the Ru nanocages will not suffer from the high temperature and pressure in the electrochemical synthesis of ammonia [45].

Currently, it is yet a challenging task in our synthesis procedure to precisely control the location of Pd impurities. Our best guess is a random distribution of Pd atoms in the as-obtained Ru icosahedral nanocages, and therefore all the local Pd configurations evaluated in the DFT study can be present in the catalyst. Our predicted best-performing surface model towards ammonia synthesis, in which the Pd atoms are located in the

immediate subsurface layer right underneath the twin boundary, likely represents an upper bound for the promotional role of Pd impurities in stabilizing the N_2* dissociation transition state. The calculation results do indicate the benefit of a more precise control of Pd impurities in improving the catalyst activity, thus raising interesting research questions and opportunities for future development of catalytic materials. For example, preferentially accumulating/depositing Pd impurities in the twin boundary region of the Pd icosahedral nanocages could potentially improve the catalytic performance towards ammonia synthesis and other catalytic processes.

4.3 Conclusion

In summary, Ru icosahedral nanocages with an *fcc* structure were successfully prepared based on a combination of seed-mediated growth and wet-chemical etching. The formation mechanism of Pd@Ru core−shell icosahedra with conformal Ru shells was well elucidated. Quantitative analysis of the reduction kinetics verifies that the presence of bromide ions was critical in guiding the layer-by-layer growth mode of Ru adatoms since the initial stage, as well as the formation of uniform Ru shells throughout the growth process. To achieve nanocages with a uniform wall thickness, both the etching time and the amount of etchant need to be precisely controlled. According to *in situ* XRD, the *fcc* structure in the Ru icosahedral nanocages could be preserved up to 300 °C. Besides, the icosahedral shape of Ru nanocages could be largely preserved at temperatures up to 300 °C. I also evaluated the shape-dependent properties of different Pd@Ru core−shell nanocrystals and Ru nanocages, demonstrating the superior performance of nanocages than their parental core−shell nanocrystals. Especially, Ru icosahedral nanocages enclosed with

twin defects on the surface displayed the most promising activity and selectivity toward both the reduction of 4-nitrophenol and the decomposition of hydrazine. Using DFT calculations, the twin boundaries of the *fcc*-Ru icosahedral nanocages with Pd impurities were also predicted to be more catalytically active than the conventional *hcp*-Ru nanoparticles towards dinitrogen dissociation (the rate-determining step in ammonia synthesis), which contribute to stabilizing the N_2 dissociation transition state and thus reducing the overall reaction barrier and the competition with the N_2 desorption process. Overall, our work provides a versatile approach to the synthesis of *fcc*-Ru icosahedral nanocages with well-retained twin structure.

4.4 Experimental Section

Chemicals and Materials. Ethylene glycol (EG, 99%) was obtained from J. T. Baker. Diethylene glycol (DEG, 99.0%), sodium tetrachloropalladate(II) (Na_2PdCl_4, 99.99%), ruthenium(III) chloride hydrate ($RuCl_3 \cdot xH_2O$, 99.99%), poly(vinylpyrrolidone) (PVP, M.W. $\approx$ 55000), L-ascorbic acid (AA, 99%), potassium bromide (KBr, 99%), hydrochloric acid (HCl, 37%), iron(III) chloride ($FeCl_3$, 97%), sodium borohydride ($NaBH_4$, 99%), 4-nitrophenol (99%), and hydrazine monohydrate ($N_2H_4 \cdot H_2O$, 98%) were all purchased from Sigma-Aldrich and used without further purification. I used deionized (DI) water, with a resistivity of 18.2 MΩ cm at room temperature, to prepare all the aqueous solutions, whose concentrations were then determined using inductively-coupled plasma mass spectrometry (ICP-MS).

Synthesis of 12-nm Pd Icosahedra. In a typical synthesis [17], 80 mg of PVP was dissolved in 2 mL of DEG and pre-heated at 130 °C under magnetic stirring. After 10 min,

1 mL of DEG solution containing Na_2PdCl_4 (15.5 mg mL^{-1}) was introduced in one shot and the reaction was allowed to proceed for 3 h. The solid products were collected by centrifugation, followed by washing once with acetone and twice with water. Finally, the Pd icosahedra were dispersed in EG for further use.

Synthesis of Pd@Ru Core−Shell Icosahedra. In a standard synthesis of the Pd@Ru core−shell icosahedra, 9 mL of EG containing 50 mg of AA, 20 mg of KBr, 100 mg of PVP, and 0.6 mg of the Pd icosahedral seeds was heated at 200 °C under magnetic stirring for 1 h. Subsequently, 20 mL of EG containing 0.6 mg of $RuCl_3 \cdot xH_2O$ was titrated into the solution at a programmable rate of 1 mL h^{-1}. After all the Ru(III) precursor solution had been added, the reaction was allowed to continue for another 2 h. Afterwards, the solid products were collected by centrifugation, washed once with acetone and twice with water, and finally dispersed in water for further use.

Preparation of Ru Icosahedral Nanocages. The Pd cores were selectively removed from the Pd@Ru core−shell icosahedra through chemical etching to obtain Ru nanocages. In a standard procedure, $FeCl_3$ (30 mg), KBr (300 mg), PVP (50 mg), and HCl (0.18 mL) were mixed in 4.82 mL of water. Then, an aqueous solution of the as-obtained core−shell icosahedra (~0.1 mg) was introduced. The mixture was transferred into an oil bath and heated at 100 °C under magnetic stirring for 1.5 h. The solid products were collected by centrifugation, washed three times with ethanol, and then dispersed in water for further characterization.

Quantitative Analysis of the Reduction Kinetics. The reduction kinetics was measured by analyzing the concentrations of unreacted Ru(III) ions remaining in the reaction solution at different time points using ICP-MS. In a standard procedure, 50 μL of

reaction solution was taken out every hour for the first six hours and last two hours, and every 2 h for the rest period of time. The aliquot was mixed with 950 μL of acetone and centrifuged to precipitate out all the nanoparticles while leave the unreacted Ru(III) ions in the supernatant, which were collected and then diluted for ICP-MS analysis. The total volume of the reaction solution was assumed to be the same during the analysis as the volume of solution taken out each time was only 50 μL and the ratio was only 1:180 (v/v) relative to the total volume of the reaction solution in the flask (9 mL at the initial stage).

Evaluation of Thermal Stability. I evaluated the thermal stability of the *fcc* structure in the Ru nanocages using *in situ* XRD. The XRD patterns were collected between 2θ = 30° and 90° by heating the sample to temperatures in the range of 100−500 °C using an Anton Paar XRK hot stage, and then processed using HighScore Plus, a software package from PANalytical. The as-synthesized Ru icosahedral nanocages were dispersed in ethanol and drop-casted on a silicon wafer prior to the XRD measurements. To avoid possible oxidation, the analysis was conducted under the protection of Ar atmosphere. Each pattern was collected for one hour to obtain sufficient signals every 50 °C, with a heating rate of 5 °C min^{-1}. Besides, I evaluated the thermal stability of the icosahedral shape of the Ru nanocages by heating the samples to different temperatures for 1 h using a thermal evaporator (Edwards E306 A). The heating process was conducted under Ar atmosphere to prevent sample oxidation, followed by cooling down to room temperature and being analyzed by TEM.

Reduction of 4-Nitrophenol by $NaBH_4$. The reaction was conducted in an aqueous system at room temperature. In a standard procedure, an aqueous suspension of a specific sample of Ru nanocrystals was diluted to 0.1 mM in terms of elemental Ru (determined by

ICP-MS). Afterwards, 1 mL of $NaBH_4$ solution (20 mM) was mixed with 1 mL of colorless 4-nitrophenol solution (0.2 mM), and the mixture immediately became yellow. After 0.5 mL of the aqueous suspension of Ru nanocrystals was quickly injected, the concentration of 4-nitrophenolate was monitored by recording its absorbance as a function of time using UV-vis spectroscopy.

Decomposition of Hydrazine. In a typical study, 0.4 mL of an aqueous suspension of the as-prepared Ru nanocrystals (0.2 mg in terms of Ru, as determined by ICP-MS) was added into a two-neck flask under magnetic stirring at room temperature, with one of the necks connected to a gas burette. After the introduction of 10 μL of N_2H_4, the produced gases were passed through 1.0 M HCl solution to ensure the complete removal of ammonia. The volume of the remaining gases was measured using a gas burette.

Characterization. All transmission electron microscopy (TEM) images were acquired using a Hitachi 7700 microscope operated at 120 kV. High-angle annular dark field scanning transmission electron microscopy (HAADF-STEM) images and energy-dispersive X-ray spectroscopy (EDX) data were acquired using an aberration-corrected Hitachi HD2700 STEM operated at 200 kV. ICP-MS (NexION 300Q, PerkinElmer) was used for the quantitative analysis of Ru(III) ions remaining in the reaction solution. X-ray diffraction (XRD) patterns were obtained with a PANalytical X'Pert PRO Alpha-1 diffractometer using 1.8 kW Ceramic Copper tube source. UV-Vis absorption spectra were measured using a UV-vis-NIR spectrometer (Lambda 750, PerkinElmer).

DFT Calculations. Periodic DFT calculations were performed using the generalized gradient approximation (GGA-PW91) to describe the exchange-correlation functional, and the projector augmented-wave (PAW) potentials to describe the electron-ion interactions,

as implemented in the Vienna *ab initio* simulation package (VASP) code[46–50]. The Kohn-Sham electron wave function was expanded in a plane wave basis set, with a kinetic energy cutoff of 400 eV. My collaborators calculated the reaction energetics of N_2 dissociation on a number of slab models of *fcc* Ru. In all calculations, successive images in the *z*-direction were separated by at least 13 Å of vacuum, to avoid unphysical inter-image interactions in that direction. In agreement with previous theoretical calculations on *fcc* Ru [51], spin polarization did not affect the computed total energies for our slab models, with and without adsorbates. Therefore, they present our results here with no spin polarization taken into account. Adsorption was allowed on only one of the exposed surfaces of the slab models, and dipole moment corrections were added to the computed total energies. They define the binding energy (BE) of a species as:

$$BE = E_{slab+species} - E_{slab} - E_{species}$$

where, $E_{slab+species}$ is the total energy of the slab with the species adsorbed on one of its surfaces, E_{slab} is the total energy of the slab with no adsorbates, and $E_{species}$ is the total energy of the species at infinite separation from the slab. This way, more negative BE indicates stronger adsorption. The activation energy barriers associated with the minimum energy path for N_2 dissociation to atomic N were calculated using the climbing image nudged elastic band (CI-NEB) method [52], with seven interpolated images between the initial and final states. They converged each image to less than 0.1 eV/Å of Hellmann-Feynman interatomic forces. Transition states were verified by a single imaginary frequency as obtained by vibrational frequency calculations. These were conducted using the harmonic oscillator approximation, with a step size of 0.015 Å for the second-order numerical differentiation of forces.

Table 4.4. Convergence of the BE of N versus unit cell size for octahedral nanocages. Each entry in the third column displays the difference in BE between the corresponding unit cell size and the (smaller) size preceding it.

Unit cell size	BE (eV)	BE difference (eV)
(2×2)	-6.02	
(4×2)	-6.14	-0.13
(6×2)	-6.18	-0.04
(8×2)	-6.17	0.02

They constructed an icosahedron model that explicitly includes a twin boundary enclosed by two surfaces exposing the {111} facets. This model agrees with the structure of atomic stacking as first reported by Mackay [53]. A graphical representation of the model is shown in Figure 4.16. Here they used a five-layer (1×2) unit cell, and each {111} terrace of the model consisted of six atomic rows. Due to the hollow, free-standing nature of the nanocages, the lattice constants for the model slabs were optimized with all atoms allowed to fully relax. The computed average interatomic distance for the icosahedral twin boundary model is 2.687 Å. However, as summarized in Figure 4.16a, they observed alternating compressive/expansive strain between adjacent rows of surface atoms. In the optimized structure, the angle between the two {111} facets joined by the twin boundary is 138.1°. The Brillouin zone of the (1×2) unit cell of the icosahedral twin boundary model was sampled with a 1×6×1 Monkhorst-Pack *k*-point mesh [54].

They compared the estimated activity of Ru icosahedral nanocages to that of Ru octahedral nanocages toward ammonia synthesis [41–44, 52]. To reliably compare their estimated activities at similar surface coverages, they could not rely on our previous results

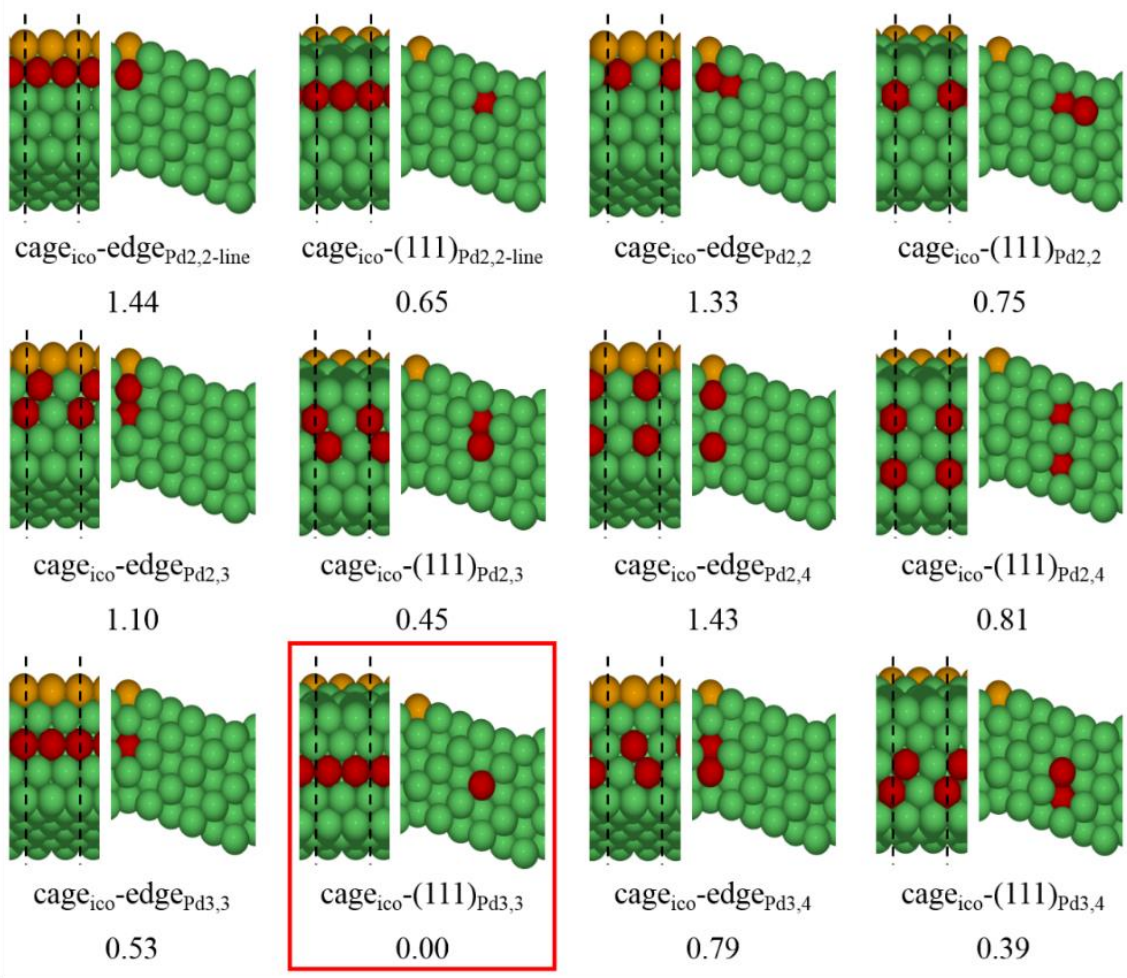

Figure 4.18. All Ru icosahedral (*fcc*) nanocage models with Pd impurities studied. Side views showing the atomic planes parallel (left, black dash lines indicate the unit cell) and perpendicular (right) to the twin boundary are presented. Numbers below each inset indicate the relative stability (in eV) of each model with respect to the most stable one (indicated by the red box). Regarding the surface nomenclature, 'edge' indicates that the Pd impurities are placed right underneath the step edge; '(111)' indicates that the Pd impurities are placed underneath the {111} terrace. Subscript Pd2,2 represents a surface with two contiguous Pd atoms in the second layer from the top. Subscript Pd2,2-line represents a surface with two contiguous Pd atoms in the second layer from the top, arranged in such a way as to give a continuous row of Pd atoms periodically. Subscript Pd2,3 represents a surface with two contiguous Pd atoms, one in the second layer and the other in the third layer from the top. Subscript Pd2,4 represents a surface with one Pd atom in the second layer and one Pd atom in the fourth layer from the top. Subscript Pd3,3 represents a surface with two contiguous Pd atoms in the third layer from the top. Subscript Pd3,4 represents a surface with two contiguous Pd atoms, one in the third layer and the other in the fourth layer from the top. Adsorption takes place on the top layer. Orange spheres represent the surface Ru atoms at the top of the step edge; the other Ru atoms are represented by green spheres. Pd atoms are represented by red spheres.

on the octahedral nanocages [28], since those were performed on a (2×2) unit cell, featuring a much higher coverage of intermediates (0.25 ML) than the coverage displayed on our model for the icosahedron. They compared the BE of atomic N on several unit cell sizes of the five-layer octahedral nanocage model and found that the BE did not change much (i.e., <0.10 eV) on unit cells larger than (4×2), as indicated in Table 4.4. Therefore, they chose a (4×2) unit cell to represent octahedral nanocages that would yield reliably comparable results to those of the icosahedral twin boundary model. Same as the icosahedral model, the lattice constants for these model slabs were optimized with all atoms allowed to fully relax. The computed interatomic distance for the five-layered pure Ru *fcc* nanocages was 2.687 Å for the (2×2) unit cell, and 2.686 Å for all other unit cell sizes. The Brillouin zone of the (4×2) unit cell was sampled with a 2×6×1 Monkhorst-Pack *k*-point mesh [54]. For comparison purposes, they also performed calculations on (4×2) unit cells of four-layered *hcp*-(0001) slab model, in which the bottom two layers were fixed, and the top two (together with the adsorbates) were allowed to fully relax. This model would represent Ru nanoparticles (as opposed to nanocages) with the conventional *hcp* structure. Our calculated lattice constants for bulk *hcp* Ru were a=2.729 Å and c/a=1.577, in good agreement with experimental data (a=2.706 Å and c/a=1.582) [55].

They investigated the effect of Pd impurities by probing the local effect of two Pd atoms in the subsurface layers, assuming that no Pd atoms would remain in the exterior layers after etching. Unlike our past studies, here they did not seek to model an accurate percentage of the Pd impurity. Doing so would be extremely costly, given the large models they were using for this work and the many combinations that several Pd atoms might take. Instead, they probed the local effect of Pd by substituting two interior Ru atoms with Pd

atoms. Figures 4.18 and 4.19 depict the different configurations they have evaluated for the Pd impurity in our icosahedral and octahedral models, respectively. The wide span of relative energies of these models indicates good sampling of different scenarios for the Pd impurity configuration.

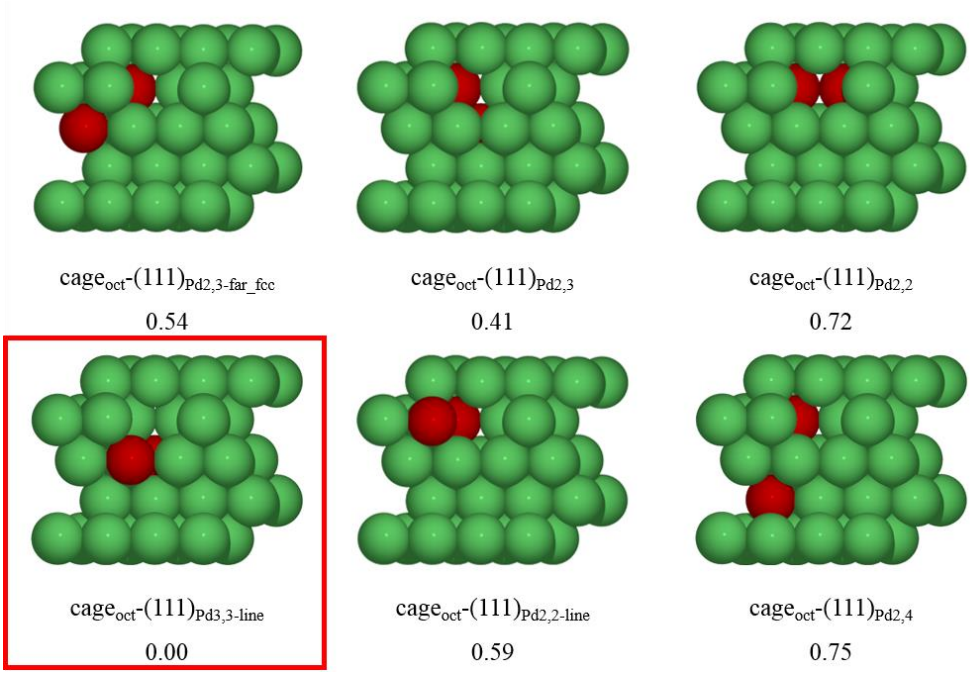

Figure 4.19. All Ru octahedral nanocage (*fcc*) models with Pd impurities studied. Numbers below each inset indicate the relative stability (in eV) of each model with respect to the most stable one (indicated by the red box). cage$_{oct}$-(111)$_{Pd2,3\text{-far\_fcc}}$ represents a surface with one Pd atom in the second layer from the top and one Pd atom in the third layer from the top, arranged so as to yield a Pd *fcc* hollow site that is not adjacent to the Pd *hcp* hollow site. cage$_{oct}$-(111)$_{Pd2,3}$ represents a surface with one Pd atom in the second layer from the top and one Pd atom in the third layer from the top, arranged so as to yield two adjacent Pd hollow sites. cage$_{oct}$-(111)$_{Pd2,2}$ represents a surface with two contiguous Pd atoms in the second layer from the top. cage$_{oct}$-(111)$_{Pd3,3\text{-line}}$ represents a surface with two contiguous Pd atoms in the third layer from the top, arranged in such a way as to give a continuous row of Pd atoms periodically. cage$_{oct}$-(111)$_{Pd2,2\text{-line}}$ represents a surface with two contiguous Pd atoms in the second layer from the top, arranged in such a way as to give a continuous row of Pd atoms periodically. Finally, cage$_{oct}$-(111)$_{Pd2,4}$ represents a surface with one Pd atom in the second layer from the top and one Pd atom in the fourth layer from the top. Adsorption takes place on the top layer. Ru and Pd atoms are represented by green and red spheres, respectively.

4.5 Notes to Chapter 4

Part of this chapter is adapted from the paper “Synthesis of Ru Icosahedral Nanocages with a Face-Centered-Cubic Structure and Evaluation of Their Catalytic Properties” published in *ACS Catalysis* [56].

4.6 References

[1] Peng, Z.; Yang, H. *Nano Today* **2009**, *4*, 143–164.

[2] Xia, Y.; Yang, X. *Acc. Chem. Res.* **2017**, *50*, 450–454.

[3] Rycenga, M.; Cobley, C. M.; Zeng, J.; Li, W.; Moran, C. H.; Zhang, Q.; Qin, D.; Xia, Y. *Chem. Rev.* **2011**, *111*, 3669–3721.

[4] Camden, J. P.; Dieringer, J. A.; Zhao, J.; Van Duyne, R. P. *Acc. Chem. Res.* **2008**, *41*, 1653–1661.

[5] Jain, P. K.; Huang, X.; El-Sayed, I. H.; El-Sayed, M. A. *Acc. Chem. Res.* **2008**, *41*, 1578–1586.

[6] Yang, X.; Yang, M.; Pang, B.; Vara, M.; Xia, Y. *Chem. Rev.* **2015**, *115*, 10410–10488.

[7] Xia, Y.; Xiong, Y.; Lim, B.; Skrabalak, S. E. *Angew. Chem. Int. Ed.* **2009**, *48*, 60–103.

[8] Wiley, B.; Sun, Y.; Xia, Y. *Acc. Chem. Res.* **2007**, *40*, 1067–1076.

[9] Xie, S.; Liu, X. Y.; Xia, Y. *Nano Res.* **2015**, *8*, 82–96.

[10] Grzelczak, M.; Perez-Juste, H.; Mulvaney, P.; Liz-Marzan, L. M. *Chem. Soc. Rev.* **2008**, *37*, 1783–1791.

[11] Tao, A. R.; Habas, S.; Yang, P. *Small* **2008**, *4*, 310–325.

[12] Wang, H.; Zhou, S.; Gilroy, K. D.; Cai, Z.; Xia, Y. *Nano Today* **2017**, *15*, 121–144.

[13] Choi, S.; Herron, J. A.; Scaranto, J.; Huang, H.; Wang, Y.; Xia, X.; Lv, T.; Park, J.; Peng, H. C.; Mavrikakis, M.; Xia, Y. *ChemCatChem* **2015**, *7*, 2077–2084.

[14] Zhou, W.; Wu, J.; Yang, H. *Nano Lett.* **2013**, *13*, 2870–2874.

[15] Kuai, L.; Geng, B.; Wang, S.; Zhao, Y.; Luo, Y.; Jiang, H. *Chem. Eur. J.* **2011**, *17*, 3482–3489.

[16] Xia, Y.; Gilroy, K. D.; Peng, H. C.; Xia, X. *Angew. Chem. Int. Ed.* **2016**, *55*, 2–38.

[17] Wang, X.; Figueroa-Cosme, L.; Yang, X.; Luo, M.; Liu, J.; Xie, Z.; Xia, Y. *Nano Lett.* **2016**, *16*, 1467–1471.

[18] Kitano, M.; Inoue, Y.; Yamazaki, Y.; Hayashi, F.; Kanbara, S.; Matsuishi, S.; Yokoyama, T.; Kim, S. W.; Hara, M.; Hosono, H. *Nat. Chem.* **2012**, *4*, 934–940.

[19] Kitano, M.; Kanbara, S.; Inoue, Y.; Kuganathan, N.; Sushko, P. V.; Yokoyama, T.; Hara, M.; Hosono, H. *Nat. Commun.* **2015**, *6*, 1–9.

[20] Li, W.; Liu, J.; Gu, J.; Zhou, W.; Yao, S.; Guo, Y.; Su, H.; Yan, C.; Li, W.; Zhang, Y.; Ma, D. *J. Am. Chem. Soc.* **2017**, *139*, 2267–2276.

[21] Ostrom, H.; Oberg, H.; Xin, H.; LaRue, J.; Beye, M.; Dell'Angela, M.; Gladh, J.; Ng, M. L.; Sellberg, J. A.; Kaya, S.; Mercurio, G.; Nordlund, D.; Hantschmann, M.; Hieke, F.; Kuhn, D.; Schlotter, W. F.; Dakovski, G. L.; Turner, J. J.; Minitti, M. P.; Mitra, A.; Moeller, S. P.; Fohlisch, A.; Wolf, M.; Wurth, W.; Persson, M.; Norskov, J. K.; Ablid-Pedersen, F.; Ogasawara, H.; Pettersson, L. G. M.; Nilsson, A. *Science* **2015**, *347*, 978–982.

[22] Yin, A.; Liu, W.; Ke, J.; Zhu, W.; Gu, J.; Zhang, Y.; Yan, C. *J. Am. Chem. Soc.* **2012**, *134*, 20479–20489.

[23] Watt, J.; Yu, C.; Chang, L. Y.; Cheong, S.; Tilley, R. D. *J. Am. Chem. Soc.* **2013**, *135*, 606–609.

[24] Fan, Z.; Zhang, H. *Acc. Chem. Res.* **2016**, *49*, 2841–2850.

[25] Kusada, K.; Kobayashi, H.; Yamamoto, T.; Matsumura, S.; Sumi, N.; Sato, K.; Nagaoka, K. Kubota, Y.; Kitagawa, H. *J. Am. Chem. Soc.* **2013**, *135*, 5493–5496.

[26] Ye, H.; Wang, Q.; Catalano, M.; Lu, N.; Vermeylen, J.; Kim, J. M.; Liu, Y.; Sun, Y.; Xia, X. *Nano Lett*. **2016**, *16*, 2812–2817.

[27] Zhao, M.; Figueroa-Cosme, L.; Elnabawy, A. O.; Vara, M.; Yang, X.; Roling, L. T.; Chi, M.; Mavrikakis, M.; Xia, Y. *Nano Lett.* **2016**, *16*, 5310–5317.

[28] Zhao, M.; Elnabawy, A. O.; Vara, M.; Xu, L.; Hood, Z. D.; Yang, X.; Gilroy, K. D.; Figueroa-Cosme, L.; Chi, M.; Mavrikakis, M.; Xia, Y. *Chem. Mater.* **2017**, *29*, 9227–9237.

[29] Xie, S.; Lu, N.; Xie, Z.; Wang, J.; Kim, M. J.; Xia, Y. *Angew. Chem. Int. Ed.* **2012**, *51*, 10266–10270.

[30] Xia, X.; Xie, S.; Liu, M.; Peng, H.; Lu, N.; Wang, J.; Kim, M. J.; Xia, Y. *Proc. Natl. Acad. Sci. U.S.A.* **2013**, *110*, 6669–6673.

[31] Peng, H.; Park, J.; Zhang, L.; Xia, Y. *J. Am. Chem. Soc.* **2015**, *137*, 6643–6652.

[32] Gu, J.; Guo, Y.; Jiang, Y.; Zhu, W.; Xu, Y.; Zhao, Z.; Liu, J.; Li, W.; Jin, C.; Yan, C.; Zhang, Y. *J. Phys. Chem. C* **2015**, *119*, 17697–17706.

[33] Zhang, L.; Roling, L. T.; Wang, X.; Vara, M.; Chi, M.; Liu, J.; Choi, S.; Park, J.; Herron, J. A.; Xie, Z.; Mavrikakis, M.; Xia, Y. *Science* **2015**, *349*, 412–416.

[34] Zhang, Z.; Liu, Y.; Chen, B.; Gong, Y.; Gu, L.; Fan, Z.; Yang, N.; Lai, Z.; Chen, Y.; Wang, J.; Huang, Y.; Sindoro, M.; Niu, W.; Li, B.; Zong, Y.; Yang, Y.; Huang, X.; Huo, F.; Huang, W.; Zhang, H. *Adv. Mater.* **2016**, *28*, 10282–20286.

[35] Fan, Z.; Chen, Y.; Zhu, Y.; Wang, J.; Li, B.; Zong, Y.; Han, Y.; Zhang, H. *Chem. Sci.* **2017**, *8*, 795−799.

[36] Fan, Z.; Zhang, H. *Chem. Soc. Rev.* **2016**, *45*, 63−82.

[37] Herves, P.; Perez-Lorenzo, M.; Liz-Marzan, L. M.; Dzubiella, J.; Lu, Y.; Ballauff, M. *Chem. Soc. Rev.* **2012**, *41*, 5577–5587.

[38] Wu, J.; Qi, L.; You, H.; Gross, A.; Li, J.; Yang, H. *J. Am. Chem. Soc.* **2012**, *134*, 11880–11883.

[39] Sneed, B. T.; Young, A. P.; Tsung, C. *Nanoscale* **2015**, *7*, 12248–12265.

[40] Singh, S. K.; Zhang, X.; Xu, Q. *J. Am. Chem. Soc.* **2009**, *131*, 9894–9895.

[41] Rod, T. H.; Logadottir, A.; Nørskov, J. K. A *J. Chem. Phys.* **2000**, *112*, 5343–5347.

[42] Vojvodic, A.; Medford, A. J.; Studt, F.; Pedersen, F. A.; Khan, T. S.; Bligaard, T.; Nørskov, J. K. *Chem. Phys. Lett.* **2014**, *598*, 108–112.

[43] Logadottir, A.; Rod, T. H.; Nørskov, J. K.; Hammer, B.; Dahl, S.; Jacobsen, C. J. H. *J. Catal.* **2001**, *197*, 229–231.

[44] Dahl, S.; Sehested, J.; Jacobsen, C. J. H.; Törnqvist, E.; Chorkendorff, I. *J. Catal.* **2000**, *192*, 391–399.

[45] Guo, C.; Ran, J.; Vasileff, A.; Qiao, S. *Energy Environ. Sci.* **2018**, *11*, 45–56.

[46] Perdew, J. P.; Wang, Y. *Phys. Rev. B* **1992**, *45*, 13244–13249.

[47] Blöchl, P. E. *Phys. Rev. B* **1994**, *50*, 17953–17579.

[48] Kresse, G.; Joubert, D. *Phys. Rev. B* **1999**, *59*, 1758–1775.

[49] Kresse, G.; Furthmüller, J. *Phys. Rev. B* **1996**, *54*, 11169–11186.

[50] Kresse, G.; Furthmüller, J. *Comp. Mater. Sci.* **1996**, *6*, 15–50.

[51] Kobayashi, M.; Kai, T.; Takano, N.; Shiiki, K. *J. Phys.: Condens. Matter* **1995**, *7*, 1835–1842.

[52] Henkelman, G.; Uberuaga, B. P.; Jónsson, H. *J. Chem. Phys.* **2000**, *113*, 9901–9904.

[53] Mackay, A. L. *Acta Cryst.* **1962**, *15*, 916–918.

[54] Monkhorst, H. J.; Pack, J. P. *Phys. Rev. B* **1976**, *13*, 5188–5192.

[55] Lide, D. R. *CRC Handbook of Chemistry and Physics*, 96th ed.; CRC Press: Boca Raton, FL, **2015**.

[56] Zhao, M.; Xu, L.; Vara, M.; Elnabawy, A. O.; Gilroy, K. D.; Hood, Z. D.; Zhou, S.; Figueroa-Cosme, L.; Chi, M.; Mavrikakis, M.; Xia, Y. *ACS Catal.* **2018**, *8*, 6948–6960.

CHAPTER 5

RUTHENIUM OCTAHEDRAL NANOCRYSTALS WITH A FACE-CENTERED CUBIC STRUCTURE, {111} FACETS, THERMAL STABILITY UP TO 400 °C AND ENHANCED CATALYTIC ACTIVITY

5.1 Introduction

Ruthenium (Ru) nanocrystals have received considerable attention as a class of catalytic materials owing to their pivotal role in an array of applications that include ammonia synthesis, Fischer–Tropsch synthesis, CO oxidation, and water splitting, as well as fabrication of Li-CO_2 batteries and supercapacitors [1–8]. Like many other noble metals, engineering the shape (and thus surface structure) of Ru nanocrystals has recently emerged as a powerful and versatile route to the optimization of their catalytic properties toward various reactions as the nature of active sites and thereby the energetics of a catalytic reaction is ultimately determined by the exposed facets [9–11]. Additionally, since the discovery of face-centered cubic (*fcc*) Ru, controlling the crystal structure (or phase) of Ru nanocrystals has become an effective strategy for pushing the properties typically associated with the hexagonal close-packed (*hcp*) Ru to new limits [12–17]. Taken together, with a tight control over both the shape and crystal structure of Ru nanocrystals, one should be able to optimize their performance toward various catalytic applications [18–21]. However, owing to the high cohesive and specific surface free energies of Ru and the intrinsic preference of *hcp* structure by Ru solid, it has been a long-lasting challenge to synthesize Ru nanocrystals in an *fcc* structure and with controllable shapes [22, 23].

Seed-mediated growth offers great capability and versatility in controlling the synthesis of Ru nanocrystals [24,25]. With the use of well-defined seeds, one can replicate both the exposed facets and crystal structure of the underlying seeds for a second metal of interest [26]. To this end, our group reported a facile approach to the synthesis of Pd@Ru core–shell nanocrystals with a cubic, octahedral, or icosahedral shape by conformally depositing Ru overlayers that were a few (up to 5) atomic layers thick on Pd nanocubes, octahedra, or icosahedra, respectively. Most interestingly, the Ru atoms in the walls took the *fcc* structure of the seeds rather than the *hcp* structure associated with bulk Ru [27–29]. Density functional theory (DFT) calculations suggested that the {100} and {111} facets, as well as twin boundaries, on *fcc*-Ru nanocrystals were more effective than the surface of conventional *hcp*-Ru nanoparticles in reducing the activation energy barrier to N-N dissociation, the rate-determining step in ammonia synthesis [27–29]. Despite the success, the synthesis is plagued by several drawbacks. In order to generate a conformal shell for the Pd@Ru core–shell octahedra and icosahedra, Br^- ions had to be used to slow down the reduction kinetics of Ru(III) ions and thus ensure layer-by-layer growth for the Ru atoms. In this case, the Pd seeds are vulnerable to oxidative etching by Br^- ions and the resultant $PdBr_4^-$ can also be reduced and incorporated into the Ru walls, giving rise to an alloy composition [30,31]. One potential solution to this problem is to work with seeds that are resistant to oxidative etching under harsh growth conditions. Another issue lies in the thermal stability of the ultrathin and porous Ru walls that were vulnerable to deformation in response to thermal stress. They tended to lose their shapes and *fcc* structure when heated to about 300 °C [28, 29, 32]. The compromised thermal stability would limit the use of the *fcc*-Ru nanocages in various reactions that are conducted at elevated temperatures. One

strategy to improve the thermal stability is to grow a thicker Ru shell on the seed. Unfortunately, the deposition of Ru atoms would be switched to an island growth mode after reaching five atomic layers owing to the weakened template effect of the seed and/or the inadequate surface diffusion. As a result, the product took a rough surface and the Ru atoms were crystallized in a *hcp* lattice [27, 28]. To address this issue, the seeds should have a size small enough to ensure adequate surface diffusion during the deposition of Ru atoms.

Herein, with the use of 4.5-nm Rh cubes as the seeds, I develop a facile approach to the synthesis of Ru octahedral nanocrystals. The small size of the Rh seeds, the resistance of Rh to oxidative etching, and the small lattice mismatch between Rh and Ru (0.5%, 3.80 *vs.* 3.82 Å) were all instrumental to the formation of a smooth surface for the Ru nanocrystals. Different from the reported Pd@Ru core–shell octahedra associated with the replication of the surface structure of Pd octahedral seeds [28], the current system involved a shape transformation from cube to octahedra. In particular, the Ru shell in the present work was about 4.5 nm in thickness, much greater than that (around 1.1 nm) of the Pd@Ru core–shell octahedra [28]. Significantly, the Ru atoms in the octahedral nanocrystals still followed *fcc* packing rather than the conventional *hcp* lattice found in bulk Ru. When subjected to a thermal stress, both the octahedral shape and the *fcc* structure can be well preserved up to 400 °C. When benchmarked against *hcp*- and *fcc*-Ru nanoparticles, the *fcc*-Ru octahedral nanocrystals exhibit enhanced specific activity toward oxygen evolution reaction (OER). Additionally, the {111} facets on Ru nanocrystals were also shown to be more active than the {100} facets in catalyzing OER.

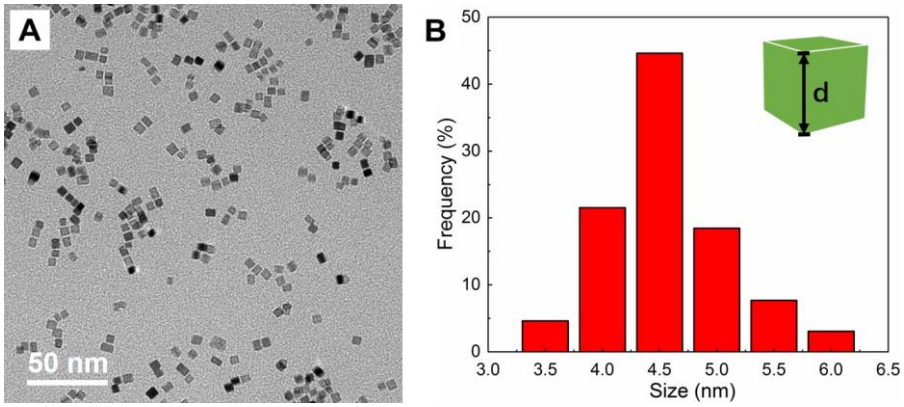

Figure 5.1. (A) TEM image of the Rh nanocubes served as seeds for the standard synthesis. (B) Size distribution of the as-synthesized Rh nanocubes, indicating an average size of 4.5±1.5 nm. The inset shows a schematic of the Rh nanocube, together with the definition of size.

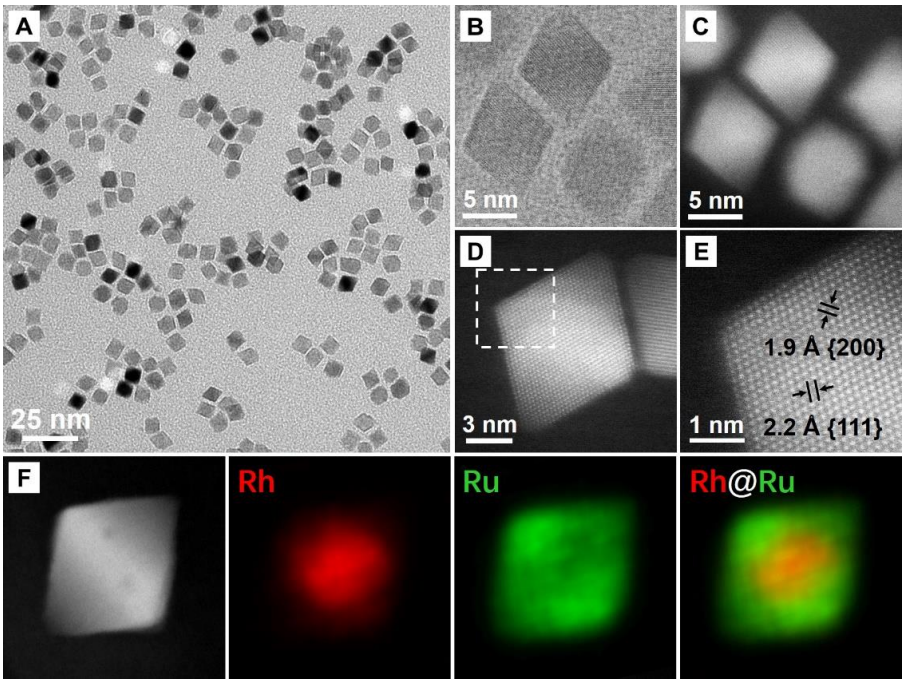

Figure 5.2. (A) TEM image of the Ru octahedral nanocrystals prepared using the standard synthesis. (B) HAABF- and (C) HAADF-STEM images of several Ru octahedral nanocrystals. (D) HAADF-STEM image of an individual Ru octahedron. (E) Atomic-resolution STEM image taken from the corner region of the Ru octahedron, marked by a box in panel (D). (F) HAADF-STEM image and EDX mapping (Rh/red, Ru/green) of an individual octahedron.

5.2 Results and Discussion

The synthesis started with the preparation of Rh nanocubes that had well-defined {100} facets and an average size of 4.5±1.5 nm (Figure 5.1) [33, 34]. The Rh nanocubes were mixed with HCHO, PVP, and $RuCl_3$, and then transferred into a Teflon-lined stainless-steel autoclave, followed by heating for 6 h at 200 °C. Figure 5.2A shows a TEM image of the nanocrystals prepared using the standard protocol, revealing an octahedral shape with well-defined {111} facets and a uniform size distribution. Figure 5.2, B and C, shows HAABF- and HAADF-STEM images of the Ru octahedral nanocrystals, respectively. For the atomic-resolution STEM image recorded on an individual nanocrystal (Figure 5.2, D and E), the lattice fringe spacing of 1.9 and 2.2 Å could be assigned to the {200} and {111} planes of *fcc* Ru, respectively. The *fcc* structure of the Ru component was also confirmed by XRD analysis. Figure 5.2F shows EDX mapping of Rh and Ru, revealing the spatial distributions of these two elements. Based on the mapping data, Rh atoms were mainly confined to the core while Ru atoms were primarily distributed across the whole nanocrystal, pointing to a core–shell structure. The elemental composition of the nanocrystals was also analyzed by ICP-MS, and a Ru/Rh atomic ratio of 3.2:1 was obtained.

Figure 5.3 shows the XPS spectra recorded from the Rh cubic seeds and the as-synthesized Ru nanocrystals. After the deposition of Ru, the binding energies of Rh $3d_{3/2}$ and Rh $3d_{5/2}$ changed from 312.10 and 307.37 eV for the Rh cubic seeds to 311.99 and 307.26 eV for the Ru nanocrystals, respectively, suggesting a down shift of 0.11 eV (Figure 5.3, A and B). The variation in binding energies could be attributed to the changes in electronic property for Rh arising from the coating of Ru [18]. With respect to the Ru 3d spectrum, the binding energies of Ru $3d_{3/2}$ and Ru $3d_{5/2}$ were determined as 284.22 and

280.04 eV, respectively, verifying the presence of metallic Ru in the resultant nanocrystals (Figure 5.3C). Figure 5.3D shows the XPS spectrum of Ru $3p_{3/2}$ peak, which was positioned at 461.48 eV, further confirming the metallic nature of Ru in the products [18].

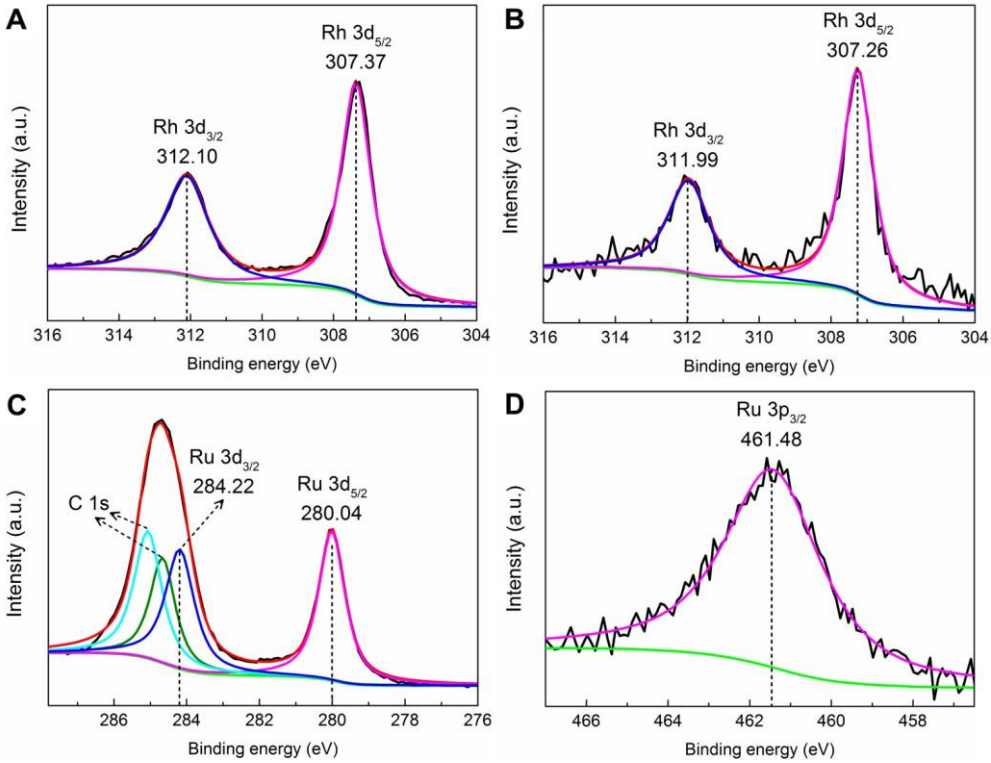

Figure 5.3. (A) Rh 3d XPS spectrum of the Rh nanocubes that served as the seeds. (B) Rh 3d, (C) Ru 3d, and (D) Ru 3p XPS spectra of the Ru octahedral nanocrystals prepared using the standard protocol. The sample for XPS analysis was deposited on a glass slide and the carbon came from the surfactants adsorbed on the nanocrystals. Note that the C 1s and Ru $3d_{3/2}$ peaks are partially overlapped at binding energies in the range of 283–286 eV.

To gain a mechanistic understanding of the formation of Ru octahedral nanocrystals, I conducted a set of control experiments. Figure 5.4 shows TEM images of the Ru nanocrystals collected at different stages of a standard synthesis. In the initial stage (Figure

5.4A, *t* = 1 h), the products still had a cubic shape, enclosed by well-defined {100} facets. Based on the ICP-MS data, the weight percentage of Ru was 11.4%, corresponding to a Ru coating of only one atomic layer in thickness. When the reaction time was extended to 2 h, truncated nanocubes became prevalent in the products, indicating preferential deposition of Ru atoms on the {100} facets (Figure 5.4B). The weight percentage of Ru was also increased to 42.1%. As the reaction time was extended to 3 h and further to 4 h, the products were dominated by cuboctahedral and truncated octahedral nanocrystals (Figure 5.4, C and D), and the weight percentages of Ru were increased to 60.5% and 71.8%, respectively. Taken together, due to the continuous deposition of Ru atoms on {100} facets, Rh cubic seeds were gradually transformed into truncated cubes, cuboctahedra, truncated octahedra, and eventually, octahedra encased by well-defined {111} facets.

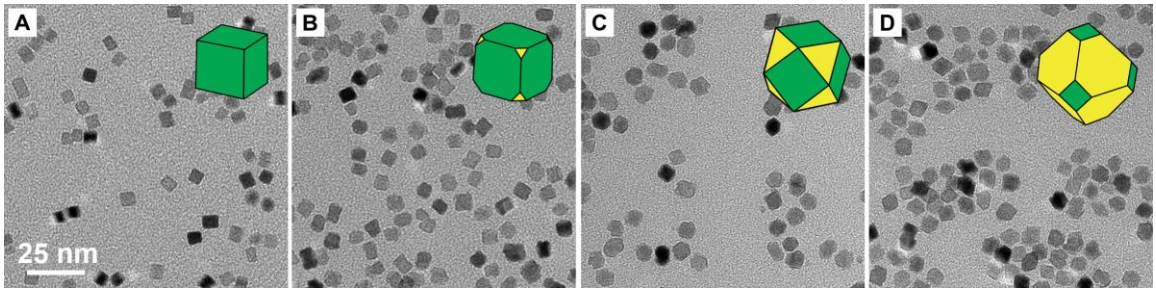

Figure 5.4. TEM images of the Ru nanocrystals collected at different stages of a standard synthesis: (A) 1, (B) 2, (C) 3, and (D) 4 h. The schematic in the inset indicates the shape taken by the nanocrystals in each sample, where the {100} and {111} facets are marked by green and yellow colors, respectively. The scale bar in panel (A) applies to panel (A–D).

In the present synthesis, the use of appropriate seeds is key to the formation of well-controlled nanocrystals. When the synthesis was conducted in the absence of Rh cubic seeds, the products were dominated by irregular nanoparticles, confirming the versatility

of Rh seeds in directing the evolution of shape. When the amount of Ru(III) precursor was fixed, the amount of seeds was also found to be critical to the formation of well-defined octahedral nanocrystals. When the amount of Rh cubic seeds was reduced to 0.25 mg, the as-synthesized nanocrystals were composed of nanoplates and irregular nanoparticles formed *via* homogeneous nucleation, in addition to octahedral nanocrystals (Figure 5.5A). If the amount of Rh seeds was increased to 1 mg, the solid products contained a mix of cuboctahedral and truncated octahedral nanocrystals (Figure 5.5B). If I further increased the amount of Rh seeds to 2 and 3 mg, the Ru atoms derived from the fixed amount of precursor would be insufficient for the formation of Ru octahedral nanocrystals, leading to the production of cuboctahedra and truncated cubes, respectively (Figure 5.5, C and D).

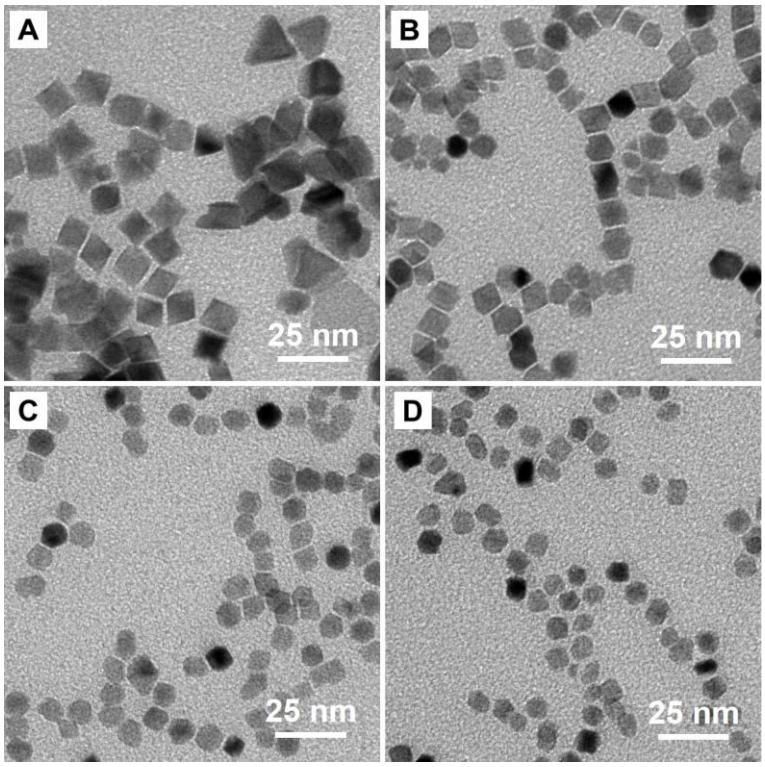

Figure 5.5. TEM images of the Ru nanocrystals prepared using the standard protocol except using different amounts of Rh cubic seeds: (A) 0.25, (B) 1, (C) 2, and (D) 3 mg.

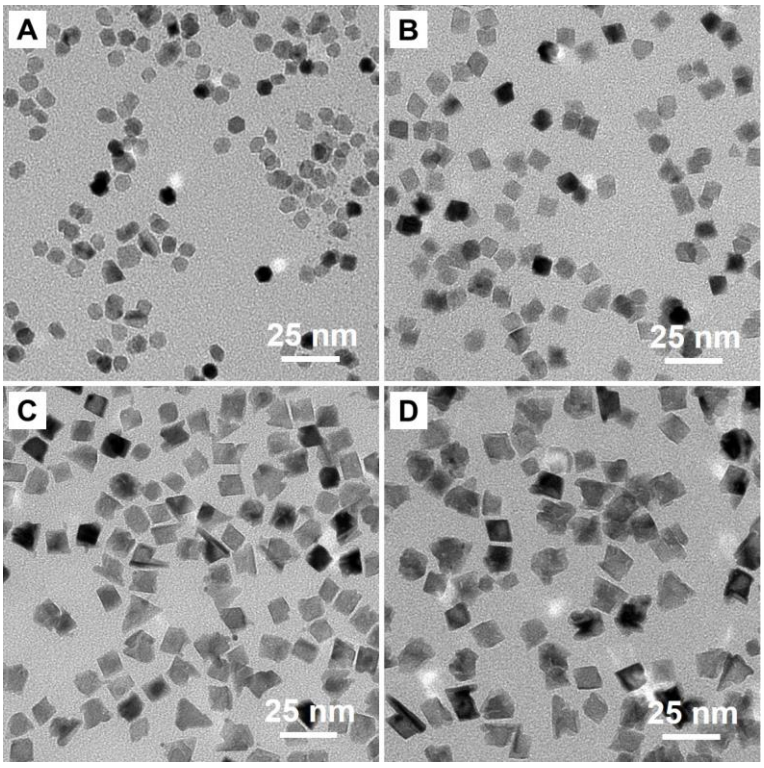

Figure 5.6. TEM images of the Ru nanocrystals prepared using the standard protocol except using different amounts of Ru(III) precursor: (A) 1, (B) 2, (C) 6, and (D) 10 mg.

To achieve high quality and uniformity for the Ru octahedral nanocrystals, I have to ensure preferential surface diffusion over the deposition of Ru atoms [35]. Since the amount of the Ru(III) precursor was strongly associated with the generation rate and thus the deposition rate of Ru atoms, I also examined its role in the formation of Ru octahedral nanocrystals. Figure 5.6A shows a TEM image of the Ru nanocrystals prepared using the standard protocol except for the involvement of 1 mg of Ru(III) precursor, indicating a mix of truncated cubes and cuboctahedra. When the amount of Ru(III) precursor was increased to 2 mg, the solid products mainly contained cuboctahedral and truncated octahedral nanocrystals (Figure 5.6B). In contrast, if I increased the amount of Ru(III) precursor to 6 mg, the solid products contained nanoplates and irregular nanoparticles, in addition to

octahedral nanocrystals, which was indicative of homogeneous nucleation (Figure 5.6C). When the amount of Ru(III) precursor was further increased to 10 mg, the proportion of irregular nanoparticles also increased accordingly (Figure 5.6D).

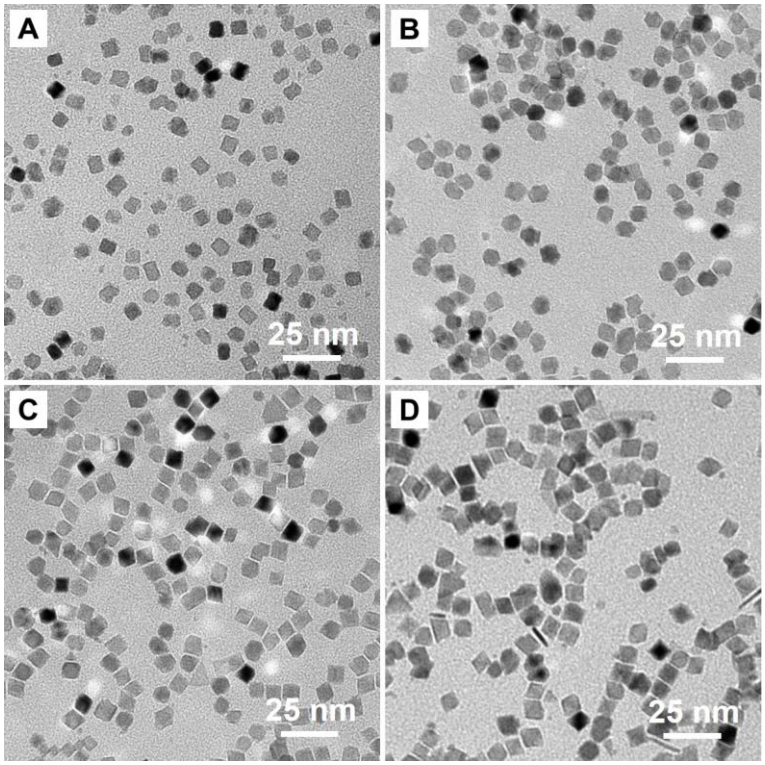

Figure 5.7. TEM image of the Ru nanocrystals prepared using the standard protocol except for the introduction of different volumes of HCHO: (A) 0, (B) 0.4, (C) 1, and (D) 4 mL.

In general, the deposition rate was dependent on the reducing power of the reductant [36], which can be adjusted by varying the volume of HCHO. When the synthesis was conducted in the absence of HCHO, the products were dominated by cubes and truncated cubes (Figure 5.7A). The slight growth of seeds could be attributed to the reduction of

Ru(III) precursor by PVP, which has been demonstrated for use as a mild reductant owing to the presence of hydroxyl end groups [37]. When the volume of HCHO was increased to 0.4 mL, a majority of the product was cuboctahedral nanocrystals (Figure 5.7B). If the synthesis was conducted with 1 mL of HCHO, truncated octahedral nanocrystals were observed as the predominant products, showing well-defined {111} facets and truncated corners (Figure 5.7C). In contrast, when 4 mL of HCHO was introduced into the synthesis, the reduction of Ru(III) precursor was substantially promoted owing to the enhanced reducing power, giving rise to a mix of nanoplates, nanowires, and irregular nanocrystals formed through homogeneous nucleation, in addition to octahedral nanocrystals (Figure 5.7D).

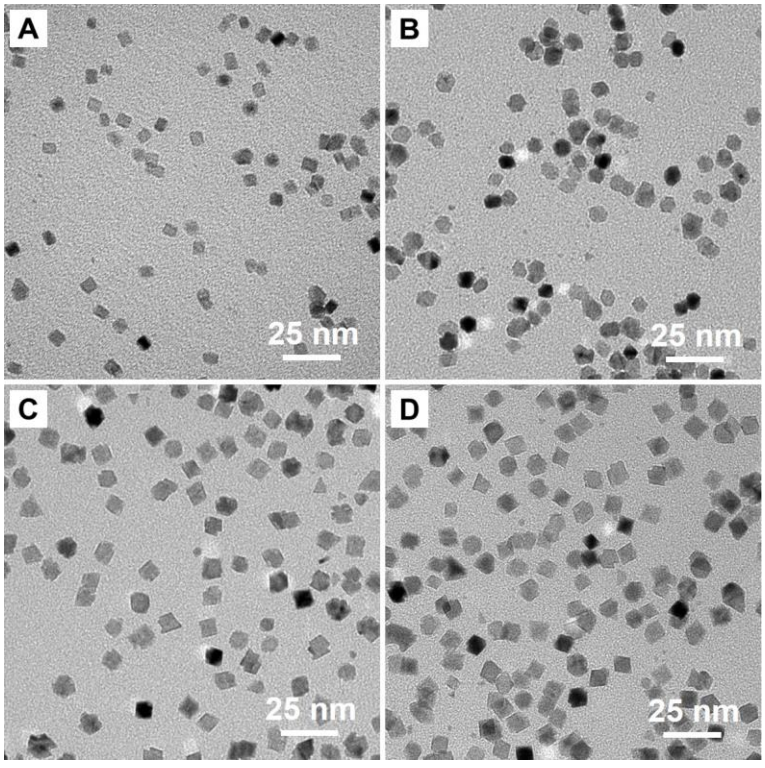

Figure 5.8. TEM images of the Ru nanocrystals prepared using the standard protocol except using different reaction temperatures: (A) 120, (B) 140, (C) 160, and (d) 180 °C.

I also varied the reaction temperature to examine its role in the formation of Ru octahedral nanocrystals. The reaction temperature not only controls surface diffusion but also affects the reducing power of the reductant and thereby the deposition rate of Ru atoms. Figure 5.8A shows a TEM image of the Ru nanocrystals prepared using the standard protocol except for the use of 120 °C. The resultant nanocrystals took a cubic shape, with a similar size to that of the original Rh cubic seeds, which could be largely ascribed to the weak reducing power of HCHO at a low temperature. When I increased the reaction temperature to 140 °C, cuboctahedral nanocrystals were observed in the products, whereas their surfaces were bumpy owing to insufficient surface diffusion (Figure 5.8B). As the reaction temperature was elevated to 160 °C and further to 180 °C, octahedral nanocrystals became prevailed in the products (Figure 5.8, C and D). Meanwhile, their surfaces became smooth due to the enhanced surface diffusion at the elevated temperature. Taken together, the reaction temperature should be optimized to ensure the generation of sufficient Ru atoms for the continuous growth and simultaneously, to achieve preferential surface diffusion over the deposition of Ru atoms.

Ru-based nanocrystals are promising catalytic materials toward CO oxidation, Fischer-Tropsch synthesis, and ammonia synthesis, which are typically conducted at elevated temperatures [1–4]. In contrast to the conventional *hcp*-Ru nanoparticles, the *fcc*-Ru nanocrystals with well-defined surface structures could only preserve the *fcc* phase and the surface structure up to 300 °C [12, 28, 29]. As the temperature was elevated, the crystal phase would change from *fcc* to *hcp* while the surface structure could also be lost [12, 28, 29]. In order to evaluate their potential toward these reactions, it is essential to have knowledge of the thermal stability of both the octahedral shape and the *fcc* structure of the

Ru octahedral nanocrystals. The thermal stability of the octahedral shape was assessed by STEM coupled with *in situ* heating, in which the sample was heated to various temperatures ranging from 200 to 600 °C. As shown in Figure 5.9A–C, the octahedral shape of the Ru nanocrystal could be well preserved when the temperature was in the range of 200–400 °C. Even when the nanocrystal was heated to 500 °C for 0.5 h, no significant change was observed, except for the mild rounding at corner sites. Upon extending the heating at 500 °C for 1 h, the nanocrystal lost its octahedral shape (Figure 5.9E). When the temperature was further elevated to 600 °C, the nanocrystal was completely transformed into a spheroid (Figure 5.9F). These results suggest that the octahedral shape of the Ru nanocrystals could be retained well up to 400 °C.

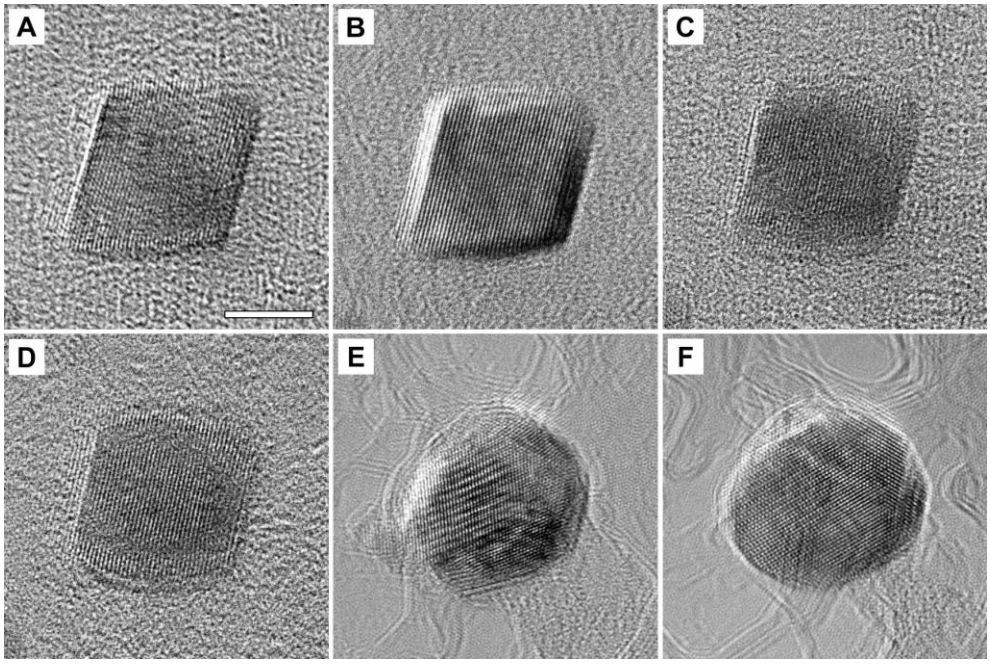

Figure 5.9. *In situ* HRTEM images recorded from the same Ru octahedron heated at various temperatures: (A) 200 °C for 0.5 h, (B) 300 °C for 0.5 h, (C) 400 °C for 0.5 h, (D) 500 °C for 0.5 h, (E) 500 °C for 1 h, and (F) 600 °C for 0.5 h. The scale bar in (A) is 5 nm and applies to all panels.

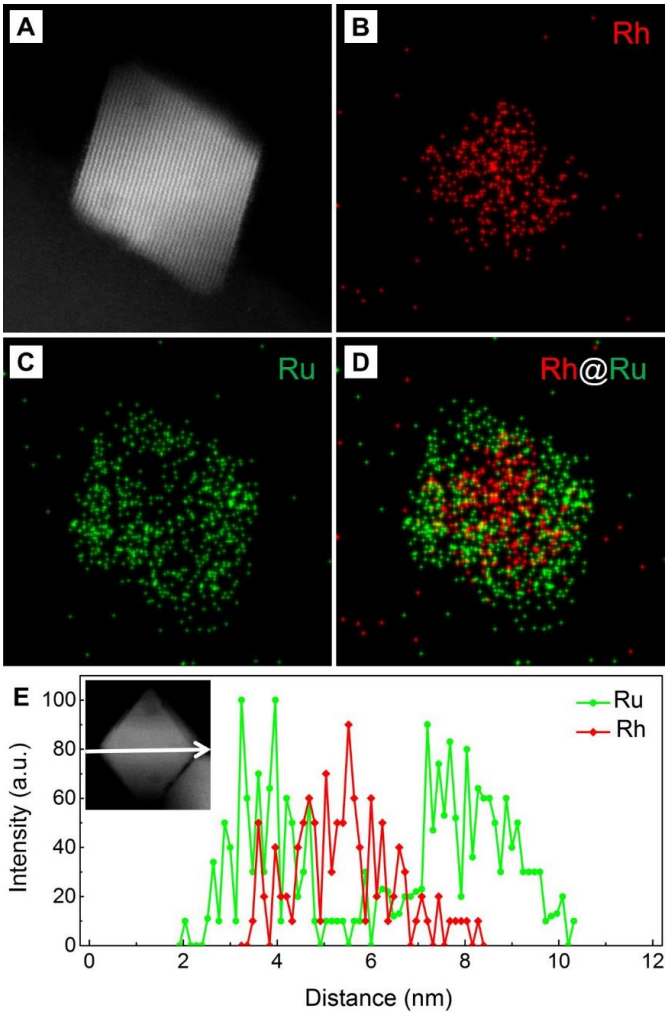

Figure 5.10. (A) HAADF-STEM and (B–D) EDX mapping (Rh/red, Ru/green) images of an individual octahedron after annealing at 400 °C for 0.5 h. (E) Elemental distribution by the EDX line scan analysis along the white arrow shown in the inset.

I also conducted EDX mapping to resolve the distributions of Rh and Ru in the annealed nanocrystal. As shown in Figure 5.10, a core–shell structure could still be resolved for the octahedral nanocrystal after annealing at 400 °C but the Rh core was enlarged relative to the original sample (Figure 5.2F), suggesting inter-diffusion between Rh and Ru at this temperature. Figure 5.10E shows the EDX line scan of an individual nanocrystal, confirming the dominance of surface by Ru. The valence states of Ru after

annealing at 400 °C were also analyzed by XPS. The intensity of C 1s peak at 284.6 eV (Figure 5.11A) was increased relative to that of the fresh sample (Figure 5.3C), which could be attributed to the employment of carbon-coated copper grid for the sample annealing and subsequent XPS analysis. The Ru $3d_{3/2}$ peaks were positioned at 284.21 and 280.03 eV, with essentially no change relative to the sample before annealing. Given that the C 1s and Ru $3d_{3/2}$ peaks are partially overlapped at binding energies in the range of 283–286 eV, I also measured the Ru $3p_{3/2}$ peak to confirm the metallic state of Ru. As shown in Figure 5.11B, the Ru $3p_{3/2}$ peak was positioned at 461.47 eV, essentially the same as that of the original sample before annealing.

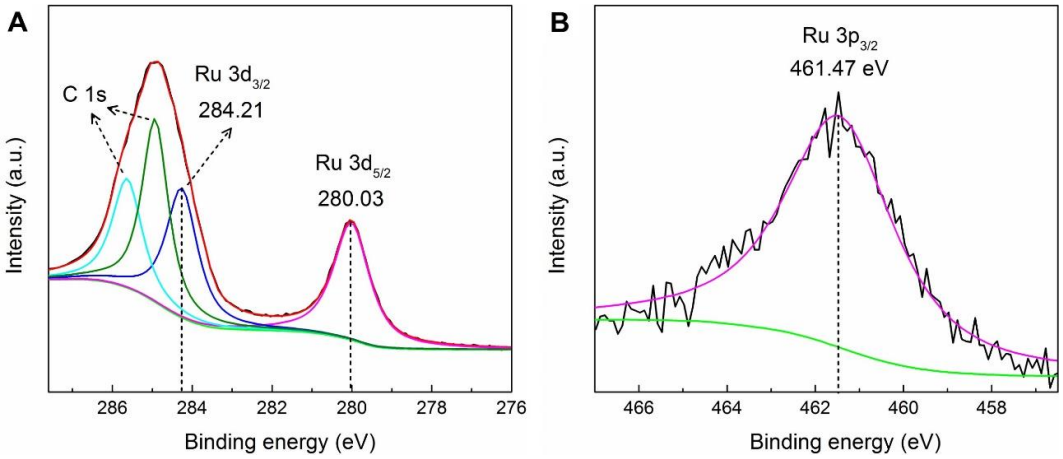

Figure 5.11. (A) Ru 3d and (B) 3p XPS spectra of the Ru octahedral nanocrystals after annealing at 400 °C for 0.5 h, indicating the presence of metallic Ru.

The thermal stability of the *fcc* structure in the Ru octahedral nanocrystals was evaluated using *in situ* XRD. Based on the *in situ* XRD data shown in Figure 5.12, it is clear that the *fcc* structure of the Ru octahedral nanocrystals could be well preserved up to 400 °C, which was confirmed by the characteristic peaks of *fcc* Ru for (111), (200), and

(220) diffraction. When the temperature was increased to 500 °C, the XRD pattern was dominated by *hcp*-(100), *hcp*-(002), *hcp*-(101), and *hcp*-(102) peaks, together with a weak *fcc*-(111) peak, showing a mix of *fcc* and *hcp* structures. As the sample was heated to 600 °C, the *fcc*-(111) peak completely disappeared. The XRD pattern was only composed of the characteristic peaks of *hcp* Ru, indicating complete transition from *fcc* to *hcp* structure. The intensity of *hcp*-(100), *hcp*-(002), *hcp*-(101), and *hcp*-(102) peaks kept increasing as I further increased the temperature to 700 and 800 °C due to sintering of the nanocrystals. The *in situ* measurements suggest that both the octahedral shape and the *fcc* structure of the Ru nanocrystals could be well preserved up to 400 °C, which was more than 100 °C higher than what was reported for Ru octahedral nanocages [28]. I believe that the superior thermal stability of the Ru octahedral nanocrystals will make them particularly useful in catalytic applications involving high temperatures [38, 39].

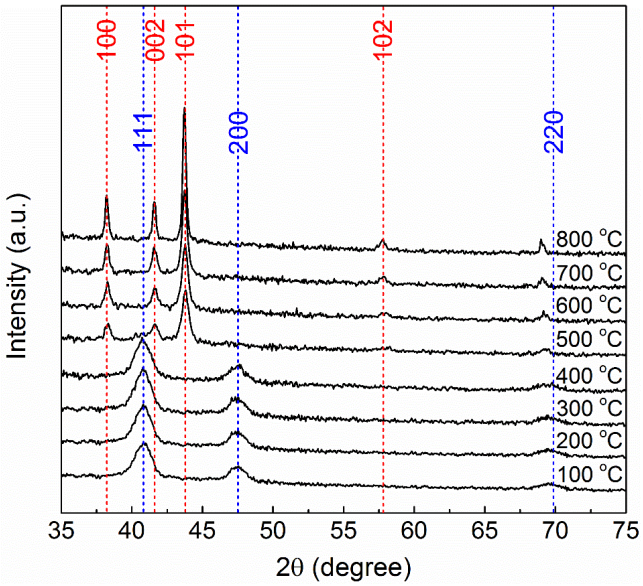

Figure 5.12. *In situ* XRD patterns of *fcc* Ru octahedral nanocrystals heated to temperatures in the range of 100–800 °C under an Ar atmosphere, suggesting the *fcc* structure could be well preserved up to 400 °C. The characteristic peaks of *fcc*- and *hcp*-Ru are marked by blue and red dashed lines, respectively.

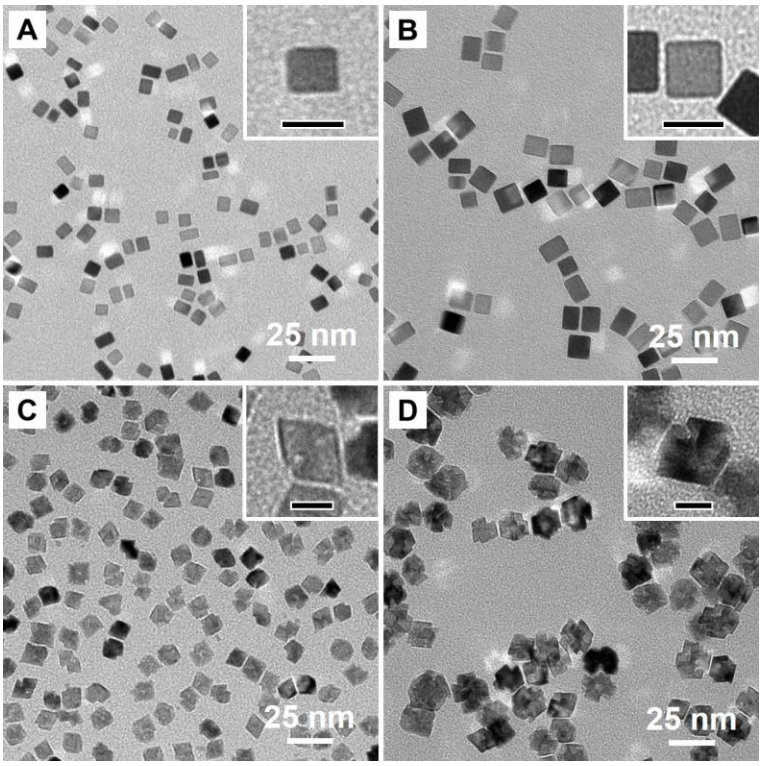

Figure 5.13. TEM images of Pd nanocubes with edge lengths of (A) 6 and (B) 10 nm, respectively, and (C and D) the corresponding Ru nanocrystals prepared from these cubic seeds. All the reaction conditions were kept the same as those in the standard synthesis. The insets show TEM images of individual nanocrystals at a higher magnification. The scale bars in the insets are 10 nm.

I also extended our synthesis to Pd cubic seeds with edge lengths of 6 and 10 nm, as illustrated in Figure 5.13, A and B, respectively, both indicating well-defined {100} facets and uniform size distributions. Figure 5.13C shows a TEM image of the Ru nanocrystals prepared using the standard protocol except for the use of 6-nm Pd cubes as seeds. The as-obtained products were dominated by octahedral nanocrystals, together with some poorly defined nanoparticles. According to the inset shown in Figure 5.13C, the Ru octahedral nanocrystals possessed a rough surface, with pinholes on the surface and truncation at the corners. These observations could be attributed to the enlarged size of the Pd seeds relative

to the Rh seeds used in the standard synthesis [35, 40, 41]. When 6-nm Pd cubes were used as seeds, the diffusion distance for the Ru adatoms were increased whereas the reaction temperature was fixed, giving rise to the formation of nanocrystals with a rough surface. Additionally, the Pd seeds are vulnerable to oxidative etching by halide ions (*i.e.*, Cl^- ions from $RuCl_3$), which could also contribute to the deviation from well-defined octahedral nanocrystals [30, 31]. The argument was further confirmed by employing 10-nm Pd cubes as seeds. As shown in Figure 5.13D, the nanocrystals feature a poorly defined shape and a rough surface. Specifically, more Ru atoms were piled up at the corners of the Pd seeds which could be attributed to the insufficient surface diffusion.

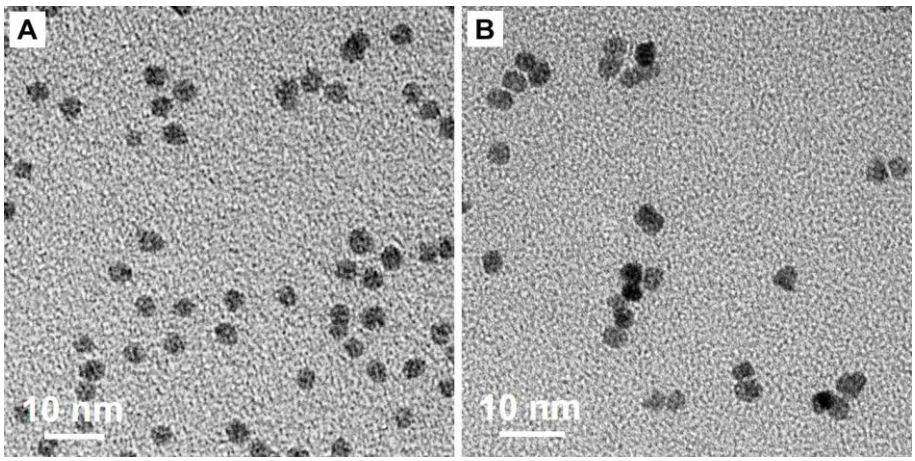

Figure 5.14. TEM images of Ru nanoparticles with (A) *hcp* and (B) *fcc* structures, respectively.

It is well documented that Ru nanocrystals are attractive catalytic materials toward OER [42–45]. The successful synthesis of Ru-based nanocrystals with an *fcc* structure and enclosed by different proportions of {100} and {111} facets allows us to investigate the

dependence of catalytic performance on both the crystal structure and facets. Figure 5.14, A and B, shows TEM images of the Ru nanoparticles in *hcp* and *fcc* structures, respectively, which were further confirmed by XRD analysis. The *hcp*-Ru nanoparticles, *fcc*-Ru nanoparticles, *fcc*-Ru truncated cubes (Figure 5.4B), and *fcc*-Ru octahedra were then loaded onto carbon for the electrochemical measurements. Figure 5.15 shows the CV curves of the different types of Ru catalysts measured in a 0.5 M H_2SO_4 solution at different scanning rates, from which the C_{dl} could be derived as 0.98, 0.83, 0.48, and 0.38 mF for *hcp*-Ru nanoparticles, *fcc*-Ru nanoparticles, *fcc*-Ru truncated cubes, and *fcc*-Ru octahedra, respectively (Figure 5.16A). The relatively small C_{dl} values for *fcc*-Ru truncated cubes and octahedra could be attributed to their enlarged sizes and thus decreased surface-to-volume ratios.

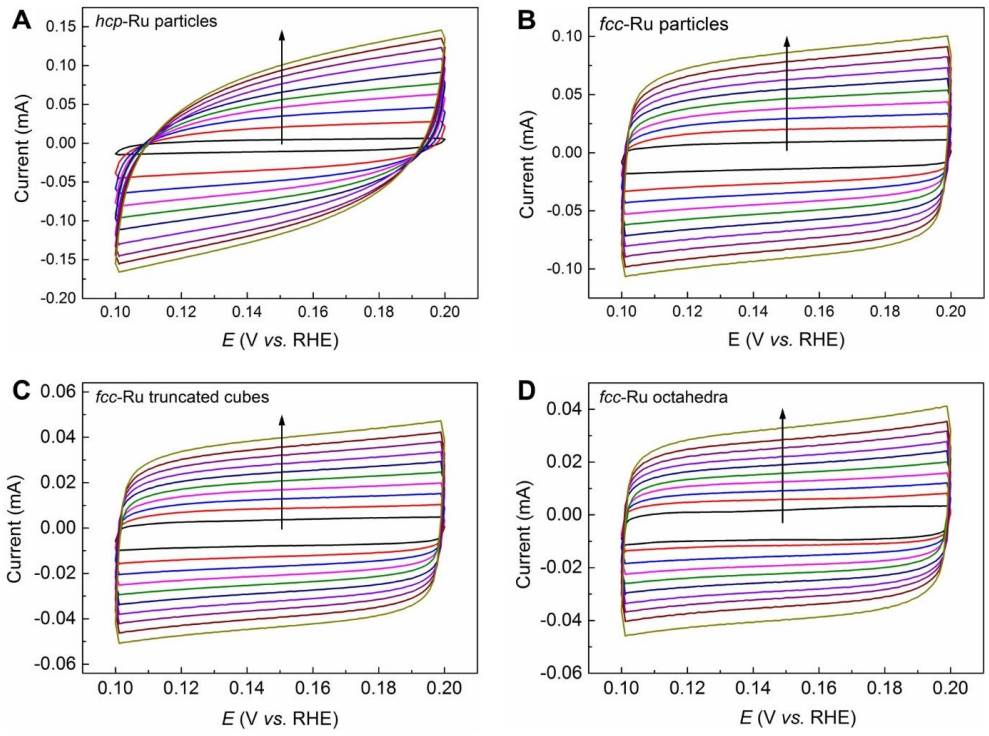

Figure 5.15. CV curves of (A) *hcp*-Ru nanoparticles, (B) *fcc*-Ru nanoparticles, (C) *fcc*-Ru truncated cubes, and (D) *fcc*-Ru octahedral nanocrystals, respectively. The arrow indicates the increase in scanning rate from 10 to 100 mV s^{-1}.

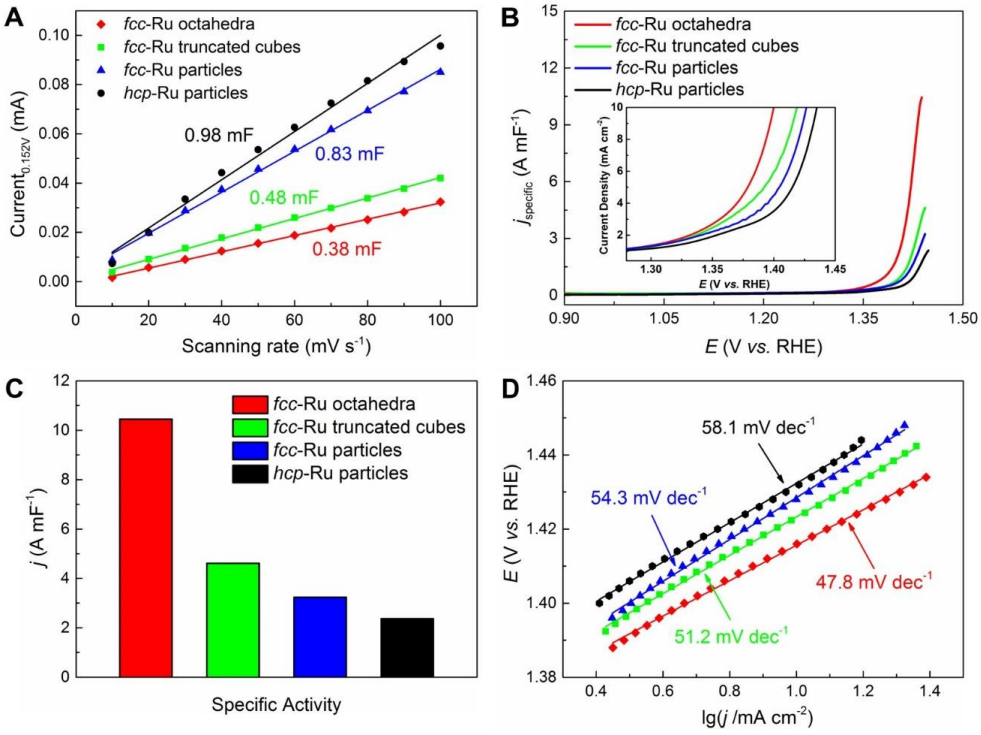

Figure 5.16. (A) Plots revealing the current at an overpotential of 0.152 V as a function of the scanning rate, from which the C_{dl} could be derived based on the slope of the linear regression. (B) C_{dl}-normalized polarization curves measured over different Ru catalysts in a 0.05 M H_2SO_4 solution at a scanning rate of 6 mV s^{-1}. The inset shows the polarization curves of various Ru catalysts in the potential range of 1.28–1.45 V. (C) Summary of the specific activity of different Ru catalysts toward oxygen evolution. (D) Tafel plots for different Ru catalysts.

Figure 5.16B shows the C_{dl}-normalized polarization curves measured in a 0.05 M H_2SO_4 solution at a scanning rate of 6 mV s^{-1} in the presence of different types of Ru catalysts. Their C_{dl}-normalized currents (*i.e.*, specific activity) are summarized in Figure 5.16C. In particular, the specific activity of *fcc*-Ru nanoparticles was derived as 3.28 A mF^{-1}, which was 1.4 times greater than that of *hcp*-Ru nanoparticles (2.36 A mF^{-1}), verifying the enhancement in catalytic activity by the *fcc* structure. Moreover, the *fcc*-Ru octahedra exhibited a specific activity of 10.45 A mF^{-1}, corresponding to 4.4- and 3.2-fold enhancements than those of *hcp*- and *fcc*-Ru nanoparticles, respectively. This date

confirmed the role of {111} facets in further boosting the catalytic performance. When the *fcc*-Ru truncated cubes were used as a catalyst, the specific activity was derived as 4.61 A mF^{-1}, which was 2.3 times lower than that of the *fcc*-Ru octahedra. Since a truncated cube is mainly covered by {100} facets while an octahedron is enclosed by {111} facets, I could conclude that Ru{111} facets are more active than Ru{100} facets toward OER. The overpotential required to reach a current density of 10 mA cm^{-2} was determined as 168 mV for *fcc*-Ru octahedral nanocrystals, which was 38, 29, and 21 mV lower than those of *hcp*-Ru nanoparticles, *fcc*-Ru nanoparticles, and *fcc*-Ru truncated cubes, respectively. Again, this result demonstrates the enhanced performance of *fcc*-Ru octahedra in catalyzing oxygen evolution.

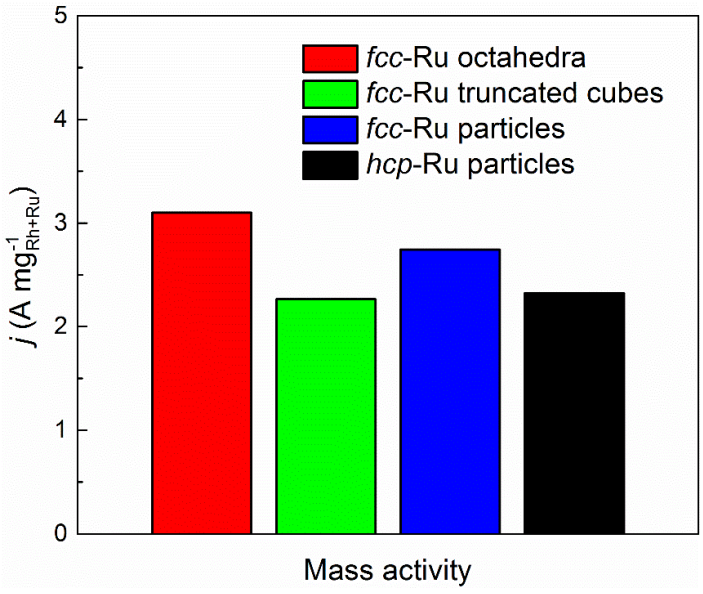

Figure 5.17. Histogram showing the peak currents of the polarization curves measured over different Ru catalysts in a N_2-saturated 0.05 M H_2SO_4 solution at a scanning rate of 6 mV s^{-1}, which were normalized to the mass of both Rh and Ru in the catalyst.

Figure 5.16D shows the Tafel plots for different Ru catalysts, from which the slops were determined as 58.1, 54.3, 51.2, and 47.8 mV dec^{-1} for *hcp*-Ru nanoparticles, *fcc*-Ru nanoparticles, *fcc*-Ru truncated cubes, and *fcc*-Ru octahedral nanocrystals, respectively. In particular, the *fcc*-Ru octahedra exhibited the steepest Tafel slop among all the Ru catalysts, corresponding to the best performance toward OER. The enhanced performance of Ru octahedral nanocrystals could be largely attributed to both the *fcc* structure and well-defined {111} facets. Additionally, the presence of Rh seeds may also contribute to the modulation of the electronic structure of the Ru nanocrystals and thereby help improve the catalytic performance. Figure 5.17 shows a summary of the Rh and Ru mass-normalized peak current (*i.e.*, mass activity) for different Ru-based catalysts. Despite the larger particle size, the *fcc*-Ru octahedral nanocrystals still exhibited a mass activity 1.4 times greater than that of *hcp*-Ru nanoparticles.

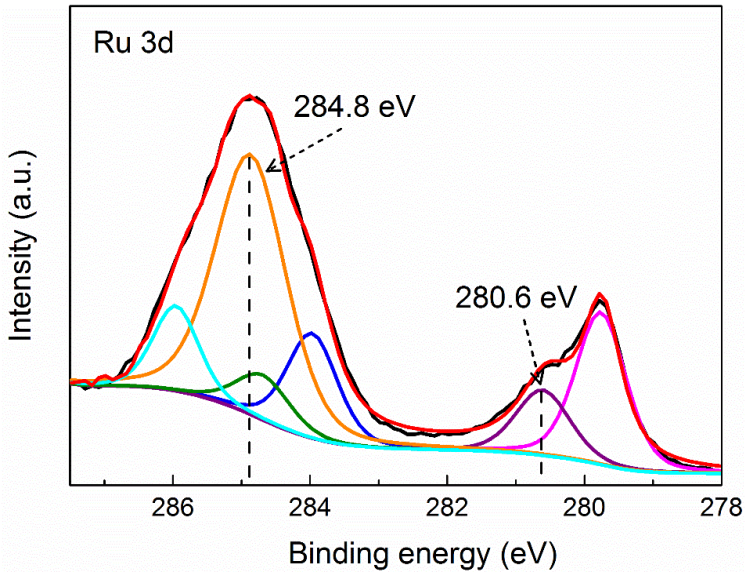

Figure 5.18. Ru 3d XPS spectrum recorded from the Ru octahedral nanocrystals after the OER test. The two peaks positioned at 280.6 and 284.8 eV suggest the formation of RuO_2.

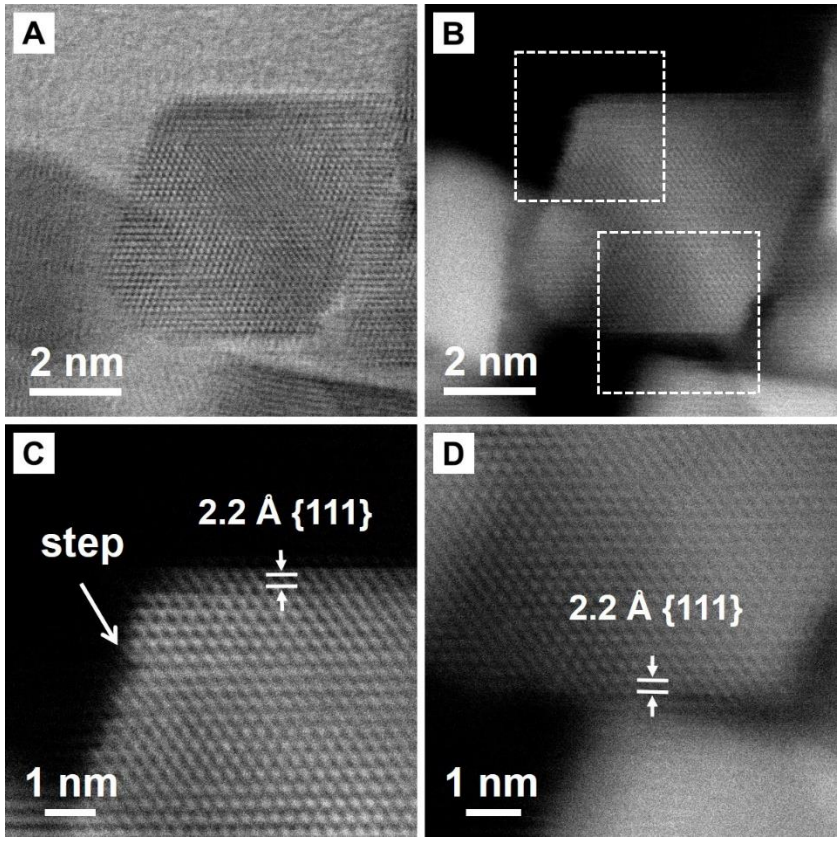

Figure 5.19. (A) HAABF- and (B) HAADF-STEM images of an individual Ru octahedron after the OER test. (C, D) Atomic-resolution STEM images of the corner regions of the octahedron shown in panel (B), marked by two boxes: (C) top left and (D) bottom right.

It is well documented that Ru nanocrystals will undergo oxidation and form RuO_2 during the OER test [5, 43–45]. Here I characterized the tested *fcc*-Ru octahedral nanocrystals by XPS and electron microscopy analyses. Figure 5.18 shows the Ru 3d XPS spectrum of the sample after electrochemical measurements. Two characteristic peaks positioned at 280.6 and 284.8 eV were observed, suggesting the formation of RuO_2. Figure 5.19, A and B, shows the HAABF- and HAADF-STEM images of an individual Ru nanocrystal after the OER test, verifying that the octahedral shape could be well preserved. Based on the atomic-resolution STEM images (Figure 5.19, C and D), the octahedral

Table 5.1. Comparison of the Ru catalysts in this work with the representative Ru/RuO_2 systems reported in the literature.

Catalyst	Electrolyte	Overpotential (mV) at 10 mA cm^{-2}	Tafel slope (mV dec^{-1})	Reference
fcc-Ru octahedra	0.05 M H_2SO_4	168	47.8	This work
fcc-Ru truncated nanocubes	0.05 M H_2SO_4	189	51.2	This work
fcc-Ru particles	0.05 M H_2SO_4	197	54.3	This work
hcp-Ru particles	0.05 M H_2SO_4	206	58.1	This work
Ru nanosheets	0.5 M H_2SO_4	260	54.0	(1)
Pd@$Ru_{1.2\ nm}$ core–shell particles	0.1 M $HClO_4$	220	77.9	(2)
Pd core–Ru nanobranches	0.1 M $HClO_4$	225	61.0	(3)
Au core–Ru nanobranches	0.1 M $HClO_4$	220	62.0	(4)
RuO_2 particles	0.1 M $HClO_4$	450	61.9	(5)
RuO_2 nanosheets	0.1 M $HClO_4$	253	38.0	(6)
rutile RuO_2	0.1 M $HClO_4$	500	40.0	(6)
Ru thin film electrode	0.1 M H_2SO_4	>190	79.1	(7)
RuO_2 thin film electrode	0.1 M H_2SO_4	>410	91.9	(7)
RuO_2	0.5 M H_2SO_4	289	---	(8)
IrO_2-RuO_2@Ru (Ir/Ru = 3/1)	0.5 M H_2SO_4	281	53.1	(8)

nanocrystal was mainly covered by {111} facets, together with the formation of some steps. The appearance of steps on the surface of the octahedral nanocrystal could be attributed to the formation of RuO_2 during the OER test. I also compare the OER performance of our *fcc*-Ru octahedra with those of the representative Ru/RuO_2 systems reported in the literature (Table 5.1) [5, 43–49]. The overpotential at 10 mA cm^{-2} of the *fcc*-Ru octahedra was lower than all the catalysts reported in literature (see Table 5.1) while the Tafel slope was smaller than most of the Ru/RuO_2 systems reported in literature. These results confirm the outstanding performance of the *fcc*-Ru octahedra.

5.3 Conclusion

I have demonstrated a facile protocol for the synthesis of Ru octahedral nanocrystals with well-defined {111} facets and an edge length of 9 nm. The use of 4.5-nm Rh cubes as seeds was critical to the formation of octahedral nanocrystals with a smooth surface. On one hand, the small lattice mismatch between Rh and Ru, as well as the resistance of Rh to oxidative etching, are beneficial to the epitaxial overgrowth of Ru on Rh seeds. On the other hand, the small size of the Rh seeds imposed a short diffusion distance for Ru adatoms, facilitating the formation of a smooth surface. In comparison, the Ru nanocrystals prepared using 6- and 10-nm Pd cubes as the seeds featured a rough surface and a poorly defined shape. Significantly, the Ru atoms in the Rh-seeded octahedral nanocrystals followed an *fcc* packing rather than the conventional *hcp* lattice typical of bulk Ru. Both the octahedral shape and the *fcc* structure of Ru octahedral nanocrystals could be well preserved up to 400 °C. When used as catalysts, the specific activity of the Ru octahedral nanocrystals was 4.4 times as high as that of *hcp*-Ru nanoparticles toward OER. I further confirmed that

Ru{111} facets were more active than Ru{100} facets in catalyzing OER. Taken together, this work offers an effective approach to engineering both the crystal and surface structures of Ru nanocrystals for various catalytic applications.

5.4 Experimental Section

Chemicals. Ethylene glycol (EG, 99%) was obtained from J. T. Baker. Sodium hexachlororhodate(III) (Na_3RhCl_6, 97%), sodium tetrachloropalladate(II) (Na_2PdCl_4, 99.99%), poly(vinylpyrrolidone) (PVP, MW≈55k), L-ascorbic acid (AA, 99%), potassium bromide (KBr, 99%), potassium chloride (KCl, 99%), formaldehyde (HCHO, 36.5–38%), ruthenium(III) chloride hydrate ($RuCl_3 \cdot xH_2O$, 99.99%), and triethylene glycol (TEG, 99%) were all obtained from Sigma-Aldrich and used without further purification. Ruthenium 2,4-pentaedionate ($Ru(acac)_3$, 24% Ru) and sulfuric acid (H_2SO_4, ≥95%) were obtained from Alfa Aesar. All the chemicals were used as received. In all experiments, deionized (DI) water with a resistivity of 18.2 MΩ cm at room temperature was used.

Synthesis of 4.5-nm Rh Nanocubes. In a typical synthesis [33, 34], 13 mL of EG solution containing PVP (133 mg), AA (52.8 mg), and KBr (108 mg) were transferred into a three-neck flask. The mixture was heated to 140 °C under magnetic stirring for 1 h. Meanwhile, 6 mL of the Na_3RhCl_6 solution in EG (7.7 mg mL^{-1}) was injected into the flask using a syringe pump at 60 and 4 mL h^{-1} for the first 1.1 mL and the remaining 4.9 mL, respectively. After 3 h, the reaction solution was quenched in an ice-water bath. The solid products were collected by centrifugation, washed once with a mixture of acetone and EG (acetone/EG = 3/1, v/v), and three times with a mixture of acetone and ethanol

(acetone/ethanol = 3/1, v/v). The Rh nanocubes were then dispersed in water for further use.

Synthesis of 6- and 10-nm Pd Nanocubes. In a typical synthesis of 6-nm Pd cubes, 60 mg of AA, 185 mg of KCl, 5 mg of KBr, and 105 mg of PVP were dissolved in 8 mL of DI water. The mixture was heated to 80 °C for 10 min. Meanwhile, 57 mg of Na_2PdCl_4 was dissolved in 3 mL of water and then added into the preheated solution in one shot. The reaction was allowed to continue for 3 h before quenching in an ice-water bath. The solid products were collected by centrifugation, washed three times with water, and dispersed in water for further use. The synthetic protocol for 10-nm Pd cubes was the same as that for 6-nm Pd cubes except that 185 mg of KCl and 5 mg of KBr were replaced with 300 mg of KBr.

Synthesis of Ru Octahedral Nanocrystals. In a standard synthesis, 0.5 mg of the as-prepared 4.5-nm Rh nanocubes, 4 mg of $RuCl_3$, 2 mL of HCHO, and 200 mg of PVP were mixed in 15 mL of water. The mixture was transferred into a 20-mL Teflon-lined stainless-steel autoclave. The sealed vessel was then heated to 200 °C for 6 h before cooling down naturally. The solid products were collected by centrifugation, washed three times with water.

Synthesis of Ru Nanoparticles with *hcp* and *fcc* Structures. In a typical synthesis of *hcp*-Ru nanoparticles, 50 mg of PVP, 7.5 mg of $Ru(acac)_3$, and 5 mL of EG were mixed in a 20-mL vial. The vial was then placed in an oil bath heated at 180 °C under magnetic stirring. After 2 h, the reaction was terminated by quenching in an ice-water bath. The *fcc*-Ru nanoparticles were prepared by modifying a reported protocol [12]. Typically, 4.2 mg of $Ru(acac)_3$ and 5.5 mg of PVP were mixed in 5 mL of TEG and then heated to 200 °C in

an oil bath for 3 h. The solid products were collected by centrifugation, washed once with a mixture of acetone and TEG (acetone/TEG = 3/1, v/v), and twice with water.

Characterization. Transmission electron microscopy (TEM) images were acquired on a Hitachi HT7700 microscope. High-resolution transmission electron microscopy (HRTEM), high-angle annular dark-field and bright-field scanning transmission electron microscopy (HAADF- and HAABF-STEM, respectively) images, and energy-dispersive X-ray (EDX) spectroscopy data were acquired using an aberration-corrected Hitachi HD2700 STEM at the Institute for Electronics and Nanotechnology (IEN, Georgia Institute of Technology) and a Cs-corrected FEI Titan 80/300 kV TEM/STEM at Oak Ridge National Laboratory (ORNL). Inductively-coupled plasma mass spectrometry (ICP-MS, NexION 300Q, PerkinElmer) was used for the quantitative analysis of metal contents in various samples. The X-ray photoelectron spectroscopy (XPS) data was recorded on a Thermo K-Alpha spectrometer with an Al Kα source (eV).

Thermal Stability of the Octahedral Shape. The thermal stability of the octahedral shape of the Ru nanocrystals was evaluated using *in situ* STEM coupled with a Protochips Aduro heating holder. An aqueous suspension of the as-prepared Ru octahedral nanocrystals was drop-cast onto the Aduro thermal device and then allowed to dry under ambient conditions. The sample was then heated to various temperatures in the range of 25–600 °C, at a heating rate of 1000 °C ms^{-1}.

Thermal Stability of the *fcc* Structure. The thermal stability of the *fcc* structure in the Ru octahedral nanocrystals was assessed using *in situ* X-ray diffraction (XRD). The sample was heated to temperatures in the range of 25–800 °C at a rate of 5 °C s^{-1}. The XRD patterns were collected between $2\theta = 30$ and 90° using an Anton Paar XRK hot stage, and

then processed with HighScore Plus (PANalytical). All the measurements were carried out under an Ar atmosphere to avoid possible oxidation.

Electrochemical Measurements. An electrochemical workstation (CHI 600E potentiostat) was used to conduct the electrochemical measurements at room temperature in a three-electrode cell. I used a Pt mesh and a reversible hydrogen electrode (RHE) as the counter and reference electrodes, respectively. The as-synthesized Ru nanoparticles were loaded on carbon (Vulcan XC-72, Cabot) at a percentage of *ca.* 20 wt.% to serve as the working electrode. The electrochemical surface area (ECSA) was determined using a double layer capacitance (C_{dl}) method, in which the double layer charging currents were measured in 0.5 M H_2SO_4 in the potential range of 0.1–0.2 V and at scanning rates ranging from 10 to 100 mV s^{-1}. By plotting the current at 0.152 V as a function of the scanning rate, the C_{dl} could be derived from the slop of the linear dependence. The linear sweep voltammograms (LSVs) were measured in a N_2-saturated 0.05 M H_2SO_4 solution at a scanning rate of 6 mV s^{-1} in the potential range of 0.8–1.8 V for the Ru-based catalysts, respectively. All polarization curves were *i*R corrected.

5.5 Notes to Chapter 2

Part of this chapter is adapted from the paper "Ru Octahedral Nanocrystals with a Face-Centered Cubic Structure, {111} Facets, Thermal Stability up to 400 °C and Enhanced Catalytic Activity" published in *Journal of the American Chemical Society* [50]

5.6 References

[1] Kitano, M.; Kanbara, S.; Inoue, Y.; Kuganathan, N.; Sushko, P. V.; Yokoyama, T.; Hara, M.; Hosono, H. *Nat. Commun.* **2015**, *6*, 6731.

[2] Li, W.; Liu, J.; Gu, J.; Zhou, W.; Yao, S.; Si, R.; Guo, Y.; Su, H.; Yan, C.; Li, W.; Zhang, Y.; Ma, D. *J. Am. Chem. Soc.* **2017**, *139*, 2267–2276.

[3] Xiao, C.; Cai, Z.; Wang, T.; Kou, Y.; Yan, N. *Angew. Chem. Int. Ed.* **2008**, *120*, 758–761.

[4] Joo, S.; Park, J. Y.; Renzas, J. R.; Butcher, D. R.; Huang, W.; Somorjai, G. A. *Nano Lett.* **2010**, *10*, 2709–2713.

[5] Kong, X.; Xu, K.; Zhang, C.; Dai, J.; Oliaee, S. N.; Li, L.; Zeng, X.; Wu, C.; Peng, Z. *ACS Catal.* **2016**, *6*, 1487–1492.

[6] Wang, J.; Wei, Z.; Mao, S.; Li, H.; Wang, Y. *Energy Environ. Sci.* **2018**, *11*, 800–806.

[7] Yang, S.; Qiao, Y.; He, P.; Liu, Y.; Cheng, Z.; Zhu, J.; Zhou, H. *Energy Environ. Sci.* **2017**, *10*, 972–978.

[8] Lou, B.; Veerakumar, P.; Chen, S.; Veeramani, V.; Madhu, R.; Liu, S. *Sci. Rep.* **2016**, *6*, 19949.

[9] Chen, G.; Zhang, J.; Gupta, A.; Rosei, F.; Ma, D. *New J. Chem.* **2014**, *38*, 1827–1833.

[10] Yin, A.; Liu, W.; Ke, J.; Zhu, W.; Gu, J.; Zhang, Y.; Yan, C. *J. Am. Chem. Soc.* **2012**, *134*, 20479–20489.

[11] Kusada, K.; Kobayashi, H.; Yamamoto, T.; Matsumura, S.; Sumi, N.; Sato, K.; Nagaoka, K. Kubota, Y.; Kitagawa, H. *J. Am. Chem. Soc.* **2013**, *135*, 5493–5496.

[12] Ge, J.; He, D.; Bai, L.; You, R.; Lu, H.; Lin, Y.; Tan, C.; Kang, Y.; Xiao, B.; Wu, Y.; Deng, Z.; Huang, W.; Zhang, H.; Hong X.; Li, Y. *J. Am. Chem. Soc.* **2015**, *137*, 14566–14569.

[13] Fan, Z.; Zhang, H. *Chem. Soc. Rev.* **2016**, *45*, 63–82.

[14] Zheng, Y.; Jiao, Y.; Zhu, Y.; Li, L.; Han, Y.; Chen, Y.; Jaroniec, M.; Qiao, S. *J. Am. Chem. Soc.* **2016**, *138*, 16174–16181.

[15] Yao, Y.; He, D.; Lin, Y.; Feng, X.; Wang, X.; Yin, P.; Hong, X.; Zhou, G.; Wu, Y.; Li, Y. *Angew. Chem. Int. Ed.* **2016**, *128*, 5591–5595.

[16] Lu, Q.; Wang, A.; Gong, Y.; Hao, W.; Cheng, H.; Chen, J.; Li, B.; Yang, N.; Niu, W.; Wang, J.; Yu, Y.; Zhang, X.; Chen, Y.; Fan, Z.; Wu, X.; Chen, J.; Luo, J.; Li, S.; Gu, L.; Zhang, H. *Nat. Chem.* **2018**, *10*, 456–461.

[17] Chandra, D.; Inoue, Y.; Sasase, M.; Kitano, M.; Bhaumik, A.; Kamata, K.; Hosono, H.; Hara, M. *Chem. Sci.* **2018**, *9*, 5949–5956.

[18] Zhang, Z.; Liu, Y.; Chen, B.; Gong, Y.; Gu, L.; Fan, Z.; Yang, N.; Lai, Z.; Chen, Y.; Wang, J.; Huang, Y.; Sindoro, M.; Niu, W.; Li, B.; Zong, Y.; Yang, Y.; Huang, X.; Huo, F.; Huang, W.; Zhang, H. *Adv. Mater.* **2016**, *28*, 10282–20286.

[19] Ye, H.; Wang, Q.; Catalano, M.; Lu, N.; Vermeylen, J.; Kim, J. M.; Liu, Y.; Sun, Y.; Xia, X. *Nano Lett*. **2016**, *16*, 2812–2817.

[20] Lu, Q.; Wang, A.; Cheng, H.; Gong, Y.; Yun, Q.; Yang, N.; Li, B.; Chen, B.; Zhang, Q.; Zong, Y.; Gu, L.; Zhang, H. *Small* **2018**, *14*, 1801090.

[21] Gu, J.; Guo, Y.; Jiang, Y.; Zhu, W.; Xu, Y.; Zhao, Z.; Liu, J.; Li, W.; Jin, C.; Yan, C.; Zhang, Y. *J. Phys. Chem. C* **2015**, *119*, 17697–17706.

[22] Vitos, L.; Ruban, A. V.; Skriver, H. L.; Kollár, J. *Surf. Sci.* **1998**, *411*, 186–202.

[23] Turchanin, M.; Agraval, P. G. *Powder Metall. Met. Ceram.* **2008**, *47*, 26–39.

[24] Xia, Y.; Gilroy, K. D.; Peng, H.-C.; Xia, X. *Angew. Chem. Int. Ed.* **2017**, *56*, 60–95.

[25] Fan, Z.; Zhang, H. *Acc. Chem. Res.* **2016**, *49*, 2841–2850.

[26] Gilroy, K. D.; Yang, X.; Xie, S.; Zhao, M.; Qin, D.; Xia, Y. *Adv. Mater.* **2018**, *30*, 1706312.

[27] Zhao, M.; Figueroa-Cosme, L.; Elnabawy, A. O.; Vara, M.; Yang, X.; Roling, L. T.; Chi, M.; Mavrikakis, M.; Xia, Y. *Nano Lett.* **2016**, *16*, 5310–5317.

[28] Zhao, M.; Elnabawy, A. O.; Vara, M.; Xu, L.; Hood, Z. D.; Yang, X.; Gilroy, K. D.; Figueroa-Cosme, L.; Chi, M.; Mavrikakis, M.; Xia, Y. *Chem. Mater.* **2017**, ***29*, 9227–9237.**

[29] Zhao, M.; Xu, L.; Vara, M.; Elnabawy, A. O.; Gilroy, K. D.; Hood, Z. D.; Zhou, S.; Figueroa-Cosme, L.; Chi, M.; Mavrikakis, M.; Xia, Y. *ACS. Catal.* **2018**, *8*, 6948–6960.

[30] Long, R.; Zhou, S.; Wiley, B. J.; Xiong, Y. *Chem. Soc. Rev.* **2014**, *43*, 6288–6310.

[31] Wang, Z.; Wang, H.; Zhang, Z.; Yang, G.; He, T.; Yin, Y.; Jin, M. *ACS Nano* **2017**, *11*, 163–170.

[32] Nanba, Y.; Ishimoto, T.; Koyama, M. *J. Phys. Chem. C* **2017**, *121*, 27445–27452.

[33] Zhang, H.; Li, W.; Jin, M.; Zeng, J.; Yu, T.; Yang, D.; Xia, Y. *Nano Lett.* **2011**, *11*, 898–903.

[34] Zhang, Y.; Grass, M. E.; Kuhn, J. N.; Tao, F.; Habas, S. E.; Huang, W.; Yang, P.; Somorjai, G. A. *J. Am. Chem. Soc.* **2008**, *130*, 5868–5869.

[35] Xia, X.; Xie, S.; Liu, M.; Peng, H.-C.; Lu, N.; Wang, J.; Kim, M. J.; Xia, Y. *Proc. Natl. Acad. Sci. U.S.A.* **2013**, *110*, 6669–6673.

[36] Rodriguse, T. S.; Zhao, M.; Yang, T.-H.; Gilroy, K. D.; da Silva, A. G. M.; Camargo, P. H. C.; Xia, Y. *Chem. Eur. J.* **2018**, *24*, 16944–16963.

[37] Washio, I.; Xiong, Y.; Yin, Y.; Xia, Y. *Adv. Mater.* **2006**, *18*, 1745–1749.

[38] Vara, M.; Roling, L. T.; Wang, X.; Elnabawy, A. O.; Hood, Z. D.; Chi, M.; Mavrikakis, M.; Xia, Y. *ACS Nano* **2017**, *11*, 4571–4581.

[39] Vara, M.; Wang, X.; Howe, J.; Chi, M.; Xia, Y. *ChemNanoMat* **2018**, *4*, 112–117.

[40] Xia, Y.; Xia, X.; Peng, H.-C. *J. Am. Chem. Soc.* **2015**, *137*, 7947–7966.

[41] Zhang, H.; Jin, M.; Xia, Y. *Angew. Chem. Int. Ed.* **2012**, *51*, 7656–7673.

[42] Reier, T.; Oezaslan, M.; Strasser, P. *ACS Catal.* **2012**, *2*, 1765–1772.

[43] Gloag, L.; Benedetti, T. M.; Cheong, S.; Wester, R. F.; Marjo, C. E.; Gooding, J. J.; Tilley, R. D. *Nanoscale* **2018**, *10*, 15173–15177.

[44] Gloag, L.; Benedetti, T. M. Cheong, S.; Marjo, C. E.; Gooding, J. J.; Tilley, R. D. *J. Am. Chem. Soc.* **2018**, *140*, 12760–12764.

[45] Gloag, L.; Benedetti, T. M.; Cheong, S.; Li, Y.; Chan, X.; Lacroix, L.; Chang, S.; Arenal, R.; Florea, I.; Barron, H.; Barnard, A. S.; Henning, A. M.; Zhao, C.; Schuhmann, W.; Gooding, J. J.; Tilley, R. D. *Angew. Chem. Int. Ed.* **2018**, *57*, 10241–10245.

[46] Lee, Y.; Suntivich, J.; May, K. J.; Perry, E. E.; Shao-Horn, Y. *J. Phys. Chem. Lett.* **2012**, *3*, 399–404.

[47] Laha, S.; Lee, Y.; Podjaski, F.; Weber, D.; Duppel, V.; Schoop, L. M.; Pielnhofer, F.; Scheurer, C.; Müller, K.; Starke, U.; Reuter, K.; Lotsch, B. V. *Adv. Energy Mater.* **2019**, 1803795.

[48] Li, G.; Li, S.; Ge, J.; Liu, C.; Xing, W. D *J. Mater. Chem. A* **2017**, *5*, 17221–17229.

[49] Cherevko, S.; Geiger, S.; Kasian, O.; Kulyk, N.; Grote, J.-P.; Savan, A.; Shrestha, B. R.; Merzlikin, S.; Breitbach, B.; Ludwig, A. Mayrhofer, K. J.J. *Catal. Today* **2016**, *262*, 170–180.

[50] Zhao, M.; Chen, Z.; Lyu, Z.; Hood, Z. D.; Xie, M.; Vara, M.; Chi, M.; Xia, Y. *J. Am. Chem. Soc.* **2019**, *141*, 7028–7036.

CHAPTER 6

RUTHENIUM NANOFRAMES IN THE FACE-CENTERED CUBIC PHASE: FACILE SYNTHESIS AND THEIR ENHANCED CATALYTIC PERFORMANCE

6.1 Introduction

Noble-metal nanocrystals with a hollow structure are intriguing catalytic materials owing to their high utilization efficiencies of metal atoms, with notable examples including nanoshells, nanoboxes, nanocages, and nanoframes [1–8]. Among these examples, nanoframes substantially differ from the rest in that they only contain vertices and edges to give the most open structure. As such, nanoframes offer a means to utilize metal atoms at remarkable efficiency. Additionally, the low-coordination sites typically exposed on the surface of nanoframes can lead to enhanced catalytic performance towards various reactions [9, 10]. In general, noble-metal nanoframes can be fabricated using two different approaches: *i*) site-selected deposition in combination with wet chemical etching and *ii*) dealloying of solid or hollow nanocrystals comprised of metals with different reactivities [7, 11–17]. As an early example of the first approach, our group demonstrated the facile synthesis of Rh or Pt cubic nanoframes [11, 13]. In such a synthesis, Br^- ions were used to selectively block the {100} side faces while confining the deposition of Rh or Pt atoms to the corners and edges terminated in {111} and {110} facets, respectively. The as-obtained core–frame nanocubes were then subjected to wet chemical etching to selectively remove the Pd in the core, generating Rh or Pt cubic nanoframes. When evaluated as an

electrocatalyst towards the oxygen reduction reaction, the Pt cubic nanoframes showed enhancement in both activity and durability relative to the Pt/C catalyst [13].

As a remarkable catalytic material, Ru has been applied to a large number of reactions, including hydrogenation, CO oxidation, CO_2 methanation, and nitrogen reduction (for the synthesis of ammonia) [18–22]. For these and other catalytic applications, it is possible to enhance the performance of Ru nanocrystals by controlling their shape or morphology and thereby engineering their surface structure. Despite the notable accomplishments for noble metals such as Pd, Pt, Au, Ag, and Rh [23–26], it has been challenging to directly synthesize Ru nanocrystals with diversified shapes owing to the hexagonal close-packed (*hcp*) structure, as well as the high cohesive and surface free energies, of Ru [27, 28]. To mitigate this issue, one can employ pre-formed nanocrystals as seeds or templates for the deposition of Ru through heterogeneous nucleation and growth [14, 29–32]. Under certain conditions, the deposited Ru atoms can be directed to take the same crystal structure as that of the underlying seed, offering a powerful method for engineering the crystal phase and surface structure of Ru nanocrystals to enhance their catalytic properties [31–34]. Using this approach, our group have demonstrated the synthesis of Pd@Ru core–shell nanocrystals crystallized in the face-centered cubic (*fcc*) phase, together with cubic, octahedral, and icosahedral shapes to provide well-defined facets [35–37]. Even after the removal of Pd templates in the core, the Ru shells could keep the *fcc* structure and well-defined facets. In parallel, Xia and co-workers reported the synthesis of Pd@Ru core–frame octahedra through site-selected deposition of Ru atoms on Pd cuboctahedral seeds, and then the production of Ru octahedral nanoframes [38]. The packing of Ru atoms also followed an *fcc* structure rather than the *hcp* lattice typical of bulk Ru. The *fcc*-Ru

octahedral nanoframes were found to exhibit enhanced performance towards both the reduction of 4-nitrophenol and dehydrogenation of ammonia borane, when compared with *hcp*-Ru nanowires.

Herein, I demonstrate the use of a combination of galvanic replacement, site-selected deposition, and wet chemical etching for the facile synthesis of Ru cuboctahedral nanoframes. Different from the synthesis reported by Xia and co-workers [38], I rely on the Br^--assisted galvanic replacement reaction between Ru(III) ions and Pd for the generation of Ru atoms. Additionally, the shape of the Pd seeds in the current system kept evolving during the synthesis, from cubes to truncated cubes in the initial stage owing to oxidative etching, and eventually to cuboctahedra as a result of Br^--assisted galvanic replacement. The as-synthesized Pd–Ru nanocrystals were characterized by a core–frame structure and a cuboctahedral shape, together with concave facets. When subjected to a wet chemical etchant for Pd, the Pd@Ru core–frame nanocrystals were transformed into Ru cuboctahedral nanoframes. I could readily tune the ridge thickness of the Ru nanoframes in the range of 3–10 atomic layers by varying the amounts of Ru(III) precursor. Most interestingly, the Ru atoms in the nanoframes were able to replicate the atomic packing of the underlying Pd seeds, displaying an *fcc* phase rather than the conventional *hcp* phase found in bulk Ru. Even under thermal stress, the Ru nanoframes could maintain the frame structure and *fcc* phase up to 350 °C. Relative to *hcp*-Ru nanoparticles, the *fcc*-Ru nanoframes exhibited greatly enhanced activity and H_2 selectivity towards the hydrazine decomposition reaction.

6.2 Results and Discussion

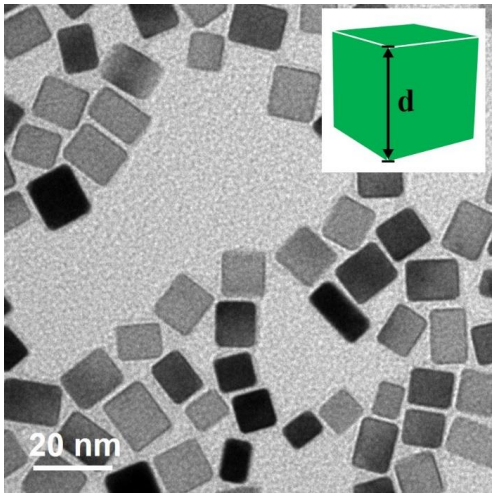

Figure 6.1. TEM image of the Pd nanocubes that served as seeds for the synthesis of Ru cuboctahedral nanoframes, showing an average size of 10 nm. The inset shows a schematic of the Pd nanocube, together with the definition of size.

Synthesis and Characterization of the Pd@Ru Core–Frame Cuboctahedra and Ru Cuboctahedral Nanoframes. I started with the preparation of Pd cubic seeds that had an average edge length of 10 nm and were mainly covered by {100} facets (Figure 6.1) [39]. The as-obtained Pd cubic seeds were mixed with poly(vinylpyrrolidone) (PVP), potassium bromide (KBr), and Ru(III) precursor in triethylene glycol (TEG), and then heated to initiate the reaction. Figure 6.2a shows a transmission electron microscopy (TEM) image of the Pd–Ru nanocrystals prepared using the standard protocol, indicating a uniform size distribution and a cuboctahedral shape. From the high-angle annular dark-field scanning transmission electron microscopy (HAADF-STEM) images (Figure 6.2b), one can clearly observe the concave facets and truncated corners. These images correlate well with the schematics of a concave cuboctahedron viewed along <100> and <110> directions. Figures 6.2, c and d, shows HAADF and high-angle annular bright-field (HAABF) STEM images of an individual Pd–Ru nanocrystal, from which the cuboctahedral shape was

further confirmed. The lattice fringe spacing of 1.9 and 2.2 Å can be assigned to the {200} and {111} planes of *fcc* Ru, respectively (Figure 6.2e). To resolve the spatial distributions of Pd and Ru in the Pd–Ru concave cuboctahedra, I also conducted energy-dispersive X-ray spectroscopy (EDX) mapping analysis. As shown in Figure 6.2f, the Pd atoms were primarily confined to the core of each nanocrystal while the Ru atoms were mainly distributed at corners and edges, consistent with a core–frame structure.

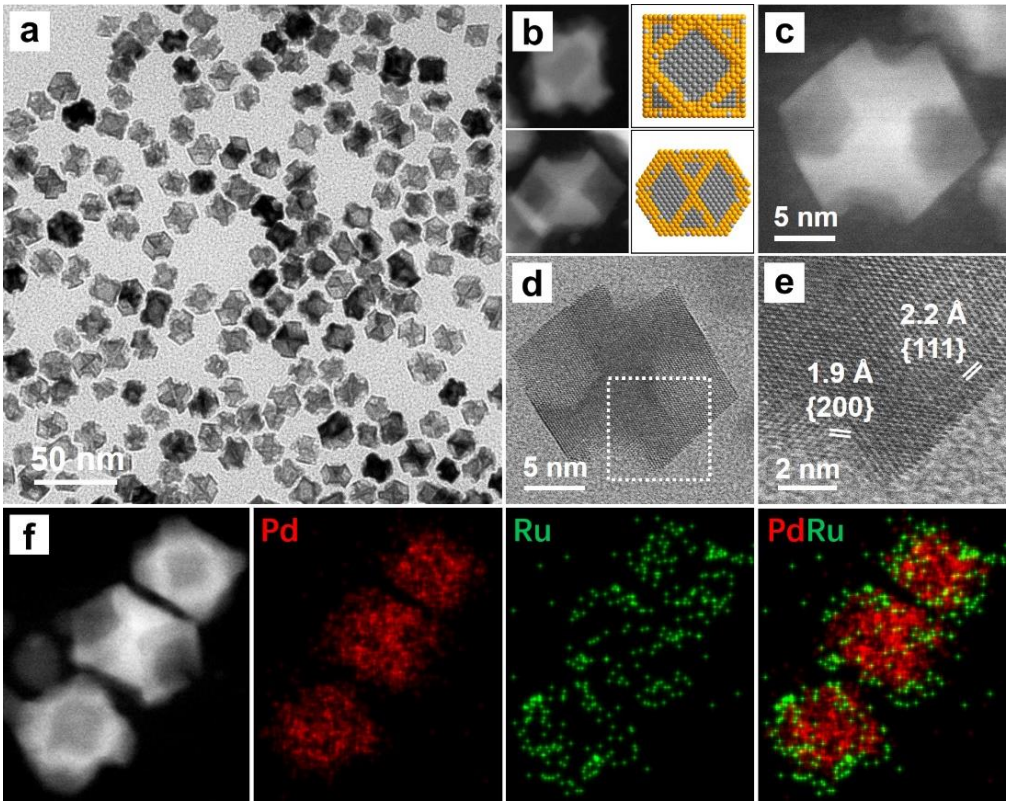

Figure 6.2. (a) TEM image of the Pd@Ru core–frame cuboctahedra prepared using the standard protocol. (b) HAADF-STEM images and schematics of the core–frame cuboctahedra viewed along <100> and <110> directions, respectively. (c) HAADF- and (d) HAABF-STEM image of an individual core–frame cuboctahedron. (e) Atomic-resolution STEM image taken from the corner region of a core–frame cuboctahedron, marked by a box in panel (d). (f) HAADF-STEM image and EDX mapping (Pd/red, Ru/green) of three core–frame cuboctahedra.

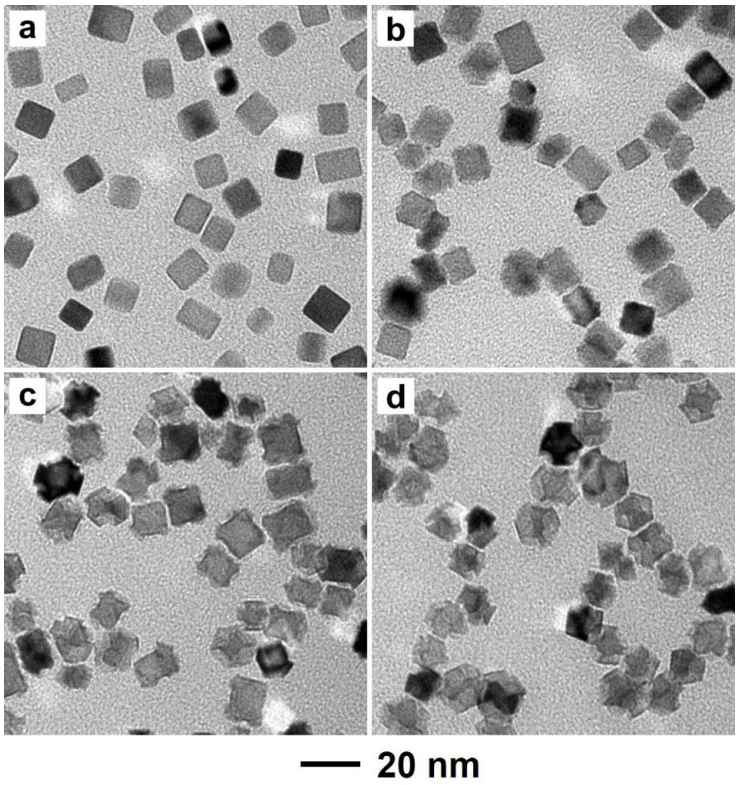

Figure 6.3. TEM images of the intermediate products obtained at different stages of a standard synthesis: (a) 10 min, (b) 1 h, (c) 2 h, and (d) 4 h, respectively.

To elucidate the formation pathway of the core–frame cuboctahedra, I collected the intermediate products at different stages of a standard synthesis and conducted TEM analysis. In the initial stage (Figure 6.3a, t = 10 min), the solid products were dominated by truncated cubes. According to the inductively-coupled plasma mass spectrometry (ICP-MS) data, the products only contained Pd, indicating that no Ru atoms had been deposited on the Pd seeds. The observed truncation can be attributed to oxidative etching, in which the passivation of all side faces by Br^- ions only led to the dissolution of Pd from the corner sites [40, 41]. After 1 h into the reaction, the corners of the nanocrystals became more truncated while the side faces developed concaveness (Figure 6.3b). The weight percentage

of Ru in the resultant nanocrystals increased to 5.8 wt.%, confirming the incorporation of Ru in the nanocrystals. As the reaction was continued up to 2 h and further to 4 h (Figures 6.3, c and d, respectively), both truncation and concaveness became increasingly more significant. Based on the ICP-MS data, the weight percentages of Ru also increased to 11.3 and 27.9 wt.% for the products obtained at t = 2 h and 4 h, respectively.

Since Ru is more resistant to oxidative etching than Pd [35–38], I was able to selectively remove the Pd remaining in the core through wet etching while leaving the Ru atoms intact. The etching process can be described using the following reaction [17]:

$$Pd + 2Fe^{3+} + 4Br^{-} \rightarrow PdBr_4^{2-} + 2Fe^{2+} \quad (1)$$

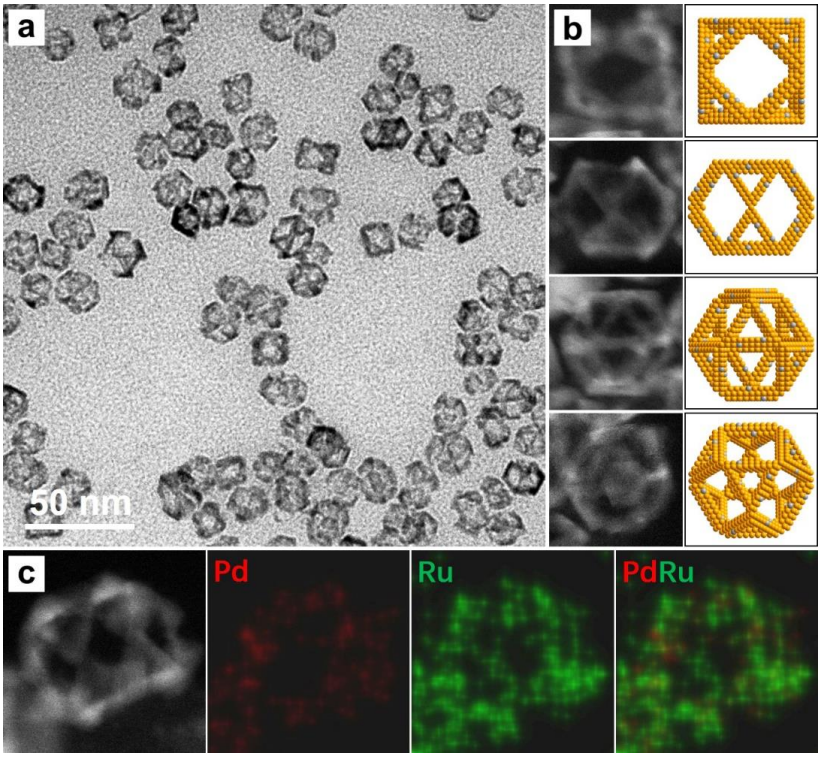

Figure 6.4. (a) TEM image of the Ru cuboctahedral nanoframes prepared using the standard protocol. (b) HAADF-STEM images and schematics of the cuboctahedral nanoframes viewed from <100>, <110>, <211>, and <111> directions, respectively. (c) HAADF-STEM image and EDX mapping (Pd/red, Ru/green) of an individual nanoframe.

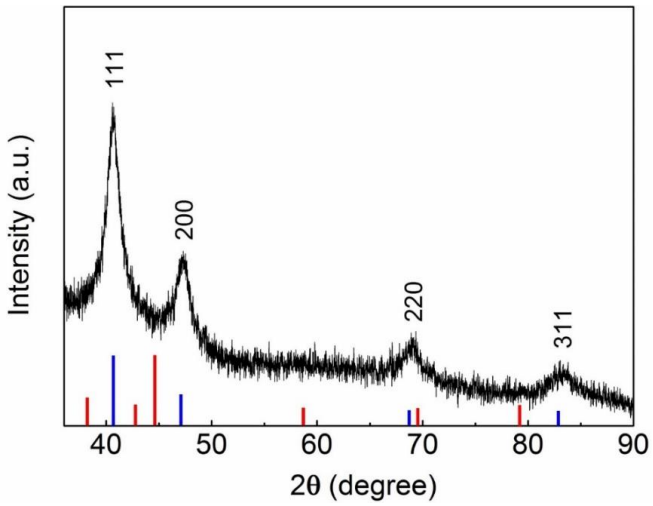

Figure 6.5. XRD pattern of the Ru cuboctahedral nanoframes prepared using the standard protocol, suggesting an *fcc* phase. Blue bars: JCPDS no. 88-2333 (*fcc* Ru). Red bars: JCPDS no. 06-0663 (*hcp* Ru).

Figure 6.4a shows a TEM image of the remaining solid products, indicating the effective removal of all Pd from the cores. The hollow nanocrystals were largely comprised of edges, which is indicative of a frame structure. Figure 6.4b shows HAADF-STEM images of the nanoframes projected along different zone axes, correlating with the models of a cuboctahedral nanoframe viewed from <100>, <110>, <211>, and <111> directions, respectively. These images indicate that the as-synthesized nanoframes took a cuboctahedral shape consistent with the core–frame nanocrystals. Based on the EDX mapping data (Figure 6.4c), the cuboctahedral nanoframe was dominated by Ru, confirming the removal of essentially all Pd from the core. The quantitative analysis based on ICP-MS confirms that the weight percentage of Pd dropped from 69.1 wt.% in the core-frame cuboctahedra to 6.6 wt.% in the nanoframes after the wet etching, whereas the weight percentage of Ru increased from 30.9 to 93.4 wt.%. Figure 6.5 shows an XRD pattern

recorded from the Ru cuboctahedral nanoframes. The diffraction peaks, including (111), (200), (220), and (311), clearly show an *fcc* phase for the Ru cuboctahedral nanoframes, in agreement with the lattice fringe assignment in Figure 6.2e. Taken together, it can be concluded that the as-synthesized Ru nanoframes feature an *fcc* structure and a cuboctahedral shape.

Mechanistic Investigation. To elucidate the mechanism underlying the formation of the Pd@Ru core–frame cuboctahedra, I varied a set of experimental parameters to examine their roles in the synthesis. Figure 6.6, a and b, shows the resultant nanocrystals prepared using the standard protocol except for the absence of Ru(III) precursor and Pd seeds, respectively. When the Ru(III) precursor was missing, the products were dominated by truncated Pd nanocubes (Figure 6.6a), which can be attributed to the oxidative etching caused by Br^- ions [42, 43]. When the synthesis was conducted in the absence of Pd seeds, the as-obtained products contained a mixture of nanoplates and irregular nanoparticles formed through homogeneous nucleation and growth (Figure 6.6b).

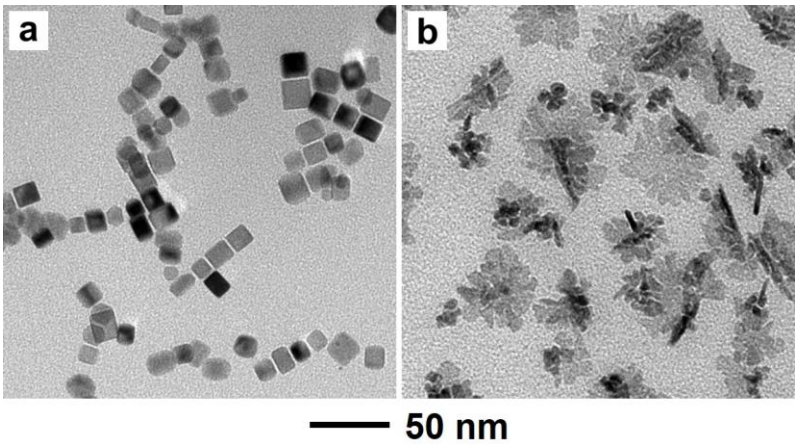

Figure 6.6. TEM images of the solid products obtained using the standard protocol except for the absence of (a) Ru(III) precursor and (b) Pd cubic seeds, respectively.

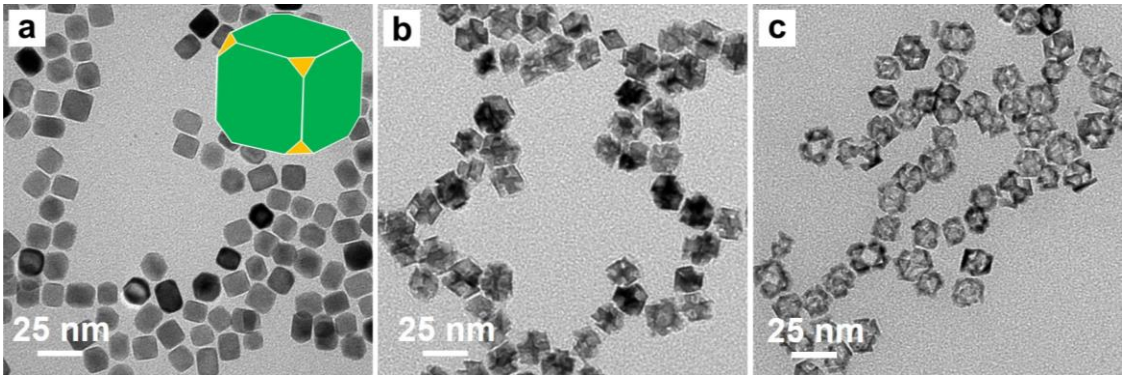

Figure 6.7. TEM images of (a) the truncated Pd nanocubes prepared from 10-nm Pd nanocubes, and the corresponding (b) Pd–Ru nanocrystals and (c) Ru nanoframes prepared using these seeds. The inset in (a) shows a schematic of the truncated Pd nanocube, in which the {100} and {111} facets are indicated by green and yellow colors, respectively.

As shown in Figure 6.3a, the products collected at 10 min into a standard synthesis were truncated Pd cubes, whose composition was confirmed by ICP-MS analysis. To verify the formation mechanism of Pd@Ru core–frame cuboctahedra, I also employed truncated Pd nanocubes as seeds to conduct the synthesis (Figure 6.7a). Figure 6.7b shows a TEM image of the as-synthesized Pd–Ru nanocrystals, indicating the formation of truncated corners and concave facets, consistent with the standard sample. After selectively etching away the Pd cores, I was able to obtain Ru cuboctahedral nanoframes, in which the Ru atoms were mainly distributed in the edges (Figure 6.7c). Based on the ICP-MS data, the weight percentage of Pd in the nanoframes was 6.9 wt.% while that of Ru was 93.1 wt.%, similar to those of the standard sample. This result further confirms that during the standard synthesis, the formation of truncated Pd cubes in the initial stage paved the way for the subsequent formation of Pd@Ru core–frame cuboctahedra *via* Br^--assisted galvanic replacement between the Pd seeds and Ru(III) ions.

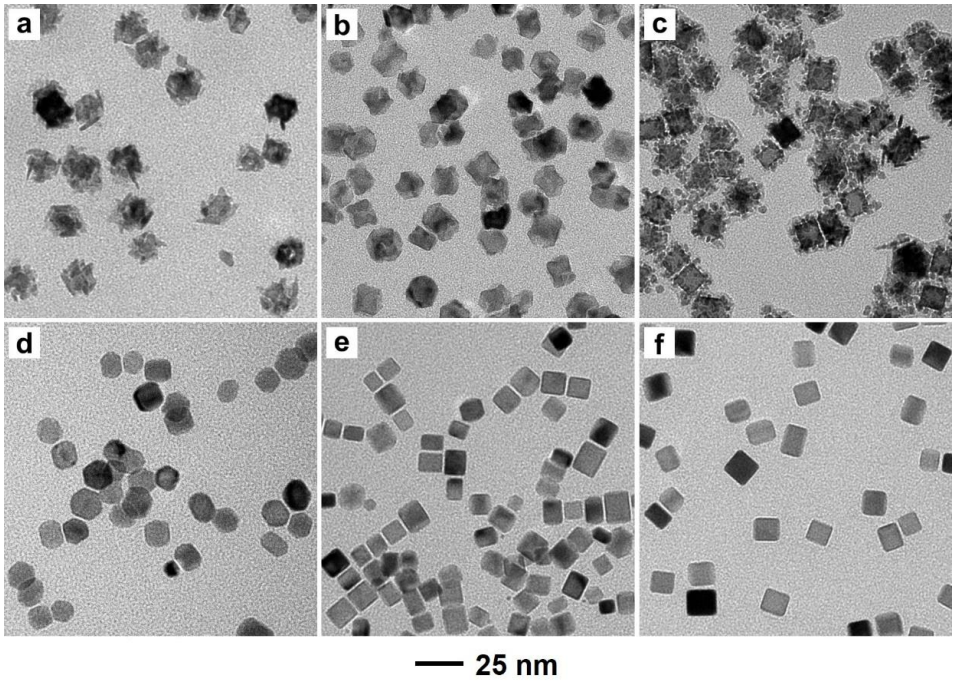

Figure 6.8. TEM images of the Pd–Ru nanocrystals prepared using the standard protocol except for the involvement of different amounts of KBr and Ru(III) precursor: (a) 50 mg of KBr and 2.4 mg of Ru(III) precursor, (b) 5 mg of KBr and 2.4 mg of Ru(III) precursor, (c) no KBr and 2.4 mg of Ru(III) precursor, (d) 50 mg of KBr and no Ru(III) precursor, (e) 5 mg of KBr and no Ru(III) precursor, and (f) no KBr and no Ru(III) precursor.

I also varied the amount of KBr to examine its impact on the formation of Pd@Ru core–frame cuboctahedra. When the amount of KBr was increased to 50 mg, the Pd cores in the resultant nanocrystals were severely deformed (Figure 6.8a), suggesting enhancement in the etching relative to the standard protocol. In contrast, if the amount of KBr was decreased to 5 mg, the obtained nanocrystals showed slightly truncated corners and concave facets, implying weakened etching than the standard protocol (Figure 6.8b). Especially, when the synthesis was conducted in the absence of KBr, the cubic shape of the Pd cores could be well preserved in the products, with Ru atoms deposited on the surface in an island growth mode (Figure 6.8c). To investigate the explicit effect of KBr

on the oxidative etching of Pd seeds, I also conducted a set of experiments in the absence of Ru(III) precursor. With the addition of 50 mg of KBr, the Pd cubic seeds evolved into cuboctahedra, clearly showing the involvement of oxidative etching (Figure 6.8d) [44]. If the amount of KBr was decreased to 5 mg, only a small portion of the Pd cubic seeds showed truncation at corners (Figure 6.8e). When the control experiment was conducted in the absence of both KBr and Ru(III) precursor, the Pd cubic seeds were able to retain their sharp corners and well-defined {100} facets (Figure 6.8f). These results suggest that the amount of KBr played a significant role in affecting the oxidative etching of Pd seeds during a synthesis, with an increase in the amount of KBr leading to more substantial oxidative etching and thus more truncation for the Pd seeds.

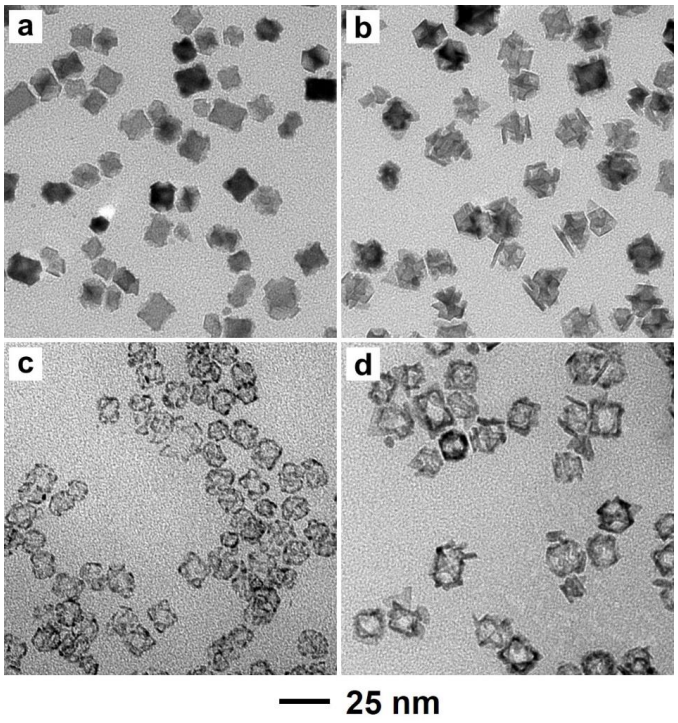

Figure 6.9. TEM images of Pd–Ru nanocrystals and the corresponding Ru nanoframes prepared using the standard protocol except for the use of (a and c) 1.2 and (b and d) 4 mg of Ru(III) precursor, respectively.

In a standard synthesis, the Pd core in the final Pd@Ru core–frame nanocrystal took a cuboctahedral shape (Figure 6.2). In comparison, when the standard synthesis was conducted in the absence of Ru(III) precursor, the Pd cubic seeds evolved into truncated cubes (Figure 6.6a), implying that the presence of Ru(III) precursor also exerted a significant impact on the shape evolution of the Pd seeds. I further varied the amount of Ru(III) precursor to investigate its impact on the formation of Pd@Ru core–frame cuboctahedra. Figure 6.9a shows the Pd–Ru nanocrystals obtained using the standard protocol except for the involvement of 1.2 mg of Ru(III) precursor. Compared with the standard sample, both the truncation at corners and the concaveness on the side faces of the products were largely suppressed. Conversely, when the amount of Ru(III) precursor was increased to 4 mg, the cores in the final products were severely deformed, confirming that an increase in the amount of Ru(III) precursor would facilitate deformation to the Pd cores (Figure 6.9b). The involved reaction could be described as the following:

$$2Ru^{3+} + 3Pd + 12Br^{-} \rightarrow 2Ru + 3PdBr_4^{2-} \quad (2)$$

This reaction can be referred to as the Br^{-}-assisted galvanic replacement between the Pd seeds and Ru(III) ions. Since the standard reduction potential of $PdBr_4^{2-}$/Pd is 0.49 V relative to the standard hydrogen electrode (SHE) while the reduction potential of Ru^{3+}/Ru is 0.39 V *versus* SHE [45], the galvanic replacement between Pd and Ru(III) ions is not thermodynamically favored under the standard conditions. However, the presence of Pd seeds was able to facilitate the reduction of Ru(III) ions, promoting heterogeneous nucleation and thereby underpotential galvanic replacement [46]. Figure 6.9, c and d, shows the resultant Ru cuboctahedral nanoframes after subjecting the Pd–Ru nanocrystals to wet chemical etching. When the amount of Ru(III) precursor was reduced to 1.2 mg, the

resultant Ru nanoframes only had a ridge thickness of 3 atomic layers. As the amount of Ru(III) precursor was increased to 4 mg, the ridge thickness of the resultant Ru nanoframes approached 2.1 nm, or approximately 10 atomic layers. Taken together, by varying the amount of Ru(III) precursor involved, I was able to tune the ridge thickness of the Ru cuboctahedral nanoframes in the range of 3–10 atomic layers.

Since galvanic replacement is strongly dependent on the reaction temperature, I also evaluated the impact of this parameter on the formation of Ru nanoframes. Figure 6.10 shows TEM images of the products obtained using the standard protocol except for the use of different reaction temperatures. When the synthesis was conducted at 140 °C, the resultant nanocrystals contained a mix of truncated cubes, cuboctahedra, and octahedra (Figure 6.10a). According to the ICP-MS data, the weight percentage of Ru in the products was only 0.6 wt.% whereas that of Pd was 99.4 wt.%. This result could be ascribed to the fact that at a relatively low reaction temperature of 140 °C, the galvanic replacement between the Pd seeds and Ru(III) ions was largely suppressed and consequently the synthesis was largely dominated by oxidative etching. As a result, the Pd cubic seeds evolved into truncated cubes, cuboctahedra, and octahedra through oxidative etching and regrowth of Pd [41]. When the reaction temperature was elevated to 160 °C, the products show truncated corners and concave facets (Figure 6.10b), but not as notable as those in the standard sample. The ICP-MS data indicates that the weight percentage of Ru in the Pd–Ru nanocrystals was 10.8 wt.%, much lower than that of the standard sample (30.9 wt.%). When the reaction temperature was elevated to 200 °C and 220 °C, respectively, the galvanic replacement reaction was substantially promoted for the formation of nanocrystals with enhanced concave facets than the standard sample (Figure 6.10, c and d).

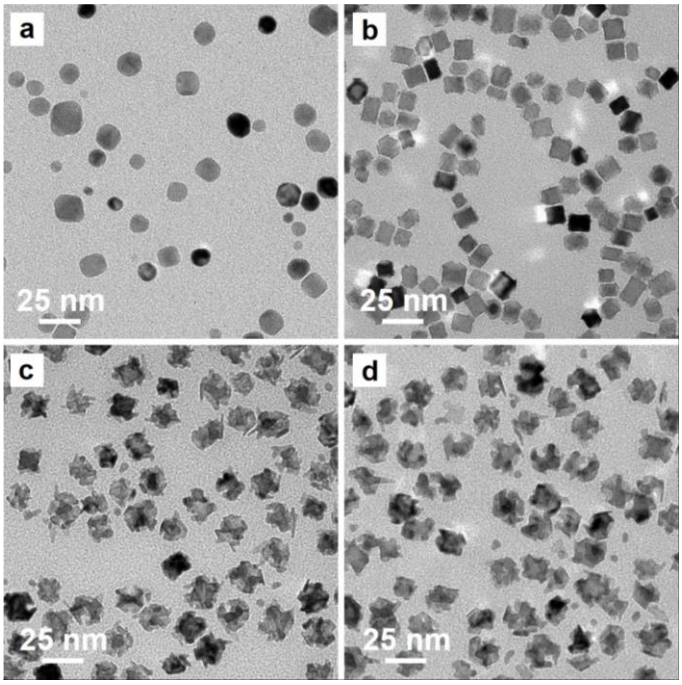

Figure 6.10. TEM images of the Pd–Ru nanocrystals prepared using the standard protocol except for the use of different temperatures: (a) 140, (b) 160, (c) 200, and (d) 220 °C.

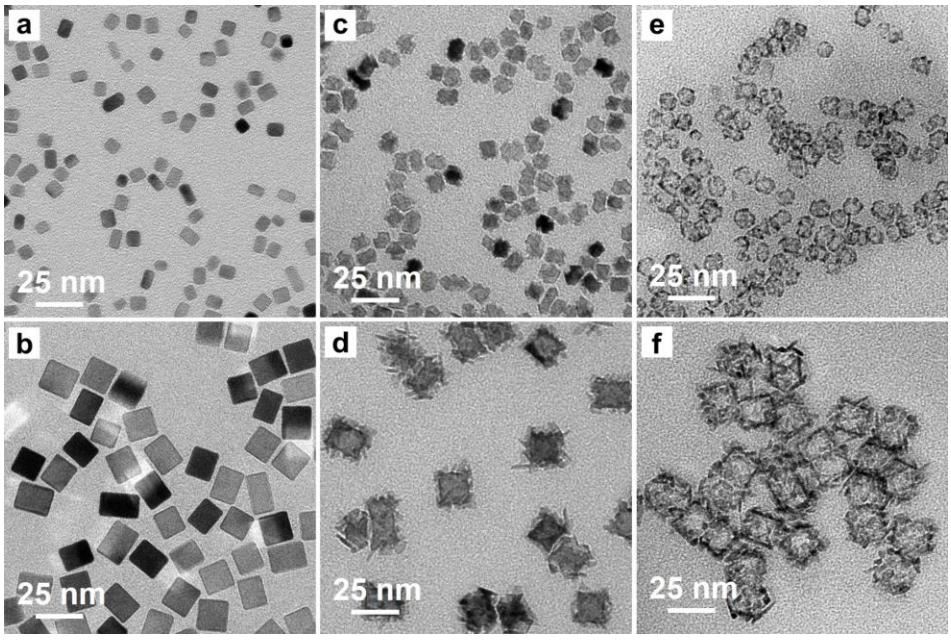

Figure 6.11. TEM images of (a) 6- and (b) 18-nm Pd cubes, and the corresponding (c and d) Pd–Ru nanocrystals and (e and f) hollow nanocrystals prepared using these seeds. All the other reaction conditions were kept the same as those in the standard protocol.

Accordingly, the weight percentages of Ru were increased to 33.1 and 36.2 wt.% for the Pd–Ru nanocrystals synthesized at 200 and 220 °C, respectively.

I also extended our synthetic protocol to Pd cubic seeds with different edge lengths to see whether I can tune the dimensions of the Ru cuboctahedral nanoframes. Figure 6.11, a and b, shows TEM images of 6- and 18-nm Pd cubic seeds, respectively, both enclosed by well-defined {100} facets. When the 6-nm Pd cubes were used as seeds, the as-obtained Pd–Ru nanocrystals featured truncated corners and concave facets, as well as a cuboctahedral shape (Figure 6.11c). In contrast, when the 18-nm Pd cubes were used, the majority of the Pd cores in the Pd–Ru nanocrystals were still cubic (with slight corner truncations only) while the Ru atoms were deposited in an island growth mode (Figure 6.11d). The distinctive growth patterns could be attributed to the different sizes of the Pd seeds. When the amount of Pd cubic seeds was fixed, the Pd nanocubes with an enlarged size have a decreased corner area owing to the low surface-to-volume ratio. Since the corner atoms are the most active sites because of the lowest coordination [13], both oxidative etching and Br^--assisted galvanic replacement would be suppressed for enlarged Pd nanocubes. As a consequence, Ru atoms were mainly generated through chemical reduction by TEG and then deposited on the Pd seeds. When the deposition of Ru atoms was faster than surface diffusion, the Ru atoms would follow an island growth mode and yield a rough surface. Figure 6.11, e and f, shows the resultant hollow nanocrystals after selective removal of the remaining Pd cores. For the products prepared from 6-nm Pd cubes, the Ru atoms were mainly distributed in the edges, which is indicative of a frame structure (Figure 6.11e). With respect to those prepared from 18-nm Pd cubes, the as-obtained hollow nanocrystals were characterized by a rough surface (Figure 6.11f).

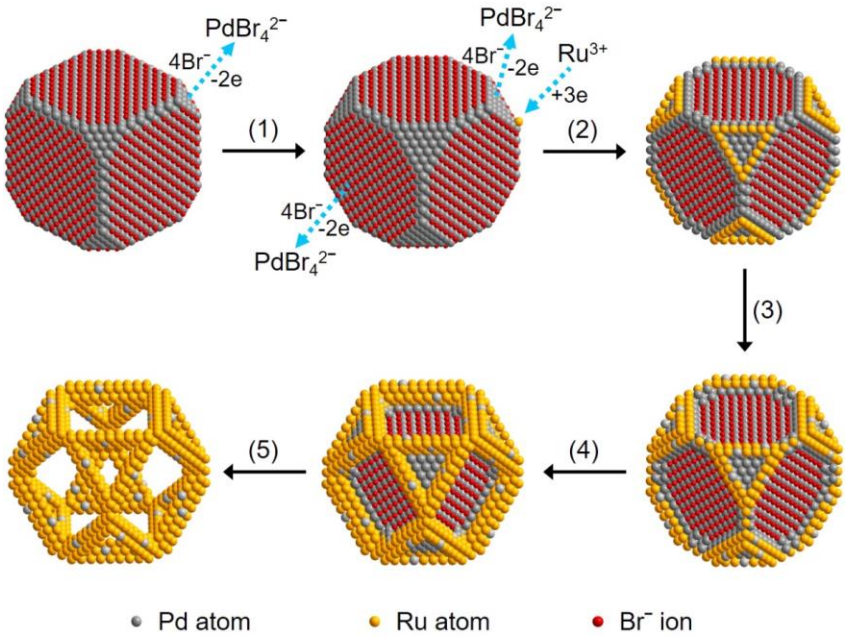

Figure 6.12. Schematic illustration of major steps involved in the formation of Ru cuboctahedral nanoframes: (1) oxidative etching of a Pd nanocube by Br^- ions; (2, 3) site-selected deposition of Ru atoms at the corners and edges *via* Br^--assisted galvanic replacement between the Pd seeds and Ru(III) ions; (4) formation of a Pd@Ru core–frame cuboctahedron with concave facets; and (5) formation of a Ru cuboctahedral nanoframe through selective removal of the remaining Pd in the core by wet chemical etching.

Figure 6.12 illustrates a plausible mechanism responsible for the formation of the Pd@Ru core–frame cuboctahedra and Ru cuboctahedral nanoframes. At the beginning of the reaction, the Pd cube was oxidatively etched by Br^- ions and evolves into a truncated Pd cube (step 1) [43]. The start of reaction with oxidative etching can be rationalized by the fact that the oxidative etching derived from Br^-/O_2 pair is more thermodynamically favorable than Br^--assisted galvanic replacement between Pd and Ru(III) ions [41]. After depletion of the dissolved O_2 in the reaction solution, Br^--assisted galvanic replacement would dominate the synthesis. Consequently, Ru(III) ions were reduced to Ru atoms at the expense of oxidation of the Pd atoms, followed by selectively deposited on the vertices and

edges of the Pd seed (step 2). As the reaction was continued, the concaveness on the surface was gradually reinforced while more Ru atoms were piled up at the edges of the Pd seed (step 3). Eventually, the Pd@Ru core–frame cuboctahedron with concaveness on the side faces was formed (step 4). By subjecting the core–frame cuboctahedron to wet chemical etching, the remaining Pd in the core was selectively removed and the cuboctahedral nanoframe mainly composed of Ru was obtained (step 5).

Evaluation of Thermal Stability. When used as catalysts for ammonia synthesis, CO oxidation, and CO_2 methanation, Ru nanocrystals are anticipated to retain their morphology and crystal phase, and thus their catalytic performance at elevated temperatures [19, 47, 48]. To this end, it is essential to investigate the stability of both the frame structure and the *fcc* phase under thermal stress for the Ru nanoframes. As for the frame structure, I evaluate the thermal stability by heating the nanoframes to various temperatures in the range of 250–400 °C under Ar atmosphere and then analyzed by TEM. When the sample was heated to temperatures below 300 °C (Figure 6.13, a and b), both the frame structure and the cuboctahedral shape remain intact. As the temperature was increased to 350°C, the sample still featured a frame structure, except for the fragmentation of a portion of their edges (Figure 6.13c). When I further elevated the temperature to 400 °C, most of the edges of the nanoframes were broken in response to the thermal stress and consequently, the frame structure was largely lost (Figure 6.13d).

I also assessed the thermal stability of the *fcc* phase in the Ru nanoframes by conducting *in situ* XRD analysis (Figure 6.14). At a heating temperature of 50 °C, I could clearly observe two diffraction peaks, including (111) and (200), in the XRD pattern, suggesting an *fcc* phase for the nanoframes. The *fcc*-(111) and *fcc*-(200)

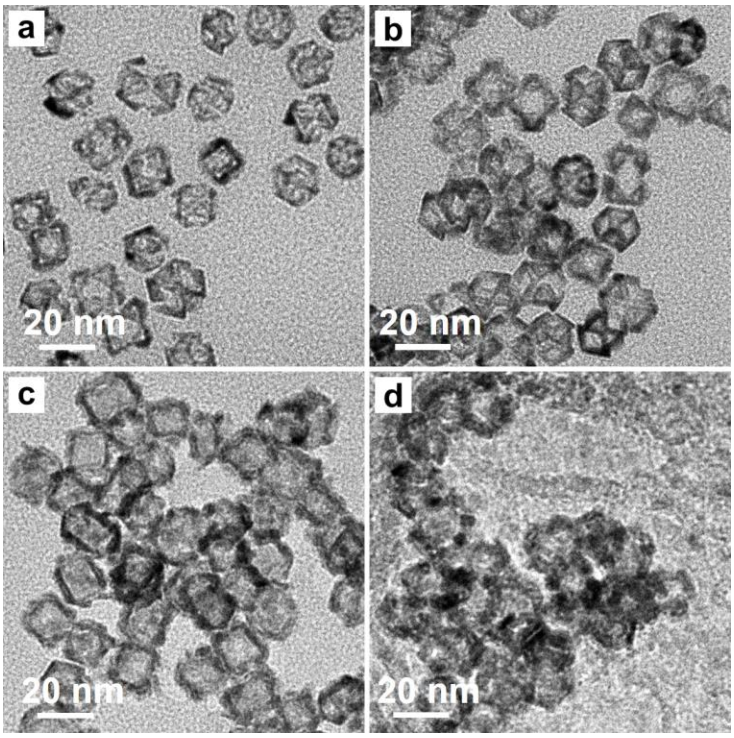

Figure 6.13. TEM images of the Ru cuboctahedral nanoframes upon heating for 1 h at various temperatures: (a) 250, (b) 300, (c) 350, and (d) 400 °C, respectively, suggesting that the frame morphology could be largely preserved up to 350 °C.

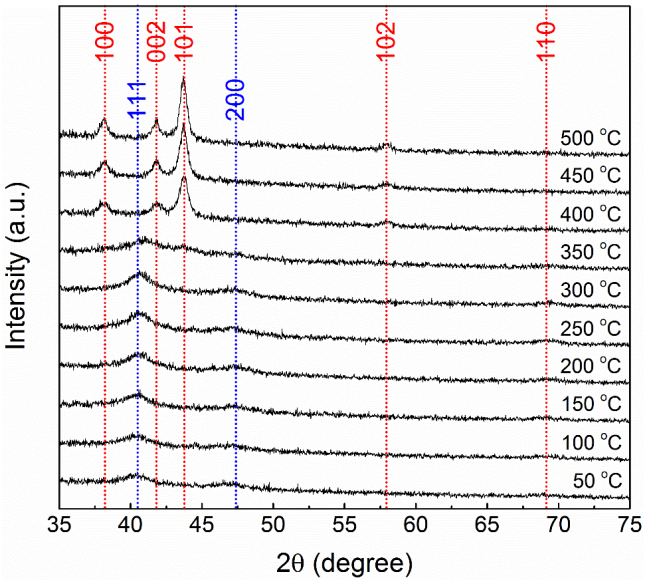

Figure 6.14. XRD patterns recorded *in situ* from the Ru cuboctahedral nanoframes after heating to different temperatures up to 500 °C under Ar atmosphere, suggesting that the *fcc* phase could be well preserved up to 350 °C. The characteristic peaks of *hcp* and *fcc* Ru are marked by red and blue dashed lines, respectively.

peaks could be well recognized until the sample was heated to 300 °C. When the temperature was increased to 350 °C, the XRD pattern was still dominated by the *fcc*-(111) and *fcc*-(200) peaks, together with a weak *hcp*-(101) peak. The appearance of the characteristic peak of *hcp* Ru suggests the initiation of crystal phase transition from *fcc* to *hcp* [36, 37]. In particular, upon heating to 400 °C, the characteristic peaks of *fcc* Ru disappeared while those of *hcp* Ru dominated the XRD pattern. As I further elevated the temperature to 450 and 500 °C, the intensity of *hcp*-(100), *hcp*-(002), and *hcp*-(101) peaks kept increasing due to sintering of the nanocrystals, indicating the complete transition from *fcc* to *hcp* phase. Taken together, the Ru nanoframes could largely retain both the frame structure and the *fcc* phase up to 350 °C when subjected to thermal stress.

Evaluation of Catalytic Performance towards Hydrazine Decomposition. Ru nanocrystals are well documented as attractive materials in catalyzing hydrazine decomposition at room temperature, which typically occurs in two pathways: incomplete ($3N_2H_4 \rightarrow 4NH_3 + N_2$) and complete ($N_2H_4 \rightarrow N_2 + 2H_2$) [49]. Here I evaluated the catalytic performance of the Ru cuboctahedral nanoframes by comparing with that of *hcp*- and *fcc*-Ru nanoparticles towards hydrazine decomposition. Figure 6.15, a and b, shows TEM images of Ru nanoparticles with *hcp* and *fcc* phases, respectively, which were confirmed by XRD analysis. Figure 6.16a shows the time course plots for hydrazine decomposition in the presence of different Ru catalysts. The molar ratios of generated H_2 and N_2 over the initially added hydrazine (denoted as $n(N_2 + H_2)/n(N_2H_4)$) were derived as 0.5 and 0.7 for the *hcp*- and *fcc*-Ru nanoparticles, respectively. Specifically, the nanoparticles with an *fcc* phase exhibited 1.4-fold enhancement in terms of activity than their *hcp* counterparts towards hydrazine decomposition, demonstrating the superior

performance stemming from the *fcc* phase. In particular, the nanoframes exhibited a $n(N_2+H_2)/nN_2H_4$ ratio of 1.5, which was 3.0 and 2.1 times as high as that of *hcp* and *fcc* nanoparticles, respectively, indicating the capability of the frame structure in further boosting the performance.

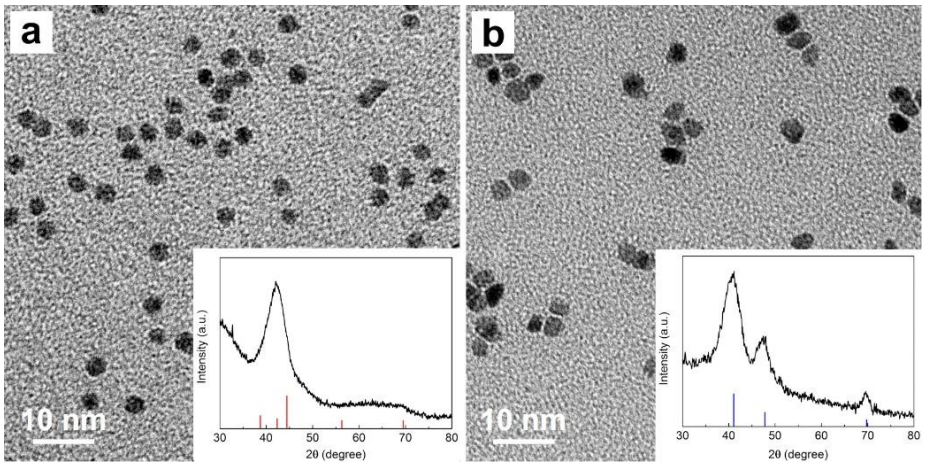

Figure 6.15. TEM images of the Ru nanoparticles with (a) *hcp* and (b) *fcc* phases, respectively. The insets show the corresponding XRD patterns. The characteristic peaks of *hcp* and *fcc* Ru are marked by red and blue lines, respectively. Red bars: JCPDS no. 06-0663 (*hcp* Ru). Blue bars: JCPDS no. 88-2333 (*fcc* Ru).

Figure 6.16b shows a summary of H_2 selectivity for the *hcp*-Ru nanoparticles, *fcc*-Ru nanoparticles, and *fcc*-Ru nanoframes, which was derived as 7.8%, 13.7%, and 43.9%, respectively. Noticeably, the nanoframes that have an *fcc* phase and a highly open structure exhibited 5.6- and 3.2-fold enhancements in terms of H_2 selectivity when compared with *hcp* and *fcc* nanoparticles, respectively. It has been reported that the decomposition of hydrazine molecules on Ru metal surfaces involves multiple steps, including the N–N bond

scission to NH_2, the stepwise H stripping from N_2H_x (x = 1−4) and/or NH_2, the formation of H_2, N_2, and NH_3, and the desorption of these small molecules from metal surfaces [50]. Density functional theory calculations suggested that compared with *hcp*-Ru nanoparticles, the *fcc*-Ru nanocrystals could reduce the activation energy of N–N bond scission and thereby facilitating hydrazine decomposition [35–37]. Besides, the low-coordination atoms exposed on the surface of the nanoframes were found to bind more strongly to the N-based molecules and intermediates, which could also enhance both the activity and H_2 selectivity [35, 50–52]. Thus far, the mechanism underlying the decomposition of hydrazine molecules on the *fcc*-Ru nanocrystals remains elusive and yet to be uncovered. In the future, both experimental and computational efforts are worth devoting to unveiling the role of the frame structure and *fcc* phase of Ru nanoframes in catalyzing hydrazine decomposition.

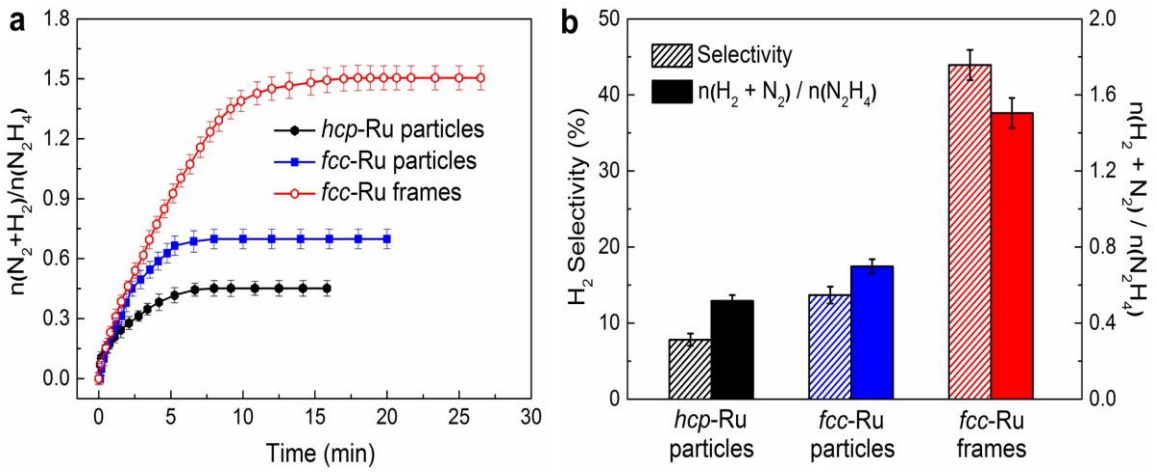

Figure 6.16. Comparison of the activities of various catalysts based upon *hcp*-Ru nanoparticles, *fcc*-Ru nanoparticles, and *fcc*-Ru cuboctahedral nanoframes towards hydrazine decomposition. (a) Time course plots for hydrazine decomposition in aqueous solutions in the presence of different catalysts. (b) Selectivity towards the generation of hydrogen from hydrazine decomposition on different Ru catalysts.

6.3 Conclusion

I have developed a method for the facile synthesis of Ru cuboctahedral nanoframes. The method involves a number of processes, including oxidative etching, galvanic replacement, site-selected deposition, and chemical etching. Specifically, I started with the synthesis of Pd@Ru core–frame cuboctahedra through the integration of Br^--assisted galvanic replacement reaction between Pd and Ru(III) ions with site-selected deposition of Ru atoms onto the edges and corners. The as-synthesized core–frame cuboctahedra were then subjected to chemical etching for the selective removal of the Pd cores, generating Ru cuboctahedral nanoframes with their ridges controllable in the range of 3–10 atomic layers thick. Significantly, the packing of the deposited Ru atoms could be dictated by the underlying Pd template to take on an *fcc* phase not favored by bulk Ru. Both the frame structure and the *fcc* phase of the Ru nanoframes could be preserved up to 350 °C under thermal stress. The Ru nanoframes, characterized by a highly open structure and an *fcc* phase, exhibited substantially enhanced activity and H_2 selectivity towards hydrazine decomposition relative to both the *hcp*- and *fcc*-Ru nanoparticles. Altogether, this work offers an effective route to the synthesis of Ru nanoframes with an unconventional crystal structure for engineering the catalytic properties of Ru nanocrystals.

6.4 Experimental Section

Chemicals and Materials. Ethylene glycol (EG, 99%) was obtained from J. T. Baker. TEG (99%), L-ascorbic acid (AA, 99%), PVP (MW ≈ 55,000), sodium tetrachloropalladate(II) (Na_2PdCl_4, 99.99%), formaldehyde (HCHO, 36.5–38%), KBr (99%), hydrochloric acid (HCl, 37%), iron(III) chloride ($FeCl_3$, 97%), and hydrazine

monohydrate ($N_2H_4 \cdot H_2O$, 98%) were all purchased from Sigma-Aldrich. Ruthenium 2,4-pentaedionate ($Ru(acac)_3$, 24% Ru) was obtained from Alfa Aesar. All the chemicals were used without further purification. Deionized (DI) water with a resistivity of 18.2 MΩ cm was used to prepare aqueous solutions.

Synthesis of 6-, 10-, and 18-nm Pd Cubes. In a typical synthesis of 10-nm Pd cubes [39], an aqueous solution containing AA (60 mg), PVP (105 mg), and KBr (300 mg) was placed in an oil bath and heated to 80 °C under magnetic stirring. After 10 min, 3 mL of an aqueous Na_2PdCl_4 solution (19 mg mL^{-1}) was injected into the preheated solution in one shot. The reaction was allowed to continue for 3 h before quenching in an ice-water bath. The solid products were collected by centrifugation, washed three times with water to remove excess PVP and inorganic ions. For the syntheses of 6- and 18-nm Pd cubes, a similar procedure was used except that 300 mg of KBr was replaced by 5 mg of KBr and 185 mg of KCl, and 600 mg of KBr, respectively.

Synthesis of Truncated Pd Cubes. The truncated Pd cubes were synthesized based on a reported protocol [40]. In a typical synthesis, 0.54 mg of 10-nm Pd cubes, 105 mg of PVP, 100 μL of HCHO, and 8 mL of DI water were mixed and heated to 60 °C in an oil bath under magnetic stirring. After 10 min, 0.6 mL of an aqueous Na_2PdCl_4 solution (9.7 mg mL^{-1}) was injected into the preheated mixture in one shot and the reaction was allowed to continue for 3 h. The solid products were collected by centrifugation, washed three times with water, and then dispersed in TEG for further use.

Synthesis of Pd@Ru Core–Frame Cuboctahedra. In a standard synthesis, 1 mg of 10-nm Pd cubes, 2.4 mg of $Ru(acac)_3$, 20 mg of KBr, and 50 mg of PVP were mixed in 10 mL of TEG and then transferred into a 20-mL vial. The mixture was heated for 6 h at 180

°C in an oil bath under magnetic stirring. After the completion of reaction, the solid products were collected by centrifugation, washed once with acetone and twice with water, and then dispersed in 2 mL of water for further use.

Fabrication of Ru Cuboctahedral Nanoframes. The etching solution was first prepared by dissolving $FeCl_3$ (30 mg), PVP (50 mg), and KBr (300 mg) in a mixture of HCl (0.18 mL) and DI water (4.82 mL). Afterwards, 0.1 mL of the aqueous suspension of the Pd@Ru core–frame cuboctahedra was injected into the etching solution. The mixture was placed in an oil bath and heated to 100 °C under magnetic stirring. After 30 min, the solid products were collected by centrifugation, washed three times with water, and then dispersed in water for further use.

Synthesis of *hcp*- and *fcc*-Ru Nanoparticles. In a typical synthesis of *hcp*-Ru nanoparticles, 7.5 mg of $Ru(acac)_3$ and 50 mg of PVP were mixed in 5 mL of EG and heated to 180 °C in an oil bath under magnetic stirring. After 2 h, the reaction was quenched in an ice-water bath. The Ru nanoparticles with an *fcc* phase were prepared using a reported protocol with minor modifications [28]. Typically, 5 mL of TEG solution containing 4.2 mg of $Ru(acac)_3$ and 5.5 mg of PVP was transferred into a 20-mL vial, which was then placed in an oil bath heated to 200 °C. After 3 h, the solid products were collected by centrifugation, washed once with acetone and twice with water. The as-synthesized *hcp*- and *fcc*-Ru nanoparticles were then dispersed in DI water for further use.

Characterizations. All TEM images were acquired on a Hitachi 7700 microscope. HAABF- and HAADF-STEM as well as EDX mapping images were acquired using an aberration-corrected Hitachi HD2700 STEM at the Institute for Electronics and Nanotechnology (IEN, Georgia Institute of Technology) and a Cs-corrected FEI Titan

80/300 kV TEM/STEM microscope at the Oak Ridge National Laboratory (ORNL). ICP-MS (NexION 300Q, PerkinElmer) was used for the quantitative analysis of metal contents in various samples.

Evaluation of Thermal Stability. To assess the thermal stability of the frame structure of the Ru nanoframes, a thermal evaporator (Edwards E306 A) was used to heat the sample to temperatures in the range of 250–400 °C, followed by TEM analysis. The stability of the crystals phase in the *fcc*-Ru nanoframes under thermal stress was evaluated using XRD coupled with *in situ* heating. The *in situ* XRD patterns were collected by heating the sample to temperatures ranging from 50 to 500 °C using an Anton Paar XRK hot stage, and then processed with HighScore Plus (PANalytical). To obtain sufficient signals, each pattern was collected for 1 h every 50 °C, with a heating rate of 5 °C min^{-1}. All the measurements were conducted under Ar atmosphere to avoid possible oxidation.

Hydrazine Decomposition. The measurement was carried out at room temperature. Typically, an aqueous suspension containing 0.1 mg of Ru catalyst was added into a two-necked round bottomed flask under magnetic stirring, with one opening connected to a gas burette. Afterwards, 10 μL of $N_2H_4 \cdot H_2O$ was added into the flask in one shot. The volume of produced gases was monitored by the gas burette after passing through a 1.0 M HCl solution to ensure the complete removal of ammonia.

6.5 Notes to Chapter 6

Part of this chapter is adapted from the paper "Ruthenium Nanoframes in the Face-Centered Cubic Phase: Facile Synthesis and Their Enhanced Catalytic Performance" published in *ACS Nano* [53].

6.6 References

[1] Wang, W.; Satyavolu, N. S. R.; Wu, Z.; Zhang, J.; Zhu, J.; Lu, Y. *Angew. Chem. Int. Ed.* **2017**, *56*, 6798–6802.

[2] Nehl, C. L.; Grady, N. K.; Goodrich, G. P.; Tam, F.; Halas, N. J.; Hafner, J. H. *Nano Lett.* **2004**, *4*, 2355–2359.

[3] Sneed, B. T.; Brodsky, C. N.; Kuo, C.; Lamontagne, L. K.; Jiang, Y.; Wang, Y.; Tao, F.; Huang, W.; Tsung, C. *J. Am. Chem. Soc.* **2013**, *135*, 14691–14700.

[4] Sun, X.; Kim, J.; Gilroy, K. D.; Liu, J.; König, T. A. F.; Qin, D. *ACS Nano* **2016**, *10*, 8019–8025.

[5] Zhao, M.; Wang, X.; Yang, X.; Gilroy, K. D.; Qin, D.; Xia, Y. *Adv. Mater.* **2018**, *30*, 1801956.

[6] Xia, Y.; Li, W.; Cobley, C. M.; Chen, J.; Xia, X.; Zhang, Q.; Yang, M.; Cho, E. C.; Brown, P. K. *Acc. Chem. Res.* **2011**, *44*, 914–924.

[7] Park, J.; Kwon, T.; Kim, J.; Jin, H.; Kim, H. Y.; Kim, B.; Joo, S. H.; Lee, K. *Chem. Soc. Rev.* **2018**, *47*, 8173–8202.

[8] Wang, X.; Ruditskiy, A.; Xia, Y. *Natl. Sci. Rev.* **2016**, *3*, 520–533.

[9] Ni, B.; Wang, X. *Adv. Sci.* **2015**, *2*, 1500085.

[10 Fang, Z.; Wang, Y.; Liu, C.; Chen, S.; Sang, W.; Wang, C.; Zeng, J. *Small* **2015**, *11*, 2593–2605.

[11] Xie, S.; Lu, N.; Xie, Z.; Wang, J.; Kim, M. J.; Xia, Y. *Angew. Chem. Int. Ed.* **2012**, *51*, 10266–10270.

[12] McEachran, M.; Keogh, D.; Pietrobon, B.; Cathcart, N.; Gourevich, I.; Coombs, N.; Kitaev, V. *J. Am. Chem. Soc.* **2011**, *133*, 8066–8069.

[13] Park, J.; Wang, H.; Vara, M.; Xia, Y. *ChemSusChem* **2016**, *9*, 2855–2861.

[14] Gilroy, K. D.; Yang, X.; Xie, S.; Zhao, M.; Qin, D.; Xia, Y. *Adv. Mater.* **2018**, *30*, 1706312.

[15] Xia, Y.; Gilroy, K. D.; Peng, H.; Xia, X. *Angew. Chem. Int. Ed.* **2017**, *56*, 60–95.

[16] Zhang, Z.; Luo, Z.; Chen, B.; Wei, C.; Zhao, J.; Chen, J.; Zhang, X.; Lai, Z.; Fan, Z.; Tan, C.; Zhao, M.; Lu, Q.; Li, B.; Zong, Y.; Yan, C.; Wang, G.; Xu, Z.; Zhang, H. *Adv. Mater.* **2016**, *28*, 8712–8717.

[17] Ham, S.; Jang, H.-J.; Song, Y.; Shuford, K. L.; Park, S. *Angew. Chem. Int. Ed.* **2015**, *127*, 9153–9156.

[18] Su, F.; Lv, L.; Lee, F. Y.; Liu, T.; Cooper, A. I.; Zhao, X. S. *J. Am. Chem. Soc.* **2007**, *129*, 14213–14223.

[19] Joo, S. H.; Park, J. Y.; Renzas, J. R.; Buycher, D. R.; Huang, W.; Somorjai, G. A. *Nano Lett.* **2010**, *10*, 2709–2713.

[20] Honkala, K.; Hellman, A.; Remediakis, I. N.; Logadottir, A.; Carlsson, A.; Dahl, S.; Christensen, C. H.; Nørskov, J. K. *Science* **2005**, *307*, 555–558.

[21] Kitano, M.; Kanbara, S.; Inoue, Y.; Kuganathan, N.; Sushko, P. V.; Yokoyama, T.; Hara, M.; Hosono, H. *Nat. Commun.* **2015**, *6*, 6731–6739.

[22] Wang, W.; Wang, S.; Ma, X.; Gong, J. *Chem. Soc. Rev.* **2011**, *40*, 3703–3727.

[23] Chen, M.; Wu, B.; Yang, J.; Zheng, N. *Adv. Mater.* **2012**, *24*, 862–879.

[24] Wang, Y.; Long, W.; Wang, L.; Yuan, R.; Lgnaszak, A.; Fang, B.; Wilkinson, D. P. *Energy Environ. Sci.* **2018**, *11*, 258–275.

[25]Grzelczak, M.; Perez-Juste, J.; Mulvaney, P.; Liz-Marzan, L. M. *Chem. Soc. Rev.* **2008**, *37*, 1783–1791.

[26] Xie, S.; Liu, X.; Xia, Y. *Nano Res.* **2015**, *8*, 82–96.

[27] Vitos, L.; Ruban, A. V.; Skriver, H. L.; Kollár, J. *Surf. Sci.* **1998**, *411*, 186–202.

[28] Kusada, K.; Kobayashi, H.; Yamamoto, T.; Matsumura, S.; Sumi, N.; Sato, K.; Nagaoka, K. Kubota, Y.; Kitagawa, H. *J. Am. Chem. Soc.* **2013**, *135*, 5493–5496.

[29] Gloag, L.; Benedetti, T. M. Cheong, S.; Marjo, C. E.; Gooding, J. J.; Tilley, R. D. *J. Am. Chem. Soc.* **2018**, *140*, 12760–12764.

[30] Gloag, L.; Benedetti, T. M.; Cheong, S.; Li, Y.; Chan, X.; Lacroix, L.; Chang, S.; Arenal, R.; Florea, I.; Barron, H.; Barnard, A. S.; Henning, A. M.; Zhao, C.; Schuhmann, W.; Gooding, J. J.; Tilley, R. D. *Angew. Chem. Int. Ed.* **2018**, *57*, 10241–10245.

[31] Fan, Z.; Zhang, H. *Chem. Soc. Rev.* **2016**, *45*, 63−82.

[32] Fan, Z.; Zhang, H. *Acc. Chem. Res.* **2016**, *49*, 2841–2850.

[33] Cheng, H.; Yang, N.; Lu, Q.; Zhang, Z.; Zhang, H. *Adv. Mater.* **2018**, *30*, 1707189.

[34] Lu, Q.; Wang, A.; Gong, Y.; Hao, W.; Cheng, H.; Chen, J.; Li, B.; Yang, N.; Niu, W.; Wang, J.; Yu, Y.; Zhang, X.; Chen, Y.; Fan, Z.; Wu, X.; Chen, J.; Luo, J.; Li, S.; Gu, L.; Zhang, H. *Nat. Chem.* **2018**, *10*, 456–461.

[35] Zhao, M.; Figueroa-Cosme, L.; Elnabawy, A. O.; Vara, M.; Yang, X.; Roling, L. T.; Chi, M.; Mavrikakis, M.; Xia, Y. *Nano Lett.* **2016**, *16*, 5310–5317.

[36] Zhao, M.; Elnabawy, A. O.; Vara, M.; Xu, L.; Hood, Z. D.; Yang, X.; Gilroy, K. D.; Figueroa-Cosme, L.; Chi, M.; Mavrikakis, M.; Xia, Y. *Chem. Mater.* **2017**, *29*, 9227–9237.

[37] Zhao, M.; Xu, L.; Vara, M.; Elnabawy, A. O.; Gilroy, K. D.; Hood, Z. D.; Zhou, S.; Figueroa-Cosme, L.; Chi, M.; Mavrikakis, M.; Xia, Y. *ACS Catal.* **2018**, *8*, 6948–6960.

[38] Ye, H.; Wang, Q.; Catalano, M.; Lu, N.; Vermeylen, J.; Kim, J. M.; Liu, Y.; Sun, Y.; Xia, X. *Nano Lett.* **2016**, *16*, 2812–2817.

[39] Jin, M.; Liu, H.; Zhang, H.; Xie, Z.; Liu, J.; Xia, Y. *Nano Res.* **2011**, *4*, 83–91.

[40] Jin, M.; Zhang, H.; Xie, Z.; Xia, Y. *Energy Environ. Sci.* **2012**, *5*, 6352–6357.

[41] Liu, M.; Zheng, Y.; Zhang, L.; Guo, L.; Xia, Y. *J. Am. Chem. Soc.* **2013**, *135*, 11752–11755.

[42] Long, R.; Zhou, S.; Wiley, B. J.; Xiong, Y. *Chem. Soc. Rev*. **2014**, *43*, 6288–6310.

[43] Zhang, H.; Jin, M.; Wang, J.; Li, W.; Camargo, P. H. C.; Kim, M. J.; Yang, D.; Xie, Z.; Xia, Y. *J. Am. Chem. Soc.* **2011**, *133*, 6078–6089.

[44] Wang, Z.; Wang, H.; Zhang, Z.; Yang, G.; He, T.; Yin, Y.; Jin, M. *ACS Nano* **2017**, *11*, 163–170.

[45] Lide, D.; Haynes, W. *CRC Handbook of Chemistry and Physics*, 90th ed.; CRC Press; Boca Raton, FL, **2009**.

[46] Zhang, Z.; Liu, Y.; Chen, B.; Gong, Y.; Gu, L.; Fan, Z.; Yang, N.; Lai, Z.; Chen, Y.; Wang, J.; Huang, Y.; Sindoro, M.; Niu, W.; Li, B.; Zong, Y.; Yang, Y.; Huang, X.; Huo, F.; Huang, W.; Zhang, H. *Adv. Mater.* **2016**, *28*, 10282–20286.

[47] Kitano, M.; Inoue, Y.; Yamazaki, Y.; Hayashi, F.; Kanbara, S.; Matsuishi, S.; Yokoyama, T.; Kim, S.-W.; Hara, M.; Hosono, H. *Nat. Chem.* **2012**, *4*, 934–940.

[48] Abdel-Mageed, A. M.; Widmann, D.; Olesen, S. E.; Chorkendroff, I.; Behm, R. J. *ACS Catal.* **2018**, *8*, 5399–5414.

[49] Singh, S. K.; Zhang, X.; Xu, Q. *J. Am. Chem. Soc.* **2009**, *131*, 9894–9895.

[50] Rauscher, H.; Kostov, K. L.; Menzel, D. *Chem. Phys.* **1993**, *177*, 473−496.

[51] Yao, Q.; Lu, Z.; Yang, K.; Chen, X.; Zhu, M. *Sci. Rep.* **2015**, *5*, 15186.

[52] Furukawa, S.; Suzuki, R.; Ochi, K.; Yashima, T.; Komatsu, T. *ChemSusChem* **2015**, *8*, 2028−2030.

[53] Zhao, M.; Hood, Z. D.; Vara, M.; Gilroy, K. D.; Chi, M.; Xia, Y. *ACS Nano* **2019**, doi.org/10.1021/acsnano.9b02890.

CHAPTER 7

CONCLUSION AND FUTURE DIRECTIONS

7.1 Conclusion

The dissertation covers a number of synthetic approaches to the facile synthesis of Ru nanocrystals with an *fcc* phase and well-controlled surface structures. I began by developing a facile strategy based on seed-mediated growth for the fabrication of Ru cubic nanocages with an *fcc* phase. The success of this synthesis relied on the addition of adequate PVP into the reaction, an elevated reaction temperature, slow injection rate of Ru(III) precursor, and an appropriate amount of Ru(III) precursor, all of which enabled the layer-by-layer growth of Ru adatoms on the Pd seeds and thus the formation of Pd@Ru core−shell nanocubes. By subjecting the core−shell nanocubes to wet chemical etching for the selective removal of the Pd core, I could obtain Ru cubic nanocages which were characterized by well-defined {100} facets. Most interestingly, the Ru shells adopted an *fcc* structure, which can be readily switched to the *hcp* phase by increasing the amount of Ru(III) precursor. The size of the cubic nanocages was readily tuned by employing the Pd seeds with different edge lengths. The DFT calculations suggested that the *fcc* Ru nanocages could bind more strongly to the atomic N than *hcp* Ru nanoparticles, leading to a reduced activation energy barrier to N_2 dissociation for ammonia synthesis.

Next, I demonstrated the extension of the same rationale to the synthesis of Ru octahedral nanocages based on the combination of seed-mediated growth and selective etching. The as-synthesized Ru nanocages were characterized by the well-defined {111} facets, an *fcc* phase, as well as a wall thickness approaching five atomic layers. Compared

with the Ru cubic nanocages, the addition of KBr was essential to the layer-by-layer growth of Ru adatoms on the Pd octahedral seeds and thereby the formation of smooth Ru shells. I also realized the size control of the octahedral nanocages in the range of 12–26 nm. Significantly, the *fcc* phase in the nanocages could be well retained up to 300 °C. Based on the evaluation of catalytic performance, the {111} facets were found to be more active than {100} facet in catalyzing the reduction of 4-nitrophenol. The calculations results indicated that the Pd impurities in the nanocages were beneficial to the stabilization and activation of nitrogen, thus exhibiting superior performance than the conventional *hcp* Ru catalysts.

I then extended the synthetic protocol used for synthesizing Ru octahedral nanocages to the icosahedral nanocages that have a number of twin boundaries on the surface. Based on the integration of seed-mediated growth and wet-chemical etching, I successfully produced Ru icosahedral nanocages with an *fcc* phase. The role of KBr in the formation of Pd@Ru core–shell icosahedral nanocrystals with smooth shells was quantitatively studied, which could decelerate the reduction rate of Ru(III) precursor and thereby promoting the layer-by-layer growth of Ru atoms. Both the *fcc* phase and icosahedral shape of the Ru nanocages could be stable up to 300 °C. When used as catalysts, the Ru nanocages with cubic, octahedral, or icosahedral shape were demonstrated to show enhanced performance than their original Pd@Ru core−shell nanocrystals toward both the reduction of 4-nitrophenol and hydrazine decomposition. In particular, the icosahedral nanocages with twin boundaries on the surface showed enhanced activity and selectivity than their cubic and octahedral counterparts. Using DFT calculations for the prediction of performance toward N_2 dissociation, my collaborators verified that the twin boundaries of the *fcc*-Ru icosahedral nanocages with Pd impurities were more active than the conventional *hcp*-Ru

nanoparticles in stabilizing the N_2 dissociation transition state and thus reducing the overall reaction barrier and the competition with the N_2 desorption process.

Despite the success in the synthesis of various *fcc* Ru nanocages, the characteristic hollow interiors, ultrathin and porous walls would compromise their thermal stability and thus limiting their use in applications at elevated temperatures, including ammonia synthesis, CO oxidation, and CO_2 methanation. To this end, I have demonstrated a facile protocol for the synthesis of Ru octahedral nanocrystals with well-defined {111} facets and an increased thickness of 4.5 nm for the Ru shells. The formation of Ru-based octahedral nanocrystals depended on the leverage of 4.5-nm Rh cubes as seeds to favor the epitaxial growth of Ru atoms while achieving the smooth surface and well-defined shape. In comparison, if 6- and 10-nm Pd cubes served as the seeds, the as-synthesized nanocrystals featured a rough surface and a poorly defined shape. Most interestingly, the Ru shells in the octahedral nanocrystals were crystallized in an *fcc* phase instead of the *hcp* phase typical of bulk Ru. When subjected to thermal stress, the octahedral nanocrystals could well retain both the octahedral shape and *fcc* phase up to 400 °C. When employed as catalysts toward OER, the *fcc* Ru octahedra displayed a specific activity 4.4 times greater than that of *hcp* Ru nanoparticles. Additionally, the {111} facets on the *fcc* Ru nanocrystals were found to be more active than {100} facets in catalyzing OER.

In addition to Ru nanocages and solid octahedral nanocrystals, I also developed a facile route to the synthesis Ru nanoframes that are comprised of only corners and edges. The Pd@Ru core–frame cuboctahedra were first synthesized, which involved two major steps: *i*) evolution of the Pd cubic seeds to truncated Pd nanocubes as a result of oxidative etching ; and *ii*) formation of Pd@Ru core–frame cuboctahedra *via* Br^--assisted galvanic

replacement between the Pd seeds and Ru(III) ions, and site-selected deposition of Ru atoms. After selective removal of the Pd cores, I obtained Ru cuboctahedral nanoframes, whose ridge thickness could be readily tuned at an atomic scale, from 3 to 10 atomic layers by varying the amount of Ru(III) precursor. Significantly, the Ru atoms in the nanoframes followed the packing of the underlying Pd atoms and took on an *fcc* phase, instead of the conventional *hcp* phase found in bulk Ru. Under thermal stress, the Ru nanoframes could well preserve both the frame structure and the *fcc* phase up to 350 °C. When used as catalysts toward hydrazine decomposition, the Ru nanoframes that feature a highly open structure and an *fcc* phase, showed substantial enhancements in terms of activity and H_2 selectivity than both the *hcp*- and *fcc*-Ru nanoparticles.

Overall, my research offers a number of synthetic methods for engineering both the crystal phase and surface structures of Ru nanocrystals. A variety of nanostructures have been achieved, including nanocages with cubic, octahedral, and icosahedral shapes, solid octahedral nanocrystals, and nanoframes. The mechanistic understanding of the formation of various Ru nanocrystals has been well elucidated. Additionally, I have also subjected the *fcc*-Ru nanocrystals to thermal stress to gain knowledge about the thermal stability of both the *fcc* phase and the shapes of those novel nanomaterials. Both experimental and computational efforts provide a comprehensive understanding of the crystal phase- and surface structure-dependent catalytic properties of the *fcc*-Ru nanocrystals. This work not only offers a novel class of nanomaterials that will find widespread use in an array of applications, but also enriches the design of nanomaterials with controllable crystal structures.

7.2 Future Directions

The synthetic strategies described in this dissertation seek to achieve cost-effective and sustainable use of Ru by exploring nanocrystals that have novel crystal phase and optimal surface structures for catalytic applications. Despite the impressive accomplishments, a number of issues still remain and need to be addressed in order to reach the ultimate goal. One of the grand challenges is to improve the thermal stability of both the *fcc* phase and surface structures of Ru nanocrystals, especially the hollow nanocrystals including nanocages and nanoframes. Since the nanocage structure is far from equilibrium, it is inevitably susceptible to changes during the operation of a catalytic device. This can potentially be addressed by employing an inexpensive material (metal or inorganic compound) as the template to produce core–shell nanocrystals, which can be directly used as catalysts with enhanced thermal stability. Additionally, other templates with various crystal phases and/or surface structures could also be utilized to extend the synthesis of Ru nanocrystals. To realize a precise control over the synthesis, a quantitative understanding of each parameter in the synthesis should be achieved, in addition to the qualitative characterizations. For example, if the quantitative parameters such as rate constant and activation energy could be well correlated with the final products, one would be able to quantitatively control the synthesis of Ru nanocrystals and even predict the outcome of a synthesis [1–3].

Another issue lies in the difficulty in producing nanocages at an industrial scale while still maintaining a tight control over their size, shape, and uniformity. This can be addressed by switching the synthesis from batch reactors to continuous-flow systems. The continuous flow reactors offer many attractive features for scaling-up, including the abilities to quickly

achieve thermal and compositional uniformity in a small volume, to rapidly screen reaction parameters, to keep the consumption of reagents low during the optimization process, to operate multiple devices in parallel, and to run the synthesis in a continuous fashion without any interruption [4–6]. In one recent study, our group has demonstrated the fabrication of a fluidic device with a polytetrafluoroethylene (PTFE) tube of 5.8 mm in inner diameter, which could be employed to generate water-in-oil droplets of 0.25 mL in volume at a frequency of 2 Hz [6]. The device could be used to produce several grams of colloidal nanocrystals within just one hour, which represents >200-fold increase in throughput relative to a typical batch-based synthesis. where the throughput can be improved for more than 200 times [4–9].

With respect to the synthetic approaches that I have developed, the involvement of pre-formed seeds is essential to the production of diverse *fcc*-Ru nanocrystals. However, the use of seeds made of a different metal could also result in the introduction of impurities into the Ru shells. Additionally, the diffusion between the atoms of the seeds and the shell during the synthesis or applications would also lead to the variations of composition and surface reconstruction of the nanocrystals, and thereby decay of catalytic performance. To mitigate this issue, more efforts should be devoted to the exploration of new synthetic methods without involving a second metal. Moreover, the catalytic properties of the as-synthesized Ru nanocrystals in the present work was evaluated mainly based on the use of model reactions and simulations. In the future, other significant reactions targeted by Ru including ammonia synthesis, CO oxidation, and CO_2 methanation, should be explored [10–12].

7.3 Notes to Chapter 7

Parts of this chapter are adapted from "Synthesis and Characterization of Ru Cubic Nanocages with a Face-Centered Cubic Structure by Templating with Pd Nanocubes" published in *Nano Letters* [13], "Facile Synthesis of Ru-Based Octahedral Nanocages with Ultrathin Walls in a Face-Centered Cubic Structure" published in *Chemistry of Materials* [14], "Synthesis of Ru Icosahedral Nanocages with a Face-Centered-Cubic Structure and Evaluation of Their Catalytic Properties" published in *ACS Catalysis* [15], "Ru Octahedral Nanocrystals with a Face-Centered Cubic Structure, {111} Facets, Thermal Stability up to 400 °C and Enhanced Catalytic Activity" published in *Journal of the American Chemical Society* [16], "Ruthenium Nanoframes in the Face-Centered Cubic Phase: Facile Synthesis and Their Enhanced Catalytic Performance" published in *ACS Nano* [17], "Hollow Metal Nanocrystals with Ultrathin, Porous Walls and Well-Controlled Surface Structures" published in *Advanced Materials* [18], and "Toward Affordable and Sustainable Use of Precious Metals in Catalysis and Nanomedicine" co-authored by me and published in *MRS Bulletin* [19].

7.4 References

[1] Wang, Y.; Peng, H.-C.; Liu, J.; Huang, C. Z.; Xia, Y. *Nano Lett.* **2015**, *15*, 1445–1450.

[2] Yang, T.-H.; Peng, H.-C.; Zhou, S.; Lee, C.-T.; Bao, S.; Lee, Y.-H.; Wu, J.-M.; Xia, Y. *Nano Lett.* **2017**, *17*, 334–340.

[3] Yang, T.-H.; Gilroy, K. D.; Xia, Y. *Chem. Sci.* **2017**, *8*, 6730–6749.

[4] G. Niu, A. Ruditskiy, M. Vara, Y. Xia, *Chem. Soc. Rev.* **2015**, *44*,5806–5820.

[5] L. Zhang, Y. Xia, *Adv. Mater.* **2014**, *26*, 2600-2606.

[6] L. Zhang, G. Niu, N. Lu, J. Wang, L. Tong, L. Wang, M.J. Kim, Y. Xia, *Nano Lett.* 2014, *14*, 6626–6631.

[7] G. Niu, M. Zhou, X. Yang, J. Park, N. Lu, J. Wang, M.J. Kim, L. Wang, Y. Xia, *Nano Lett.* **2016**, *16*, 3850–3857.

[8] G. Niu, L. Zhang, A. Ruditskiy, L. Wang, Y. Xia, *Nano Lett.* **2018,** *18*, 3879–3884.

[9] H. Wang, G. Niu, M. Zhou, X. Wang, J. Park, S. Bao, M. Chi, Z. Cai, Y. Xia, *ChemCatChem* **2016,** *8*, 1658–1664.

[10] Honkala, K.; Hellman, A.; Remediakis, I. N.; Logadottir, A.; Carlsson, A.; Dahl, S.; Christensen, C. H.; Norskov, J. K. *Science* **2005**, *307*, 555−558.

[11] Joo, S. H.; Park, J. Y.; Renzas, J. R.; Butcher, D. R.; Huang, W.; Somorjai, G. A. *Nano Lett.* **2010**, *10*, 2709−2713.

[12] Sharma, S.; Hu, Z.; Zhang, P.; Mcfarland, E. W. *J. Catal.* **2009**, *266*, 92−97.

[13] Zhao, M.; Figueroa-Cosme, L.; Elnabawy, A. O.; Vara, M.; Yang, X.; Roling, L. T.; Chi, M.; Mavrikakis, M.; Xia, Y. *Nano Lett.* **2016**, *16*, 5310–5317.

[14] Zhao, M.; Elnabawy, A. O.; Vara, M.; Xu, L.; Hood, Z. D.; Yang, X.; Gilroy, K. D.; Figueroa-Cosme, L.; Chi, M.; Mavrikakis, M.; Xia, Y. *Chem. Mater.* **2017**, *29*, 9227–9237.

[15] Zhao, M.; Xu, L.; Vara, M.; Elnabawy, A. O.; Gilroy, K. D.; Hood, Zhou, S.; Figueroa-Cosme, L.; Chi, M.; Mavrikakis, M.; Xia, Y. *ACS Catal.* **2018**, *8*, 6948–6960.

[16] Zhao, M.; Chen, Z.; Lyu, Z.; Hood, Z. D.; Xie, M.; Vara, M.; Chi, M.; Xia, Y. *J. Am. Chem. Soc.* **2019**, *141*, 7028–7036.

[17] Zhao, M.; Hood, Z. D.; Vara, M.; Gilroy, K. D.; Chi, M.; Xia, Y. *ACS Nano* **2019**, doi.org/10.1021/acsnano.9b02890.

[18] Zhao, M.; Wang, X.; Yang, X.; Gilroy, K. D.; Qin, D.; Xia, Y. *Adv. Mater.* **2018**, *30*, 1801956.

[19] Xia, Y.; Zhao, M.; Wang, X.; Huo, D. *MRS Bull.* **2018**, *43*, 860–869.